Technical Report Documentation Page

| 1. Report No. | 2. Government Accession No. | 3. Recipient's Catalog No. |
|---|---|---|
| CA13-2296 | | |

| 4. Title and Subtitles | 5. Report Date |
|---|---|
| **Resilient Bridges: Replaceable Structural Fuses for Post-Earthquake Accelerated Service, Phase I: Analytical Investigation** | **June 2013** |
| 7. Author(s) | 6. Performing Organization Report No. |
| **Xiaone Wei and Michel Bruneau** | |
| 9. Performing Organization Name and Address | 10. Work Unit No. (TRAIS) |
| **Department of Civil, Structural and Environmental Engineering**<br>**School of Engineering**<br>**University at Buffalo, State University of New York**<br>**Buffalo, New York 14260** | 11. Contract or Grant No.<br>**65A0432** |
| 12. Sponsoring Agency Name and Address | 13. Type of Report and Period Covered |
| **California Department of Transportation**<br>**Division of Engineering Services**<br>**Structure Policy & Innovation**<br>**1801 30th Street, MS #9-2/5I**<br>**Sacramento, CA 95816** | **Final**<br>14. Sponsoring Agency Code |
| 15. Supplementary Notes | |

16. Abstract

Research was conducted to investigate the possible implementation of Structural Fuses (SFs) in a typical California bridge for seismic applications. Several types of metallic hysteretic damping devices and connection details between the columns and fuses were considered. Buckling restrained Braces (BRBs) were found to provide the best SF solution. A design procedure was proposed for designing BRBs using the geometry and properties of typical California Bridge bent, but using concrete filled steel tube columns to facilitate connections with the fuses and help achieve the SF design objectives better. In all cases, the bridge columns yield displacement was chosen as the maximum (i.e. target) system displacement as part of the design procedure. The force-deformation relationships of the bridge bent with BRBs obtained from nonlinear pushover and time-history analyses matched the theoretical one used in the design procedure. Recommendations were provided for a next phase of study.

| 17. Keywords | 18. Distribution Statement |
|---|---|
| **Seismic design, concrete bridge, structural fuse, buckling restrained braces, accelerated return to service, post-earthquake performance, resilience, composite columns.** | **No restriction. This document is available to the public through the National Technical Information Service, Springfield, Virginia 22161** |

| 19. Security Classification (of this report) | 20. Security Classification (of this page) | 21.No. of Pages | 22. Price |
|---|---|---|---|
| | | **306** | |

Form DOT F 1700.7 (8-72) Reproduction of completed page authorized

# Resilient Bridges: Replaceable Structural Fuses for Post-Earthquake Accelerated Bridge Construction/Repair under Continued Service

## Phase I: Analytical Investigation

by
Xiaone Wei
Graduate Research Assistant, University at Buffalo
Michel Bruneau
Professor, University at Buffalo

Final Report to the California Department of Transportation
Project 65A0432

Department of Civil, Structural and Environmental Engineering
University at Buffalo, SUNY
Amherst, NY 14260

JUNE, 2013

# Disclaimer

This document is disseminated in the interest of information exchange. The contents of this report reflect the views of the authors who are responsible for the facts and accuracy of the data presented herein. The contents do not necessarily reflect the official views or policies of the State of California or the Federal Highway Administration. This publication does not constitute a standard, specification or regulation. This report does not constitute an endorsement by the Department of any product described herein.

For individuals with sensory disabilities, this document is available in Braille, large print, audiocassette, or compact disk. To obtain a copy of this document in one of these alternate formats, please contact: the Division of Research and Innovation, MS-83, California Department of Transportation, P.O. Box 942873, Sacramento, CA 94273-0001

# Abstract

This report presents research conducted to investigate the possible implementation of Structural Fuses (SFs) in a typical California bridge for seismic applications. The objectives of the structural fuse concept considered here are: (i) concentrate hysteretic energy dissipation to SFs during an earthquake, to prevent damage to other structural elements such as the columns, and; (ii) allow for the possibility to easily remove and replace the fuses if so desired following an earthquake.

Several metallic hysteretic damping devices (such as Buckling Restrained Braces (BRBs), Steel Plate Shear Walls (SPSWs), and Triangular Added Damping and Stiffness Devices (TADAS)) have been considered as SFs to explore their possible implementation in a Reinforced Concrete (RC) bridge bent. Different connection details between the columns and fuses have also been considered. It was found that BRBs provide the best SF solution, and can be used over a wider range of possible applications compared to the others devices considered. A design procedure has been proposed for designing BRBs using the geometry and properties of typical California Bridge bent, but using Concrete Filled steel Tube (CFT) as columns instead. The steel shell of the CFT columns can facilitate the column connections with the fuses. Their greater flexibility for a given moment strength also help achieve the SF design objectives better. Two design configurations were considered, including: (i) a two-column bent with BRBs (which provide SF only in the bridge's transverse direction and would have to be combined with other energy dissipating devices in the longitudinal direction), and; (ii) four-column box piers with BRBs in both the transverse and longitudinal directions. In all cases, the bridge columns yield displacement was chosen as the maximum (i.e. target) system displacement as part of the design procedure (note that, in the cases considered, seismic demands on the bridge columns governed their design). The force-deformation relationships of the bridge bent with BRBs obtained from nonlinear pushover analysis (conducted with

SAP2000) were found to match the theoretical one used in the design procedure. Strength of the CFT columns was not exceeded and the force demands were satisfied under both the seismic and service loads. Nonlinear time history analysis was performed to verify the predicted bridge bent behaviors from the pushover analysis. Displacement demands were found to slightly exceed predictions, and verified with results from earlier studies. Recommendations were provided for a next phase of study.

# Acknowledgements

This study was sponsored by the California Department of Transportation (Caltrans) under research Contract No. 65A0432. This support is gratefully appreciated. Caltrans' project manager was Charles Sikorsky, and Caltrans' Project Advisory Panel consisted of Mark Mahan, Fadel Alameddine, Tariq Masroor and Don Lee. The authors acknowledge their valuable comments and feedback. However, any opinions, findings, conclusions, and recommendations presented in this report are those of the writers and do not necessarily reflect the views of the sponsor.

# Table of Contents

## List of Figure

## List of Table

# Chapter 1 Introduction

## 1.1 Objectives

Most of the existing seismic bridge design procedures still rely, to a large degree, on the detailing of bridge columns for ductile response to provide lateral load resistance. As columns are also part of the gravity load resisting system, inelastic deformations in the columns may compromise the stability of a bridge during an earthquake, or result in permanent damage that is beyond repair afterwards. For well detailed ductile reinforced concrete columns, prevention of the bridge's total collapse can be achieved, but the seismic damage sustained could often require temporary closure of the bridge for days or even weeks to bring the bridge back to service condition.

In a post-earthquake perspective, Accelerated Bridge Construction (ABC) implies an ability to expedite bridge repairs, and if possible, execute those repairs while keeping the bridge open, or at worse limiting disturbance by requiring only short duration closures (typically, accomplishing work at night). Towards that objective, using Structural Fuses (SFs) is attractive because they can be effective in dissipating hysteretic energy in select structural element separate from the columns, in a way such that the columns are left intact and the Fuses can be removed and replaced.

The objective of this project is to investigate whether Structural Fuses could be implemented in typical California bridges (or types of bridges that would be compatible with Caltrans' practice), to address the relevant performance issues, and develop the necessary new knowledge to achieve effective implementations (the focus of this Phase I research being on analytical investigations).

## 1.2 Scope of Work

The design concept for SF systems is presented in Chapter 2, along with a preliminary study conducted to investigate how various types of SFs could be implemented as energy dissipation devices in a representative California bridge bent with Reinforced Concrete (RC) columns; the feasibility of implementing each system was assessed based on the results from this study (in support of that study, a literature review of hysteretic energy dissipation devices that could be used as SFs in bridges is summarized in Appendix A). Several metallic hysteretic damping devices (such as Buckling Restrained Braces (BRBs), Steel Plate Shear Walls (SPSWs), and Triangular Added Damping and Stiffness Devices (TADAS)) were investigated in this preliminary study, for their possible use in a Reinforced Concrete (RC) bridge bent. Also presented in Chapter 2, in a preliminary way, are a few different types of details proposed to connect SFs to the bridge columns.

Following on the finding in Chapter 2 that BRBs provide the most practical SF solution, with a wider range of possible applications compared to the others devices considered, a design procedure to implement BRBs in California bridge bents was formulated and is presented in Chapter 3. To facilitate the design of the SF system and connection of BRBs to the columns, Concrete Filled steel Tubes (CFT) columns were used. BRBs were sized to meet the structural fuse objectives under the governing seismic lateral loads for two proposed bridge bent configurations. (detailed design calculations are provided in Appendix B). First, a two-column bent (considering single inclined BRB and inverted-V BRBs configurations) for which response of the bent under seismic excitation in the transverse direction was studied, understanding that this implementation of the Fuse strategy would have to be coupled with another system in the longitudinal direction (which could be SFs in series with Lock-up Devices connecting the bridge deck to the abutments, for example). Second,

a box-pier configuration was designed to allow implementation of structural fuses to resist earthquake excitations in both the longitudinal and transverse directions. Comparison of theoretical and actual pushover curves obtained using non-linear push-over analysis was performed. The seismic and service load demand check on the CFT columns was conducted.

Chapter 4 presents results from nonlinear time history analyses of all the previously designed bridge bent with BRBs, subjected to spectra-compatible synthetic ground motions. The displacement demands of the system with BRBs were compared with the bare bridge bents without BRBs to prove the benefit of adding BRBs into the bridge bents. These nonlinear time history analysis results also allowed to verify the bridge bent displacements predicted from the design procedure.

Given that BRBs can be added to an existing bridge bent to implement the structural fuse system, details of how BRBs could potentially be connected to transfer their loads to CFT columns, foundations and cap beams are investigated in Chapter 5. Primary focus of the connection to CFT columns is by welding the gusset plate of a BRB to the steel shell of a CFT. Details using concrete anchor bolts or anchor rods to connect BRBs to the foundation or cap beam were also studied. Strength equations for these three types of connection are provided and possible connections details are developed.

Chapter 6 presents conclusions for the work conducted to date, and recommendations for future work.

# Chapter 2 Structural Fuse Concept and Preliminary Study

This chapter illustrates examples of possible options for implementing structural fuses in bridges – either as retrofit of existing bridges, or as possible solutions for consideration in new bridges. The benefit of using structural fuses and its design objectives are first introduced. Possible structural fuses are listed, primarily focusing on the types of metallic hysteretic energy dissipation devices that have been most studied in the literature. The results of a case study investigating how various structural fuses could be implemented in an ordinary California bridge are presented. A following generic bridge case study also examines applicability of the various structural fuses considered to help narrow down the viable choices that will be further studied in subsequent (and more thorough) analyses.

## 2.1 Structural Fuse Concept

### 2.1.1. General

In seismic design, structures are typically designed to undergo inelastic deformations during severe earthquake. In those instances, most of the seismic energy is dissipated through hysteretic behaviors of the structural members, which provide the lateral load resistance. Ductile detailing strategies exist to ensure that the stability of a structure is not compromised if the inability of structural elements to accommodate these inelastic deformations, especially for critical load resisting components. However, even for the most ductile members, permanent system deformation and damage following an earthquake could make repairs expensive, or in some cases impossible. Thus concentrating earthquake damage in a certain part of a structure is desirable, but special design and detailing approaches are needed to facilitate

achievement of such a goal.

Among the many strategies proposed in the past to dissipate earthquake energy and improve structural performance of bridges by minimizing inelastic demands on the primary lateral load resisting elements, the use of hysteretic energy dissipating devices (sometimes called hysteretic dampers) is the approach taken here, combined with a design strategy to limit system displacement such as to concentrate all inelastic demands into the devices.

### 2.1.2. Structural Fuse Design Objectives

A structural fuse system can be divided into two parts, namely, the frame that is intended to remain elastic (i.e., the bridge bent in the case at hand), and the structural fuse that is the hysteretic energy dissipating element. Key parameters that define the proposed structural fuse system are its stiffness, displacement, and lateral shear strength. In addition, ductility factors and strength ratios are important to evaluate the effect of adding structural fuses to the bridge bent. A brief summary of the various parameters that drives the design of structural fuse systems is presented in this section. Most of the information here is a summary of work presented in Vargas and Bruneau (2006) and El-Bahey and Bruneau (2010).

In a generic sense, the overall stiffness of the bridge bent, $K_{tot}$, is equal to the sum of the lateral stiffness, $K_s$, provided by the structural fuse, and the lateral stiffness of the bare bridge bent/frame, $K_f$. Correspondingly, a stiffness ratio, $\alpha$, is defined as the ratio between $K_s$ and $K_f$ such that:.

$$K_{tot} = K_f + K_s \tag{2-1}$$

$$\alpha = \frac{K_s}{K_f} \tag{2-2}$$

The system's displacement ductility capacity, $\mu_D$, which is the maximum ductility that the structural fuse can develop before the frame yields, is defined as:

$$\mu_D = \frac{\Delta_{yf}}{\Delta_{ys}} \tag{2-3}$$

where: $\Delta_{ys}$ = the displacement reached by the bridge bent when the structural fuse yields;

$\Delta_{yf}$ = the yielding displacement of the bare bridge bent

Note that most efficient use of the structural fuse is achieved when the difference between frame and fuse yield displacement is maximized.

Other useful non-dimensional parameters are related to the strength of the system. The seismic demand of the total system, $V_e$, if the system behaved elastically, corresponds to the expected displacement, $\delta_e$. The yield strength of the RC frame, $V_{yf}$, is the force resisted by the frame when the yielding displacement of the column is reached. The yield strength of the structural fuse, $V_{ys}$, is the force resisted by the fuse after the fuse yields.

The maximum displacement ductility that the bridge bent frame needs to withstand is given by the ductility ratio calculated at the system displacement reached for the maximum credible earthquake (expected displacement), $\delta_e$. When the expected displacement $\delta_e$ is in the constant velocity region of the spectrum:

$$\delta_e = \frac{V_e}{K_{tot}} \tag{2-4}$$

The displacement and force values used to calculate the above terms are shown in Figure 2-1, in terms of push-over force-displacement curves for the base frame, the structural fuse system, and the total structural fuse system.

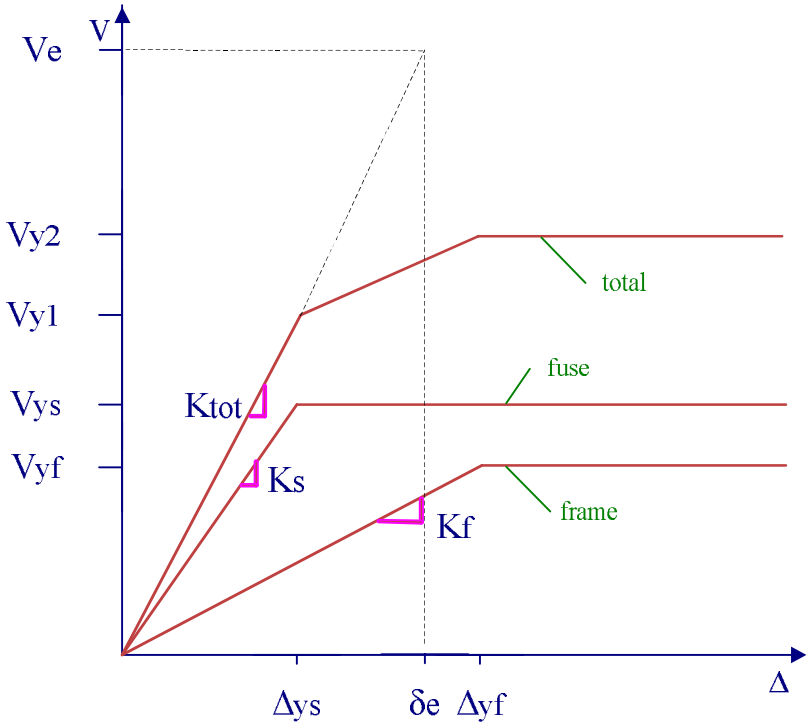


Figure 2-1 General Pushover Curve for the Bridge Bent System with Structural Fuses

For the structural fuse system to be effective, the expected displacement $\delta_e$ should be larger than the yield displacement $\Delta_{ys}$ that the bent reaches when the structural fuse yields, while smaller than the yield displacement $\Delta_{yf}$ corresponding to yielding of the bent columns. Among all the parameters defined above, the ductility factor $\mu_D$ and the stiffness ratio $\alpha$ can be thought of as those that govern the design of the structural fuses for the system.

Vargas and Bruneau (2006a) recommended that the ductility factor $\mu_D$ be no less than 5 to ensure the elastic behavior of the bent, based on results from a parametric study conducted using nonlinear dynamic analysis for a steel building prototype. Along those lines, Bahey and Bruneau (2010) plotted the fuse strength ratio $V_e / V_{ys}$

with respect to the stiffness ratio $\alpha$ for a certain target structural fuse ductility $\mu_D$. The study showed that a slight change in the stiffness ratio $\alpha$, for values smaller than 2, would significantly affect the structural fuse strength ratio needed to achieve a target the structural fuse ductility, $\mu_D$. When $\alpha$ is larger than 2, such a sensitivity is not present. In order to more easily achieve $\delta_e < \Delta_{yf}$, which correspond to elastic behavior of the frame, the suitable range for $\mu_D$ should be $\mu_D \geq 5$. For the sections later used to study the applicability of various kinds of structural fuses, $\alpha$ of 3 and $\mu_D$ of 5 are used. However, numerical analysis of typical bridge bents is required to verify the admissible ranges of these parameters to ensure the desired system behavior.

There is actually no fixed relationship between the bare bent strength $V_{yf}$ and the fuse strength $V_{ys}$. Figure 2-1 is just a schematic to illustrate that there will be a difference between the bare bent and fuse strength.

### 2.1.3. Structural Fuse Configurations for Bridges

Adding structural fuse to the bridge bents could mitigate damage to those bridges by keeping the gravity supporting elements (mainly the columns) intact and concentrating the damage on the fuses. Moreover, if the bare bridge bent remains elastic after the earthquake, self-centering of the bridge would occur once the ductile fuse devices are removed, and the bridge would return to its original undeformed position. For inspection purposes, the fuses and their connections would be visible. The following is a sample of applicable structural fuses using metallic hysteretic damping devices, for bents with either largely or closely spaced columns. Note that further details on each of the metallic hysteretic fuses mentioned are presented in the literature review in Appendix A.

#### 2.1.3.1 Bent with Largely Spaced Columns

### a) BRB Systems

A structural fuse system can be achieved by inserting a pair of Buckling Restrained Brace (BRBs), an inverted-V chevron configuration, into a general Reinforced Concrete (RC) bridge bent, as shown in Figure 2-2. While a sensitivity analysis was performed by El-Bahey and Bruneau (2010) for a single bridge geometry similar to the case investigated here (Figure 2-2) to find how some parameters affect the bridge's seismic performance, that work cannot be used to establish the effectiveness of using BRBs as structural fuses for a broad range of heights and diameters of bridge columns and bent aspect ratio, or for other structural fuse configurations (for example, as diagonal single braces).

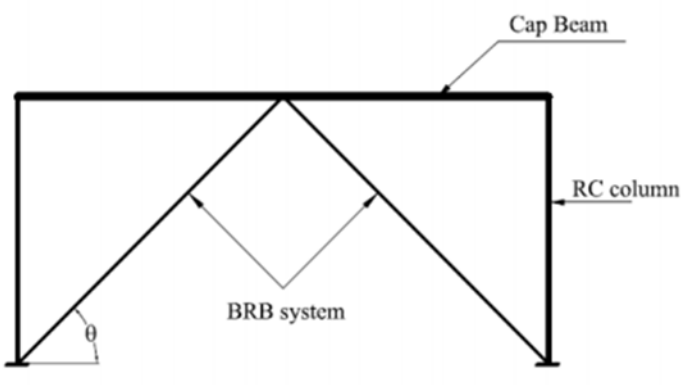


Figure 2-2 Layout of BRB Retrofit Scheme (El-Bahey and Bruneau, 2010)

### b) Eccentrically Braced System

Eccentrically braced systems have been frequently used in steel buildings. For the structural fuse approach taken here, the transformation from traditional bracing to a eccentrically braced system could be achieved by inserting special hysteretic energy dissipative devices between the point of intersection of the diagonal brace members (purposely located below the bent-beam) and the bent-beam itself, as shown in Figure 2-3. The inverted Y-Shaped assembly could have various types of metallic dampers installed between the braces and the overlying concrete bent cap beam. The

link connection at mid-span of the RC beam would require special detailing; an example of how the link could be connected to braces and anchored to the RC beam is shown in Figure 2-4. Horizontal forces are transferred to the brace members through bending and shear forces developed in the ductile steel link, which is sized to dissipate energy at forces lower than those that would produce buckling of the brace members. In other words, while plastic deformations occur in the dissipative device, the diagonal braces have to remain elastic both in tension and compression. Note that, per the structural fuse concept, the connection at the link ends must be detailed to allow easy removal of a link damaged after a severe seismic event.

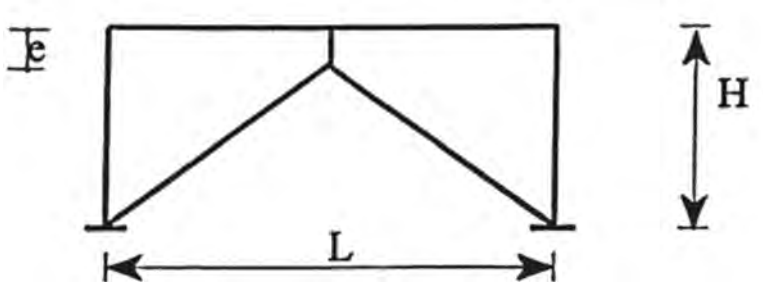


Figure 2-3 Original RC Bridge Bent Frame with Eccentric Bracing Systems (Ghobarah et al ,2001)

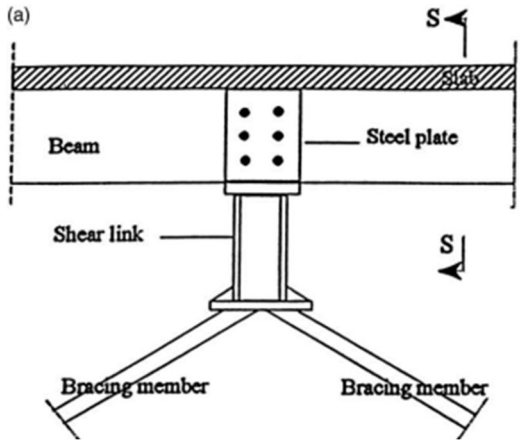

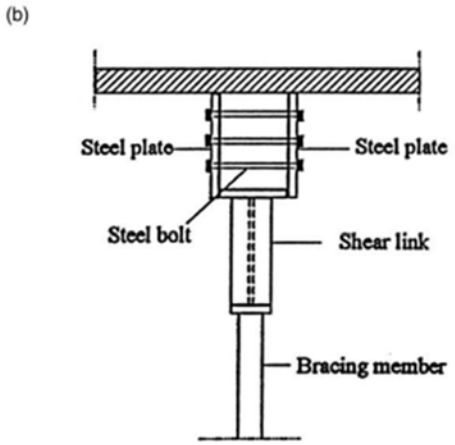


Figure 2-4 Connection Details of a Vertical Steel Link (a) Elevation, and (b) Section S-S (Ghobarah et al., 2001)

The types of ductile links that could be used in this eccentric bracing scheme to provide a stable source of energy dissipation include (among many possibilities):

(1) Steel plates triangular added damping and stiffness (TADAS) device

(2) Steel Shear Panel Links

(3) Steel Slit Dampers

Section 2.3 discusses the applicability of these above mentioned devices as structural fuses.

### 2.1.3.2 Bent with Closely Spaced Columns

When structural fuses are added between two closely spaced RC columns, the total pier behaves like a cantilever beam with the columns acting as flanges and the fuses acting as webs. The expected system behavior before yielding of the structural fuses results in one column being in compression while the other one is in tension. When the fuses yield while the columns remain elastic, behavior changes from the single cantilever system to a moment frame behavior. Each column then behaves independently and the fuses resist part of the lateral loads. For the structural fuse concept, the fuses can be designed to improve the bridge pier performance when subjected to earthquakes.

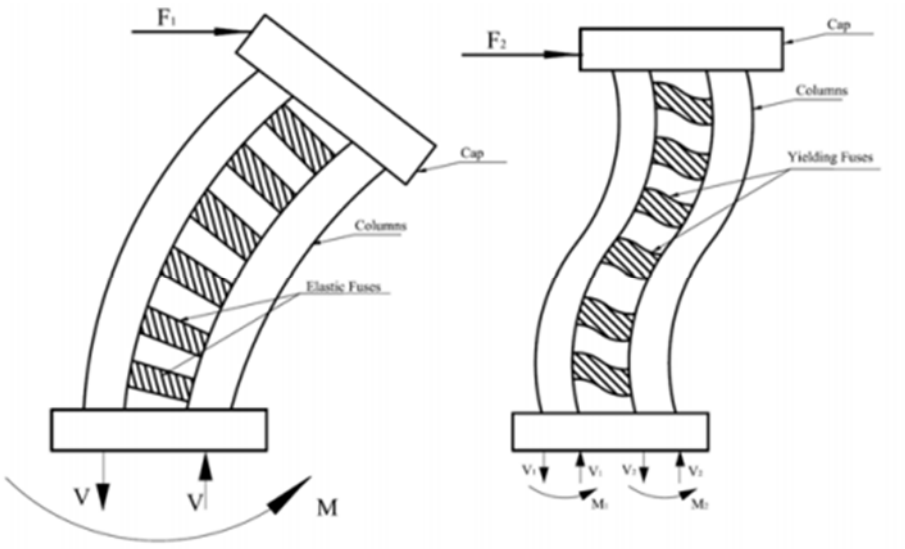


(a) (b)

Figure 2-5 Total System Behavior, (a) Before Yielding of Fuses, (b) After Yielding of Fuses (El-Bahey And Bruneau, 2010)

The types of links that could be inserted between such closely spaced columns to form a unit pier system capable of dissipating hysteretic energy include (among many):

(1) Steel Plate Shear Links (SPSLs)

(2) Short BRBs

(3) Steel plates added damping and stiffness device

(4) Shear Panel Devices

Section 2.3 also discusses the applicability of these devices as structural fuses.

### 2.1.3.3 Steel Plate Shear Wall

The multi-hazard bridge pier proposed by Keller and Bruneau (2009) can also be used here to develop a pier system similar in concept to steel plate shear walls (SPSWs), as shown in Figure 2-6. SPSWs add significant redundancy and strength to the system, as well as a substantially ductile behavior. To achieve the objectives of the structural fuse concept, the vertical boundary elements (VBEs) must remain elastic when subjected to earthquake loads, while the steel plates connected to them yield through

tension field action developing over the pier height (by using suitable size of bridge pier and steel connecting beams, tension field action can be achieved across the entire web plates). In development of the full sway plastic mechanism, plastic hinges would develop at the ends of the HBEs; these plastic mechanisms help mitigate deformation and therefore damage in the columns (VBEs).

The sketch in Figure 2-7(a) provides a 3-D view of the structural system in Figure 2-6(e). An exploded view is shown in Figure 2-7(b). A careful detailing can make the system aesthetically pleasing, while keeping the yielding elements visible for inspection purposes.

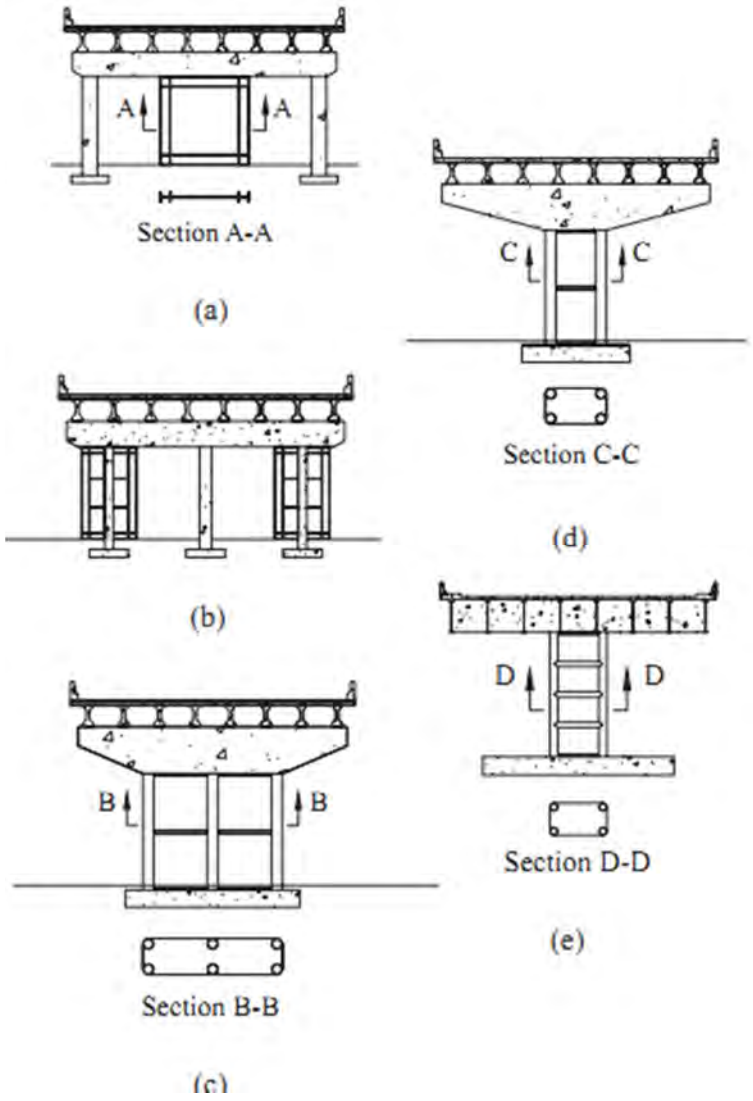


Figure 2-6 Multi-hazard Resistant SPSWs Bridge Pier Concept (Keller D., Bruneau M., 2009)

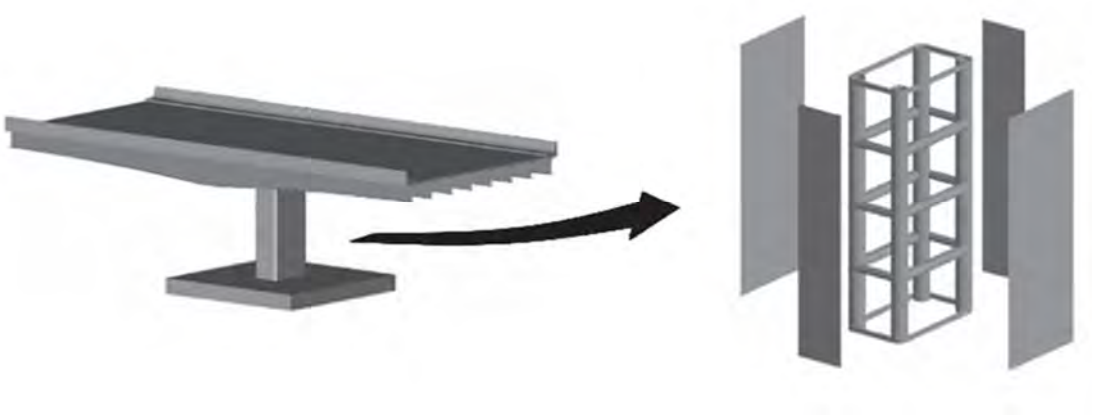

(a) (b)

Figure 2-7 Final Box Pier with SPSWs Configuration (Keller and Bruneau, 2008)

## 2.2 Caltrans Concrete Bridges with Fuses

Before going into generic bridge investigations of applicable structural fuses for different bridge schemes proposed, a case study investigating how various structural fuse concepts could be implemented in an ordinary California bridge was first conducted. This chosen case study bridge was the Caltrans generic bridge "Ordinary Standard Bridge 1" (OSB1, revision date 07-21-2011), for which drawings were provided by Caltrans for this purpose. This two span continuous bridge has a total abutment-to-abutment length of 300 ft and is supported on an integral two-column bent at mid-span, as shown in Figure 2-8.

Note that the case study bridge provided by Caltrans, and described in the "Ordinary Standard Bridge" drawings, had an integral bent. For the non-integral bent, the bare bent stiffness would be smaller than the integral bent (the non-integral bent would be considered free at the top of the cap beam, contrary to the integral bent system which was considered fixed at that location), and the stiffness of the BRB needed to achieve the structural fuse design objective would be different. Comparison of the results obtained using different types of boundary conditions was not part of the scope of this project. However, the methodology presented remains valid, and the structural fuse

concept would still be applicable to the type of California bridges considered in this study.

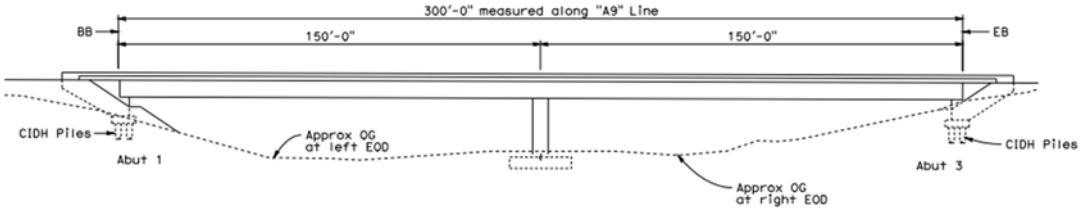


(1) elevation

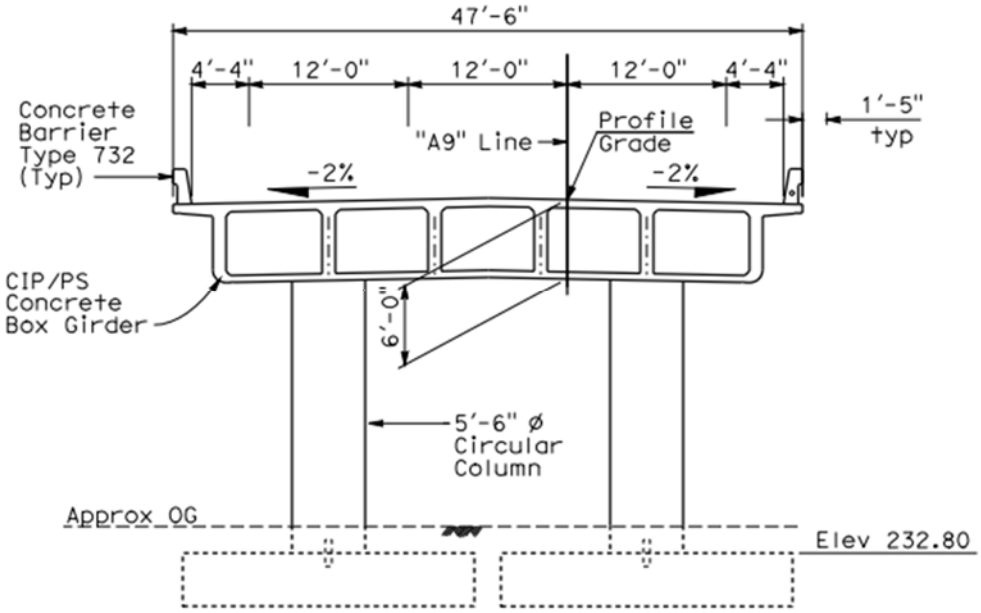


(2)

Figure 2-8 Caltrans ordinary standard bridge 1: (1) elevation (2) bridge bent at the center of the bridge span

## 2.2.1. Retrofit Bridge Bent

For the provided ordinary standard bridge with two RC columns of 5.5 ft in diameter, eight structural fuse schemes have been considered as possible retrofit scenarios, namely:

- BRBs implemented as: (1) Inverted chevron BRB frame, or; (2) Single inclined BRB frame configuration

- SPSWs considered, as: (1) Supplementary SPSW system; or; (2) SPSW Integral with RC Columns
- Eccentrically Braced systems, with vertical links consisting of either: (1) TADAS devices; (2) Added Damping and Stiffness Devices (ADAS); (3) Slit Dampers; (4) Shear Panel Devices

The stiffness ratio of the structural fuses to the bare bridge bent was arbitrarily chosen to be 3, while the structural fuses yield displacement was chosen to be 1/5 of the yielding displacement of the columns in the bent without fuses. Reasons for choosing these parameters are mentioned in a previous section, recognizing that other values can also provide satisfactory implementations. The structural fuse concept is achieved when the columns in the bridge bent do not yield while the structural fuses yield over a range of displacements smaller than the yielding displacement of the columns. Ductility of the structural fuses after yielding helps the system dissipate energy while keeping the bridge columns elastic.

The bridge bents were designed using the acceleration response spectrum shown in Figure 2-9. The expected displacement of the bridge bent with fuses was taken equal to the yield displacement of the RC column. The fuses were designed to provide the required strength based on the pushover curve in Figure 2-1.

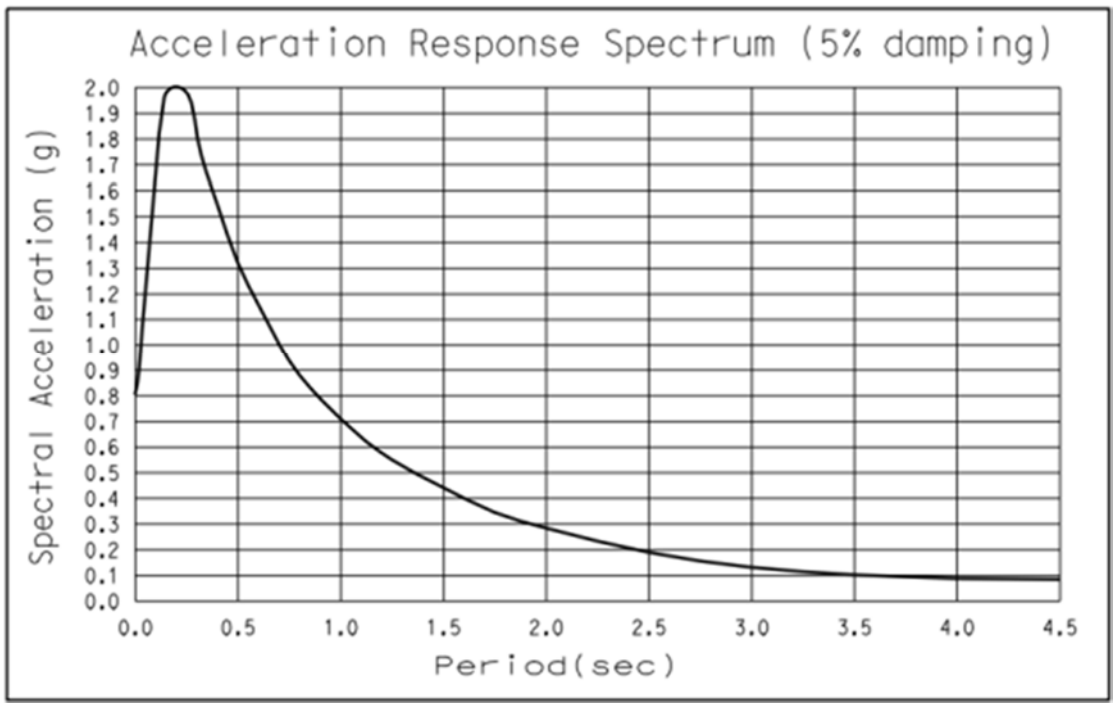


Figure 2-9 Acceleration Response Spectrum with 5% Damping

Trial designs showed that BRBs and SPSWs could be designed to implement the structural fuse concept, but that eccentrically braced system with vertical links consisting of either TADAS, ADAS, or Slit Dampers would have required steel plates of impractical thicknesses or an excessive number of plates (or both). While the use of Shear Panels Devices might have been possible, their length was long to the extent that their stability would be an issue.

### 2.2.2. New Bridge Bent

In addition to the above, structural fuse schemes are also possible for new bridges. To allow comparison of results with the designs for the retrofitted case, the stiffness of the Caltrans bridge bent was kept the same when multi-column bents were considered (note that to achieve this, the diameter of the columns in a multi-column bent would not be the same as in a two column bent). With respect to dynamic properties of these new bridges, the weight of the columns was assumed to be only a small part of the total weight of the bridge, and the period of these bridges (without the fuses) was

still taken to be the same as that of the case study bridge. The same target design spectrum was therefore used for the new-bridge case studies. The additional systems considered that would likely be only applicable to new bridges include:

- Bridge bents with closely spaced columns, linked with: (1) Steel Plate Shear Links (SPSLs); (2) Short BRBs; (3) SPSWs-type plates; (4) ADAS
- Bridge with box pier relying on SPSWs action.

Trial designs showed that the thickness of the SPSLs and ADAS plates would have been excessive, to the point that these systems were deemed impractical. On the contrary, the trial designs showed that BRBs and SPSWs could be designed to work for new bridges.

Note that the case study bridge provided by Caltrans seemed to have columns somewhat larger than those in bridges designed based from the onset to be part of a structural fuse concept. When column diameters are large, it is more difficult to size practical structural fuses to provide stiffness equal to 3 times that of the concrete bridge bent. It should be kept in mind that having the benefit of structural fuses to provide resistance to lateral seismic forces would normally allow the diameter of bridge columns to be less than those considered in the case study, which would help make the structural fuses concept more broadly applicable.

## 2.3 Generic RC Bridge Study with Fuses

After a specific study of the Caltrans bridge with RC bents, a generic bridge with columns of different heights was studied to investigate how structural fuses would perform in a broader range of configurations, with structural elements sized based on simple assumptions. The bridge column heights considered for that purpose were selected to range from 12 ft to 44 ft, because Priestley and Seible (1996) reported this range to encompass most columns encountered in practice. To estimate column

stiffness, a relationship for the diameter of RC columns, *D*, as a function of column height was first developed.

The effect of key parameters on the column yielding curvature, such as longitudinal reinforcement ratio and axial load ratio was described by Priestley et al. (2007) for typical bridge columns. Data from analyses to determine yielding curvature, $\phi_y$, were plotted in dimensionless form in Figure 2-10. The dimensionless yield curvature, $\phi_{Dy}$, is expressed as $\phi_y D / \varepsilon_y$, where $\varepsilon_y = f_y / E_s$ is the flexural reinforcing steel yield strain. As observed in Figure 2-10, the yielding curvature for circular sections does not vary much for different axial forces. The average dimensionless curvature of 2.25, along with lines at 10% above and 10% below this average, is shown in that figure. Though the data is generated for a specific column size and material strengths, the dimensionless results are expected to apply, with only insignificant errors, to other column sizes and material strengths within the normal range expected for standard design (Priestley et al. 1997), leading to the following equation for circular columns:

$$\phi_y D = 2.25\varepsilon_y \pm 10\% \tag{2-5}$$

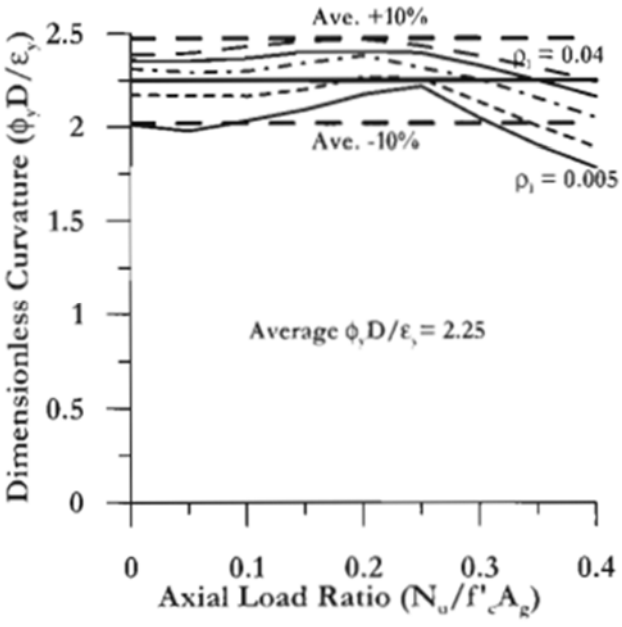


Figure 2-10 Dimensionless Yield Curvature for Circular Bridge Columns (Priestley et al., 2007)

An estimate of column yielding displacement of $\Delta_y = 0.005H$ was used (Priestley et al. 1997). By relating the yielding displacement and curvature of the column, an estimate of the diameter of circular RC column, *D*, was obtained as a function of its height, *H*.

The stiffness of the bridge bent column can be related to the column diameter *D*, as the inertia of the section *I* can be expressed as $\frac{\pi D^4}{64}$.

For cantilever column, $K = \frac{3EI}{H^3}$ (2-6)

For fixed-fixed column, $K = \frac{12EI}{H^3}$ (2-4)

Bridges with both cantilever and fixed-fixed end columns were considered. The same values of structural fuse design parameters were chosen as for the Caltrans bridge, namely, 3 for the stiffness ratio of the structural fuses to bare bridge bent, and 5 for the yielding displacement of the column to the structural fuses. Therefore, the required stiffness and yielding displacement of the fuse can be derived regarding to the height of the bridge bent.

Bridges that needed retrofit and new bridge construction were both considered in this generic bridge study. For two RC columns braced by a single inclined BRB, it could be demonstrated using the above equations that the strength of the BRB is proportional to the square of height $H^2$. There is no known factor that could limit the strength of a BRB. However, because this is a relatively new structural system, building specifications require full scale testing of BRBs to demonstrate satisfactory performance before implementation, unless tests results are already available for BRBs of equivalent strength from the same manufacturer. At the time this parametric study was conducted, it was assumed that the largest BRBs that had been previous tested had

a strength 2155kN (485kips), based on information provided by Aiken et al. (2000). Subsequent personal communications with BRB suppliers revealed that BRBs of up to 2000 kips have been tested to date, but the information below is nonetheless valuable in illustrating the range of column heights for which structural fuses can be implemented for a given limit on BRB strength (note that for stronger BRBs, problems will arise as connections will become progressively more difficult to accomplish). Note that bridge bents with fixed-fixed columns would require smaller BRBs than the ones with cantilever columns. Structural fuse calculations indicated that the required BRBs strength would be less than 485 kips for the case of a bridge bent with fixed-fixed column if the height of the columns did not exceed 16.5 ft. However, all BRBs for the comparable bents having cantilever columns (i.e., fixed-pin ends) required a strength exceeding 485 kips. Theoretically, nothing prevents the fabrication of stronger BRBs. However, the real challenge lies in the development of connections to transfer those loads to existing concrete columns.

For the case of RC bridge bent having a vertical link between the cap beam and chevron brace, the possible use of TADAS, ADAS, Slit Dampers, and Shear Panel Devices were investigated to serve as potential vertical links. It was found that either the thickness of the required steel panel was excessive, or the design required an impractically large numbers of steel panels. The stability of the vertical link would also be an issue making the implementation of vertical hysteretic links difficult.

As mentioned previously, structural fuses can also be installed between closely spaced columns in bridge bents. The distance between such closely spaced columns in this study was assumed to be equal to the diameter of the column, recognizing that other values could also be used. Assuming that SPSLs of up to 0.5" thickness were acceptable, such SPSLs could be used in bridge bent having fixed-fixed columns of up to 27 ft. No such solution was found for bridges with cantilever columns. The

use of ADAS plates between the columns was also considered but found to require too many plates to be practical. Note that connections of SPSLs or ADAS plates to the RC columns would require steel-and-concrete connection all over the columns' height. The option of introducing BRBs between the columns was also considered. If BRBs' strength of up to 485 kips could be developed (within their short length), BRB could be a solution for cantilever bridge column shorter than 24 ft, and for fixed-fixed bridge columns ranging from 12 ft to 44 ft.

For bridge bents with supplementary SPSWs system of the type shown in Figure 2-6a, assuming a steel plate width equal to twice the column diameter, solution was found possible for column height ranging between 20 ft and 42 ft for cantilever columns and fixed-fixed end columns, respectively, providing the SPSWs' thickness did not exceed 0.5 in. For SPSWs that do not fill in the full space between the columns, additional steel column acting as Vertical Boundary Elements would be required, so this didn't prove to be an attractive solution.

For the case of SPSWs inserted between closely spaced RC columns, for various ratios of the wall width-to-column diameter, the required thickness of the SPSWs plate is inversely proportional to the width of the SPSWs for a given column height. For SPSWs system integral with RC columns in Figure 2-6b, it requires two steel columns on each side of the RC column. For a certain ratio of steel plate widths to column diameter, the thickness of SPSWs is proportional to the bridge height.

The required thickness of the SPSWs in a box-pier configuration, as in Figure 2-6e but with two box piers, is half of that for the SPSW system integral with the RC columns. If the ratio between the wall's steel plate width and the column diameter is 2 in all these three cases, it was found possible to limit the thickness of the SPSWs steel plate to less than 0.5 in for columns ranging from 12 ft to 44 ft tall for both cases

of cantilever and fixed end columns. Note that for SPSWs, link beams serve as horizontal boundary elements and need to be designed to ensure that the force demand on the columns remain within their capacity.

In conclusion, BRBs and SPSWs are more easily implemented as structural fuses in RC bridge bents, given the assumptions stated above. No other options were found to be practical. Note that, the stiffness ratio and the fuse ductility were arbitrarily chosen for the generic study. These two parameters are not exactly independent. More studies needs to be done to establish appropriate admissible ranges for cases where this dependency exists for fuses to be implemented in each of the above configuration.

## 2.4 Connections

For structural fuses to be effective when added to existing concrete bents, connection concepts must be formulated to transfer these forces to the concrete bridge components. Three different strategies were investigated for the fuse-column connections, namely: (i) steel plates wrapped around concrete columns ("jacketed columns") to which other elements can be connected; (ii) anchor bolts embedded in the concrete columns; and (iii) through-columns anchor rods. This section only investigates the inverted-V chevron BRBs and inserted SPSWs between closely spaced columns for the typical Caltrans bridge bent configurations described in Section 2.2. The connection of SPSW's steel plates to RC columns needed anchor rods through the entire height of the columns, while the BRBs only requires anchor rods connections at the two ends where BRBs were connected to the columns.

### 2.4.1. Steel Jacketing

Steel jacketing is an external encasement of columns achieved by welding

prefabricated steel shells in situ. It has commonly been implemented as a seismic retrofit approach for RC column bridges. Here, it is solely considered as a detail to facilitate the connection of hysteretic energy device (via steel plates) to RC columns. In this application, the steel plates transferring the forces developed in the structural fuse are welded to the steel jacket, which is itself wrapped around the concrete columns.

The steel jackets that have been typically used in the retrofit of RC columns are slightly oversized and the gap between the jacket and column is usually filled with cement-based grout to ensure composite action between the jacket and column. Figure 2-11 shows the schematic seismic retrofit of a RC bridge column using steel jacketing. Its purpose in seismic applications is to enhance the flexural and shear performance of deficient bridge columns (Chai et al., 1994).

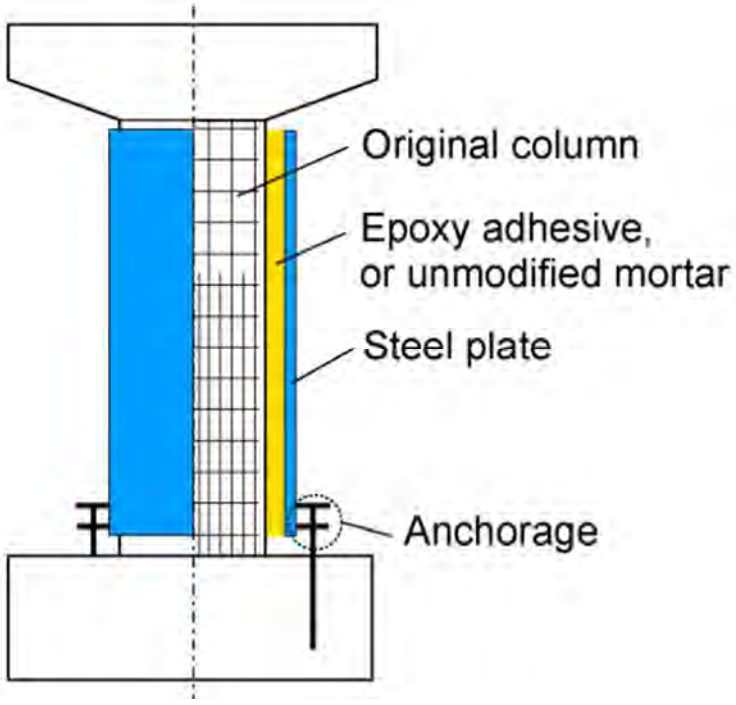


Figure 2-11 Steel jacketing of a RC column (Zhang et al., 2009)

Note that steel jacketing is typically not extended into the foundation or cap beam of the column, as vertical gaps are left between the steel jacketing and the foundation and cap beam, such as to not increase the column flexural demands on those adjacent

structural elements. The enhancement to the bridge column is in terms of greater flexural ductility, as well as to prevent shear failures. The steel jacketing does not help the RC column resist additional axial compression force or moment induced by lateral displacement.

When a steel jacket is subjected to the axial tension from a steel plate perpendicular to its surface (i.e. a "branch plate"), the concrete columns inside of the jacket helps the side faces of the steel jacket from getting close to each other, as shown in Figure 2-12. Therefore, the perpendicular pulling forces *N* that can be resisted by such steel jackets may be larger than on a hollow section of same thickness and diameter.

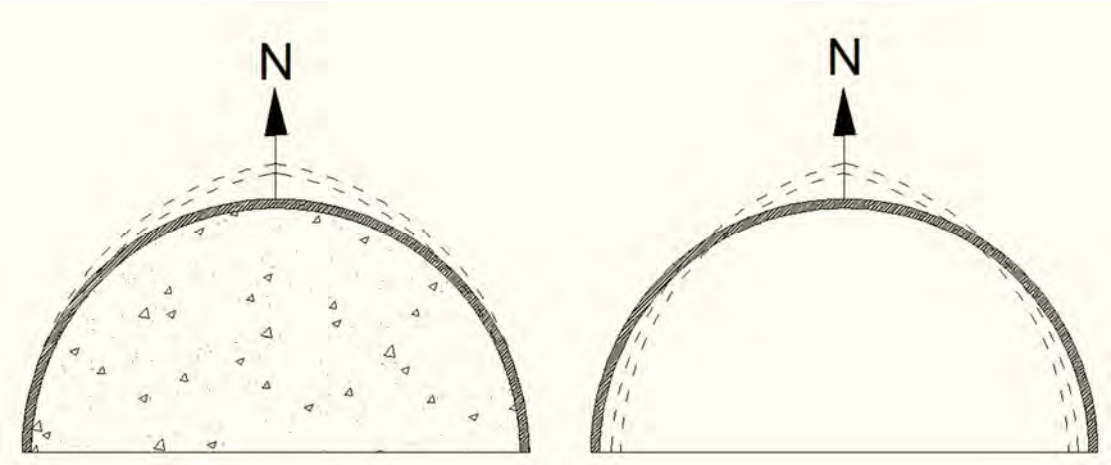


Figure 2-12 (a) Concrete column wrapped with steel jacketing under perpendicular tension loading; (b) CHS section under perpendicular tension loading

Equations for the strength that can be developed when tension is acting on longitudinal branch steel plates connected to a Circular Hollow Section (CHS) are provided by the CIDECT design guide No.1 (Wardennier et al., 2008). Longitudinal branch plates are subjected to either tension force, shear force, or both. However, no equations have been found to calculate the strength of comparable Concrete Filled Tubes (CFT) under such pulling load.

Therefore, a SAP2000 model replicating the conditions of a steel jacket around a

concrete column was built to investigate the load carrying capacity of the steel jacket to transfer tension loads acting perpendicularly to concrete columns. In this computer model, the symmetry of the steel jacket around the circular concrete column was considered, and only half of the steel jacket was modeled. To capture the location and sequence of plastic hinging in the steel jacket due to the applied tensile load, the arch was divided into multiple frame elements, as shown in Figure 2-13. Each frame would have plastic hinges assigned at each end. At the joint of each frame, a gap link was used to account for the presence of concrete resisting inward deformations of the steel tube. The gap link element was set to have zero stiffness when the gap was larger than zero, which allowed the steel jacket to separate from the concrete columns under tensile load. The stiffness of the gap link was set to be large (arbitrarily set to be 100,000 kips/in) when the gap closed and resisted compression, which kept the steel jacket from moving inward.

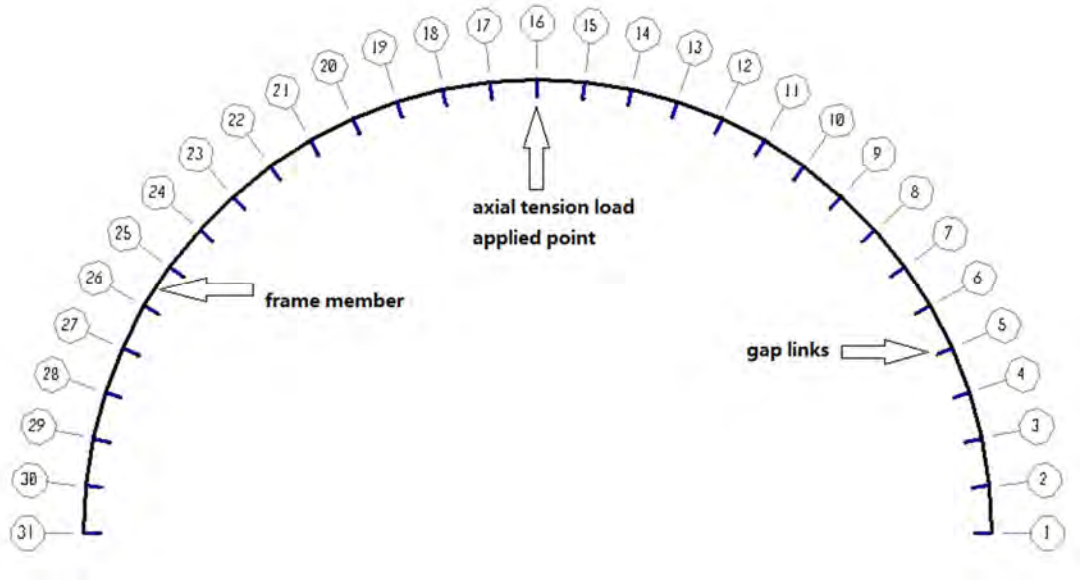


Figure 2-13 Steel jacketing plate model in Sap2000

The maximum applied axial load reached in this non-linear inelastic analysis was obtained as a plastic mechanism developed in the steel jacket plate. The plastic hinges appeared at the locations where the steel plate yielded and the plastic moment of the steel plate was reached (the analysis also took into account axial forces concurrently developing in the arch and reducing flexural strength). Only a segment

of the steel jacket was considered here, as this conservatively neglects increased strength that could be provided by the constraint at the ends of the plate in the longitudinal direction; this would correspond to an exact solution for a uniform tension load applied along the entire length of the column. Therefore the width of the arch in this model was arbitrarily taken as 1 in (unit length), for expediency, to get the strength of the jacket when resisting a perpendicular distributed tensile force.

Case studies considering the column diameter and thickness of the steel jacket were conducted in SAP2000 to get the pulling strength. For the resulting strength, it was found that the required length of the BRB's gusset plate is substantial if a BRB is only connected to the bottom of the column rather than also to the foundation. It was also found that the steel shell thickness required to resist the tensile typically developed by SPSWs would be unpractical.

### 2.4.2. Anchor Bolts

Headed steel studs, as cast-in anchors, are usually welded to a steel endplate and encased in concrete for connections. It has been the most common method for transferring forces between steel and concrete in composite constructions. The failure modes of such anchors bolts are shown in Figure 2-14. The strength corresponding to each failure mode is provided in ACI 318. Various limit states of "in-field" anchors (defined as the case when the edge distance of the anchor to the free side of the concrete member is greater than a specified value such that edge failure cannot develop) are listed below corresponding to the failure modes in Figure 2-14.

(1) Steel strength of anchors in tension (Figure 2-14 (a)i);

(2) Steel strength of anchors in shear (Figure 2-14 (b)i);

(3) Concrete breakout strength of anchors in tension (Figure 2-14 (a)iii);

(4) Concrete pullout strength of anchors in tension (Figure 2-14 (a)ii);

(5) Concrete pryout strength of anchor in shear (Figure 2-14 (b)ii)

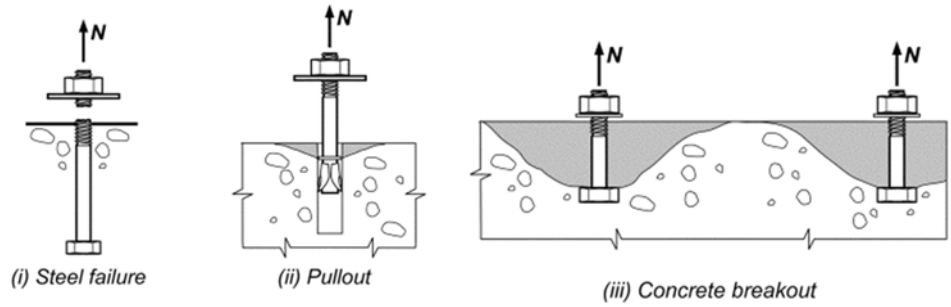


(a) Failure modes for anchors in tension

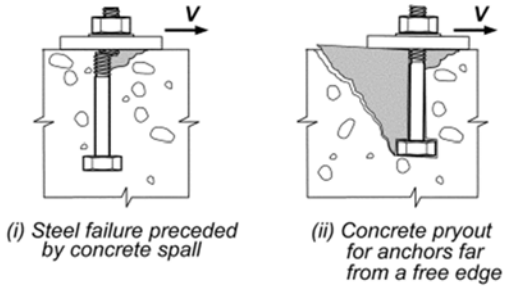


(b) Failure modes for anchors in shear

Figure 2-14 Failure modes of anchors under different conditions (ACI 318 Appendix D Commentary RD.4.1)

A generic configuration of the headed studs that connect a steel endplate to a RC column is shown in Figure 2-15. The anchors are welded to the steel endplate, to which the structural fuse can be connected to. There can be several rows and columns of headed studs.

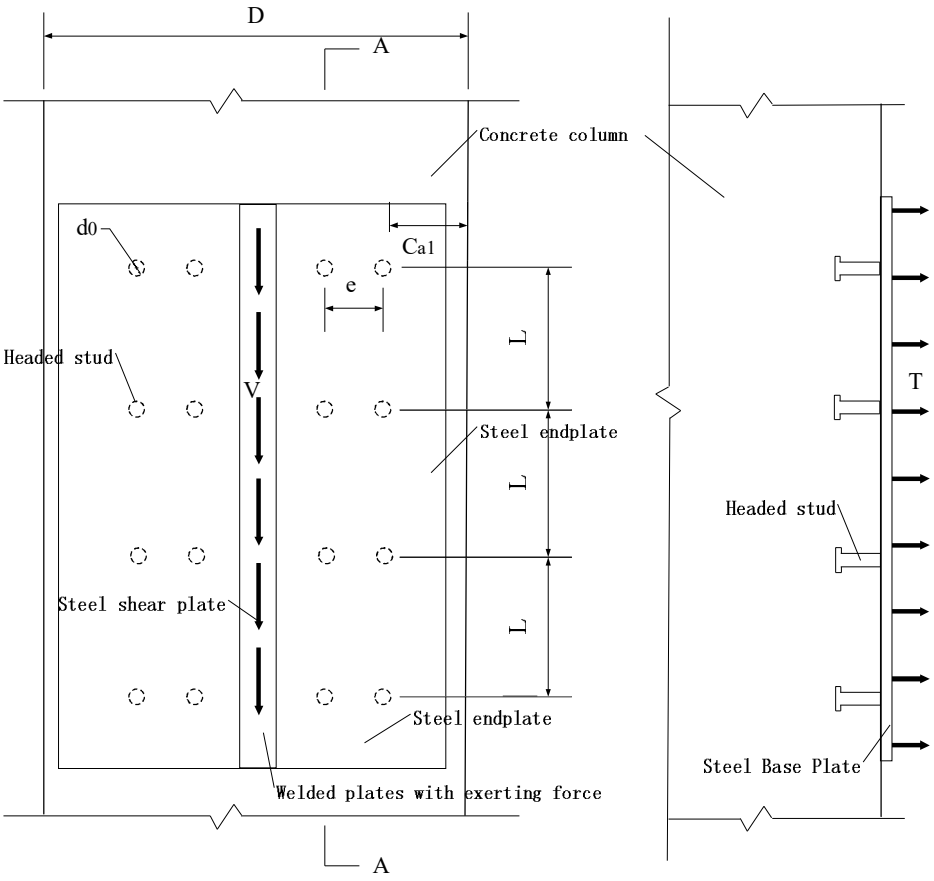


Figure 2-15 (a) A group of anchors loaded in shear parallel to the side edge and illustrated dimensions (b) View of Section A-A in (a)

A case study of specified headed studs was performed to obtain their strength under tensile and shear forces using equations provided in ACI 318 and PCI (2004). The cast-in headed studs with the largest available shank diameter, $d_0$, of 7/8" (per PCI 2004) were used. The shear and tensile strength of these studs was evaluated as a function of the embedded length of headed studs. Group effect was excluded by providing the code-required distance between each headed stud. Simple connections of SPSWs and BRBs were evaluated using the largest strength that can be developed by a single headed stud. The available contact area between the concrete column and steel endplate was less than necessary for the studs to develop the needed strength (in both cases, the required number of headed studs was found to be impractical).

## 2.4.3. Anchor Rods

The connections of steel plates to RC columns can also be accomplished using bolted endplates, using the layouts shown in Figure 2-16. Concrete or grout can be used to fill the space between the endplates and the circular RC columns. The anchor rods are installed in conduits prior to casting RC columns, or in ducts drilled in the existing RC columns. Then the anchor rods are fixed by the nuts at each ends.

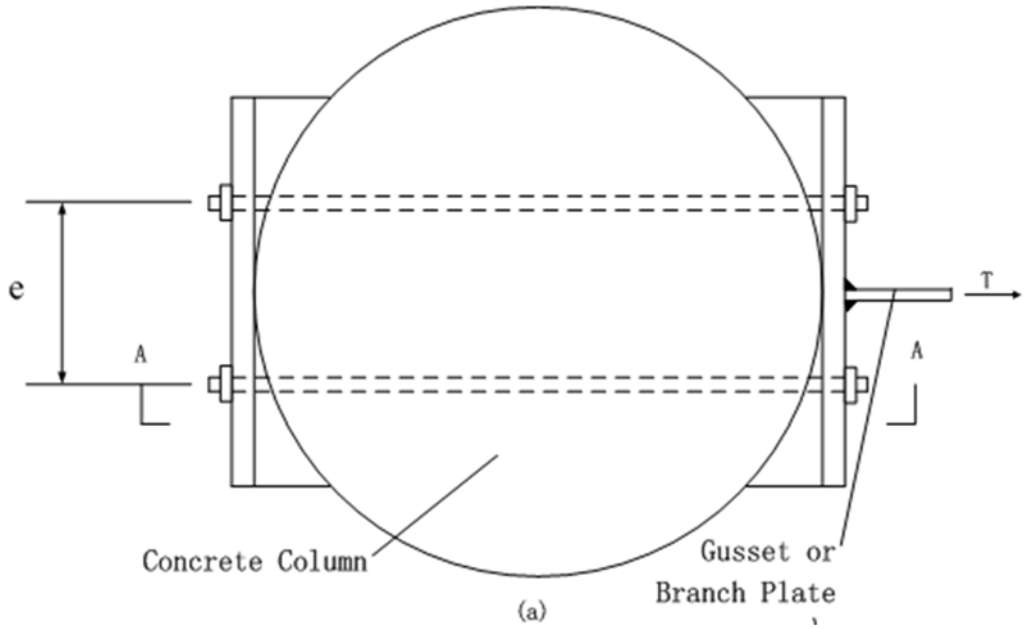

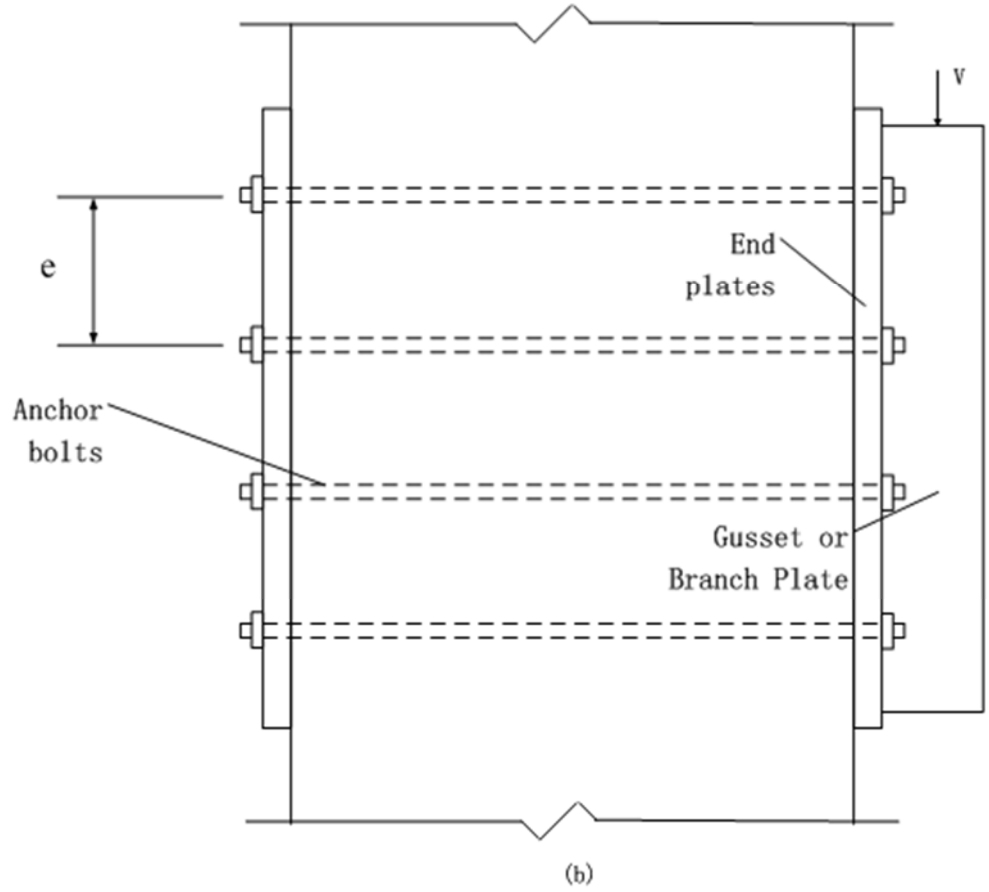


Figure 2-16 (a) Connections of steel plates with circular concrete columns using anchor bolts (b) Section view of A-A

Different types of cast-in-place anchor rods are shown in Figure 2-17. These include anchor rods with a head, threaded rods with nut, threaded rods with a plate washer, hooked bars or U-bolts. The most common anchor rods are type c in Figure 2-17. Anchor rods are supplied in conformance with ASTM F1554 “Standard Specification for Anchor Bolts, Steel, 36, 55, and 105 ksi Yield Strength.” ASTM F1554 recommends the use of a standard Grade 36 rod, ¾ in diameter, for most practical cases. However, when more strength is required, it is possible to increase the rod’s diameter up to about 2 in for ASTM F1554 Grade 36 steel before switching to a higher-strength material grade.

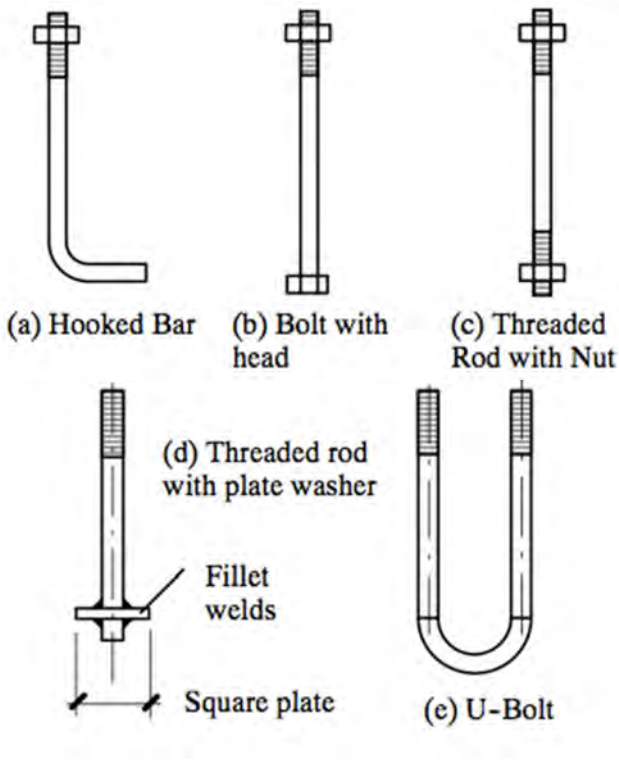


Figure 2-17 Types of Anchor Bolts (Hogan and Thomas, 1994)

The endplate thickness, anchor holes size and the distance between the anchor rods must be designed to ensure transfer of the force from the endplate to the anchor rods and allow an even redistribution of forces. The design of the end plate is not considered here. Simple connections of SPSWs and BRBs were designed based on strength of single anchor rods (i.e., neglecting strength reduction for group effect), but connecting to columns using anchor rods was found to be not practical due to the limited space available.

### 2.4.4. Comparison

For the two bridge bent configurations considered for the typical Caltrans bridge investigated, none of the three details considered was found to be fully satisfactory to connect the fuse to RC columns. The three types of connections considered required the RC columns to have an added steel component to achieve connection: either a steel jacket or a bolted end-plate, to which the structural fuses could be connected. This observation suggests that Concrete Filled steel Tubes (CFT) columns would be

an effective substitute for RC columns in new bridge construction, relying on the CFT's steel shell to facilitate connections. This type of column will be considered in subsequent Chapters. In particular, the strength that can be developed by the shell of a CFT (or steel jacket) under a perpendicularly applied tensile force is investigated more specifically in Chapter 5 (together with corresponding anchor rods and headed studs details for comparison purposes). Comparing details required to connect SPSWs and BRB to columns, it was found that SPSWs required connection over the entire column height, while BRB connections could be located to the locations at their ends, which might be more cost effective to implement (although such effectiveness was not calculated).

## 2.5 Conclusion

Based on preliminary studies using both a specific Caltrans standard bridge and generic RC bridge, BRBs and SPSWs were found as the most practical energy dissipating systems for the implementation of structural fuses in a bridge bent. SPSWs, because they require the design of link beam (Horizontal Boundary Element) and overall assessment of the SPSWs yielding force demand on the columns, are more complicated to implement than BRBs. Besides, SPSWs require to be connected through the entire height of the columns, whereas the connections of BRBs are only needed at the location where they are connected to the columns at the two ends.

The above results show challenges in connecting structural fuses to some RC columns (when neglecting the possibility of partially connecting to the footing). Work on connections indicated the advantage of using steel jackets around columns compared to other types of details considered. Based on that observation, for applications of the SF concept in new bridges, the following chapters focus on the BRBs design in bridge bents with CFT columns. Such CFT columns are also able to provide the needed strength with a smaller stiffness, which helps achieve the SF objectives.

# Chapter 3 Design Example of Structural Fuse in Bridges using BRBs

Per discussion in Chapter 2, the design procedure for structural fuses in bridge bents were developed focusing on BRBs, for the two bent configurations described in this chapter. Then, the two bridge bents with BRBs were analyzed using SAP2000 to verify that the force demands from seismic and service load did not exceed the capacity of the columns. The same Caltrans Ordinary Bridge geometry described in Section 2.2 was used here. Recall that the bridge bent is located at the center of that bridge.

## 3.1 General

Two scenarios having different column layout were considered. First, a two-column bent with BRB fuses and having the same column spacing as Caltrans' Ordinary Bridge example was studied. Concrete Filled Tube (CFT) columns were used, and single inclined BRB and inverted-V BRBs configurations were both considered). Response of the bent to seismic excitations in the transverse direction was studied, understanding that this implementation of the fuse strategy would have to be coupled with another system in the longitudinal direction (which could be structural fuses in-series with Lock-up Devices connecting the bridge deck to the abutments, for example).

Second, a box-pier configuration concept that allows implementation of BRBs to resist earthquake excitations in both transverse and longitudinal directions was studied. In this concept, the BRBs are inserted between closely spaced CFT columns to form the box-pier configuration.

In both cases, although the use of RC columns was considered in the early phases of the

study, the final designs were conducted with concrete-filled steel tube columns, as this provided many advantages for the current application. Figures of the two bridge cases are shown in analysis models in later sections.

## 3.2 Design Procedure

This section provides a general overview of the design procedure followed to design the structural fuse system, and summarizes the underlying assumptions made in the process. The flow-chart in Figure 3-1 summarizes this procedure, recognizing that the process was iterative.

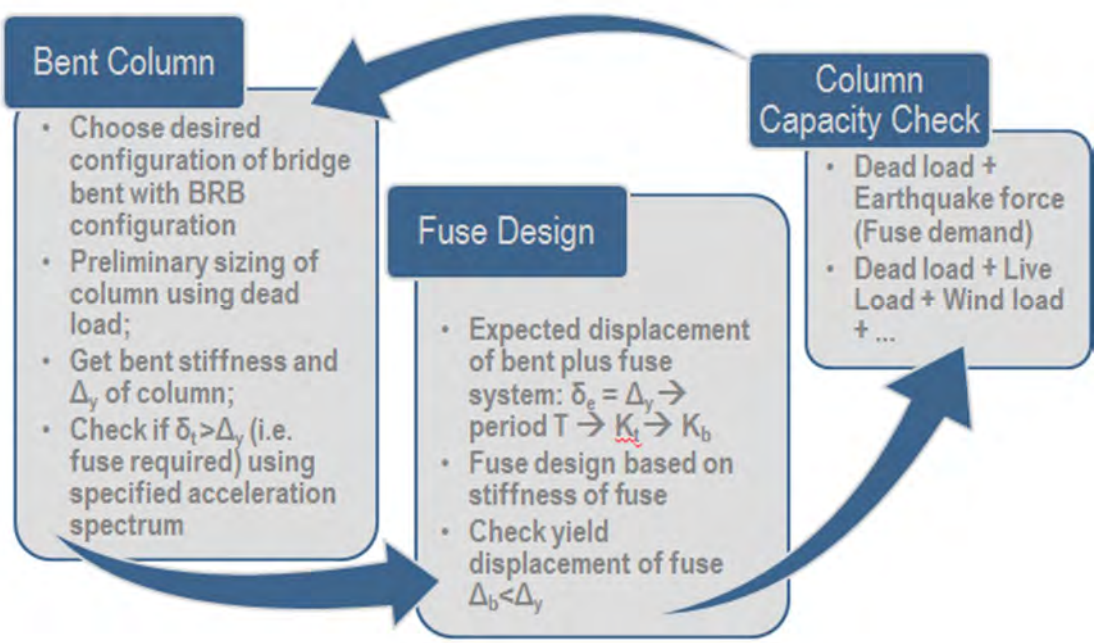


Figure 3-1 Design Flow-chart of Bridge Bent with BRBs

Following that flow-chart, the design procedure can be broken down in the following steps:

**STEP 1**: **Calculations of the Bent Target Displacement and Bare Bent Stiffness**

In this step, the maximum displacement permissible with the structural fuse concept is set equal to the yield displacement of the column (also called the "expected displacement" in subsequent steps). This can be calculated knowing the stiffness of

the bare bent. For preliminary design, to size column diameter, the gravity dead load of the bridge's superstructure tributary to the column bent was assumed to be distributed equally to each column of the center bridge bent, and dead load demand was taken to be approximately 5% of the overall axial strength of each CFT column (considering the column buckling). Note that CFT columns have no reinforcement in the concrete infill and that their properties and strengths (in particular, their axial compressive and tensile strength, flexural strength, and yielding curvature) were obtained through fiber analysis using Section Designer in SAP2000. These strengths were compared with the equations provided in the AASHTO LRFD Seismic Design Specification (2009) and AISC Steel Construction Manual (2010) in Appendix D. The yielding displacement, $\Delta_y$, and the effective stiffness of the CFT column, $K_{col}$, were calculated as:

$$\Delta_y = 2\phi_y \frac{\left(\frac{h}{2}\right)^2}{3} \tag{3-1}$$

$$K_{col} = \frac{2M_y}{h\Delta_y} \tag{3-2}$$

where: $\phi_y$ is the yielding curvature of the CFT section;

$h$ is the height of the CFT column;

$M_y$ is the yielding strength of the column;

**STEP 2: Calculation of Required Fuse Stiffness**

The fuse stiffness required is selected to be the minimum value required to prevent column yielding. For this purpose, the expected displacement of the bridge bent with BRBs, $\delta_e$, was calculated based on the assumption of "equal elastic and inelastic displacements for a given period" commonly used in earthquake resistant design. As mentioned in STEP 1, it was set to be equal to the yield displacement of the

column, $\Delta_y$. The provided acceleration spectrum gives a relationship between the maximum acceleration, *S,* and period, *T* in Equation 3-3. The total stiffness of the bridge bent with BRBs was derived for the given superstructure weight, $W_{super}$ in Equation 3-4, assuming that no lateral resistance was provided by the abutments. The self-weight of the columns was ignored since it is typically small compared with that of the superstructure. The expected displacement of the bare bridge bent, $\delta_t$, was calculated using Equation 3-5, and checked to be larger than the columns' yielding displacement $\Delta_y$, thus making the addition of BRBs worthwhile in reducing the displacement demand.

$$\delta_e = S_a T_s^2 \frac{g}{4\pi^2} = \Delta_y \tag{3-3}$$

$$K_t = \frac{W_{super} 4\pi^2}{386 T_s^2} \tag{3-4}$$

$$\delta_t = S_b T_1^2 \frac{g}{4\pi^2} > \delta_e \tag{3-5}$$

where: $S_a$, $S_b$ are the accelerations from the target spectrum and respectively corresponding to the period of the bridge bent with BRBs, $T_s$, and period of the bare bridge bent, $T_1$. $T_1$ equals to $\sqrt{\frac{W_{super} 4\pi^2}{386 K_c}}$;

$K_t$, $K_c$ are, respectively, the stiffness of the total bridge bent with BRBs, and of the bare bridge bent

**STEP 3: BRB Design**

BRB were designed to reach a strain limit of 1.5% in their yielding core when the columns reach the yield displacement, $\Delta_y$. Note that strain up to 3% can be typically developed in BRBs and that such a limit could have been used instead, resulting in smaller BRB sizes. Figure 3-2 schematically illustrates the composition

of a BRB, identifying three specific zones: the yielding core in the center of the BRB that is encased in a mortar-filled steel hollow section to restrain buckling; the buckling restrained transition segments, and; the non-yielding unrestrained end zones at the two ends.

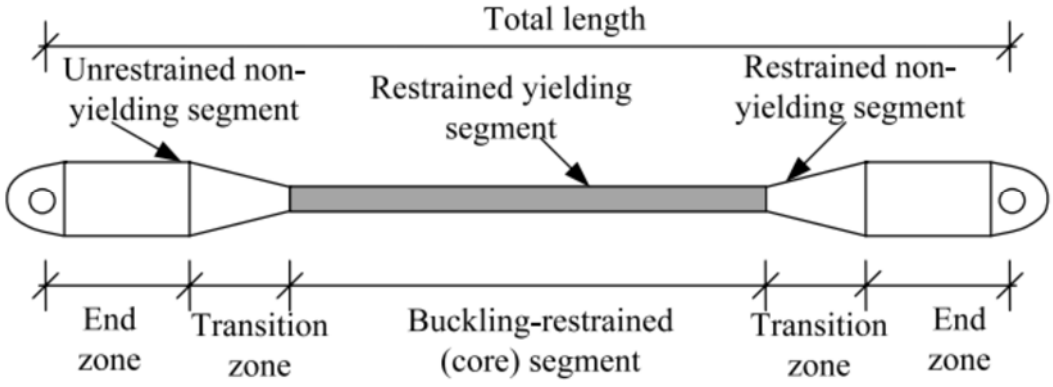


Figure 3-2 Typical section of a BRB (Sahoo and Chao, 2010)

For the two general bridge configurations considered in this study, namely, two-column bent with BRBs and box-pier bent with BRBs, the area and length ratio of the required BRBs are designed differently.

***(i) Two-CFT-column bent with BRBs***

Behavior of this system depends on the length ratio of the BRB, $c_b$, which is the ratio of the yielding core length to the entire BRB length (given by Equation 3-7), and the angle of the BRB from the horizontal, $\theta$, which differs for the single inclined BRB case and inverted-V chevron BRBs case, as shown in Figure 3-3.

$$c_b = \frac{\Delta_y}{\varepsilon_{bm} L_{brb}} \cos\theta \tag{3-7}$$

where: $\varepsilon_{bm}$ is the strain limit of BRB's yielding core;

$L_{brb}$ is the length of BRB;

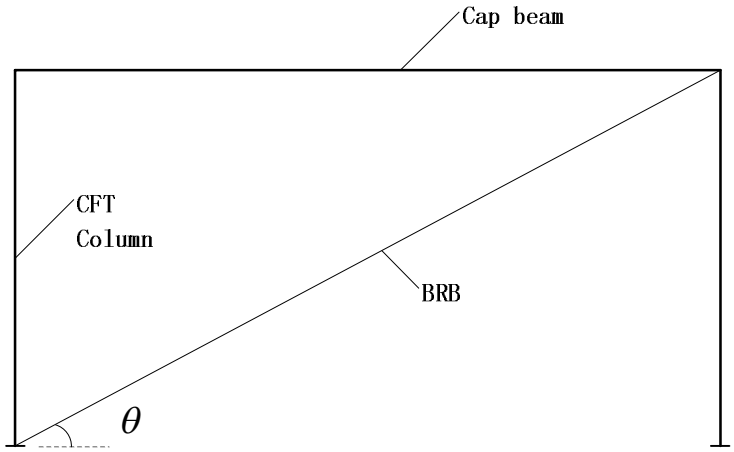


(a) Single Brace of Two-column Bent

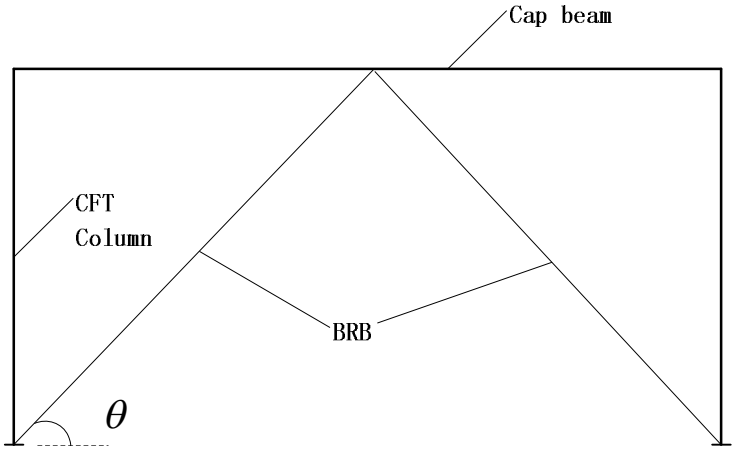


(b) Inverted Chevron of Two-column Bent

Figure 3-3 Two-CFT-column bent with BRBs

The displacement of the bent corresponding to the yielding of BRB, $\Delta_b$, as a minimum requirement for the structural fuse concept to work, must be smaller than the expected displacement of the bridge bent, $\delta_e$. This is expressed by Equation 3-8.

$$\Delta_b = \frac{f_{yb} c_b L_{brb}}{E_s \cos\theta} < \delta_e \tag{3-8}$$

where: $f_{yb}$ is the yielding strength of the steel used in the core of BRB, material used in the design example in this chapter is A500GrB42 with supplemental yield requirements $f_{yb} = 42ksi(\pm 4ksi)$, coupon test required. (Lopez and Sabelli, 2004)

Based on the required stiffness obtained for all BRBs from STEP 2, the stiffness of each BRB is $K_b$, which equals to $K_t - K_c$ for single inclined BRB case, and $\frac{K_t - K_c}{2}$ for inverted-V chevron BRBs case, as illustrated in Figure 3-3. The cross sectional area of each BRB $A_{brb}$ is:

$$A_{brb} = \Delta_b \frac{K_b}{f_{yb} \cos\theta} \tag{3-9}$$

***(ii) Box-pier bent with BRBs***

The typical geometry of a box-pier bent with BRBs is shown in Figure 3-4. The number of BRBs between the closely spaced CFT columns in the composite box-pier can be generically taken as *n*. For example, for the bridge bent in Figure 3-4, *n* equals 4.

In this case, the length ratio of BRB, $c_b$, is

$$c_b = \frac{\Delta_y / n}{\varepsilon_{bm} L_{brb}} \cos\theta \tag{3-10}$$

Again, the displacement of the bent corresponds to the yielding of the BRB, $\Delta_b$, must be smaller than the expected displacement of the bridge bent, $\delta_e$

$$\Delta_b = \frac{n f_{yb} c_b L_{brb}}{E_s \cos\theta} < \delta_e \tag{3-11}$$

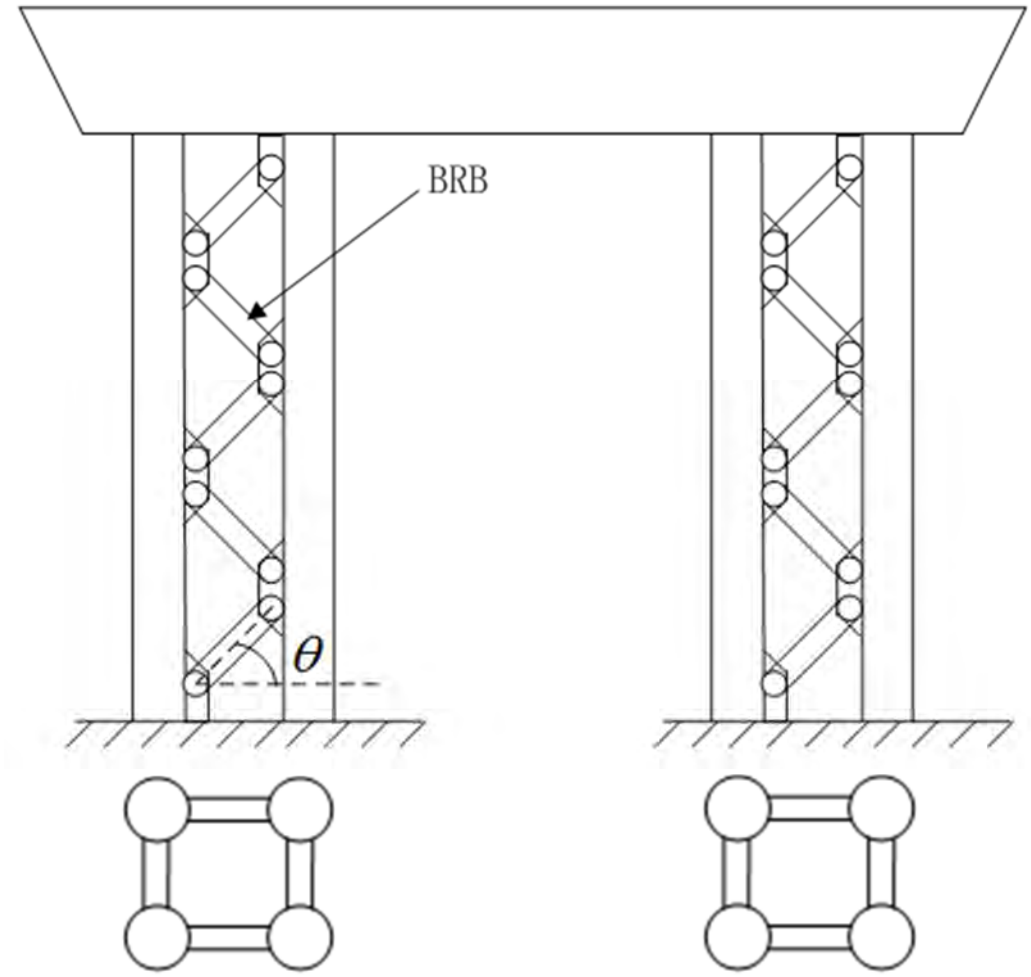


Figure 3-4 Box pier with BRBs in the transverse direction, four BRBs between the closely spaced columns

The total stiffness of BRBs $K_b$ equals to $K_t - K_c$, based on calculation from STEP 2. The cross sectional area of the BRB, $A_{brb}$, is:

$$A_{brb} = \Delta_b \frac{K_b}{4} \frac{1}{nf_{yb} \sin\theta \frac{L_c}{h}} \tag{3-12}$$

where: $L_c$ is the clear distance between the closely spaced CFT column in the box-pier bent case

The BRB's yielding strength $F_{ybrb}$ is

$$F_{ybrb} = f_{yb} A_{brb} \tag{3-13}$$

After a BRB yields, strain hardening is assumed to develop in the yielding core. The largest compressive strength $P_{ybrb}$ and tensile strength $T_{ybrb}$ that will develop in the BRB at a given strain must be considered in design, particularly for capacity design purposes. Those strengths are given by:

$$P_{ybrb} = \omega\beta f_{yb} A_{brb} \tag{3-14}$$

$$T_{ybrb} = \omega f_{yb} A_{brb} \tag{3-15}$$

where: $\omega\beta$, and $\omega$ are strain hardening factors, which vary with BRB size and suppliers. Figure 3-5 shows the backbone curve for an example BRB whose characteristics will be used in design examples later in this chapter. In that example, at the assumed 1.5% strain limit, $\omega\beta = 1.5$ and $\omega = 1.35$.

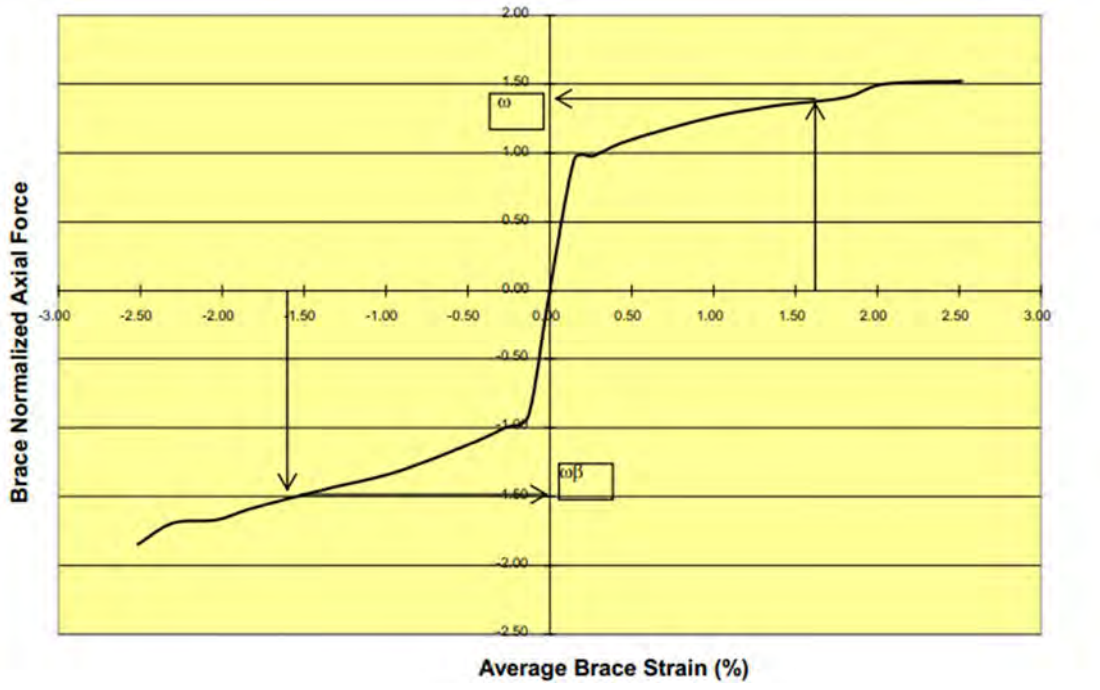


Figure 3-5 Strain hardening factors vs brace strain for an example BRB (Lopez and Sabelli, 2004)

**STEP 4: Column Capacity Check and Design Iteration**

Once a tentative design has been reached, the column capacity at the expected displacement, $\delta_e$, must be checked to ensure that the column axial, flexural and shear

strength are not exceeded, considering both the seismic and service load demands. Details of such calculations are presented in Section 3.3 and 3.4 for the two design bridge configurations. If column strength is exceeded under the lateral force loading on the bent and the yielding forces coming from BRBs (from capacity design), the column must be redesigned. Design iteration must continue until a column of satisfactory strength is found.

## 3.3 Two-CFT-Column Bent with BRBs Capacity Check

Following the design procedures in Section 3.2, the two-CFT-column bent with (a) single inclined BRB and (b) inverted-V chevron BRBs are designed. The calculations are shown in Appendix B.

In this section, the seismic and service load check is presented. Firstly, an analytical model built in SAP2000 to verify the bridge behavior. The force demand of the columns in the pushover analysis is checked at the target displacement, which is obtained from elastic response spectrum analysis. Pushover curve from analysis result is plotted and compared with the theoretical one developed from the structural fuse concept. Sections 3.3.1.1 to 3.3.1.6 focus on the case of a bridge bent having a single inclined BRB. Sections 3.3.1.7 to 3.3.1.10 are for the case of a bent with inverted-V (a.k.a. inverted-chevron) BRBs.

Secondly, it was observed during the process of implementing structural fuses in this bridge that the design of the bridge columns was governed by the seismic load cases. However, to illustrate that this is the case, Section 3.3.2 presents the results of bridge analysis under the gravity dead and live load, as well as for wind loads.

## 3.3.1. Bent Pushover Analysis

### 3.3.1.1 Model Information – Bent with Single BRB

Instead of performing a 3-D global analysis of the bridge, a local analysis of the bent in the middle of the bridge is considered adequate and is performed to verify the structural fuse concept. In order to model the clear distance between the adjacent CFT columns where the BRBs are added to the bent, the bridge bent is modeled as the bold lines shown in Figure 3-6. The CFT columns are fixed at the top to the cap beam, and at the bottom to the ground. The footing is not modeled. The BRBs are designed to be pin connected to the columns (i.e. moments are released at both ends of the beam elements used to model the BRBs). The overhang of the box girder at each side of the bridge bent is 9 ft, which is 1.5 times of the height of the box pier.

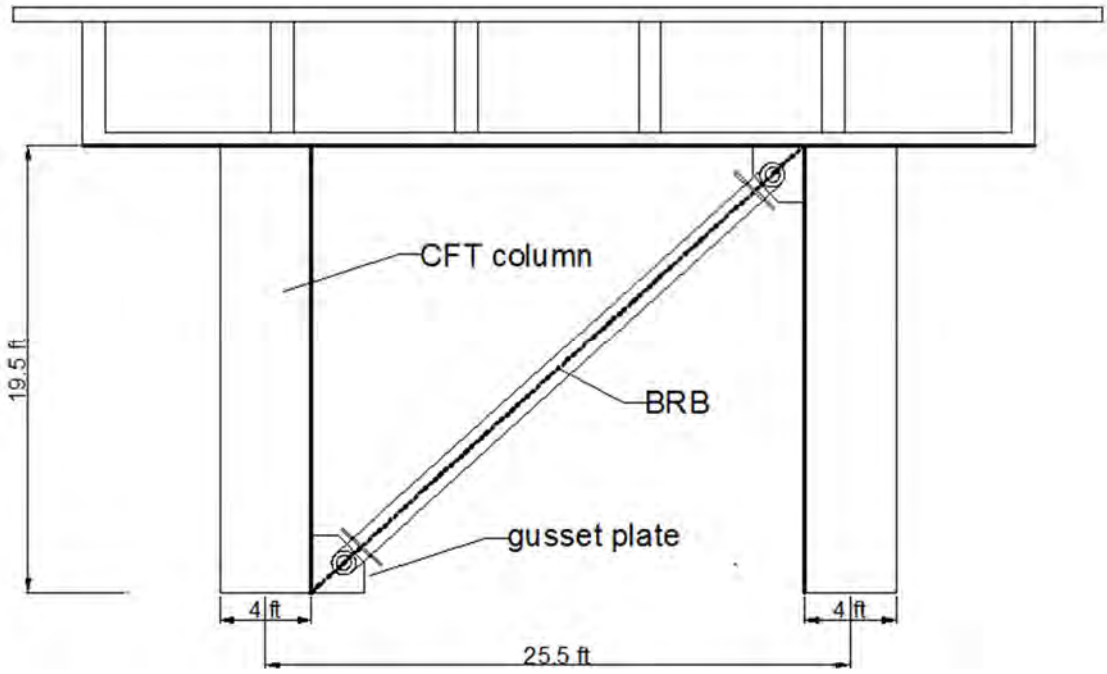


Figure 3-6 Transverse bridge bent with a single inclined BRB

#### 3.3.1.1.1 Material

Table 3-1 lists the materials used for the cap beam, CFT column, and the BRB. Concrete in the CFT columns has the same strength as in the cap beam.

Table 3-1 Materials for different members in the model

| Member | Material |
|---|---|
| Cap beam | Concrete 4 ksi (unconfined) |
| CFT column | Steel shell A572 Grade 60<br>Concrete 4 ksi (confined) |
| BRB | A500Gr. B with yielding strength requirement of 42 ksi |

Concrete in the cap beam is defined as having an ultimate unconfined strain capacity of 0.005. The uniaxial compressive strength and the corresponding strain of the unconfined concrete are $f_c^{'}$ and $\varepsilon_c^{'}$ as shown in Figure 3-7. The value $\varepsilon_c^{'}$ is usually around the range of 0.002-0.003. A representative value 0.002 is normally used. When the concrete is subjected to laterally confining pressure, the uniaxial compressive strength $f_{cc}^{'}$ and the corresponding strain $\varepsilon_{cc}^{'}$ are much higher than the unconfined concrete. The ultimate strain of the confined concrete is about 11 times of $\varepsilon_{cc}^{'}$. The strain capacity of the confined concrete in the CFT columns is correspondingly increased to 0.02.

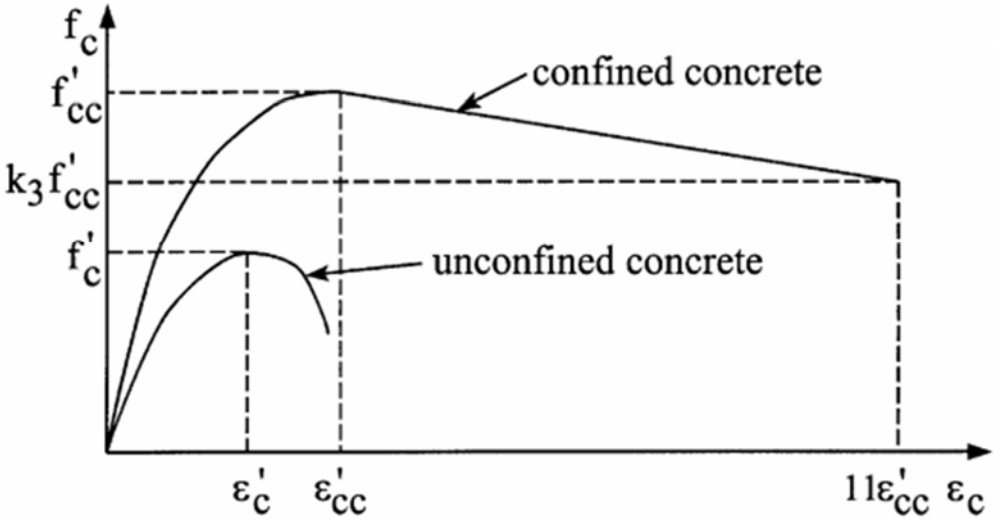


Figure 3-7 Stress-strain curve for concrete (Hu and Huang, 2005)

The BRB in the SAP2000 model yields over its entire length. In the real case, however, the deformation of the BRB is concentrated in the yielding core. The calculated yielding length ratio, *c*, is calculated to be 0.101 in Appendix B. To make the overall deformation of the BRB in the SAP2000 model match that of the actual BRB, the modulus of elasticity of A500 Gr.B (42 ksi) is increased to $Es = 29000 / 0.101 = 287128.71$ ksi.

The idealized nonlinear material model for A500 Gr.B (42 ksi), shown in Figure 3-8, has been "calibrated" to match the BRB properties shown in Figure 3-4. As such, at strains of 1.5%, the material reaches its maximum compressive stress of 63 ksi, corresponding to a strain hardening factor of 1.5, and maximum tensile stress of 56.7 ksi, corresponding to a strain hardening factor of 1.35.

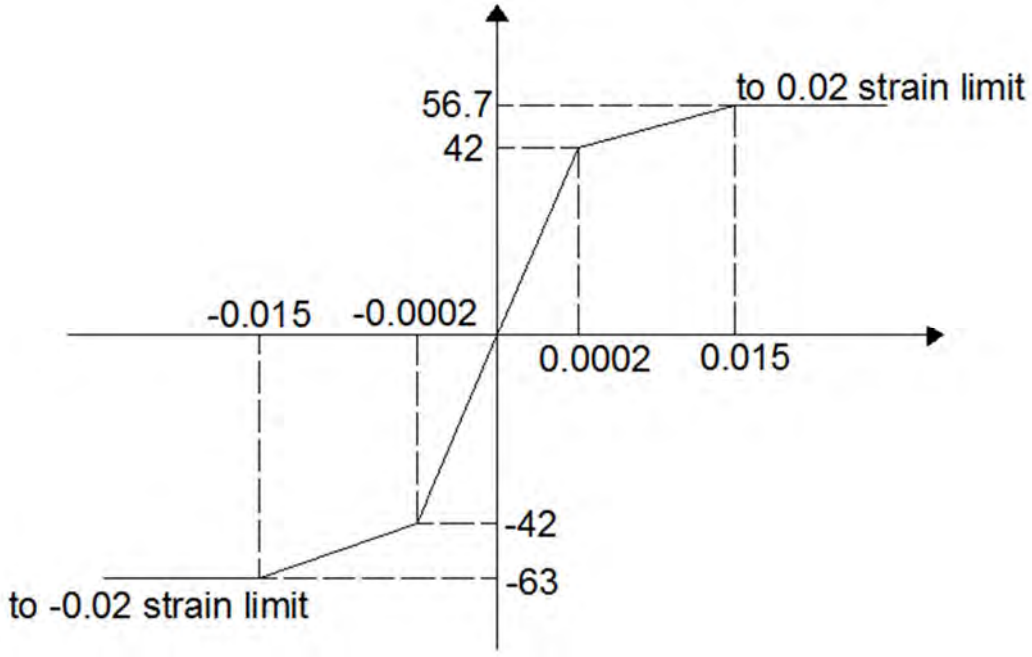


Figure 3-8 Stress-strain curve of A500 Gr.B (42 ksi) (not to scale)

#### 3.3.1.1.2 Section property

According to Caltrans Seismic Design Criteria (2010) Section 7.4.2.1, the minimum cap width, $B_{cap,}$ is calculated to be the diameter of the column plus 2 ft. Therefore,

the bent cap section is modeled as rectangle of 6'(width) by 6'(depth). For expediency, the cap beam is modeled as "infinitely rigid" relative to the columns by making the moment of inertia 1000 times larger than that corresponding to a 6' by 6' beam (to reflect the fact that flexure of the cap-beam would also engage the flexural rigidity of the box-girder in that direction).

The CFT column in the analytical model is built using SAP2000's Section Designer. The diameter of the section is 48". The thickness of the steel shell is 1.25". A grid of 20 by 20 fibers is used for calculating the capacity of the section and plastic hinge analysis. The BRB has a cross section of 22.39 $in^2$.

#### 3.3.1.1.3 Fiber hinge assignment

The columns are modeled in four segments. Fiber P-$M_2$-$M_3$ hinges are used at the ends of each segment. Each fiber hinge length is 10% of the length of the member.

A fiber P-$M_2$-$M_3$ hinge locates in the middle of each BRB. However, because moments are released at the ends of the BRB (pin-ends), the fiber P-$M_2$-$M_3$ hinge is only used to model the nonlinear axial behavior. As such, it is equivalent to a fiber P hinge model (which could also have been used for that matter).

### 3.3.1.2 Load assignment

The dead loads are applied on the cap beam as point load where the webs of the box-girder are located (See Figure 3-9). The dead loads are applied on the bent as a starting step of the non-linear pushover analysis.

The lateral load used for the pushover analysis in the transverse bent consists of a horizontal load applied at the center of the cap beam. The lateral load is applied from right to left in order to put the BRB brace in compression and thus get the largest

axial force in the column. The horizontal displacement of the cap beam is the monitored displacement used in the displacement-control method in the pushover analysis.

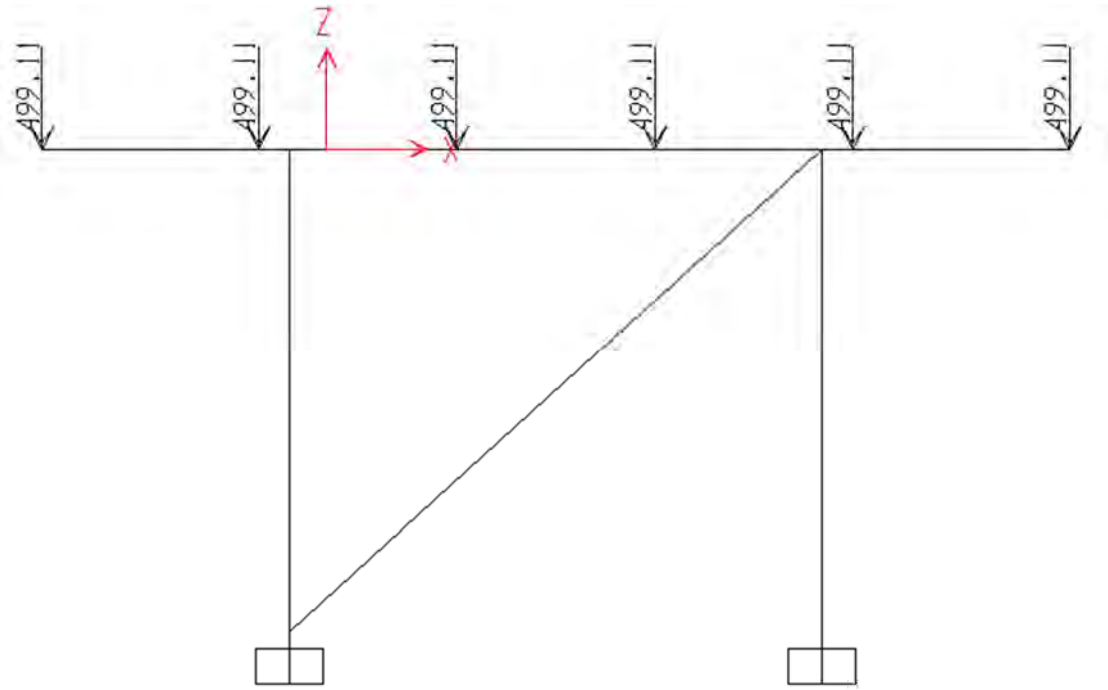


Figure 3-9 Dead loads applied to the bridge bent before push-over analysis in the transverse direction

### 3.3.1.3 Response Spectrum Analysis

The elastic demand of the bridge model is obtained from a simple response spectrum analysis to assess the displacement and force demand of the bent. The seismic force capacity check of the columns will be examined when the bridge bent reach the elastic displacement demand. In order to be consistent with the time history analysis in Chapter 4, the modified NEHRP 2003 response spectrum in Figure 3-10 is used.

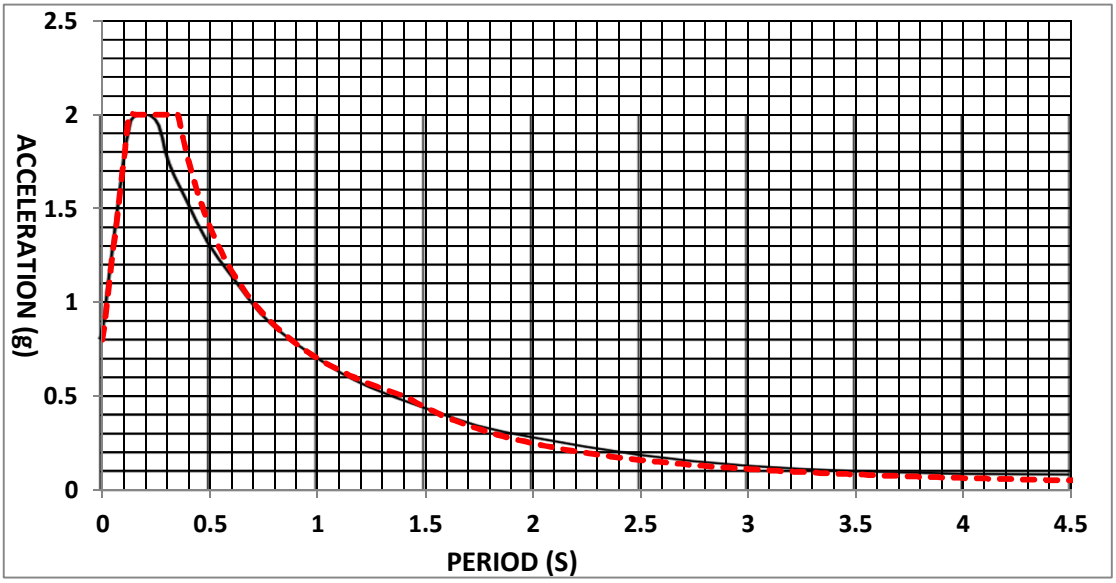


Figure 3-10 Caltrans acceleration response spectrum and corresponding NEHRP 2003 target design spectrum

The displacement demands of the two-CFT-column bent with BRBs are shown below in Table 3-2. The column yielding displacement is assumed to be the target displacement at the top of the bent in the design hand calculation. The difference in results obtained for the design assumption and response spectrum analysis cases is caused by the slightly different bent stiffness considered in the SAP2000 analyses. The designed strength and stiffness were obtained by assuming that the columns developed their yield moment, $M_y$, at both of their ends (assuming an infinitely rigid superstructure). The corresponding shear resistance of the frame at yield is $2M_y/h$, where $h$ is the height of the column. In the SAP2000 model, the superstructure was not modeled as infinitely rigid, resulting in a more flexible bent overall, and the moment at the top of the columns $M_{top}$ is less than $M_y$ when $M_y$ is reached at the column bases (i.e., $V = (M_{top}+M_y)/h$).

Table 3-2 The displacement demand comparison of the two-CFT-column bents

| Two-CFT-column with | Design | Analysis (Response Spectrum) | Difference |
|---|---|---|---|
| Single inclined BRB | 0.71” | 0.94” | 24% |
| Inverted-V BRBs | 0.71” | 0.81” | 12% |

### 3.3.1.4 Two-CFT-column bent with single inclined BRB analysis results

When the bridge bent reach the expected elastic displacement at the cap beam level of 0.94" in the pushover analysis, the moment demand in the columns is shown in Figure 3-11(a). The axial tensile and compressive force is shown in Figure 3-11(b). The reactions at the bottom of the CFT columns are shown in Figure 3-11(c).

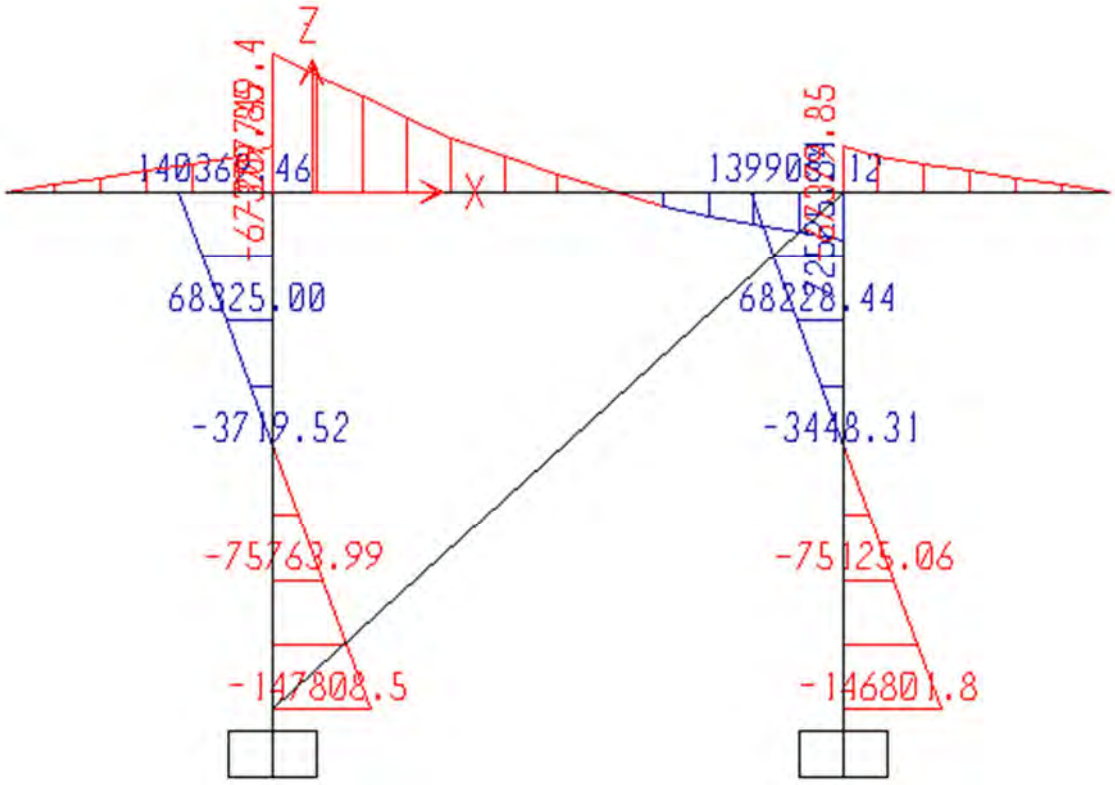


Figure 3-11 (a) Moment diagram of the bent when the expected displacement is reached in the transverse direction

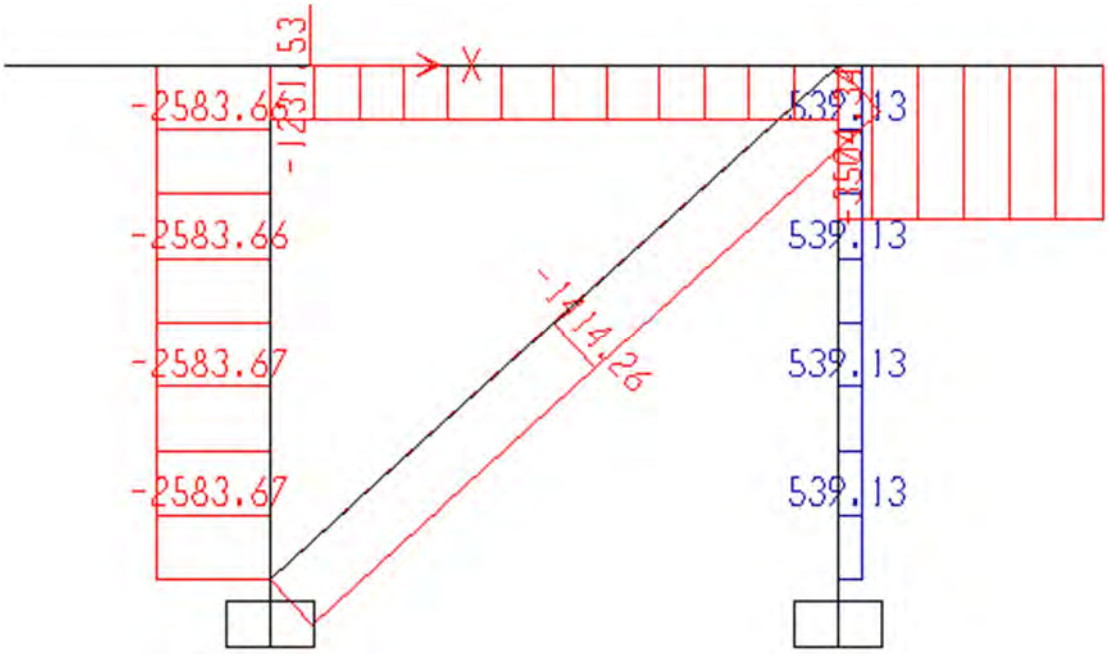


Figure 3-11 (b) Corresponding axial forces in the members of the bent

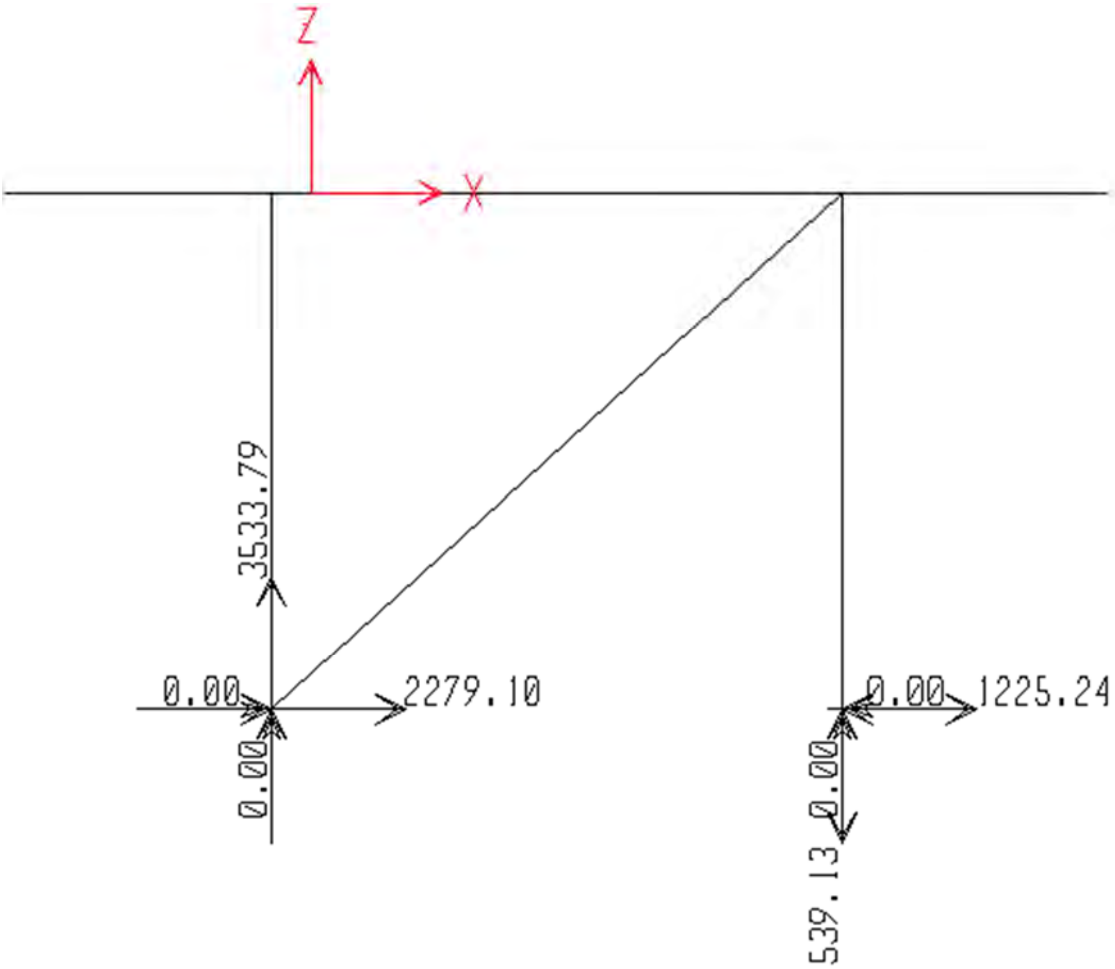


Figure 3-11 (c) Corresponding reactions at the bottom of the CFT columns

The reaction forces are used here to check the column capacities, in which case the eccentricity between the point where the brace and column workline meet around the foundation exist, as shown in Figure 3-12a. The maximum forces used would be larger than the corresponding forces when the eccentricity does not exist in Figure 3-12b, since the forces in the braces goes to the ground.

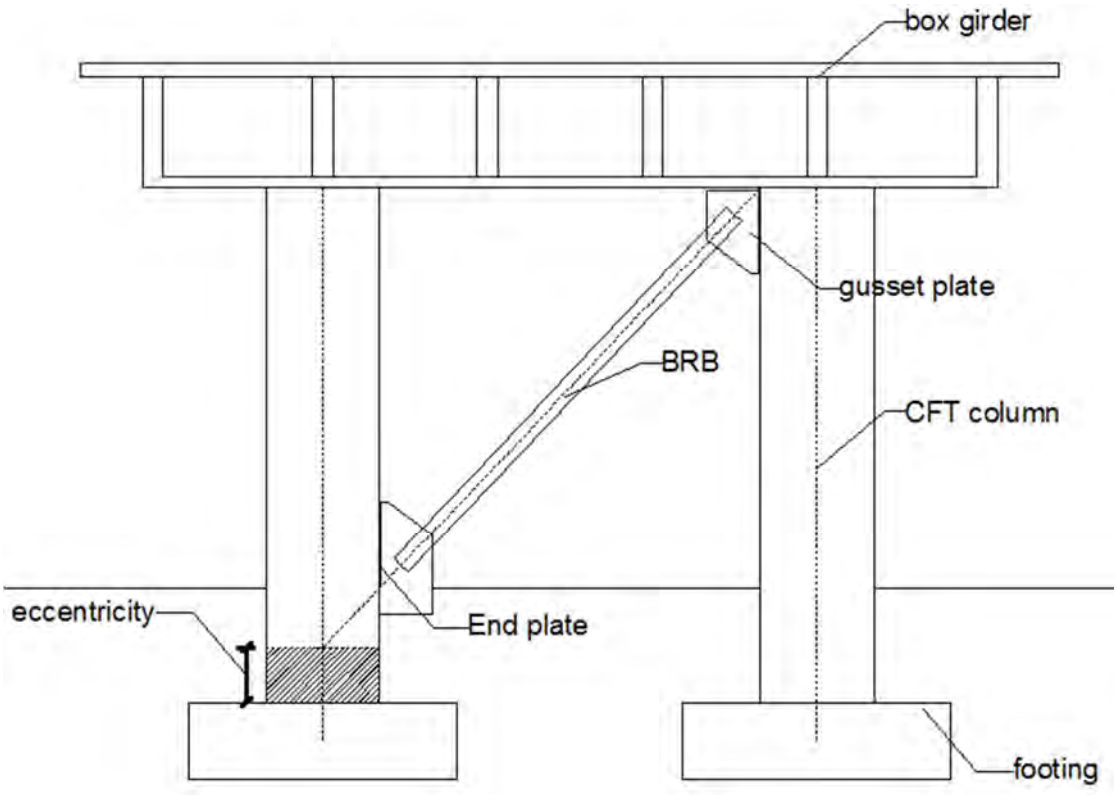


(a)

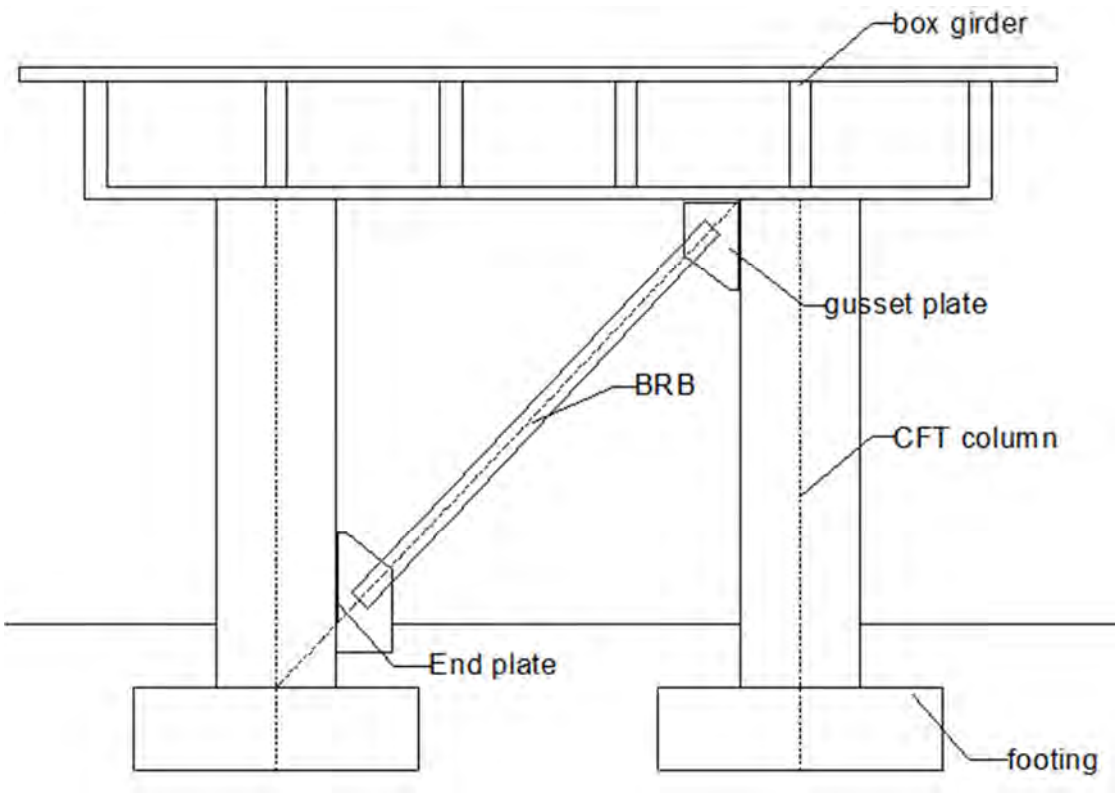


(b)

Figure 3-12 The bridge bent with single inclined braces in the transverse direction (a) considering a possible eccentricity, *e* (b) no eccentricity

The moment and axial force demands shown in Figure 3-11 are compared against the provided member strengths, as shown in Table 3-3. The flexural plastic strengths and yield strength obtained from Section Designer are listed in Table 3-4. The plastic flexural strength of column is the full composite flexural strength. The resistance reduction factors $\Phi$ for the strength values from Section Designer are all 1.0. Checking the plastic strength and axial strength interaction at that drift gives an indication of the columns' reserve strength beyond the first yielding. The ratios are all smaller than 1.0. This indicates that the columns have sufficient strength to resist the forces at the target displacement. Note that the interaction equation used in Table 3-3 for the axial force and plastic flexural strength is a simple linear relationship.

Table 3-3 Summarized force demands in the columns

| Column Type | Moment Demand $M_u$ (kip-in) | Reaction Force Demand $P_u$ (kips) | Plastic Strength $\Phi M_n$ (kip-in) | Axial Strength $\Phi P_n$ (kip) | $M_u/\Phi M_n + P_u/\Phi P_n$ |
|---|---|---|---|---|---|
| Ten. | 147,809 | 539 | 185,621 | 11,020 | **0.84** |
| Comp. | 146,802 | -3534 | 185,621 | -164,37 | **1.00** |

The interaction diagram is equivalent to what is shown in Figure 3-13 for a B factor of 1.0. In reality, for CFT columns, B is typically less than 1.0, which provides for further reserve strength. Note that all the above are interaction equations based on cross-section strength. Columns were designed considering the actual column slenderness. However, as shown in appendix B, the columns are quite stocky and slenderness has a minimal impact of strength for this particular example.

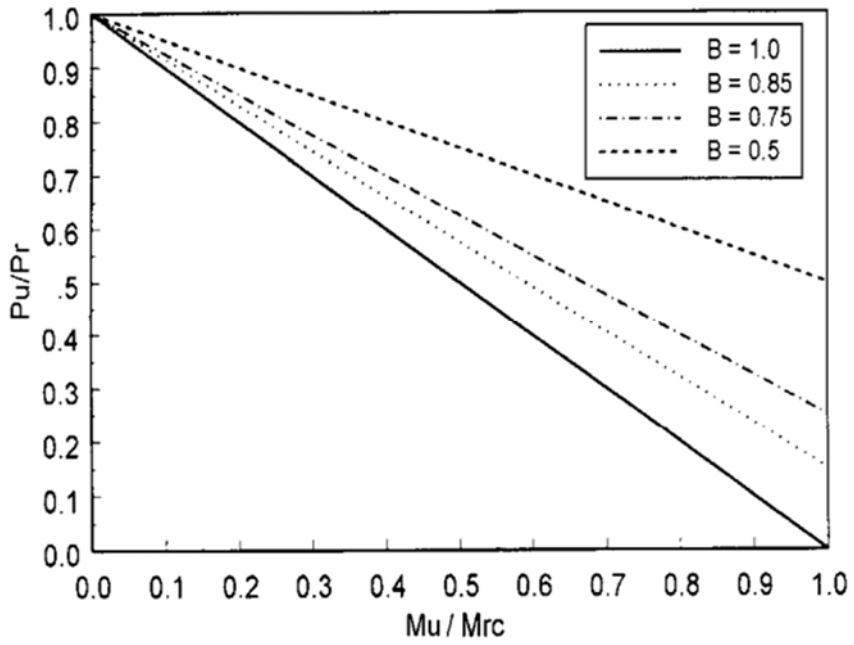


Figure 3-13 Interaction curve for CFT column (AASHTO seismic design specification, figure C7.6.1-1)

It is conservative to use that linear interaction equation here, instead of the interaction equations provided in the AASHTO LRFD Seismic design specification (2009) Section 7.6.1 for axial compression and moment (which uses a calculated B value, typically less than 1.0). Note that there exists no equation in AASHTO for the axial tensile and flexural interaction of CFT sections.

Following is an arbitrary example to show the difference in the strength calculated from the AASHTO equation and the value obtained from Section Designer given the axial force. The AASHTO compression-flexure interaction equation for CFT gives:

$$\frac{P_u}{\phi_c \mathrm{P}_n} + B\frac{M_u}{M_n} \le 1 \quad (7.6.1\text{-}1) \text{ and } \quad \frac{Mu}{Mn} \le 1 \quad (7.6.1\text{-}2)$$

$$B = 1 - \frac{\mathrm{P}_{rc}}{\phi_c P_n} = 1 - \frac{\phi_{c1} f_c A_c}{\phi_c P_n} = 1 - \frac{4878}{0.75 \times 17120} = 0.62$$

where: $\phi_{c1} = 0.75$

therefore the ratio of $BM_u/M_n+P_u/P_n$ for the compressive column check would be 0.70, which made the columns to have more marginal capacity than in the linear capacity check.

### 3.3.1.5 Pushover curve for two-CFT-column bent with single inclined BRB

Figure 3-14 shows the theoretical pushover curves of lateral shear resistance versus top displacement of the column for the frame, BRB, and the combined system, obtained using a bilinear force deformation relationship for the columns (yielding at a moment of $M_y$=126,891 kip-in) and tri-linear relationship for BRBs yielding at 42 ksi and strain hardening to 63 ksi at a strain of 0.015). The purple line of the theoretical BRB shows the yielding of the BRB at the displacement of 0.069", and point where the maximum strain hardening considered is reached at 0.71". The target displacement of the bent is reached when the BRBs have the largest strain hardening. The theoretical frame curve in navy blue dash lines shows that the frame yields at the

displacement of 0.71". The two parts add up to the total theoretical curve for the combined system plotted in red dash lines. The left green vertical dash dotted line represents the expected displacement for the structural fuse system. The right pink vertical dash dotted line shows the expected displacement for the bent frame alone (without the BRB) if using the same acceleration spectrum.

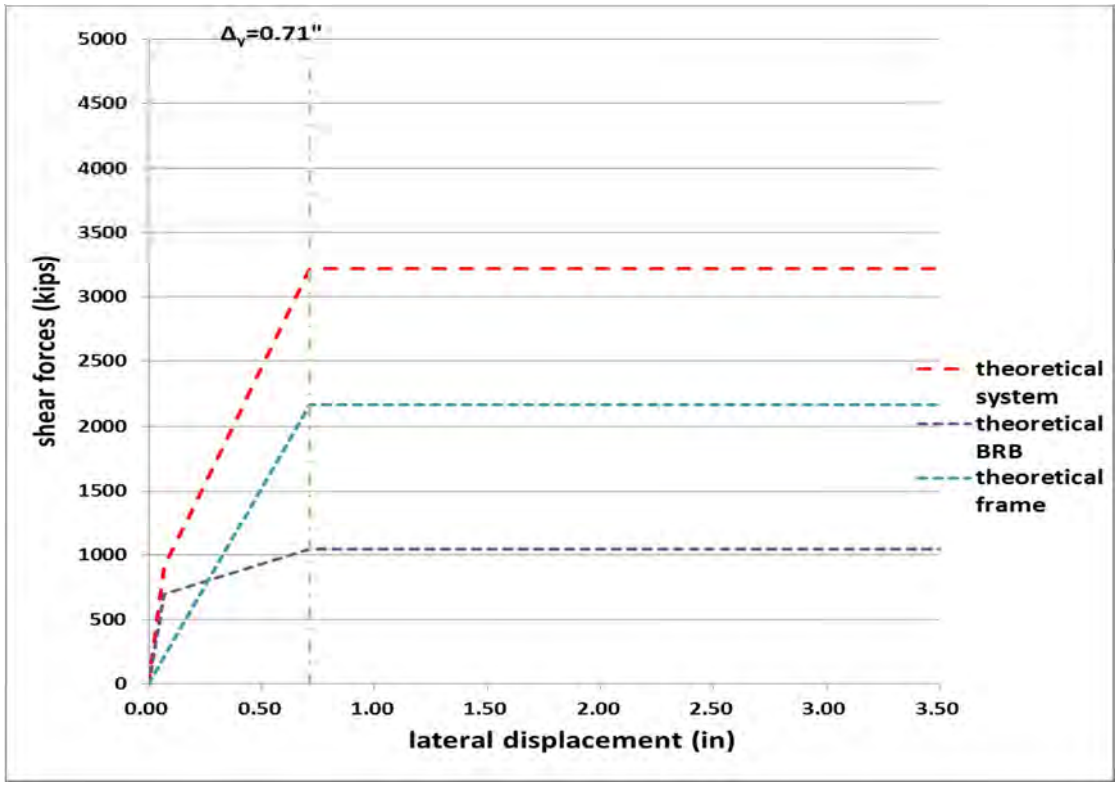


Figure 3-14 Theoretical pushover curves of the frame, BRB and the combined system

Figure 3-15 overlays, on top of the results from Figure 3-14, the pushover curve obtained from the SAP2000 analysis (in solid lines). The solid blue line shows the total base shear versus lateral displacement at top of the bent. By subtracting the lateral forces resisted by the BRBs (equal to the horizontal component of the forces in the BRB) shown in solid green line, the solid brown line gives the portion of the base shear forces resisted by the frame itself.

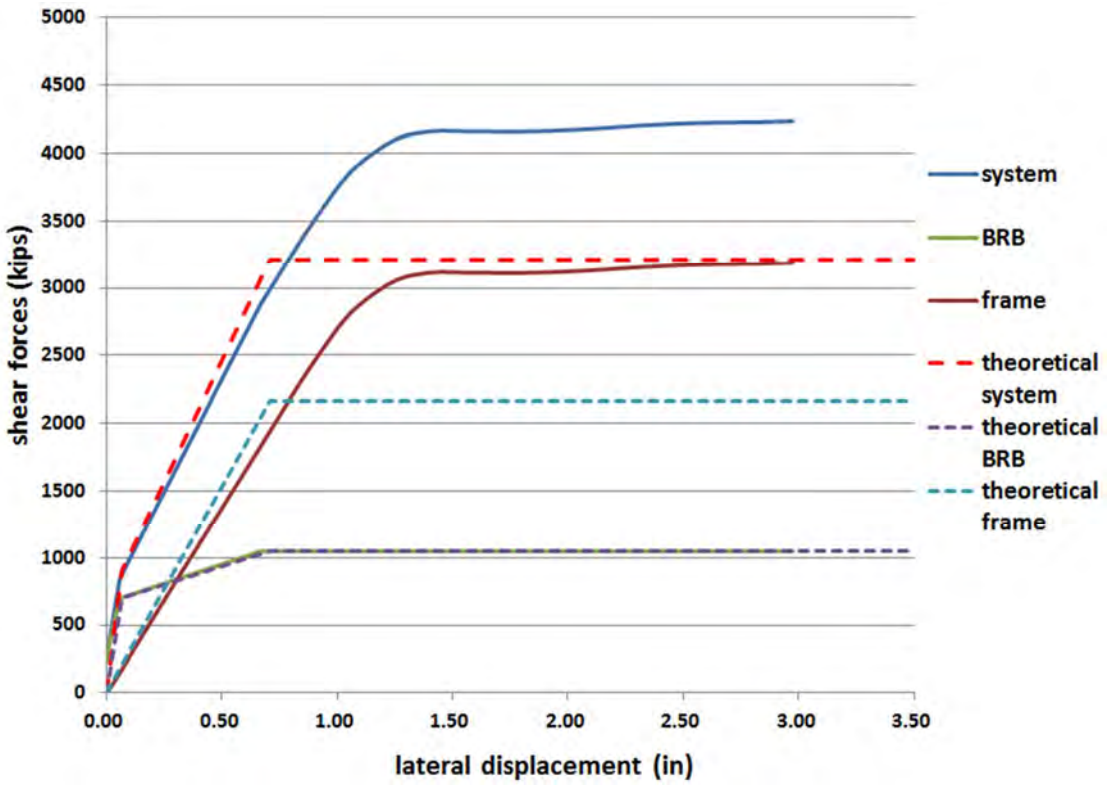


Figure 3-15 Comparison between the theoretical curve and the analytical curve

Figure 3-16 shows the target displacement demand of 0.94" from response spectrum analysis as the orange vertical line. Note that SAP2000 analyses consider strain hardening of the columns as well as the BRBs. In Figure 3-16, the push-over analysis results indicate that column yield is first reached at the bottom of the right column; the orange lower horizontal dotted line identifies the base shear resisted by the columns when that happens (which incidentally happens in a CFT column in tension). The middle grey light blue upper horizontal dotted lines show the starting of the strain hardening of the same section. For comparison, the upper blue dotted line is shown for the reaching shear resistance of the frame $V$ corresponding to the $2M_p/h_{column}$ calculated, where $M_p$ equals to 187,851 kip-in obtained from SAP2000 Section Designer.

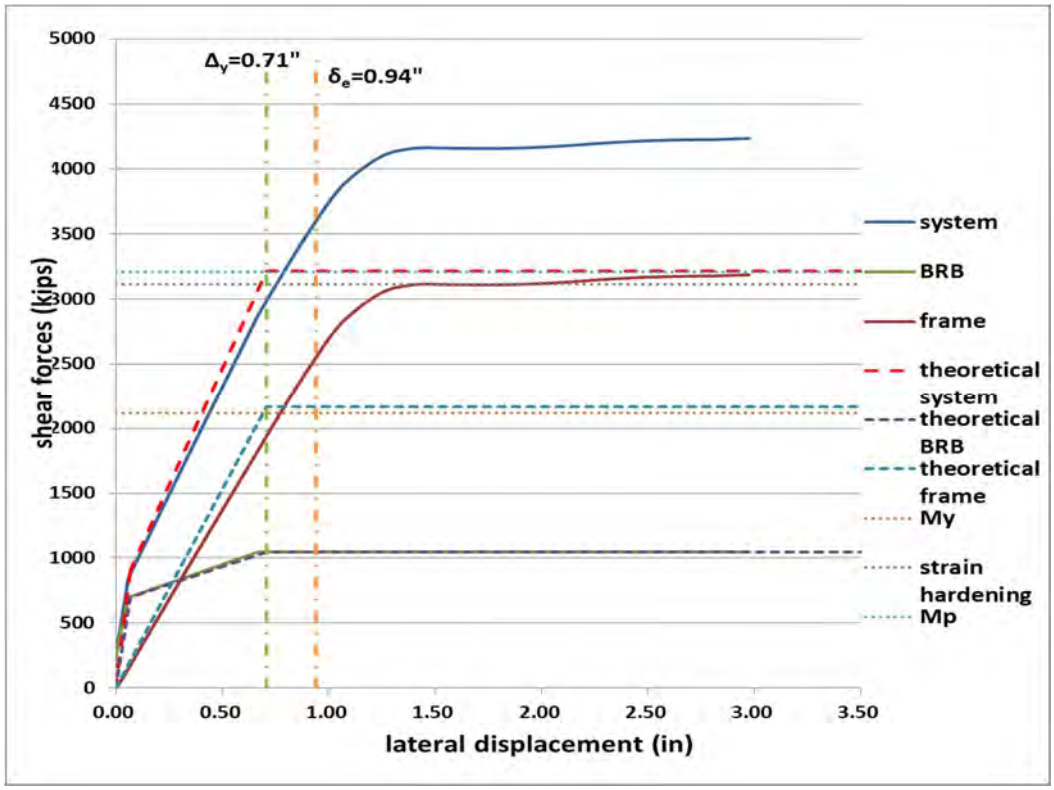


Figure 3-16 Pushover curve comparison between the analysis result and theoretical design value for the single inclined BRB case

The sequence of yielding at top and bottom of the CFT columns (i.e. the point when the extreme fiber yields) and reaching the capacity (i.e. from which strain hardening starts to develop at each of those locations) is tabulated in Table 3-4. As an example of the notation used in that table, "$R_b$" stands for bottom ("b") of the right ("R") column. Note that the yielding (and onset of strain hardening) in these column is not happening at the same time, but they are doing so over small increases of frame drift. However, what happens beyond the onset of frame yielding is of some interest, but is not expected to happen since the structural fuse will limit displacements to prevent frame yielding.

Figure 3-16 shows that limiting the column demands to $M_y$, to prevent any column yielding, is conservative. The use of a more liberal design limit is arguably possible.

Table 3-4 Displacement and shear forces resisted by the frame when the yielding strength is reached and when the capacity of the section is reach before strain hardening happen

| Critical section | Yielding Disp. (in) | Yielding Shear Force (kips) | Capacity Disp. (in) | Capacity Shear Force (kips) |
|---|---|---|---|---|
| $R_b$ | 0.77 | 2120.67 | 1.53 | 3113.63 |
| $R_t$ | 0.81 | 2222.38 | 1.70 | 3110.19 |
| $L_b$ | 0.89 | 2419.59 | 1.80 | 3110.35 |
| $L_t$ | 0.93 | 2530.43 | 2.03 | 3122.80 |

#### 3.3.1.6 BRB design details for two-CFT-column bent with single inclined BRB

BRBs and their gusset plates used for the connections are usually designed by the BRB manufacturers. BRBs can be pin connected to the CFT columns, and this is the option that has been considered in this report. Equation 3-16 can be used to design BRB pins.

$$P_n = 0.6 \times 0.75 \times pin\_area \times F_u(pin) \times 2(two\_shear\_plane) \quad (3\text{-}16)$$

where: $F_u$ equals to 115 ksi for pin diameter greater than 2.5" and 125 ksi for pin diameter of 2.5" or less

Therefore, for a BRB to develop the strain hardened loads of 1414.26 kips calculated above, a pin of 4.25" would be necessary (note that BRBs having strengths of 2000 kips have already been implemented in many instances).

A BRB supplier (StarSeismic) indicated that a 1.5" thick gusset plate can be used for

the BRB connection to resist the forces. Distance from the pin to the edge of the gusset would be 9".

### 3.3.1.7 Model information for two-CFT-bridge bent with inverted-V BRBs

For the Inverted-V BRBs with the same bridge columns design, the bridge columns are still modeled with the clear distance as shown in the bold lines in Figure 3-17.

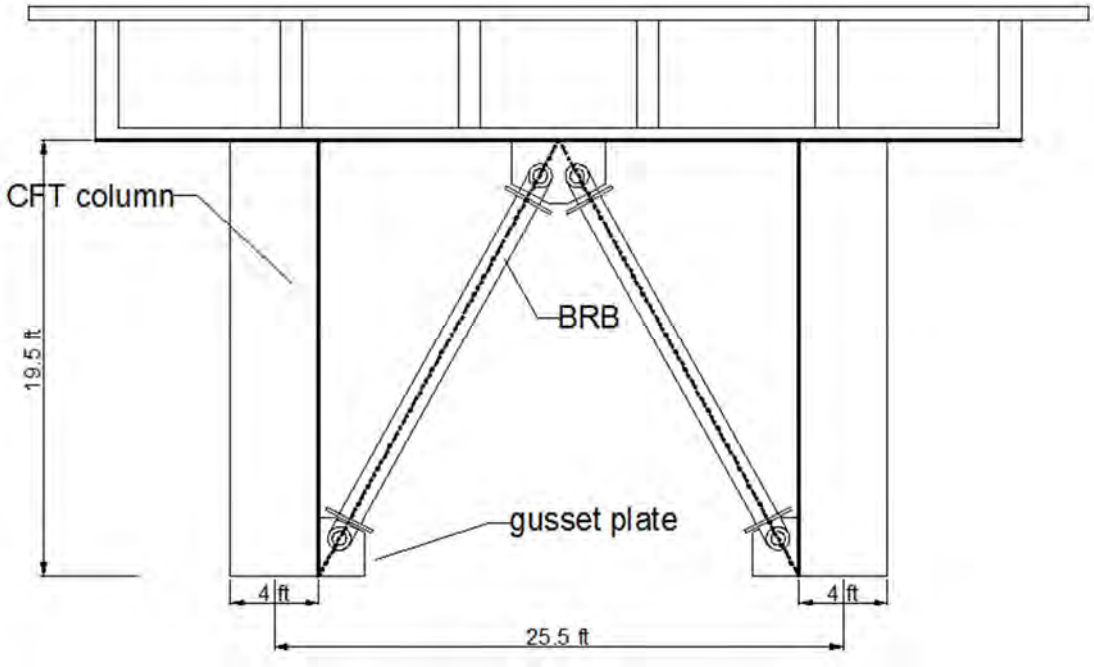


Figure 3-17 Transverse bridge bent with BRBs in inverted-V

This section only shows the part of the modeling and results that are different from the bridge bent with single inclined BRB case.

The calculated yielding length ratio is only 0.085 for the BRBs designed in the inverted-V configuration. To make the overall deformation of the BRB in the SAP model match that of the actual BRB, the modulus of elasticity of A500 Gr.B (42 ksi) is increased to $Es = 29000 / 0.085 = 341176.47$ ksi. BRB has a cross section of 17.178 $in^2$.

### 3.3.1.8 Two-CFT-column bent with inverted-V BRBs analysis results

The expected displacement of the bent at the cap beam level $\Delta_y$=0.81" is reached, the moment demand in the columns is shown in Figure 3-18(a). The corresponding axial tensile and compressive forces are shown in Figure 3-18(b). The reactions at the bottom of the CFT columns are shown in Figure 3-18(c).

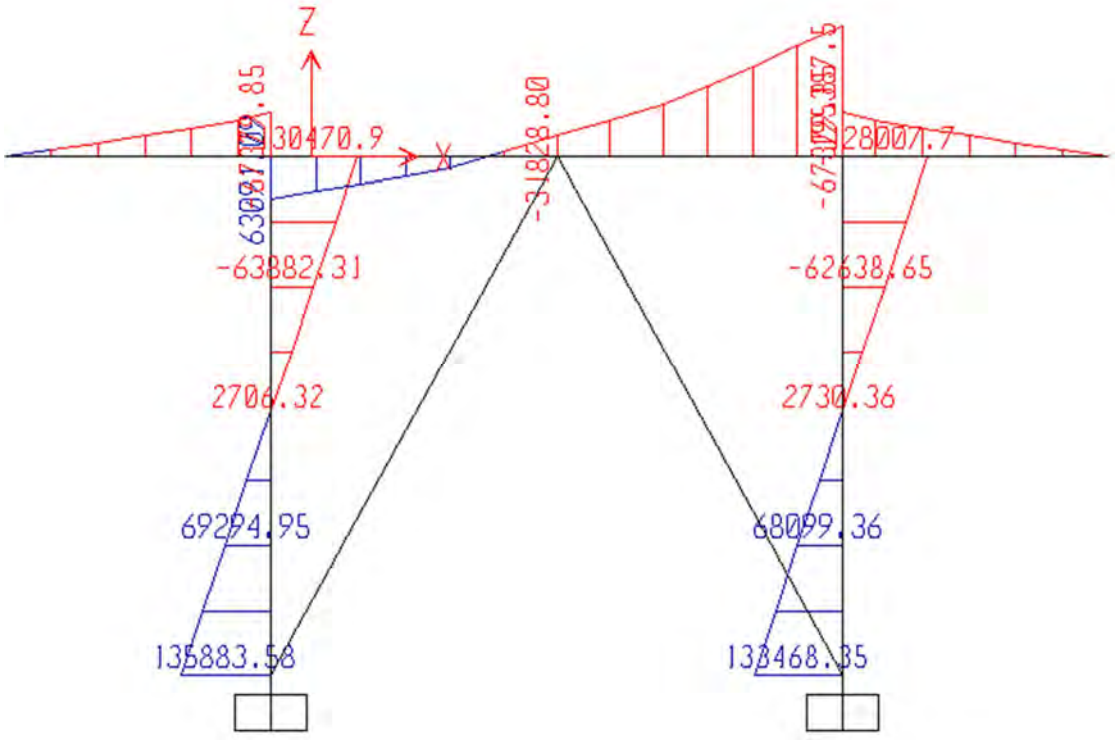


Figure 3-18 (a) Moment diagram of the bent when the expected displacement is reached in the transverse direction

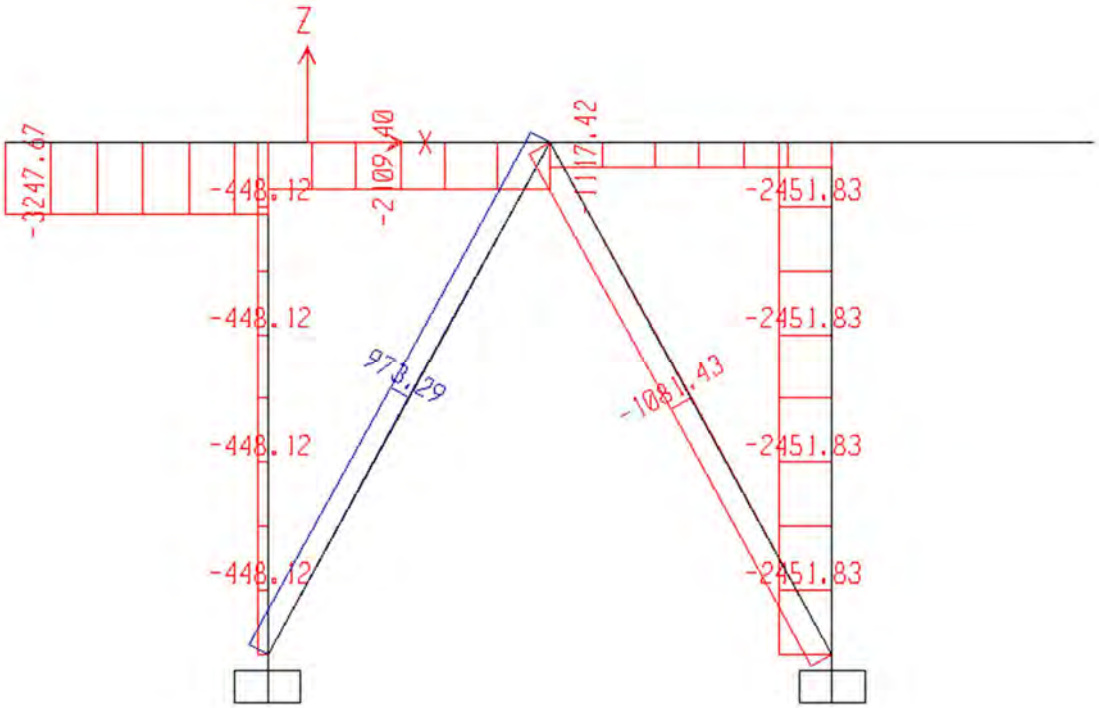


(b) Corresponding axial forces in the members of the bent

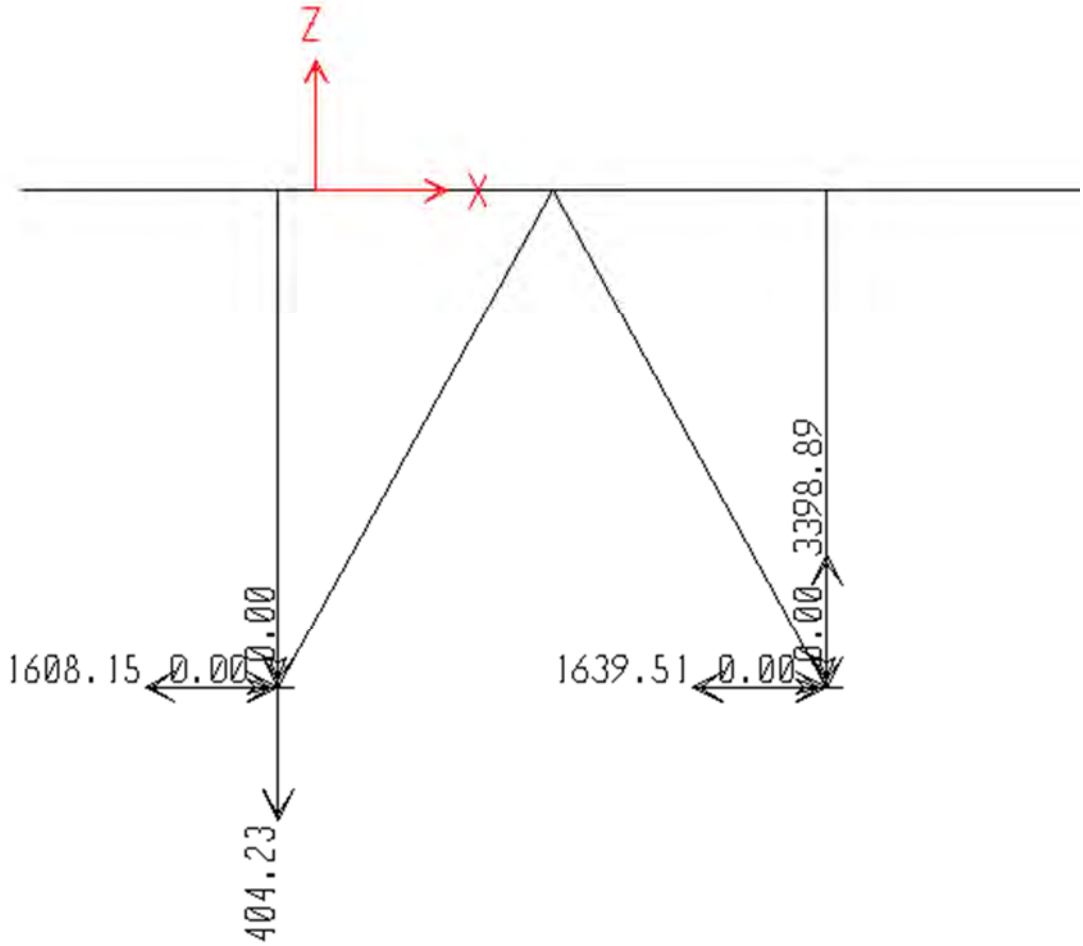


Figure 3-18 (c) Corresponding reactions at the bottom of the CFT columns

The moment and axial force demands shown in Figure 3-18 are compared against the provided member strengths, as shown in Table 3-5. The plastic and yield strengths listed in Table 3-5 are from Section Designer. With the ratio less than 1.0, the columns are proved sufficient to resist the forces under the plastic strength and axial strength interaction check.

Table 3-5 Summarized force demands in the columns

| Column Type | Moment Demand $M_u$ (kip-in) | Axial Load Demand $P_u$ (kips) | Flexural Strength $\Phi M_n$ (kip-in) | Axial Strength $\Phi P_n$ (kip) | $M_u/\Phi M_n + P_u/\Phi P_n$ |
|---|---|---|---|---|---|
| Ten. | 135,884 | 404 | 185,621 | 11,020 | **0.77** |
| Comp. | 133,468 | -3399 | 185,621 | -16,437 | **0.93** |

Following is an arbitrary example to show the difference in the strength calculated from the AASHTO equation and the value obtained from Section Designer given the axial force. The AASHTO compression-flexure interaction equation for CFT gives:

$$\frac{P_u}{\phi_c P_n} + B\frac{M_u}{M_n} \le 1 \quad (7.6.1\text{-}1) \text{ and } \frac{Mu}{Mn} \le 1 \quad (7.6.1\text{-}2)$$

$$B = 1 - \frac{P_{rc}}{\phi_c P_n} = 1 - \frac{\phi_{c1} f_c A_c}{\phi_c P_n} = 1 - \frac{4878}{0.75 \times 17120} = 0.62$$

where: $\phi_{c1} = 0.75$

therefore, the ratio of $BM_u/M_n + P_u/P_n$ for the compressive column check would be 0.65, which made the columns to have more marginal capacity than in the linear capacity check.

### 3.3.1.9 Pushover curve for two-CFT-column bent with inverted-V BRBs

The overall comparison of the pushover curve between the analysis result and the

theoretical ones is directly shown in Figure 3-19. The theoretical curves are the same as in the single inclined BRB case. The purple dash line of the theoretical BRB shows the yielding of the BRB at the displacement of 0.069", and point where the maximum strain hardening considered is reached, at 0.71". The theoretical frame curve in navy blue dash lines shows that the frame yields at the displacement of 0.71". The two parts add up to the total theoretical curve for the combined system plotted in red dash lines. The pushover curves obtained from SAP2000 analysis overlay on top of the theoretical results as solid lines. The solid blue line shows the total base shear versus lateral displacement at top of the bent. By subtracting the lateral forces resisted by the BRBs (equals to the horizontal component of the forces in the BRBs) shown in solid green line, the solid brown line gives the portion of the base shear forces resisted by the frame alone. The target displacement demand of 0.81" from response spectrum analysis is shown as the orange vertical line.

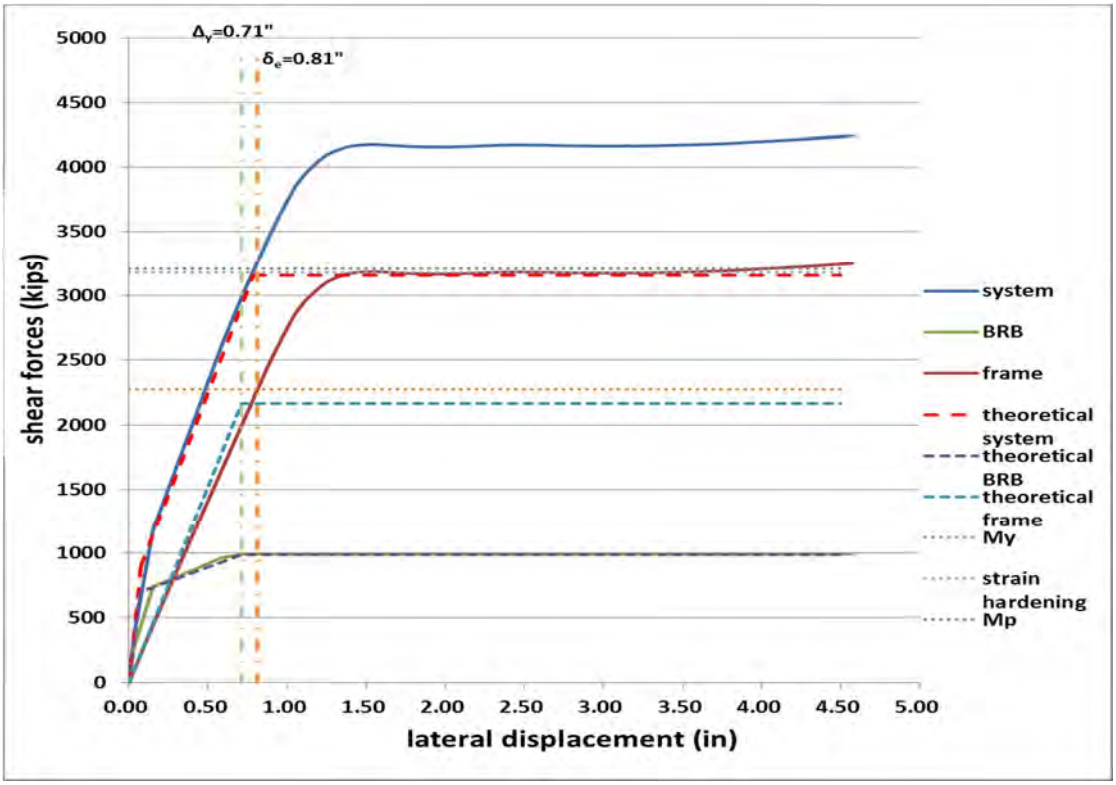


Figure 3-19 Pushover curve comparison between the analysis result and theoretical design value for the Chevron Inverted-V BRB case

The pushover analysis results indicate that column yielding is first reached at the bottom of the left column where the tension and flexure interaction exists. The orange lower horizontal dotted line identifies the base shear resisted by the columns when that happens. The middle grey light blue upper horizontal dotted lines show the starting of the strain hardening of the same section. For comparison, the upper blue dotted line is shown for the reaching shear resistance of the frame $V$ corresponding to the $2M_p/h_{column}$ calculated, where $M_p$ equals to 187851 kip-in obtained from SAP2000 Section Designer.

The sequence of yielding at top and bottom of the CFT columns (i.e. the point when the extreme fiber yields) and reaching the capacity (i.e. from which strain hardening starts to develop at each of those locations) is tabulated in Table 3-6. As an example of the notation used in that table, "$R_b$" stands for bottom ("b") of the right ("R") column. Note that the yielding (and onset of strain hardening) in these column is not happening at the same time, but they are doing so over small increases of frame drift.

Table 3-6 Displacement and shear forces resisted by the frame when the yielding strength is reached and when the capacity of the section is reached before the strain hardening happens

| Member | Yielding Disp. (in) | Yielding Force (kips) | Capacity Disp. (in) | Capacity Force (kips) |
|---|---|---|---|---|
| $L_b$ | 0.81 | 2272.01 | 1.63 | 3180.71 |
| $L_t$ | 0.84 | 2356.72 | 1.78 | 3170.68 |
| $R_b$ | 0.88 | 2457.41 | 1.81 | 3169.54 |
| $R_t$ | 0.92 | 2552.48 | 1.98 | 3166.37 |

### 3.3.1.10 BRB design details for two-CFT-column bent with inverted-V BRBs

BRBs and the gusset plates used for the connections are usually designed by the BRB manufacturers. Using the same equation as shown in section 3.3.1.5, for BRB to develop the strain hardened loads of 1081.43 kips, a pin of 3.75" would be necessary. A BRB supplier (StarSeismic) indicated that a 1.5" thick gusset plate can be used for the BRB connection to resist the forces. Distance from the pin to the edge of the gusset would be 9".

### 3.3.1.11 Two-CFT-column bent with BRBs analysis summary

The CFT columns, designed in Appendix B, are found to have adequate strength to reach the force demands when the bridge bent reaches the target displacement (elastic displacement demand from response spectrum analysis, which is larger than the yielding displacement of the column assumed in the design process). Note that the demand versus capacity check were performed considering the reaction forces and the moment demand in the columns, as this would be the more critical case if there was an eccentricity between the point where the work-lines of the column and BRB intersected and the foundation. Table 3-7 shows the force demand on the foundation for the two cases from Figures 3-11c and 3-18c. For the inverted-V BRBs case, the force demand is 134.9 kips less than the single inclined BRB case, for both the compressive and tensile columns.

Table 3-7 Force demand on the foundation for the two cases in the two-CFT-column bent

| | Compression (kips) | Tension (kips) |
|---|---|---|
| Single inclined BRB | -3533.79 | 539.13 |
| Inverted-V BRB | -3398.89 | 404.23 |

In absence of that eccentricity, for the single BRB case, only slightly smaller results would be obtained considering the axial and flexural forces acting on the columns.

For the inverted-V BRBs case, the axial force in the columns would be considerably smaller compared with the single BRB case, since the reaction for the vertical component of the BRB force would not appear in the column. Therefore, a smaller column section might be sufficient for this structural fuse design example using inverted-V BRBs.

The difference between the single BRB case and the inverted-V BRBs case also lies in the resulting smaller BRB sizes needed in the latter case (and correspondingly, smaller force demands on the connections). Compared with the single inclined BRB case, the force demand in the BRBs is reduced by 24% in the inverted-V BRBs case.

## 3.3.2. Service Load Check for Two-CFT-column Bent with BRBs

### 3.3.2.1 Global bridge model

The global model developed in SAP2000 is used to determine the forces in the columns due to the dead load, live load and wind load. Note that since the design of the superstructure may need to be revised because of the locations of the new columns and the fact that they are CFTs (instead of RC columns), the permanent loads due to secondary prestress forces, creep, and shrinkage are not calculated here.

As mentioned above, the abutments allow longitudinal movement of the superstructure, limited only by the width of the gap between the superstructure and the abutment back wall (which is not considered to be a limiting factor here). The support provided by the abutment is assumed to be fixed against translation in the vertical and transverse directions and fixed against rotation about the longitudinal axis. The bent resists all the seismic force in the longitudinal direction while in the transverse direction part of the lateral force is taken by the abutments. The behavior of the bridge under the lateral load in the transverse directions is shown in Figure 3-20.

In the SAP2000, the bridge superstructure is modeled analyzed as a line element (i.e. spine) located at mid-width of the bridge deck.

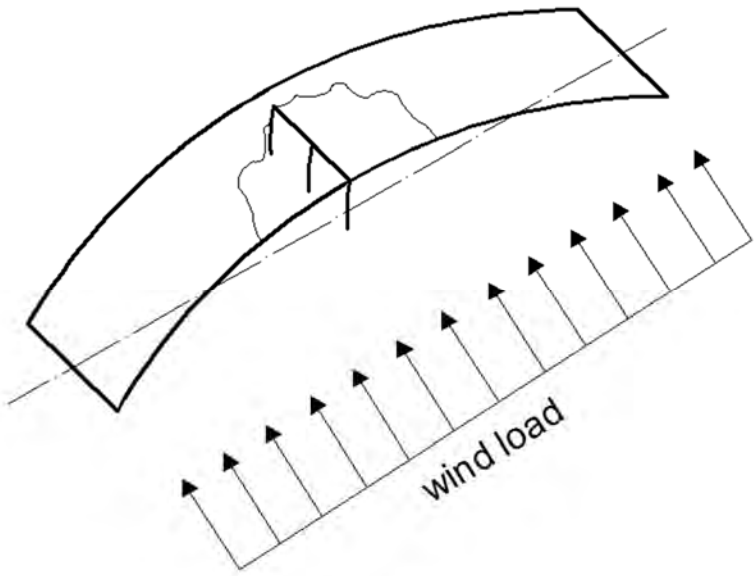


Figure 3-20 Wind load applied to the bridge in the transverse direction

A 3-D view of the spine bridge model is shown in Figure 3-21. The braces are assumed to not take the gravity load. So the bridge is modeled without the BRBs. The service load check for the single inclined BRB and inverted-V Chevron BRBs case is the same.

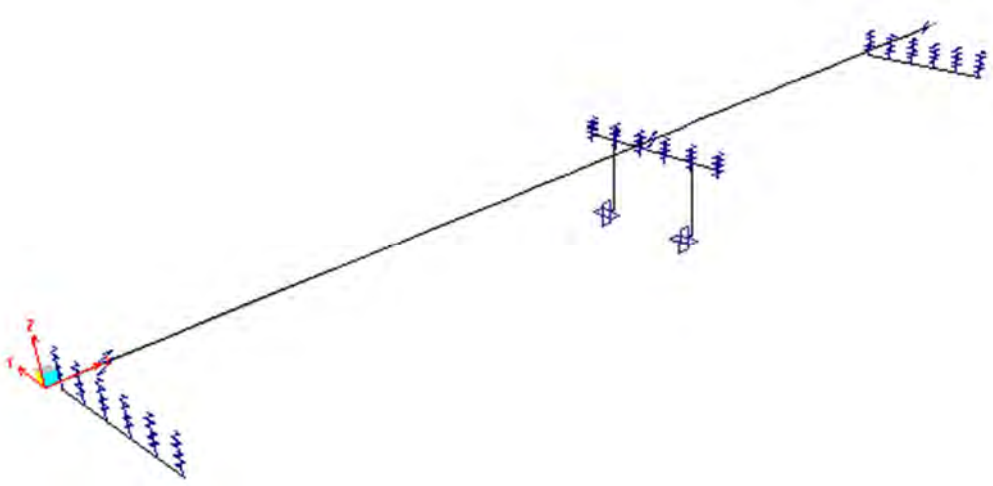

Figure 3-21 Global spine model of the bridge in 3-D view

The number of design lanes should be determined by taking the integer part of the

ratio $w$/12.0, where $w$ is the clear roadway in ft, between curbs or barriers. The top width of the box girder between the barriers is 44.67 ft.

$$n = round(w/12) = round(44.67/12) = 3$$

Therefore, the bridge deck is modeled with three lanes, each having 12 ft in width.

Details for the dead loads, live loads, and wind loads considered in the "service" load analyses are provided in the following sections.

#### 3.3.2.2 Bridge loads

##### 3.3.2.2.1 Dead load

Dead load includes the gravity loading from structural components and nonstructural attachments (DC), as well as that from wearing surfaces and utilities (DW), where DC and DW are the respective AASHTO parameters used to refer to those loads.

The area of the concrete box girder is 81.7 $ft^2$. The unit weight of the concrete girder is 0.15 $kip/ft^3$. Concrete barrier type 732 was also used, with a distributed weight of 0.41 kip/ft per barrier. With one barrier on each side of the bridge, the applied load is 0.82 kip/ft.

The total DC loading is therefore:

$$DC = 81.7 \times 0.15 + 0.41 \times 2 = 13.08 kip/ft$$

The self weight of the superstructure is automatically calculated by the program for the provided geometry of the box-girder and column's cross section, and material densities. Only the additional 0.82 kip/ft loads is therefore be applied directly on the bridge.

An allowance for a wearing surface of 35 psf was assumed. The top width of the concrete box girder between the barriers is 44.67 ft. Two bridge rails also give the distributed load of 0.5 kip/ft on each side of the bridge.

The total DW loading is therefore:

$DW = 0.035 \times 44.67 + 2 \times 0.5 = 2.56 kip / ft$

#### 3.3.2.2.2 Live load

There are two vehicular load types considered here:

(1) The standard vehicular live load condition for the roadways of the bridges, designated as HL-93 in the AASHTO bridge design specification (2010), and equivalent to HS 20-44 in the Caltrans bridge specification (2012).

(2) The permit truck load P15

In SAP2000, vehicle classes are defined; these may include any number of individual vehicles. The maximum and minimum force and displacement response quantities for a vehicle class will be the maximum and minimum values obtained for any individual vehicle in that class. Only one vehicle ever acts at a time. For the standard truck HL-93 load class, three vehicles standard type HL-93K, HL-93M, and HL-92S are used. For the permit truck load class, the P15 is used.

HL-93K load consists of the code-specified design truck and its related design lane load. HL-93M represents a design tandem truck and its related design lane load. HL-93S contains two code-specified design trucks and the design lane load, all scaled by 90%. The axle spacing for each truck is fixed at 14 feet. The spacing between the rear axle of the lead truck and the lead axle of the rear truck varies from 50 feet up to the length of the lane.

The static effects of the design truck or tandum are increased by a dynamic magnification factor of 33%. The force effect from the design lane load is not subject to a dynamic load allowance. The dynamic load allowance factor must be included in the live wheel load.

The truck wheel-line load can be placed in the design lane such that the center of any wheel load is not closer than 2' from the edge of the design lane or 1' from the edge of an overhang barrier.

The live load force effect shall be determined by considering each possible combination number of loaded lanes multiplied by a corresponding multiple presence factor to account for the probability of simultaneous lane occupation by the full truck design live load. The multiple presence factors are listed in Table 3-7. The vehicular loads are applied on the bridge lanes as shown in Figure 3-22 to illustrate the location of the live truck wheel load.

Table 3-8 Multiple presence factor for multi-lane truck load (AASHTO Bridge Design Specification, 2010)

| Number of loaded lanes | Multiple presence factors *m* |
|---|---|
| 1 | 1.20 |
| 2 | 1.00 |
| 3 | 0.85 |
| >3 | 0.65 |

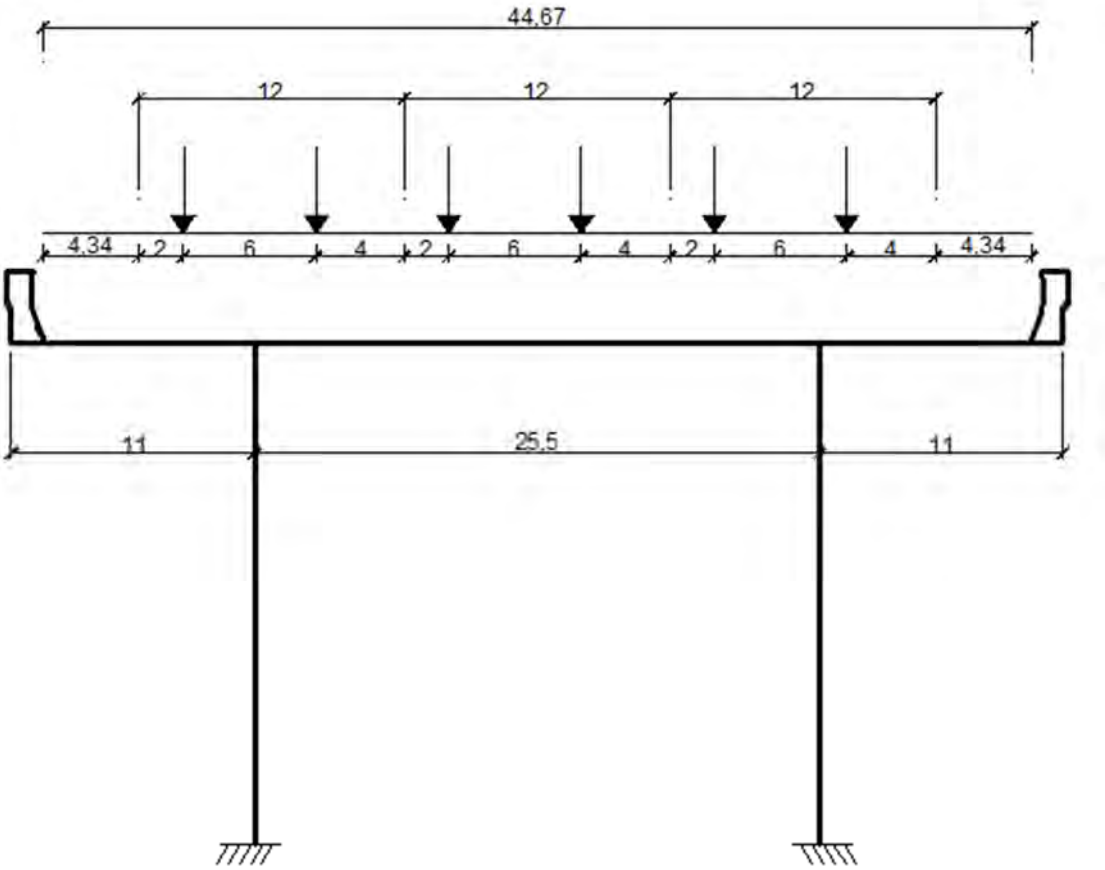


Figure 3-22 (1) Live load for three lanes

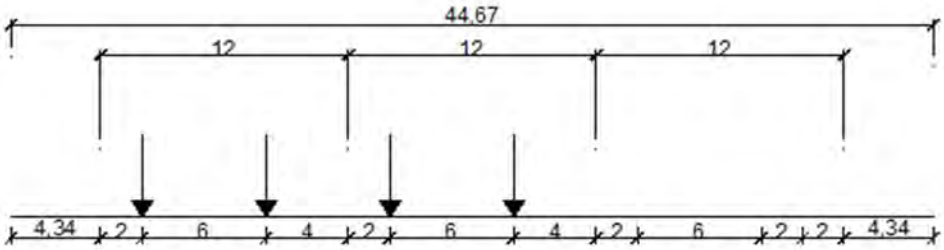


Figure 3-22 (2) Live load for lane 1 and 2

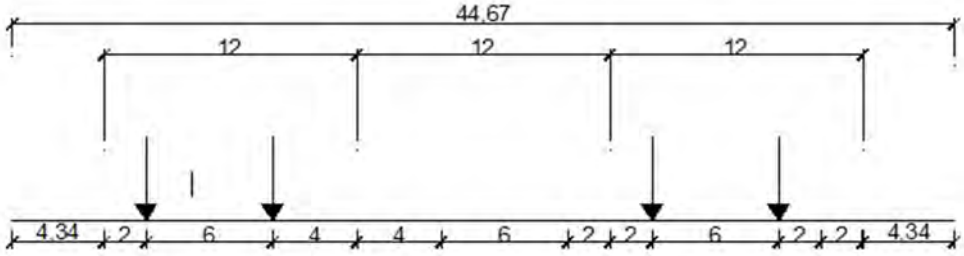


Figure 3-22 (3) Live load for lane 1 and 3

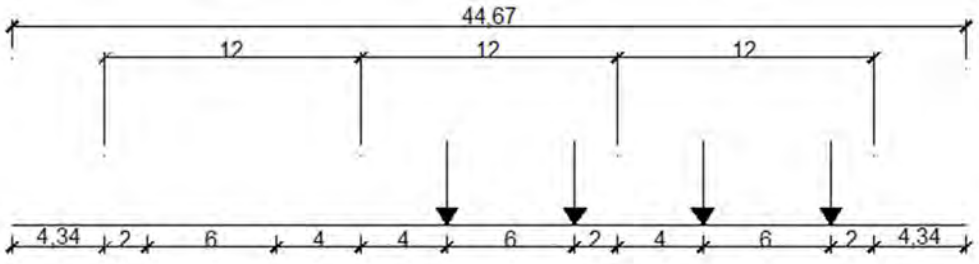


Figure 3-22 (4) Live load for lane 2 and 3

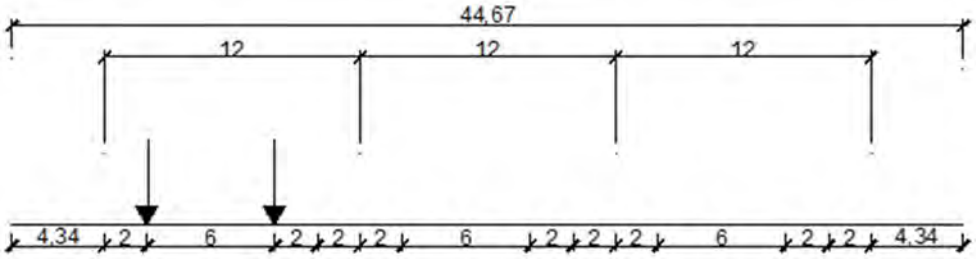


Figure 3-22 (5) Live load for lane 1

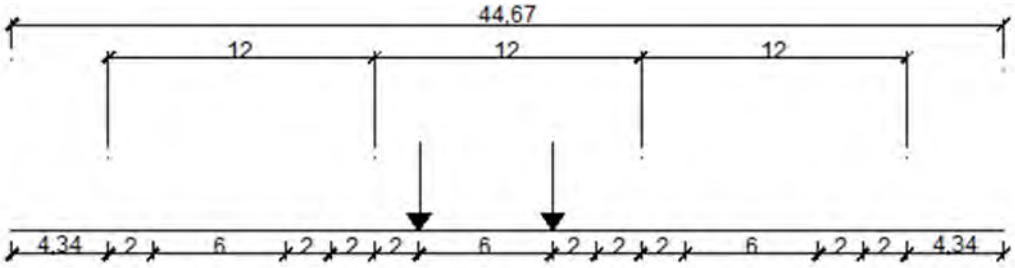


Figure 3-22 (6) Live load for one lane 2

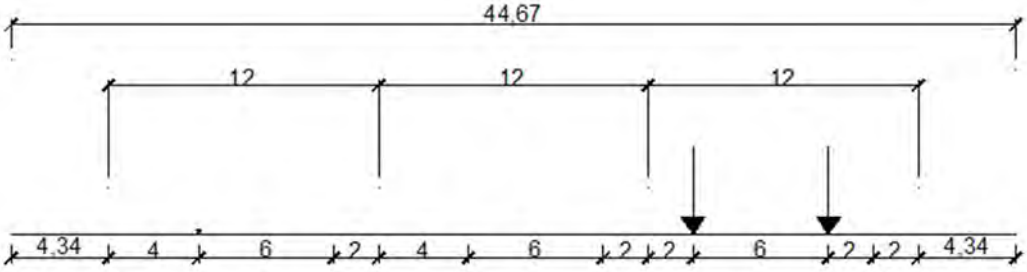


Figure 3-22 (6) Live load for one lane 3

Figure 3-22 Live load distribution on different road lanes

### 3.3.2.2.3 Wind load

The wind is assumed to act uniformly on the bridge area exposed to the wind. The exposed area is the sum of the areas of all components, as seen in elevation taken

perpendicular to the assumed wind direction. The skew angle is measured from the perpendicular to the longitudinal axis and the assumed wind direction shall be that which produces the maximum stress in the substructure. The transverse and longitudinal forces shall be applied simultaneously at the elevation of the center of gravity of the exposed area of the superstructure.

Wind pressure is assumed to be caused by a base design wind velocity $V_B$ of 100 mph. The bridge height is within 30.0' above the ground; as a result, the design wind velocity does not need to be adjusted for height.

Table 3-9 Base wind pressure for various angles of attack and $V_B$ = 100 mph (AASHTO bridge design specification, 2010)

| | Trusses | | Girders | |
|---|---|---|---|---|
| Skew Angle of Wind | Lateral Load | Longitudinal Load | Lateral Load | Longitudinal Load |
| Degrees | PSF | PSF | PSF | PSF |
| 0 | 75 | 0 | 50 | 0 |
| 15 | 70 | 12 | 44 | 6 |
| 30 | 65 | 28 | 41 | 12 |
| 45 | 47 | 41 | 33 | 16 |
| 60 | 24 | 50 | 17 | 19 |

The base wind pressure corresponding to the design wind velocity $V_B$ of 100 mph on the box girder is 0.05 ksf. The total wind loading shall not be taken less than 0.30 kip/ft on the beam or girder spans. The height of the barrier is 32 in.

The total height of the superstructure is

$$H_{super} = 32/12 + 6 = 8.67\,ft$$

The controlling distributed longitudinal wind load is

$$q_{long} = 8.67 \times 0.019 = 0.1647 \quad \text{kip/ft}$$

with the corresponding transverse wind load of $8.67 \times 0.017 = 0.1474$ kips/ft

The controlling distributed transverse wind load is

$V_{trans} = 8.67 \times 0.050 = 0.4335$ kip/ft > 0.30 kip/ft

with zero corresponding longitudinal load

### 3.3.2.3 Axis of members

The indication of the global and local axis in the bridge model is shown in Figure 3-23.

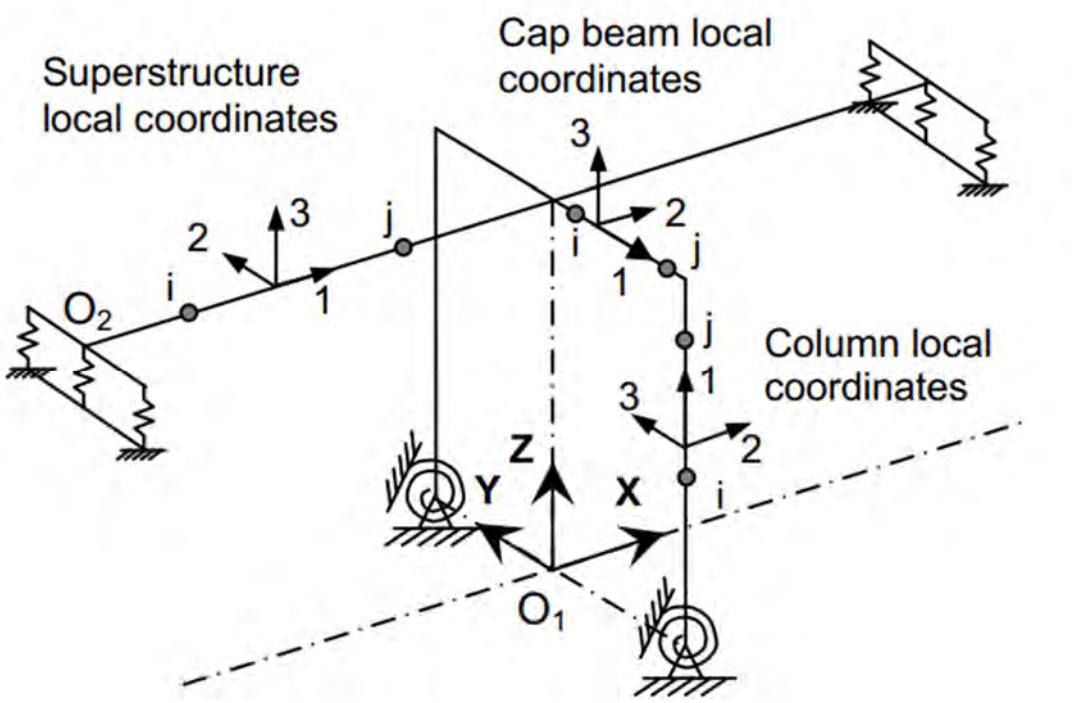


Figure 3-23 Global and local coordinate indication for cap beams and columns (Aviram, Mackie and Stojadinovic, 2008)

### 3.4.2.4 Service load analysis results

The critical forces in the columns are shown in Table 3-9 for the considered load cases. The numbering of the column element is shown in Figure 3-24.

Table 3-10 Analysis result of all the service load cases

| Load cases | Element | P (kips) | $V_2$ (kips) | $V_3$ (kips) | $M_2$ (kip-in) | $M_3$ (kip-in) |
|---|---|---|---|---|---|---|
| DC | 34 | -1431.7 | -0.29 | 0 | 0 | 36.36 |
| | 35 | -1469.71 | -0.29 | 0 | 0 | -21.12 |
| | 36 | -1431.7 | 0.29 | 0 | 0 | -36.36 |
| | 37 | -1469.71 | 0.29 | 0 | 0 | 21.12 |
| DW | 34 | -223.68 | -0.05 | 0 | 0 | 7.08 |
| | 35 | -223.68 | -0.05 | 0 | 0 | -4.08 |
| | 36 | -223.68 | 0.05 | 0 | 0 | -7.08 |
| | 37 | -223.68 | 0.05 | 0 | 0 | 4.08 |
| Wind | 34 | -22.75 | 0 | -28.00 | 2460.24 | 0 |
| | 35 | -22.75 | 0 | -28.00 | -3083.52 | 0 |
| | 36 | 22.75 | 0 | -28.00 | 2460.24 | 0 |
| | 37 | 22.75 | 0 | -28.00 | -3083.52 | 0 |
| Live maximum compression | 34 | -653.85 | 0 | -0.31 | -492.72 | -14514.7 |
| | 35 | -653.85 | 0 | -0.31 | -288.96 | -14514.7 |
| | 36 | -311.25 | 0 | -0.26 | -513.24 | -14514.7 |
| | 37 | -311.25 | 0 | -0.26 | -292.8 | -14514.7 |
| Live maximum tension | 34 | 7.21 | 0 | 0 | 531.48 | 8708.88 |
| | 35 | 7.21 | 0 | 0 | 303.96 | 8708.88 |
| | 36 | 7.21 | 0 | 2.30 | 0 | 8708.88 |
| | 37 | 7.21 | 0 | 2.30 | 0 | 8708.88 |
| Live Moment | 34 | -615.91 | 0 | -1.89 | -418.8 | -18506.3 |
| | 35 | -615.91 | 0 | -1.89 | -245.64 | -18506.3 |
| | 36 | -615.91 | 0 | -1.75 | -436.2 | -18506.3 |
| | 37 | -615.91 | 0 | -1.75 | -248.88 | -18506.3 |

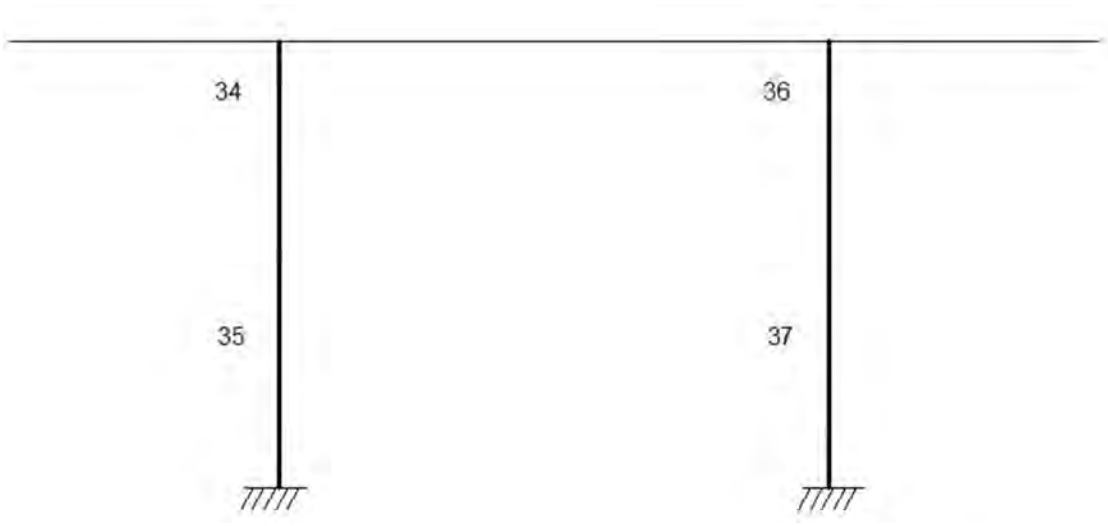


Figure 3-24 Element locations in the transverse bent

The combination load cases that are considered for column design are: Strength I, III, V, listed in AASHTO bridge design specification (2010).

Strength I= 1.25 DC + 1.50 DW + 1.75LL

Strength III = 1.25 DC + 1.50 DW + 1.40 WS

Strength V= 1.25 DC + 1.50 DW + 1.35 LL + 0.4WS

The governing forces resulting from these load combinations, and used to verify the adequacy of the design of columns, are presented in Table 3-10.

Table 3-11 The controlling force to design the bridge columns

| Governing Load cases | Element | P (kips) | $V_2$ (kips) | $V_3$ (kips) | $M_2$ (kip-in) | $M_3$ (kip-in) |
|---|---|---|---|---|---|---|
| Strength I, maximum column moment | 35 | -3250.5 | -0.4375 | -3.3075 | -429.87 | -32418.5 |
| Strength I, maximum column axial force | 34 | -3269.38 | -0.4375 | -0.5425 | -862.26 | -25344.7 |

The axial force and flexural moment interaction is checked for the columns strength in Table 3-11, where $P_u$ and $M_u$ are the force demand in the columns, $P_n$ and $M_n$ are the axial and flexural plastic strength of the CFT column obtained from Section Designer respectively, without considering the resistance factors. The results from the interaction equation confirm that column capacity to resist all non-seismic load combinations considered is sufficient.

Table 3-12 Capacity check for the CFT column

| Case | Axial load $P_u$ (kips) | Moment Demand $M_u$ (kip-in) | Flexural Strength $M_n$ (kip-in) | Axial strength $P_n$ (kips) | $P_u/P_r$ $+M_u/M_r$ |
|---|---|---|---|---|---|
| Strength I, maximum column Moment | -3250.5 | 32,421.39 | 185,621 | -16,437 | 0.37 |
| Strength I, maximum column axial force | -3269.38 | 25,359.32 | 185,621 | -16,437 | 0.34 |

## 3.4 Box-Pier Bents with BRBs Capacity Check

This section describes the analytical model built in SAP2000 to verify the bridge behavior of the box-pier bents with BRBs. The capacity of the columns is checked. Pushover curves from analysis result is plotted and compared with the theoretical one developed from the structural fuse concept. Section 3.4.2 presents the results of bridge analysis under the gravity dead and live load, as well as for wind loads.

## 3.4.1. Bent Pushover Analysis

### 3.4.1.1 Model information

The box-pier bridge configuration is shown in Figure 3-25. There are total eight CFT columns. The number of BRBs inserted between the columns is 16. Instead of performing a 3-D global analysis of the bridge, local analyses of the bent are considered adequate and are performed to verify the structural fuse concept in both the transverse and longitudinal directions.

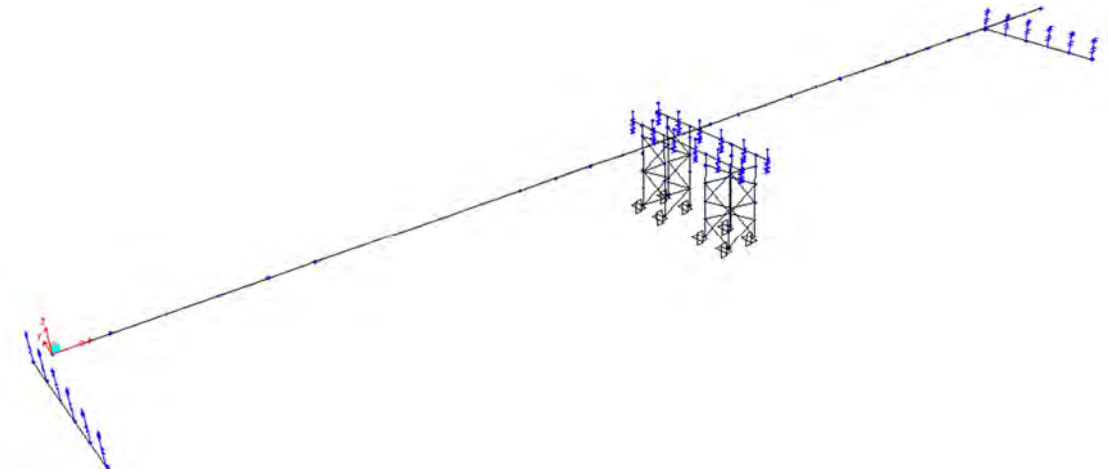

Figure 3-25 3-D bridge model of the bridge system

A close-up view of the bridge bent in the middle is shown in Figure 3-26. There are two bents with four columns and four BRBs between the adjacent columns in the transverse direction. Only one of them is modeled in Figure 3-27 (with column number of 187,189,191 and 193). The bridge bent is modeled as the bold lines as shown in Figure 3-26 for the BRBs to working within the clear distance of the CFT columns. The CFT columns are fixed at top to the cap beam, and at bottom to the ground. The footing is not modeled. The BRBs are designed to be pin connected to the columns (i.e. moments are released at both ends of the beam elements used to model the BRBs). The overhang of the box girder at each side of the bridge bent is 3 ft. The brace layout in the transverse bridge bent is symmetric; therefore only one pushover analysis of the bent in the transverse direction is needed.

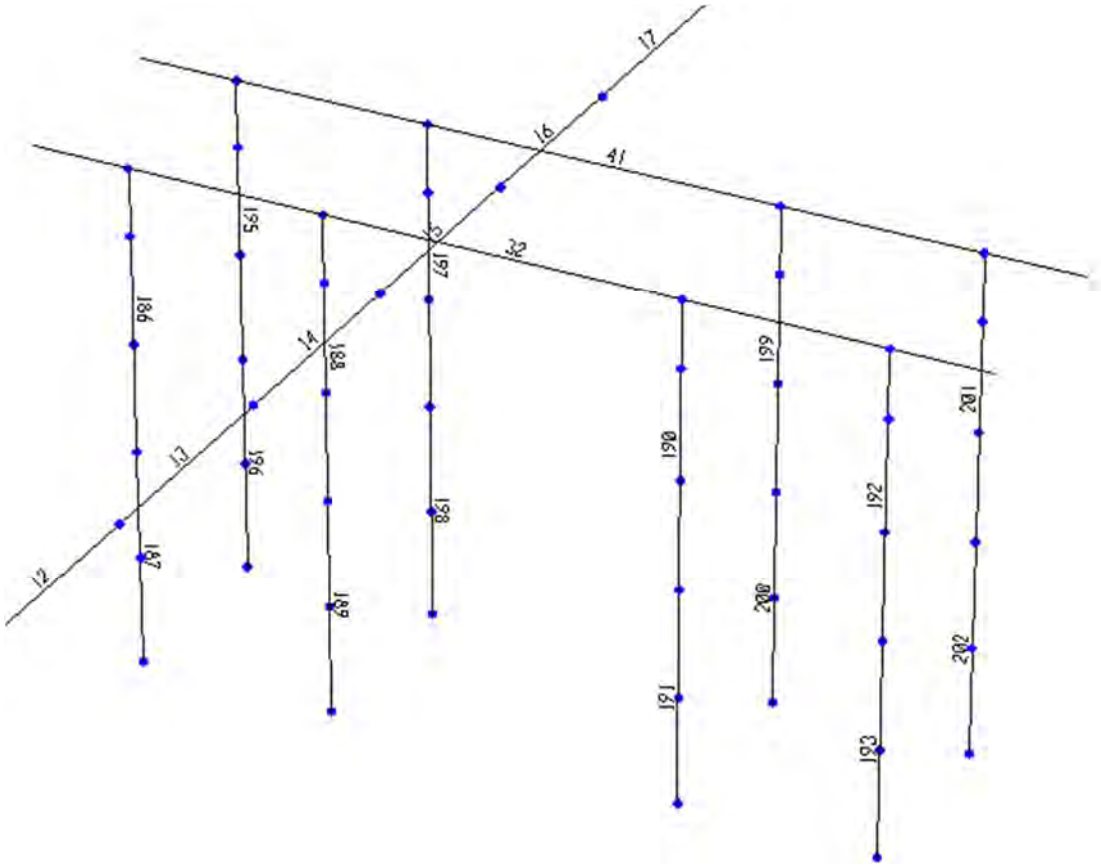


Figure 3-26 Enlarged 3-D view of the bridge bents in the middle of the bridge (with column numbers)

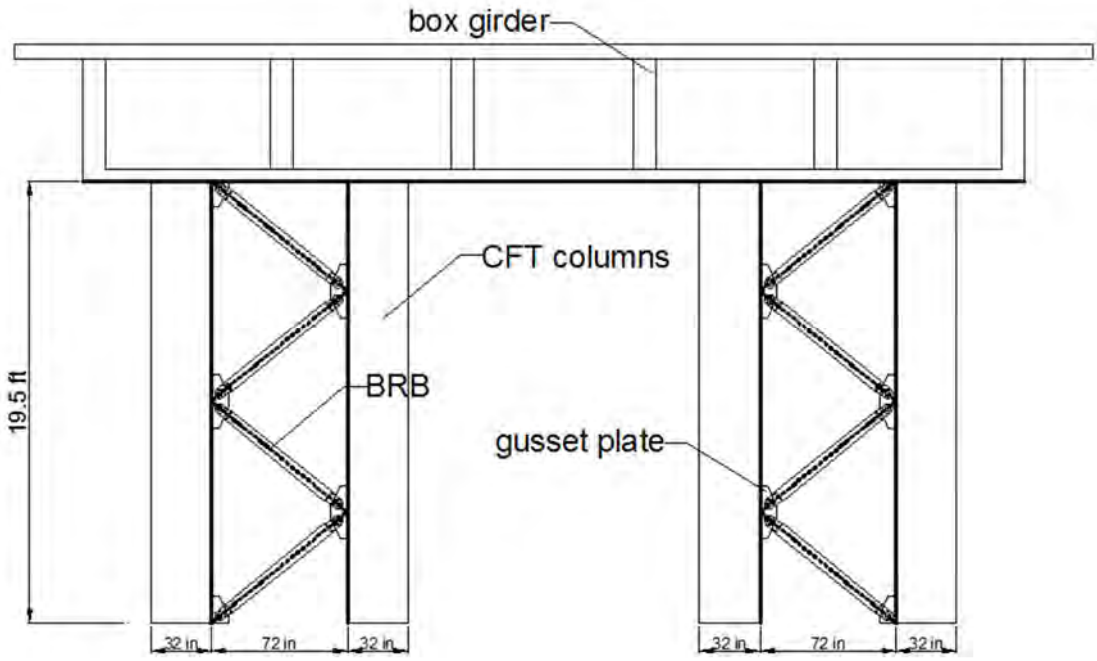


Figure 3-27 Transverse bridge bent with inserted BRBs

A similar model of one of the four longitudinal parallel bent frames with BRBs is also built to investigate the behavior of the bent in the pushover analysis for the longitudinal direction (with column number of 187 and 196). The elevation view of the longitudinal bent is provided in Figure 3-28, and the longitudinal bridge bent is built as the bold lines shown. In order to represent the restraint of the bent from the bridge box girder in the longitudinal direction, the cap beam level is restrained from rotation by providing a rigid body constraint in the vertical direction of the cap beam.

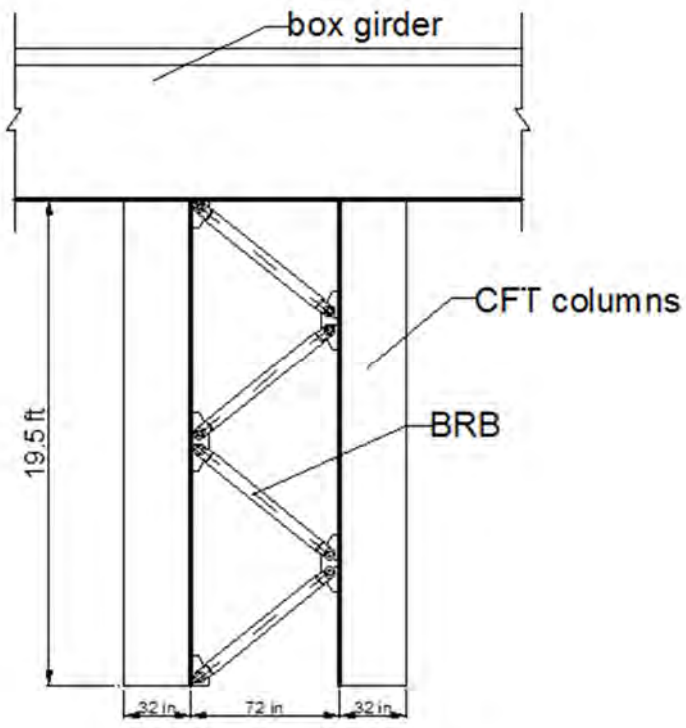


Figure 3-28 Longitudinal bridge bent with inserted BRBs

For the longitudinal direction, it is conceivable that all top BRBs could be in compression, or all in tension, depending on the overall layout used and direction of seismic loading. For a two-column bent, forces in columns were affected by the direction of loading (as BRBs in compression develop more force than in tension at the same drift). To investigate whether this is still the case here, two "layouts" are considered, namely Layout A and Layout B. For the frame shown in Figure 3-28, Layout A corresponds to the case of having a lateral load applied from left to right. Layout B corresponds to the same frame, but with the load applied from right to left.

In the analyses presented in Section 3.4.2, loads will always be applied from left to right, so the mirror image of the frame shown in Figure 3-28 will be used as Layout B. Arguably, it may been easier to simply refer to direction of loading while presenting results, but since the direction of lateral loads applied is not shown in the moment and axial force diagrams obtained from SAP2000, "Layouts" are used instead to differentiate between the two cases.

The same materials of the cap beam, CFT column, and the BRB as in the two-CFT -column bent with BRBs. The calculated yielding length ratio, *c*, is calculated to be 0.147 for the box-pier bent with BRBs. To make the overall deformation of the BRB in the SAP model match that of the actual BRB, the modulus of elasticity of A500 Gr.B (42 ksi) is increased to $Es = 29000 / 0.147 = 197279$ ksi. BRB has a cross section of 5.22 $in^2$.

According to Caltrans Seismic Design Criteria (2010) Section 7.4.2.1, the minimum cap width, $B_{cap,}$ is calculated to be the diameter of the column plus 2 ft. Therefore, the bent cap section is modeled as rectangle of 5'(width) by 6'(depth). For expediency, the cap beam is modeled as "infinitely rigid" relative to the columns by making the moment of inertia 1000 times larger than that corresponding to a 5' by 6' beam (to reflect the fact that flexure of the cap-beam would also engage the flexural rigidity of the box-girder in that direction).

The CFT column in the analytical model is built using SAP2000's Section Designer (which provides cross-section properties and moment-curvature strength using a fiber analysis). The diameter of the section is 32". The thickness of the steel shell is 0.75". A grid of 20 by 20 fibers is used for calculating the capacity of the section and plastic hinge analysis.

The same fiber hinge assignment for both the CFT column and BRB is also the same as the two-CFT-column bent with BRBs.

### 3.4.1.2 Load assignment

The dead loads are applied on the cap beam as point load where the webs of the box-girder are located (See Figure 3-29) for the bent model in the transverse direction. The dead loads are applied on the bent as a starting step of the nonlinear pushover analysis.

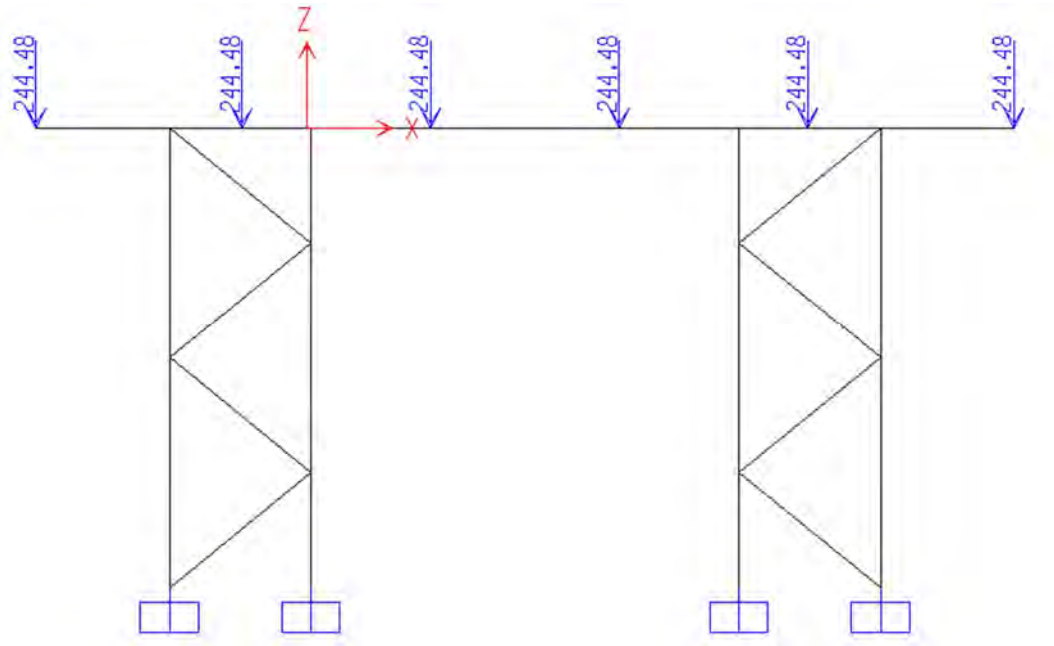


Figure 3-29 Dead loads applied to the bridge bent before push-over analysis in the transverse direction

The analysis result of the dead load applied to the transverse bent is shown in Figure 3-30. Note that the BRBs resist a negligible amount of dead loads, which justifies the design assumption of neglecting their contribution to resist gravity forces. Axial force ranging from 362 to 368 kips are resisted by the columns. The largest axial force of 368.03 appears in the middle column, which would be directly used as the point dead load applied to the longitudinal bent as shown in Figure 3-31.

The lateral load used for the pushover analysis consists of a horizontal load applied at

the center of the cap beam. The lateral load is applied from left to right. The horizontal displacement of the cap beam is the monitored displacement used in the displacement-control method in the pushover analysis.

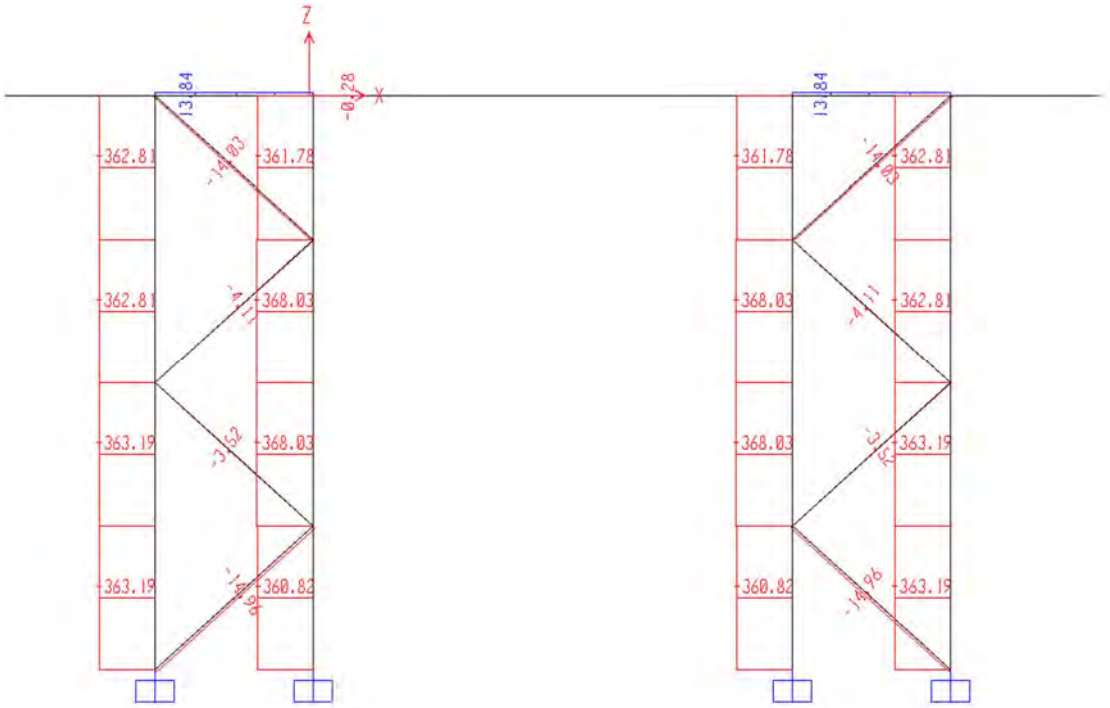


Figure 3-30 Axial loads in the transverse bridge bent members when the dead loads in figure 3-28 is applied on the cap beam

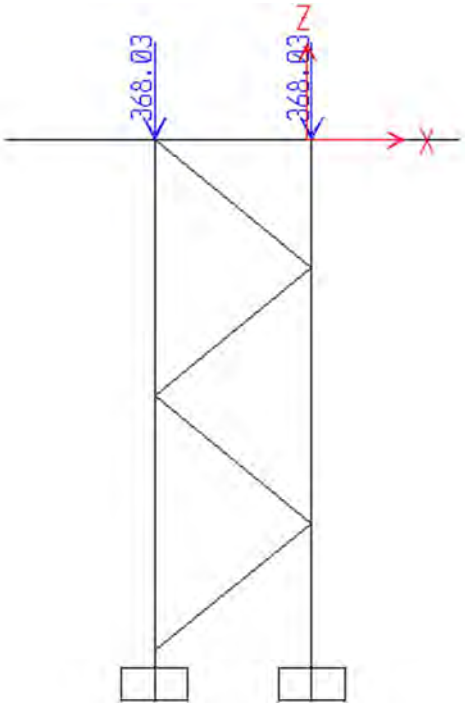


Figure 3-31 Dead loads applied to the bridge bent before push-over analysis in the longitudinal direction

### 3.4.1.3 Bent pushover analysis

#### 3.4.1.3.1 Response Spectrum Displacement Demand

As for the two-CFT-column bent case, the seismic force demand of the bridge model is assessed in the pushover analysis at the bent displacement value obtained from response spectrum analysis. The displacement demands of the box-pier bent with BRBs are shown below in Table 3-12. Smaller stiffness of the box-pier bent in both transverse and longitudinal directions can be observed, for the same reasons as those already presented in Section 3.3.1.3.

Table 3-13 The displacement demand comparison of the two-CFT-column bents

| Box-pier bents | Design | Analysis (Response Spectrum) | Difference |
|---|---|---|---|
| Transverse direction | 1.05” | 1.28” | 18% |
| Longitudinal direction | 1.05” | 1.17” | 10% |

#### 3.4.1.3.2 Transverse direction

When the bridge bent has a lateral displacement at the expected displacement of 1.28”, the moment demand in the columns is shown in Figure 3-32(a). The axial tensile and compressive forces in the columns are shown in Figure 3-32(b). The reactions at the bottom of the CFT columns are shown in Figure 3-32(c). The reaction forces are used to check the column strengths for the case when an eccentricity exists between the point where the bottom brace and column workline meet around the foundation.

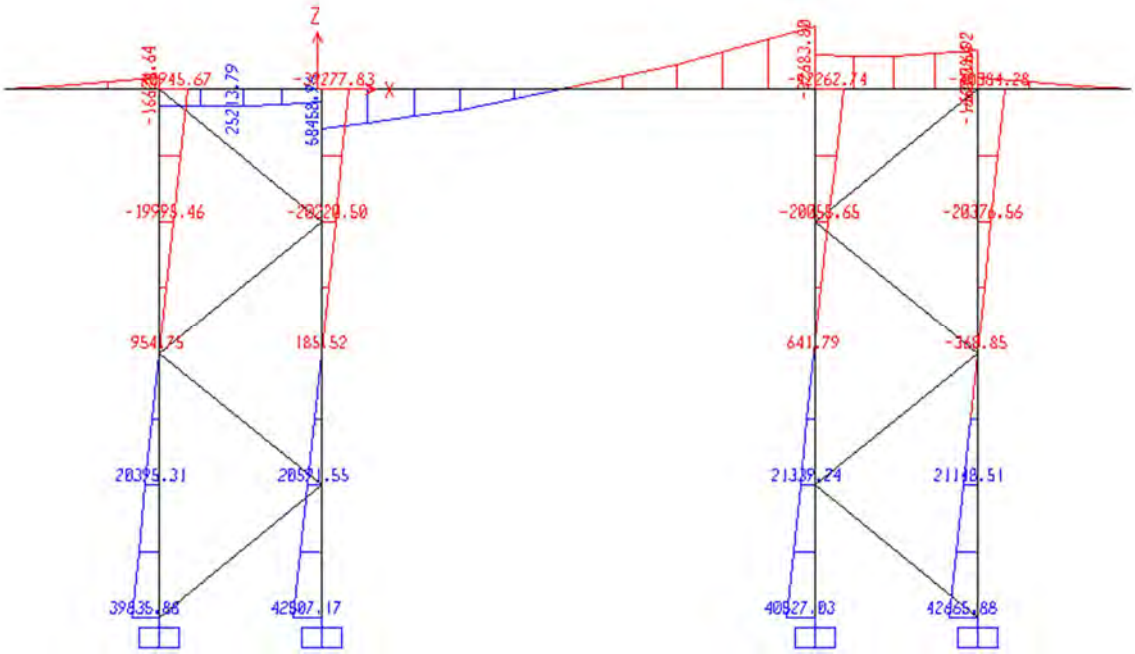


Figure 3-32 (a) Moment diagram of the bent when the expected displacement is reached at the top of the bent in the transverse direction

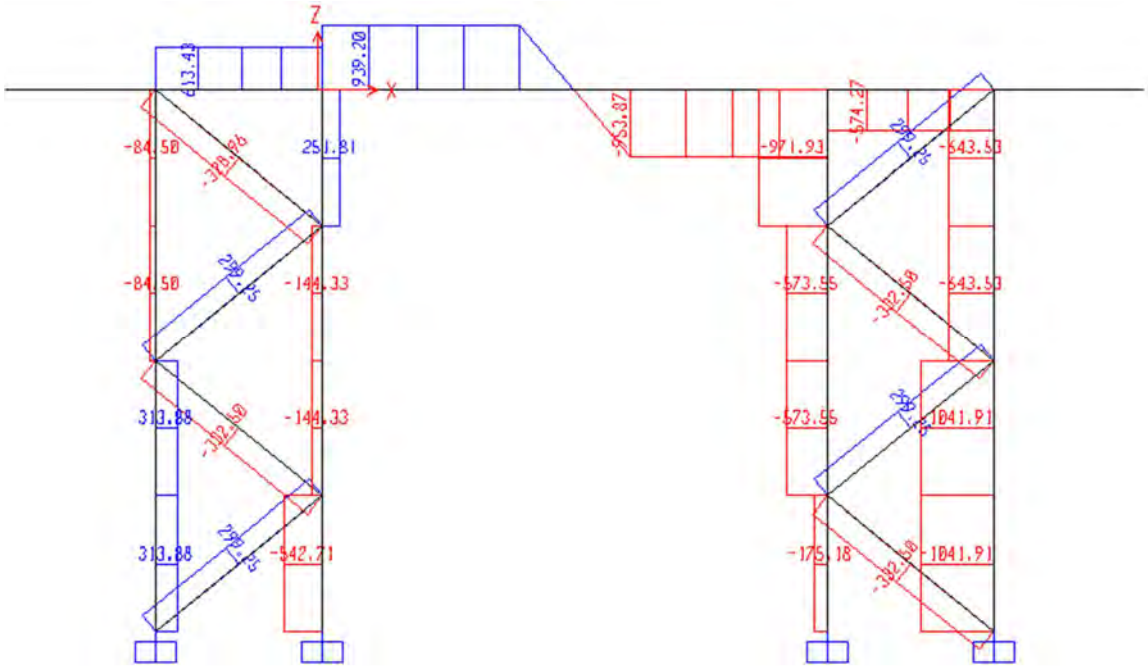


Figure 3-32 (b) Corresponding axial forces in the members of the bent

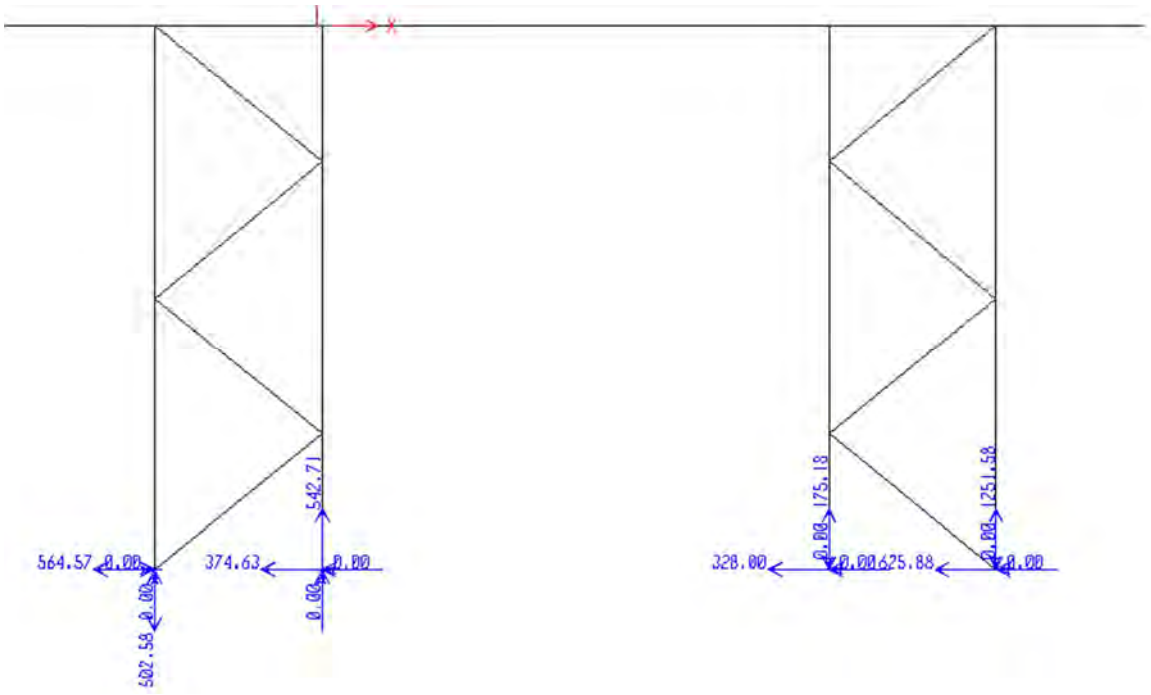


Figure 3-32 (c) Corresponding reactions at the bottom of the CFT columns

For the directional combination of the forces in the transverse and longitudinal directions, the reactions at the base of the columns are decomposed into three parts: (1) the overturning effect of the lateral load; (2) the forces applied by the yielding BRBs; and (3) the dead load. As demonstrated in Table 3-13 by subtracting the axial forces added by the BRBs and the dead loads, the axial forces left in the columns are those solely induced by the lateral forces. The compressive forces in the columns have minus signs.

Table 3-14 Components of the reaction at the bottom of the CFT in the transverse direction

| Reaction force location of corresponding column number | Analysis result (kips) | Dead loads (kips) | BRBs (kips) | Lateral load (kips) |
|---|---|---|---|---|
| 187 | 502 | -363 | 795 | 70 |
| 189 | -543 | -361 | -795 | 613 |
| 191 | -175 | -361 | 795 | -609 |
| 193 | -1252 | -363 | -795 | -94 |

### 3.4.1.3.3 Longitudinal direction

There are two longitudinal frames model required for the pushover analysis.

1) Layout A

At the expected displacement 1.17", the moment demand in the columns is shown in Figure 3-33(a). The corresponding axial tensile and compressive forces are shown in Figure 3-33(b). The reactions at the bottom of the CFT columns are shown in Figure 3-33 (c).

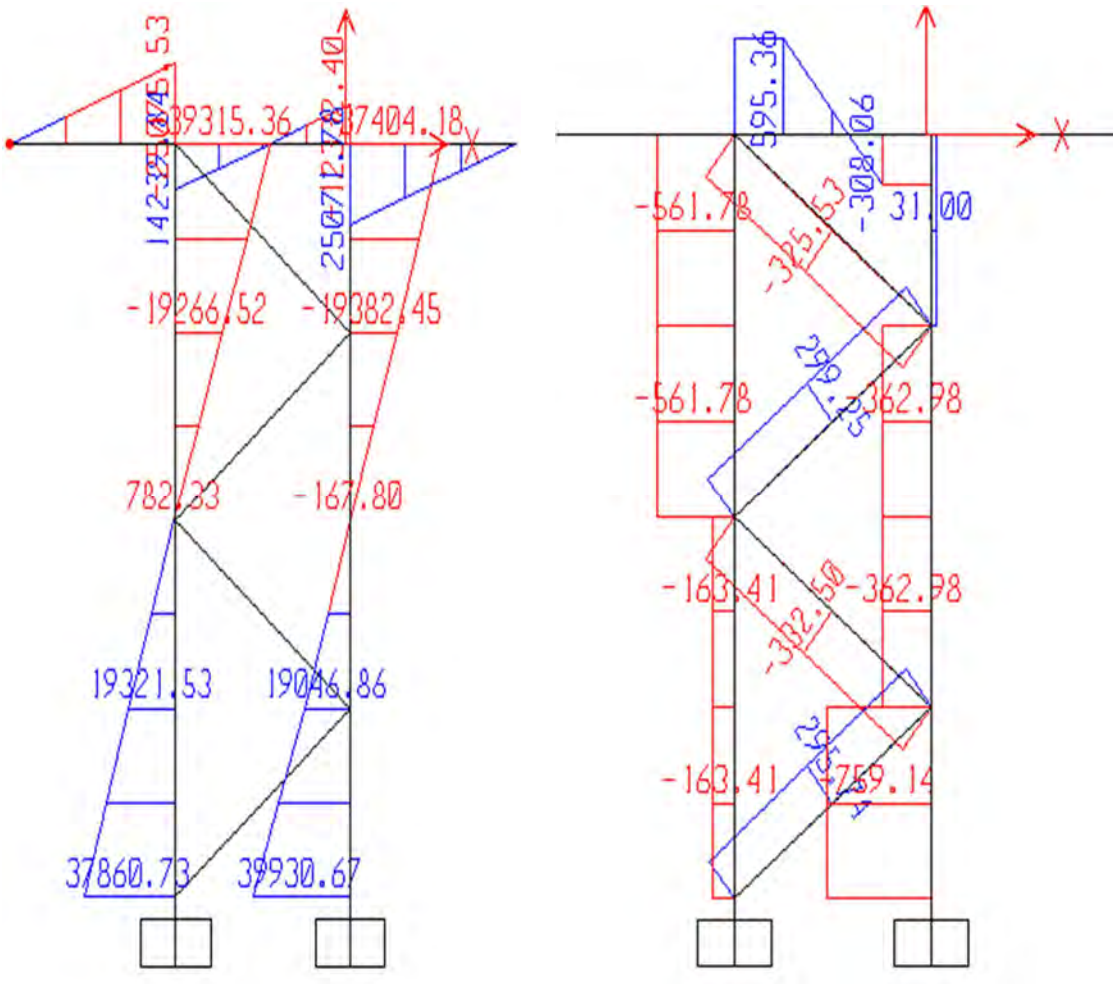


(a) (b)

Figure 3-33 (a) Moment diagram of the longitudinal bent in layout A when the expected displacement at the top of the bent is reached (b) Corresponding axial forces in the members of the bent

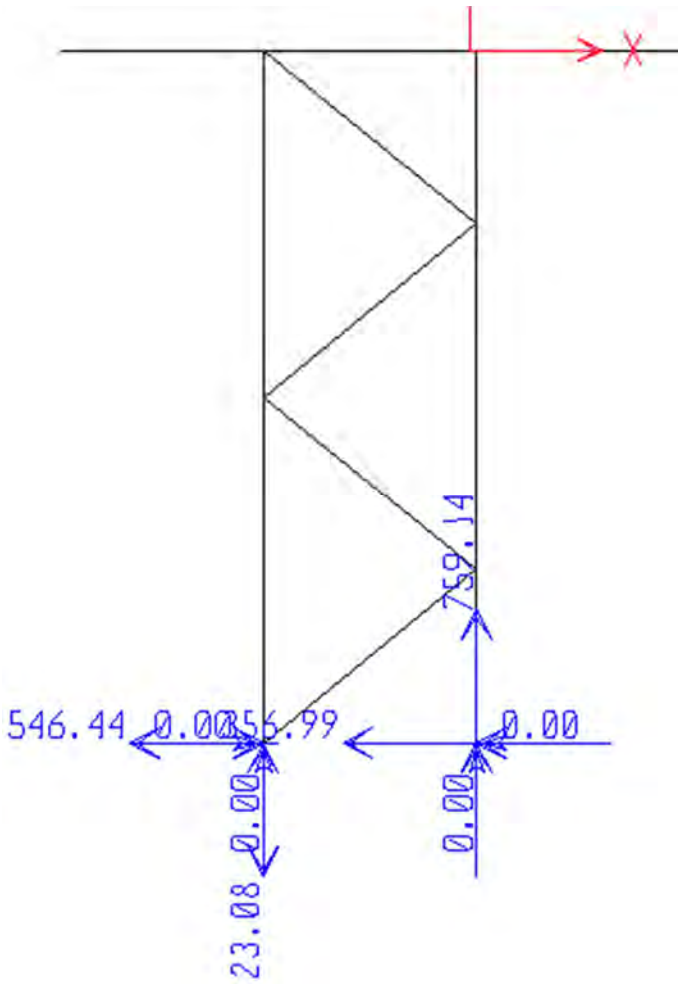


Figure 3-33 (c) Corresponding reactions at the bottom of the CFT columns

2) Layout B

The force diagrams shown in Figure 3-34 are obtained at the same expected displacement 1.17".

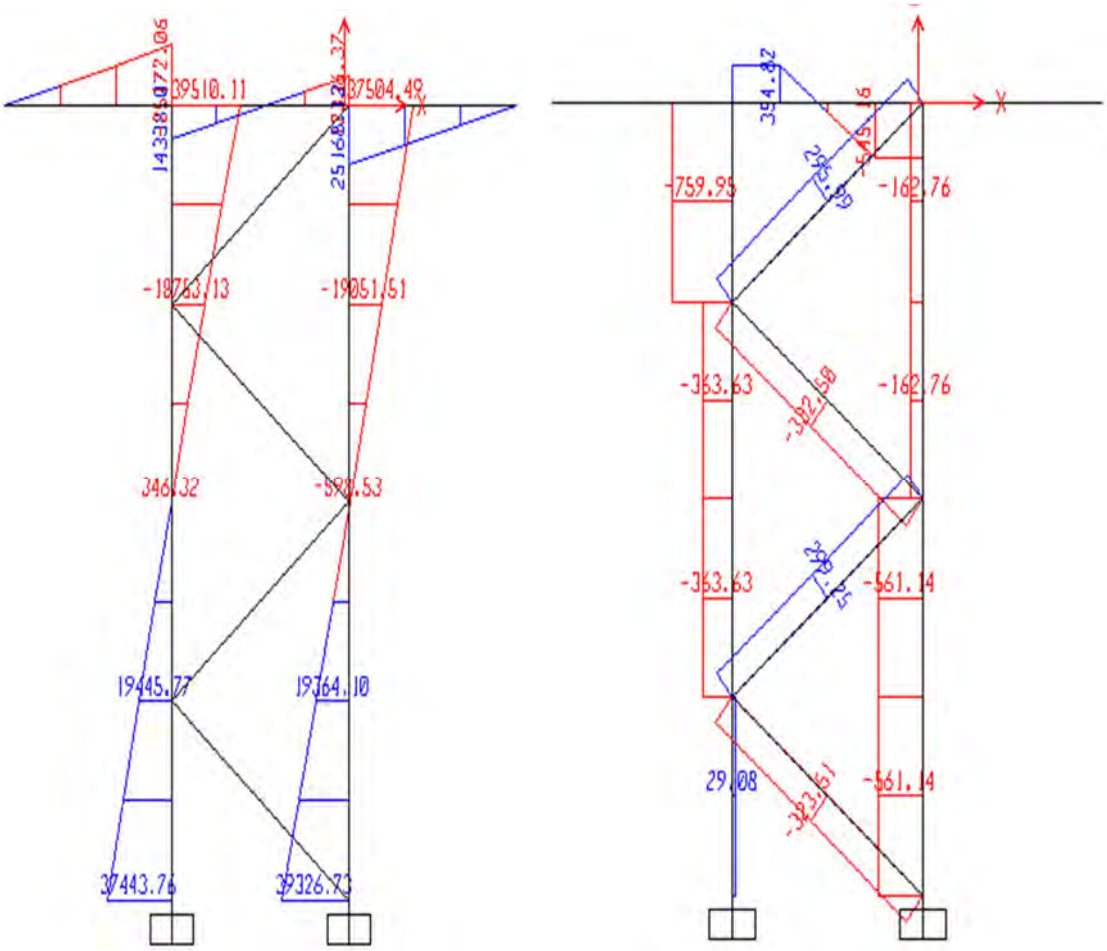


(a) (b)

Figure 3-34 (a) Moment diagram of the longitudinal bent in layout B when the expected displacement is reached at the top of the bent; (b) Corresponding axial forces in the members of the bent

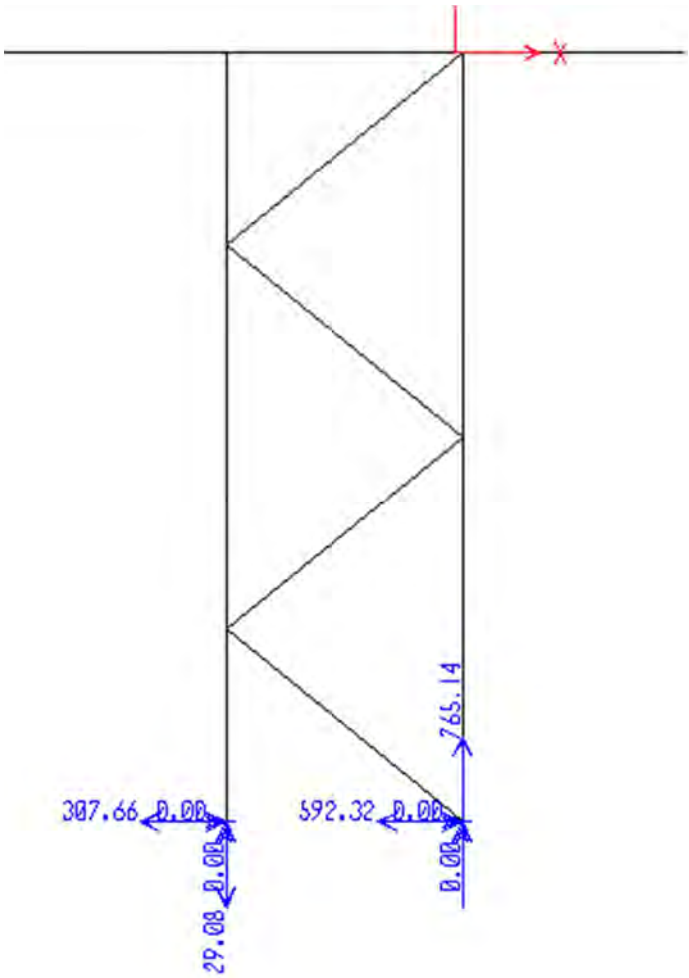


Figure 3-34 (c) Corresponding reactions at the bottom of the CFT columns

Same as what is done for the case of lateral loading applied in the transverse direction, the reactions at the base of the CFT columns in the longitudinal direction are also broken down in Table 3-14 into the various contributions to those reactions, for both layout A and B.

Table 3-15 Components of the reactions at the bottom of the columns in the longitudinal direction

| Reaction force location of corresponding column number | Analysis result (kips) | Dead loads (kips) | BRBs (kips) | Lateral load (kips) |
|---|---|---|---|---|
| A-187 | 23 | -368 | 790 | 399 |
| A-196 | -759 | -368 | -790 | -399 |
| B-187 | 29 | -368 | 790 | 393 |
| B-196 | -765 | -368 | -790 | -393 |

#### 3.4.1.3.4 Directional combination

In an actual earthquake, the seismic forces are simultaneously applied to the bent in difference directions. Therefore, given that the structural fuse concept is intended to be effective for seismic excitation in any horizontal direction, the bi-direction combination of the force demand in the transverse and longitudinal direction is considered here. This section performs the capacity check for axial force and flexure interaction, and shear as well.

1) Axial force and flexure interaction

The moment demands in both directions, shown in Figure 3-32, 3-33 and 3-34 are listed in Table 3-15.

Table 3-16 Moment demand at the base of the column in both directions

| | Column number | Moment demand (kip-in) | | |
|---|---|---|---|---|
| | | Transverse | Longitudinal Layout A | Longitudinal Layout B |
| Bent 1 | 187 | 39,837 | 37,861 | 37,444 |
| | 189 | 42,507 | 37,861 | 37,444 |
| | 191 | 40,527 | 37,861 | 37,444 |
| | 193 | 42,666 | 37,861 | 37,444 |
| Bent 2 | 196 | 39,837 | 39,931 | 39,327 |
| | 198 | 42,507 | 39,931 | 39,327 |
| | 200 | 40,527 | 39,931 | 39,327 |
| | 202 | 42,666 | 39,931 | 39,327 |

Note: The two parallel bent seen from the transverse direction as shown in Figure 3-26.

Table 3-16 presents the critical controlling vertical reactions at the bottom of the CFT column. The reaction induced by the dead loads is conservatively taken as the largest column axial force appearing in the columns as shown in Figure 3-30.

It is clear from Tables 3-13, 3-14, and 3-15, that results from Layout A and Layout B are nearly identical, for all practical purposes. Therefore, direction of lateral loading is not significant in this case as far as member forces are considered. However, for the case where there would be an eccentricity between the foundation and the intersection of the worklines of the column and the lower BRB, the demands at the lowest segment of the columns would be different for Layouts A and B.

Table 3-17 Components of the controlling vertical reactions at the base of the columns considered for the combination

| Column number | | Longitudinal lateral force induced axial load (kips) | Transverse lateral force induced axial load (kips) | BRB induced axial load in transverse direction (kips) | BRB induced axial load in longitudinal direction (kips) | Dead load induced axial load (kips) |
|---|---|---|---|---|---|---|
| Layout A | 187 | 399 | 70 | 795 | 790 | -368 |
| | 189 | -399 | 613 | -795 | -790 | -368 |
| | 191 | 399 | -609 | 795 | 790 | -368 |
| | 193 | -399 | -94 | -795 | -790 | -368 |
| Layout B | 196 | 393 | 70 | 773 | 752 | -368 |
| | 198 | -393 | 613 | -773 | -752 | -368 |
| | 200 | 393 | -609 | 774 | 752 | -368 |
| | 202 | -393 | -94 | -774 | -752 | -368 |

The Caltrans Seismic Design Criteria (2010) section 2.1.2 requires that the earthquake effects shall be determined from horizontal ground motion applied by one of two possible methods. The method used here consists of applying the ground motion in two orthogonal directions along a set of global axes, where the longitudinal axis is typically represented by a chord connecting the two abutments: two cases must be considered

- Case I: Combine the response resulting from 100% of the transverse loading with the corresponding response from 30% of the longitudinal loading
- Case II: Combine the response resulting from 100% of the longitudinal loading

with the corresponding response from 30% of the transverse loading

Here, the overall moment demand at base of the columns is decided based on the square root of the sum of the squares of 100% of the moment in one direction plus 30% of the moment in the other direction.

The total controlling reaction forces at the base of the CFT columns are calculated to be the maximum of:

(1) 100% of longitudinal + 30% of transverse + BRB (transverse + longitudinal) + dead; or

(2) 30% of longitudinal + 100% of transverse + BRB (transverse + longitudinal) + dead.

where "BRB (transverse + longitudinal)" means that the BRBs have yielded in both directions, and that the corresponding forces at their strain-hardening level of 1.5% strain have been added together. Note that this is somewhat conservative, as the 1.5% strain may not necessarily be reached in the direction in which 30% of the lateral load is applied.

The moment and axial load demands with directional combination are tabulated in Table 3-18. As an example of the notation used in this table, "$L_A$" stands for longitudinal ("L") analysis for layout A ("A").

Table 3-18 Summarized force demands at the base of the columns

| Column type | | Moment Demand $M_u$ (kip-in) | Vertical Reaction Demand $P_u$ (kips) |
|---|---|---|---|
| 187 | (100%T+30%$L_A$) | 41424.6 | 1406.7 |
| | (30%T+100%$L_A$) | 39702.4 | 1637 |
| | (100%T+30%$L_B$) | 41390.5 | 1404.9 |
| | (30%T+100%$L_B$) | 39305.0 | 1631 |

| | | | |
|---|---|---|---|
| 189 | (100%T+30%$L_A$) | 43998.4 | -1220.3 |
| | (30%T+100%$L_A$) | 39950.9 | -1370.1 |
| | (100%T+30%$L_B$) | 43966.2 | -1222.1 |
| | (30%T+100%$L_B$) | 39555.9 | -1376.1 |
| 191 | (100%T+30%$L_A$) | 42088.6 | 727.7 |
| | (30%T+100%$L_A$) | 39765.2 | 1433.3 |
| | (100%T+30%$L_B$) | 42055.0 | 725.9 |
| | (30%T+100%$L_B$) | 39368.4 | 1427.3 |
| 193 | (100%T+30%$L_A$) | 44152.0 | -1927.3 |
| | (30%T+100%$L_A$) | 39966.1 | -1582.2 |
| | (100%T+30%$L_B$) | 44120.0 | -1929.1 |
| | (30%T+100%$L_B$) | 39571.3 | -1588.2 |
| 196 | (100%T+30%$L_A$) | 41599.2 | 1107.3 |
| | (30%T+100%$L_A$) | 41681.1 | 779 |
| | (100%T+30%$L_B$) | 41547.3 | 1109.1 |
| | (30%T+100%$L_B$) | 41102.8 | 785 |
| 198 | (100%T+30%$L_A$) | 44162.8 | -1399.7 |
| | (30%T+100%$L_A$) | 41917.8 | -2108.1 |
| | (100%T+30%$L_B$) | 44113.9 | -1397.9 |
| | (30%T+100%$L_B$) | 41342.8 | -2102.1 |
| 200 | (100%T+30%$L_A$) | 42260.4 | 429.3 |
| | (30%T+100%$L_A$) | 41740.9 | 576.3 |
| | (100%T+30%$L_B$) | 42209.4 | 431.1 |
| | (30%T+100%$L_B$) | 41163.5 | 582.3 |
| 202 | (100%T+30%$L_A$) | 44315.8 | -2107.7 |
| | (30%T+100%$L_A$) | 41932.3 | -2321.2 |
| | (100%T+30%$L_B$) | 44267.2 | -2105.9 |
| | (30%T+100%$L_B$) | 41357.6 | -2315.2 |

The flexural yield strength $M_y$, plastic strength $M_p$, tensile axial strength $P_{nt}$, and compressive axial strength $P_{nc}$ are obtained from SAP2000 Section Designer fiber

analysis and listed in Table 3-19. The controlling moment and axial forces are checked for the axial force and moment interaction. No resistance reduction factors are applied. Also note that reactions are used for the axial forces, again accounting for the possibility of an eccentricity between the foundation and the intersection of the worklines of the column and the bottom BRB. If that eccentricity doesn't exist, the corresponding results are shown in Table 3-20.

Table 3-19 Column capacity checking (case with eccentricity)

| Column Type | Moment Demand $M_u$ (kip-in) | Reaction Demand $P_u$ (kips) | Plastic Strength $M_n$ (kip-in) | Axial Strength $P_n$ (kips) | $M_u/M_n$ $+P_u/P_n$ |
|---|---|---|---|---|---|
| Ten. | 41424.6 | 1406.7 | 49,687 | 4389.5 | 1.15 |
| Comp. | 44267.2 | -2105.9 | 49,687 | -6857.7 | 1.20 |

Table 3-20 Refined column axial and flexure interaction capacity checking

| Column Type | Moment Demand $M_u$ (kip-in) | Reaction Demand $P_u$ (kips) | Plastic Strength $M_n$ (kip-in) | Axial Strength $P_n$ (kips) | $M_u/M_n$ $+P_u/P_n$ |
|---|---|---|---|---|---|
| Ten. | 41424.6 | 1031.5 | 49,687 | 4389.5 | 1.07 |
| Comp. | 44,152 | -1692.2 | 49,687 | -6857.7 | 1.14 |

The plastic moment and axial force interaction check gives values slightly larger than 1.0 for some cases. However, it is recognized that using a linear interaction diagram is a conservative approximation; results are compared below with the actual interaction diagram for CFT columns.

The interaction equation used in Table 3-19 and 3-20 for the axial force and plastic

flexural strength is a simple linear relationship. It is equivalent to the interaction diagram shown in Figure 3-12, for a B factor equal to 1.0. In reality, for CFT columns, in compression, B is typically less than 1.0, which provides for further reserve strength.

It is conservative to use that linear interaction equation here, instead of the interaction equations provided in the AASHTO LRFD Seismic design specification (2009) section 7.6.1 for axial compression and moment (which uses a calculated B value, typically less than 1.0). Note that there exists no equation in AASHTO for the axial tension and flexural interaction of CFT sections. The AASHTO compression-flexure interaction equation for CFT gives:

$$\frac{P_u}{\phi_c \mathrm{P}_n} + B\frac{M_u}{M_n} \le 1 \quad (7.6.1\text{-}1) \text{ and } \frac{Mu}{Mn} \le 1 \quad (7.6.1\text{-}2)$$

$$B = 1 - \frac{\mathrm{P}_{rc}}{\phi_c P_n} = 1 - \frac{\phi_{c1} f_c A_c}{\phi_c P_n} = 1 - \frac{0.75 \times 4 \times 730.6}{\phi_c P_n}$$

where: $\phi_{c1} = 0.75$, $\phi_c = 1.0$

Table 3-21 gives the axial-flexure interaction check for compression column considering the *B* factor. There is no B factor check for tensile columns.

Table 3-21 Refined column capacity checking considering B factor for compression column

| Column Type | Moment Demand $M_u$ (kip-in) | Axial Load Demand $P_u$ (kips) | Plastic Strength $M_n$ (kip-in) | *B* factor | Axial Strength $P_n$ (kips) | $BM_u/M_n + P_u/P_n$ |
|---|---|---|---|---|---|---|
| Comp. | 44,152 | -1692.2 | 49,687 | 0.68 | -6857.7 | 0.85 |

Note that all the above are interaction equations based on cross-section strength. Columns were designed considering the actual column

slenderness. However, as shown Appendix B, the columns are quite stocky and slenderness has a minimal impact of strength for this particular example.

2) Shear force

The horizontal reaction forces from Figures 3-31c, 3-32c and 3-33c are listed in Table 3-22.

Table 3-22 Column shear capacity check

| Column number | | Transverse horizontal reaction (kips) | Largest Longitudinal horizontal reaction (kips) | Square root of reactions from two directions |
|---|---|---|---|---|
| Layout A | 1 | 565 | 546 | 588 |
| | 2 | 375 | 546 | 557 |
| | 3 | 328 | 546 | 554 |
| | 4 | 626 | 546 | 647 |
| Layout B | 1 | 565 | 592 | 616 |
| | 2 | 375 | 592 | 603 |
| | 3 | 328 | 592 | 600 |
| | 4 | 626 | 592 | 651 |

The shear forces are not divided based on the origin of the shear force as done for the large axial force. Given that the column's cross section is circular; a square root combination of the demands in the two orthogonal directions is conservatively carried out, which gives the vectorial resultant shear force acting on the columns (the largest of corresponding to a 100% and 30% combination of seismic forces), when the eccentricity exists between the point where the bottom brace and column workline meet around the foundation. The shear strength calculated based on the equations provided

by AISC (2010) and AASHTO Bridge Design Specifications (2010) is 1192.5 kips with the resistance factor 0.9. The shear force demands calculated are all within this strength limit.

Note that these large shear forces would reduce the column flexural strength. Since there is currently no equations provided in AASHTO or AISC quantifying the magnitude of this interaction for CFT columns under the combined shear and flexural strength, the strength check for the column is only performed for the axial and flexural combination.

#### 3.4.1.4. Pushover curve

The pushover curve verification is done for the transverse bent and longitudinal bent in layout A.

##### 3.4.1.4.1 Transverse bent

Figure 3-35 shows the theoretical pushover curves of lateral shear resistance versus top displacement of the column for the frame, BRB, and the combined system, obtained using a bilinear force deformation relationship for the columns (yielding at a moment of $M_y$=34199) and tri-linear relationship for BRBs yielding at 42 ksi and strain hardening to 63 ksi at a strain of 0.015). The purple line of the theoretical BRB shows the yielding of the BRB at the displacement of 0.101", and point where the maximum strain hardening considered is reached, at 1.05". The target displacement of the bent is reached when the BRBs reaches the strain hardening value of 1.5% strain. The theoretical frame curve in navy blue dash lines shows that the frame yields at the displacement of 1.05". The two parts add up to the total theoretical curve for the combined system plotted in red dash lines. The left green vertical dash dotted line represents the expected displacement for the structural fuse system.

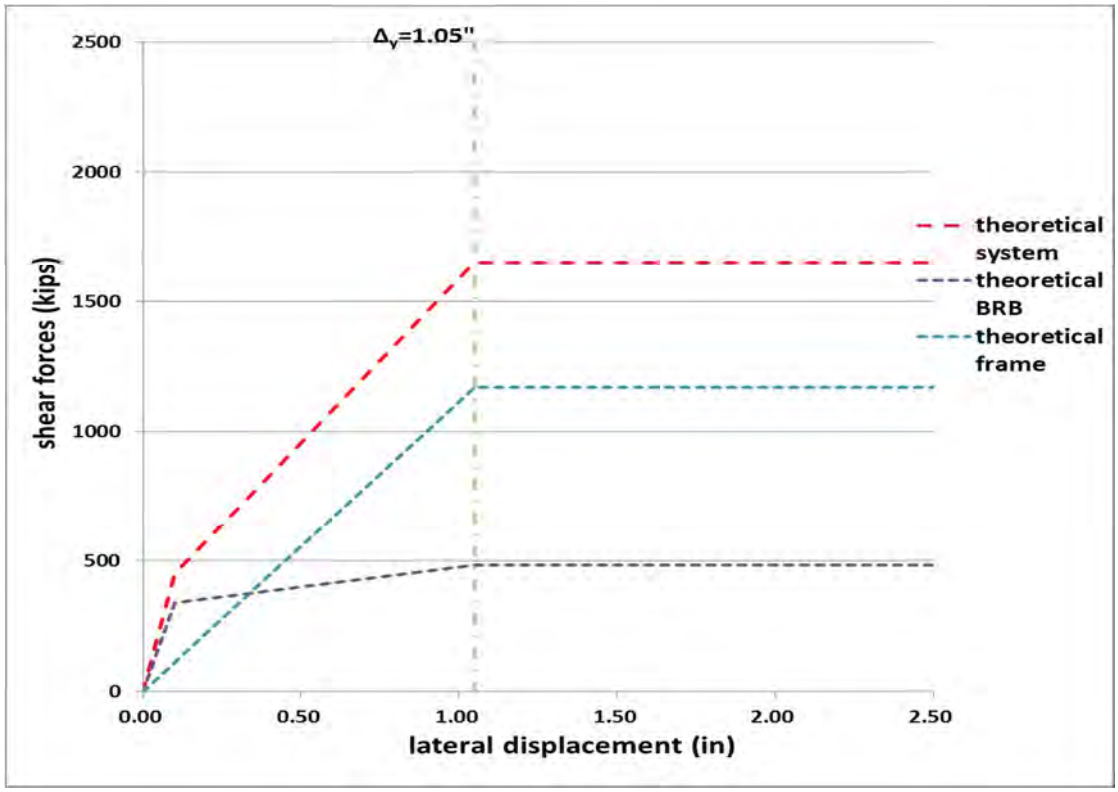


Figure 3-35 Theoretical pushover curves of the frame, BRB and the combined system in the transverse direction

The pushover curve obtained from the SAP2000 analysis (in solid lines) overlays on top of the results from Figure 3-35 in Figure 3-36. The solid blue line shows the total base shear versus lateral displacement at top of the bent. By subtracting the lateral forces resisted by the BRBs (equal to the horizontal component of the forces in the BRB) shown in solid green line, the solid brown line gives the portion of the base shear forces resisted by the frame. Note that the SAP2000 analyses consider both yielding and strain hardening of the BRBs and columns.

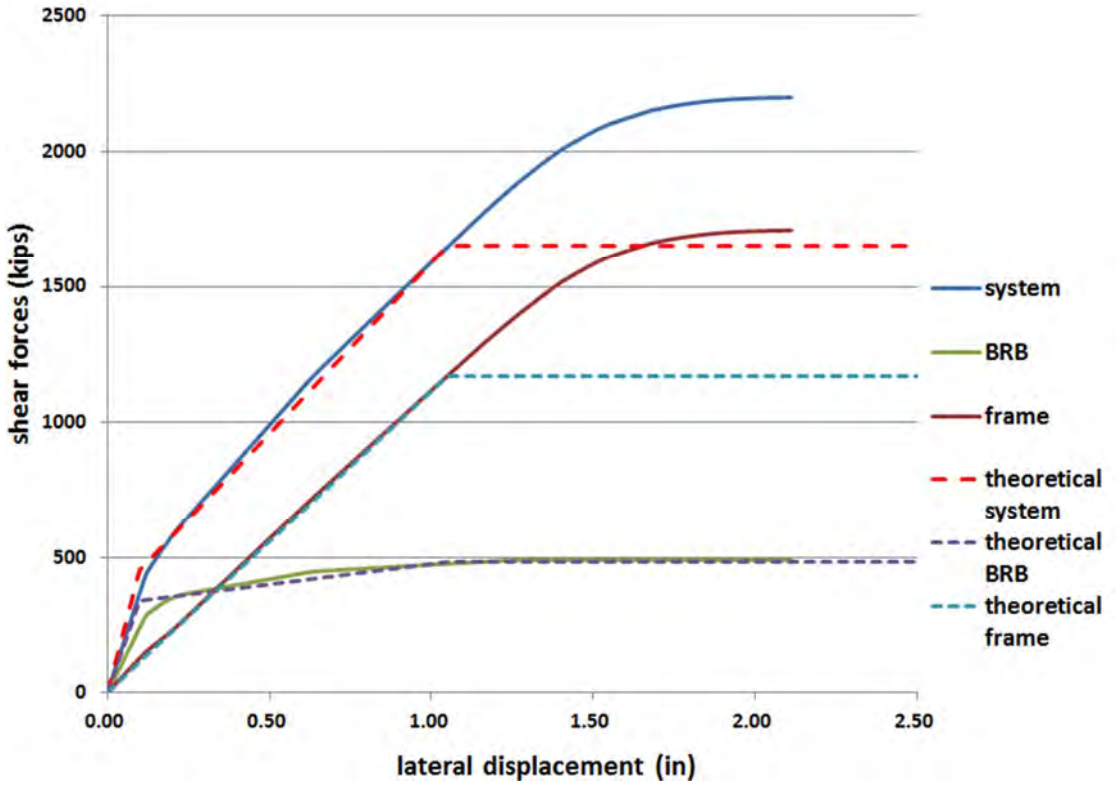


Figure 3-36 Comparison between the theoretical curve and the analytical curve in the transverse direction

In Figure 3-37, the target elastic displacement demand of 1.28" from response spectrum analysis is shown as the orange vertical line. The pushover analysis results in Figure 3-37 indicate that column yielding is first reached at bottom of the left column; the orange lower horizontal dotted line identifies the base shear resisted by the columns when that happens (which incidentally happens in a CFT column in tension). The upper blue dotted line is shown for the reaching shear resistance of the frame $V$ corresponding to the $2M_p/h_{column}$ calculated, where $M_p$ equals to 49687 kip-in obtained from SAP2000 Section Designer.

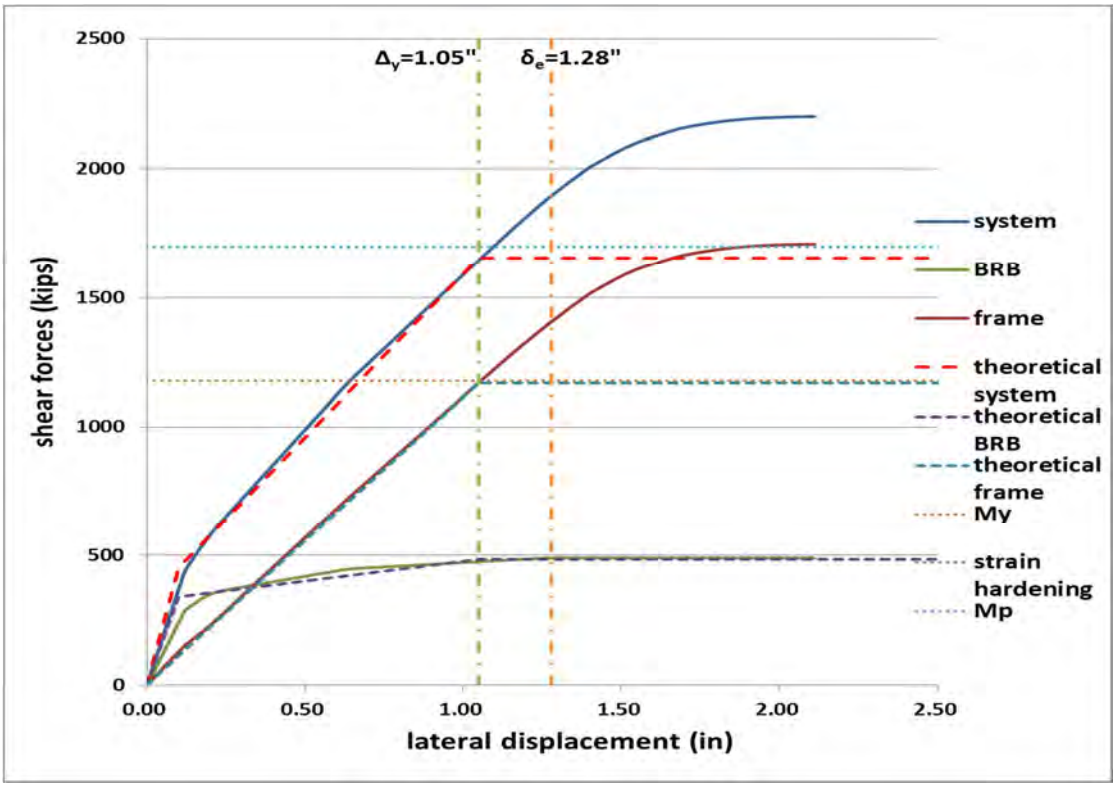


Figure 3-37 Pushover curve comparison between the analysis result and theoretical design value for the box-pier with BRBs in transverse direction

The sequence of yielding at top and bottom of the CFT columns (i.e. the point when the extreme fiber yields) is tabulated in Table 3-22. The column numbers are shown in Figure 3-26. As an example of the notation used in that table, "$187_b$" stands for bottom ("b") of the column ("187"). Note that the yielding in these columns is not happening at the same time, but they are doing so over small increases of frame drift. If anything, Figure 3-37 shows that limiting the column demands to $M_{y,}$ to prevent any column yielding, is conservative. The use of a more liberal design limit is arguably possible.

Table 3-23 Displacement and shear forces resisted by the frame when the yielding strength is reached

| Critical section | Yielding Displacement (in) | Yielding Force (kips) |
|---|---|---|
| $187_b$ | 1.06 | 1178 |
| $188_t$ | 1.07 | 1197 |
| $186_t$ | 1.11 | 1238 |
| $191_b$ | 1.15 | 1273 |
| $189_b$ | 1.18 | 1307 |
| $193_b$ | 1.20 | 1331 |
| $190_t$ | 1.22 | 1350 |
| $192_t$ | 1.27 | 1396 |

#### 3.4.1.4.2 Longitudinal bent (Layout A)

The overall comparison of the pushover curve between the analysis result and the theoretical ones is directly shown in Figure 3-38 (note that nearly identical results are obtained for Layout B, and are therefore not presented here).

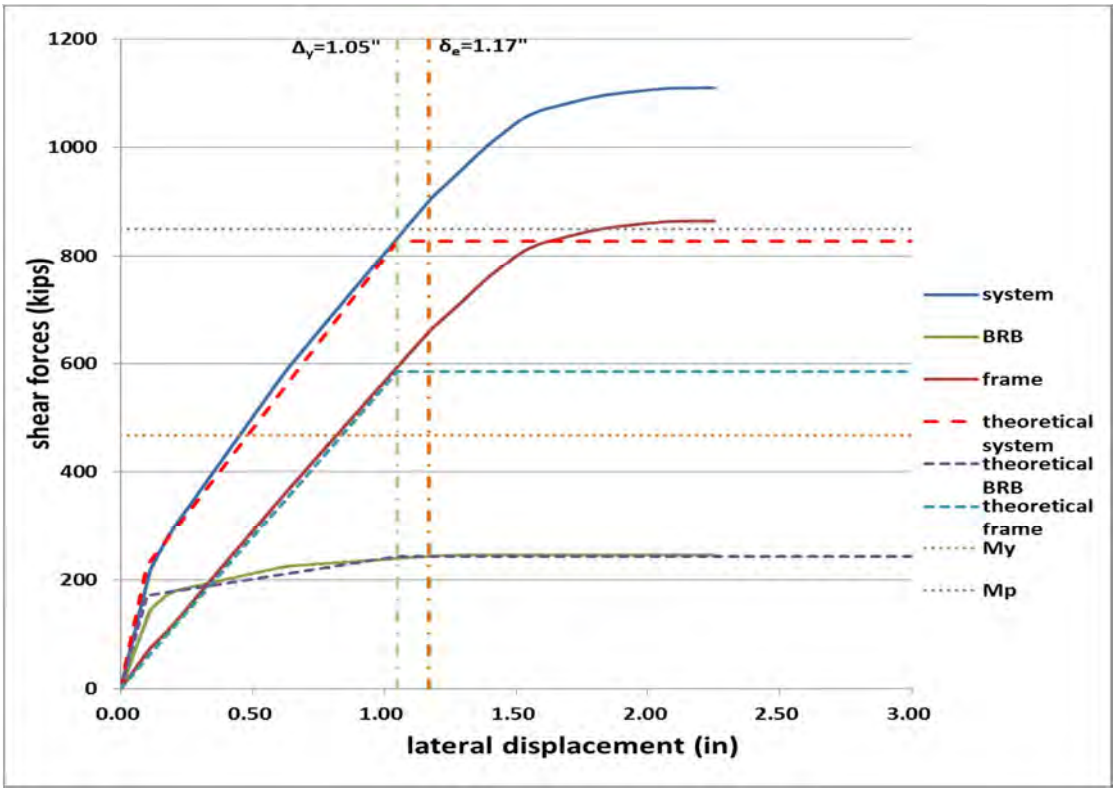


Figure 3-38 Pushover curve comparison between the analysis result and theoretical design value for the longitudinal bent layout A

The dashed purple line of the theoretical BRB shows the yielding of BRBs at the displacement of 0.101", and point where the maximum strain hardening considered is reached, at 1.05". The theoretical frame curve in navy blue dash lines shows that the frame yields at the displacement of 1.05". The two parts add up to the total theoretical curve for the combined system plotted in red dash lines. The pushover curves obtained from SAP2000 analysis overlay on top of the theoretical results as solid lines. The solid blue line shows the total base shear versus lateral displacement at top of the bent. By subtracting the lateral forces resisted by the BRBs (equals to the horizontal component of the forces in the BRBs), shown in solid green line, the solid brown line gives the portion of the base shear forces resisted by the frame. The target elastic displacement demand of 1.17" from response spectrum analysis is shown as the orange vertical line.

The pushover analysis results indicate that column yielding is first reached at the bottom of the left column where the tension and flexure interaction exists. The orange lower horizontal dotted line identifies the base shear resisted by the columns when that happens. The upper blue dotted line is shown for the reaching shear resistance of the frame $V$ corresponding to the $2M_p/h_{column}$ calculated, where $M_p$ equals to 49687 kip-in obtained from SAP2000 Section Designer.

The sequence of yielding at top and bottom of the CFT columns (i.e. the point when the extreme fiber yields) is tabulated in Table 3-24. As an example of the notation used in that table, "$L_b$" stands for bottom ("b") of the left ("L") column. Note that the yielding in these columns is not happening at the same time, but they are doing so over small increases of frame drift. If anything, Figure 3-38 shows that limiting the column demands to $M_{y,}$ to prevent any column yielding, is conservative. The use of a more liberal design limit is arguably possible.

Table 3-24 Displacement and shear forces resisted by the frame when the yielding strength is reached

| Critical section | Yielding Displacement (in) | Yielding Force (kips) |
|---|---|---|
| $L_b$ | 1.13 | 638 |
| $R_b$ | 1.18 | 664 |
| $L_t$ | 1.17 | 660 |
| $R_t$ | 1.10 | 619 |

### 3.4.1.5 BRB design details for box-pier bent with BRBs case

BRBs and the gusset plates used for the connections are usually designed by the BRB manufacturers. Using the same equation as shown in section 3.4.1.5, for BRB to develop the strain hardened loads of 332.50 kips, a pin of 2" would be necessary. A BRB supplier (StarSeismic) indicated that a 0.75" thick gusset plate can be used for

the BRB connection to resist the forces. Distance from the pin to the edge of the gusset would be 6".

#### 3.4.1.6 Pushover analysis summary

The CFT columns, designed in Appendix B, are found to have adequate strength to reach the force demands when the bridge bent reaches the target displacement (the elastic displacement demand from response spectrum analysis). Conservatively, the demand versus capacity check were performed considering the reaction forces and the moment demand on the column, as this would be the more critical case if there was an eccentricity between the point where the work-lines of the column and BRB intersected and the foundation. In absence of that eccentricity, smaller results would be obtained considering the axial and flexural forces acting on the columns. The box pier design was also shown to be satisfactorily for simultaneous earthquake demands from both the transverse and longitudinal directions.

### 3.4.2. Service Load Check for Box-pier Bent with BRBs

#### 3.4.2.1 Global bridge model

The global model developed in SAP2000 is used to determine the forces in the columns due to the dead load, live load and wind load. Note that since the design of the superstructure may need to be revised because of the locations of the new columns and the fact that they are CFTs (instead of RC columns), the permanent loads due to secondary prestress forces, creep, and shrinkage are not calculated here.

As mentioned above, the abutments allow longitudinal movement of the superstructure, limited only by the width of the gap between the superstructure and the abutment back wall (which is not considered to be a limiting factor here). The support provided by the abutment is assumed to be fixed against translation in the

vertical and transverse directions and fixed against rotation about the longitudinal axis. The bent resists all the seismic force in the longitudinal direction while in the transverse direction part of the lateral force is taken by the abutments. In the SAP2000, the bridge superstructure is modeled analyzed as a line element (i.e. spine) located at mid-width of the bridge deck.

The braces are assumed to not take the gravity load. For the live load analysis, the brace would affect the results since they links the two bridge bents together. So the bridge is modeled with the BRBs. Similar to the two-CFT-column bent with BRBs, the bridge deck is modeled with three lanes, each having 12 ft in width. Details for the dead loads, live loads, and wind loads considered in the "service" load analyses are provided in the following sections.

#### 3.4.2.2 Bridge loads

##### 3.4.2.2.1 Dead loads

Same as the two- CFT-column bent with BRBs case.

##### 3.4.2.2.2 Live loads

The vehicular loads are applied on the bridge lanes as shown in Figure 3-39 to illustrate the location of the live truck wheel load.

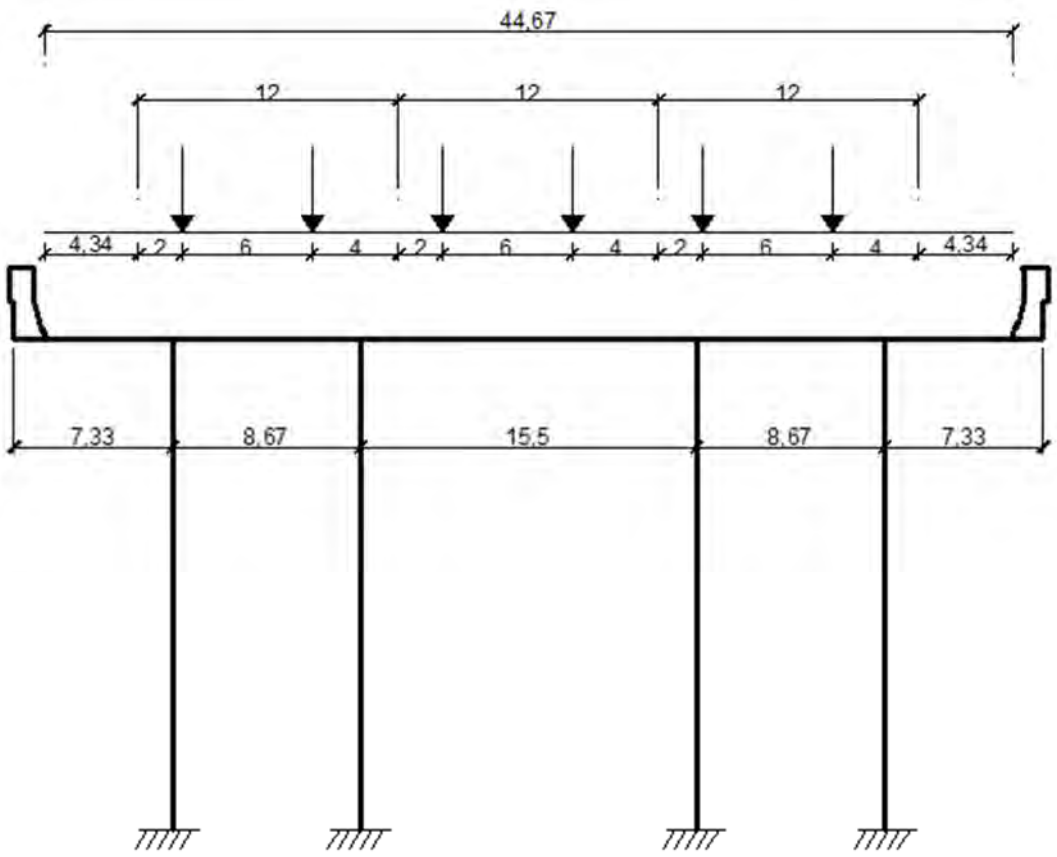


Figure 3-39 (1) Live load for three lanes

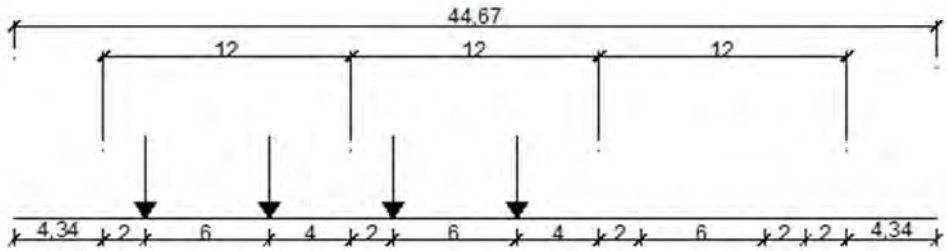


Figure 3-39 (2) Live load for lane 1 and 2

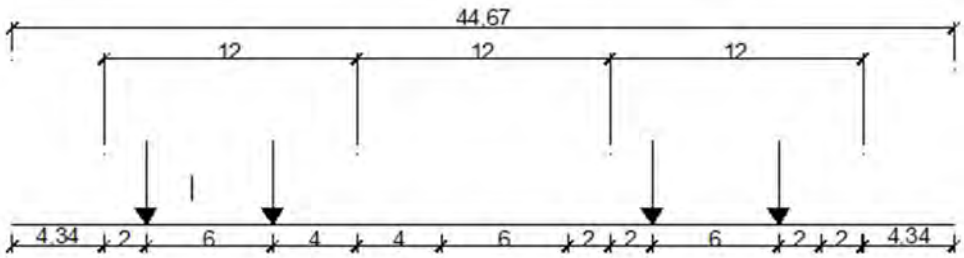


Figure 3-39 (3) Live load for lane 1 and 3

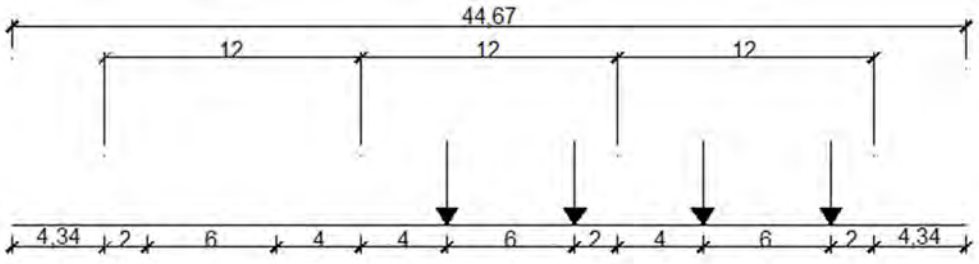


Figure 3-39 (4) Live load for lane 2 and 3

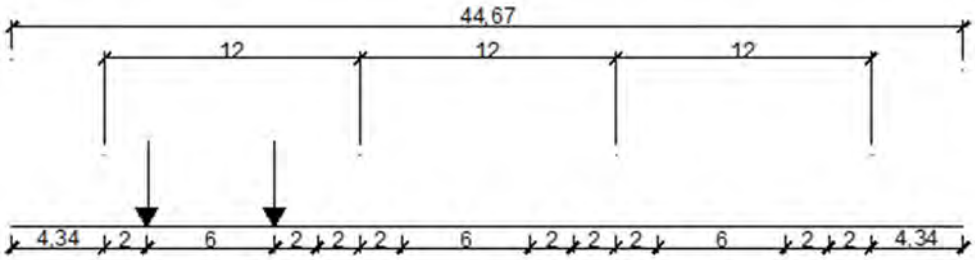


Figure 3-39 (5) Live load for lane 1

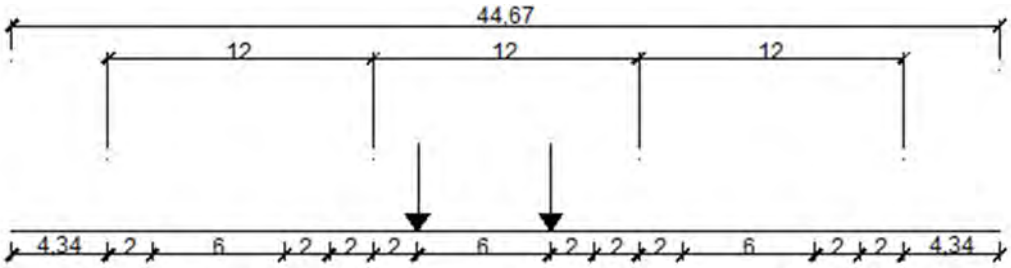


Figure 3-39 (6) Live load for one lane 2

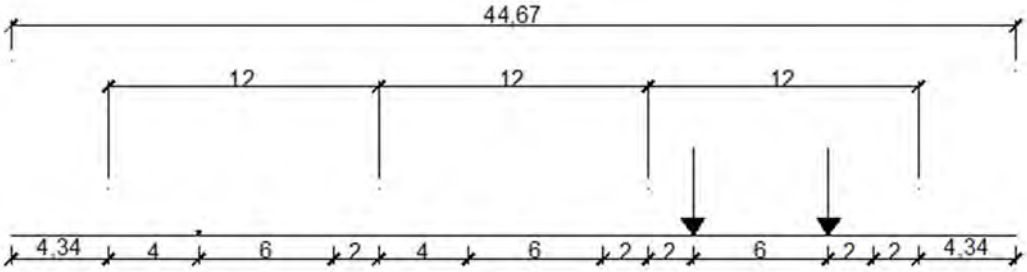


Figure 3-39 (7) Live load for one lane 3

Figure 3-39 Live load distribution for different lanes

### 3.4.2.2.3 Wind loads

Same as the two-CFT-column bent with BRBs case.

### 3.4.2.3 Service load analysis results

The critical forces in the columns are shown in Table 3-25 for the considered load cases. The numbering of the column element is shown in Figure 3-26, for the columns in the parallel bent frames. Only the columns with the possible largest axial force or moment are listed here.

Table 3-25 Analysis result of all the load cases for critical members

| Load cases | Element | P (kips) | V2 (kips) | V3 (kips) | M2 (kip-in) | M3 (kip-in) |
|---|---|---|---|---|---|---|
| DC | 186 | -424.3 | 143.4 | 6.4 | -56.4 | -3934.8 |
| | 187 | -414.3 | -15 | -2.0 | -122.4 | -518.4 |
| | 192 | -378.0 | -143.4 | 6.5 | -62.4 | 6736.8 |
| | 193 | -419.2 | 18.3 | -2.1 | -132 | 776.4 |
| | 195 | -424.3 | 143.4 | -6.4 | 56.4 | -3934.8 |
| | 196 | -414.3 | -15 | 2.0 | 122.4 | -518.4 |
| | 201 | -378.0 | -143.4 | -6.5 | 62.4 | 6736.8 |
| | 202 | -419.2 | 18.3 | 2.1 | 132 | 776.4 |
| DW | 186 | -64.3 | 24.5 | 1 | -8.4 | -674.4 |
| | 187 | -59.3 | -2.5 | -0.3 | -18 | -86.4 |
| | 192 | -56.4 | -24.5 | 1 | -9.6 | 1153.2 |
| | 193 | -60.1 | 2.8 | -0.3 | -19.2 | 120 |
| | 195 | -64.3 | 24.5 | -1 | 8.4 | -674.4 |
| | 196 | -59.3 | -2.5 | 0.3 | 18 | -86.4 |
| | 201 | -56.4 | -24.5 | -1 | 9.6 | 1153.2 |
| | 202 | -60.1 | 2.8 | 0.3 | 19.2 | 120 |
| Wind | 186 | -4.5 | 0.1 | -1.8 | -5.3 | 4.6 |
| | 187 | -20.3 | -0.1 | -2.7 | -326.9 | -4.5 |

| | | | | | | |
|---|---|---|---|---|---|---|
| | 192 | 4.5 | -0.1 | -12.8 | -5.3 | -4.6 |
| | 193 | -20.3 | 0.1 | -2.8 | -326.9 | 4.5 |
| | 195 | -4.7 | -0.1 | -1.8 | -5.3 | -5.8 |
| | 196 | 20.6 | 0.6 | -2.8 | -326.9 | 23.8 |
| | 201 | 4.7 | 0.1 | -1.8 | -5.3 | 5.8 |
| | 202 | 20.6 | -0.1 | -2.8 | -326.9 | -23.8 |
| Live maximum compression | 186 | -644.4 | -1.8 | -8.0 | -145.5 | -3845.5 |
| | 187 | -657.1 | -6.6 | -3.2 | -118.3 | -450.2 |
| | 192 | -644.4 | -1.8 | -11.8 | -97.3 | -3845.5 |
| | 193 | -657.1 | -6.6 | -2.2 | -176.4 | -450.2 |
| | 195 | -629.8 | -65.3 | -7.6 | -150.7 | -337.5 |
| | 196 | -658.3 | -0.1 | -3.4 | -121.9 | -1425.1 |
| | 201 | -629.8 | -65.3 | -11.5 | -99.6 | -337.5 |
| | 202 | -658.3 | -2.3 | -0.1 | -185.4 | -1425.1 |
| Live maximum tension | 186 | 435.1 | 29.1 | 2.4 | 176.3 | 1229.3 |
| | 187 | 437.4 | 0.2 | 2.2 | 176.3 | 1229.3 |
| | 192 | 435.1 | 29.1 | 1.6 | 118.3 | 1229.3 |
| | 193 | 437.4 | 0.2 | 3.2 | 118.3 | 1229.3 |
| | 195 | 435.1 | 6.8 | 2.6 | 185.4 | 808.0 |
| | 196 | 436.5 | 7.8 | 2.3 | 153.6 | 1101.9 |
| | 201 | 435.2 | 6.8 | 1.6 | 121.9 | 808.0 |
| | 202 | 436.8 | 6.8 | 3.4 | 121.9 | 808.0 |
| Live maximum moment | 186 | -644.4 | -1.8 | -8.0 | -145.5 | -3845.5 |
| | 187 | 437.4 | 0.2 | 2.2 | 176.3 | 1229.3 |
| | 192 | -644.4 | -1.8 | -11.8 | -97.3 | -3845.5 |
| | 193 | 437.4 | 0.2 | 3.2 | 118.3 | 1229.3 |
| | 195 | 414.8 | 0.4 | 11.5 | 99.6 | 4593.7 |

| | | | | | | |
|---|---|---|---|---|---|---|
| | 196 | -658.3 | -0.1 | -3.4 | -121.9 | -1425.1 |
| | 201 | 414.8 | 0.4 | 7.6 | 4593.7 | 150.7 |
| | 202 | -658.3 | -2.3 | -0.1 | -185.4 | -1425.1 |

The combination load cases that are considered for column design are: Strength I, III, V, listed in AASHTO bridge design specification (2010).

Strength I= 1.25 DC + 1.50 DW + 1.75LL

Strength III = 1.25 DC + 1.50 DW + 1.40 WS

Strength V= 1.25 DC + 1.50 DW + 1.35 LL + 0.4WS

The governing forces resulting from these load combinations, and used to verify the adequacy of the design of the column, are presented in Table 3-26.

Table 3-26 The controlling force to design the bridge columns

| Element | P (kips) | $V_2$ (kips) | $V_3$ (kips) | $M_2$ (kip-in) | $M_3$ (kip-in) |
|---|---|---|---|---|---|
| 186 | -1754.5 | -4.5 | 212.9 | -12659.7 | -337.7 |

The axial force and flexural moment interaction is checked for the columns strength in Table 3-27, where $P_u$ and $M_u$ are the force demand in the columns, $P_n$ and $M_n$ are the axial and flexural strength of the CFT column obtained from Section Designer respectively, without considering the resistance factors. The results from the interaction equation confirm that column capacity to resist all non-seismic load combinations considered is sufficient.

Table 3-27 Capacity check for the CFT column

| Axial load $P_u$ (kips) | Moment Demand $M_u$ (kip-in) | Flexural Strength $M_n$ (kip-in) | Axial strength $P_n$ (kips) | $P_u/P_n+$ $M_u/M_n$ |
|---|---|---|---|---|
| -1754.5 | -12659.7 | 49,687.0 | -6857.7 | 0.51 |

# Chapter 4 Nonlinear Time History Analysis

In order to validate the system responses previously obtained for the bridge bents using response spectrum and pushover analysis, nonlinear time history analysis of all the previously designed bridge bents with BRBs have been performed using SAP2000. Nonlinear dynamic time history analysis can account for the nonlinearities in different members of the bridge bent and ground motion characteristics. The nonlinear time history analysis results allow assessing the effectiveness of adding the structural fuse to limit displacements by comparing them with those for the bare bridge bents without BRBs.

## 4.1 Ground Motions and Analysis Setting

### 4.1.1. Ground Motion Selections

The Target Acceleration Spectra Compatible Time Histories (TARSCTHS) Program (Pagageorgiou et al, 2000) was used to generate spectra-compatible synthetic ground motions. That program is set up to match ground motions to the NEHRP 2003 design acceleration spectrum as a target. Therefore, the acceleration response spectrum provided by Caltrans in the drawing of the Ordinary Standard Bridge was replaced by an equivalent NEHRP 2003 spectrum shape, as shown in Figure 3-10. The black solid line and red dotted lines, respectively, correspond to the Caltrans design acceleration spectrum and the NEHRP 2003 target design acceleration spectrum with design spectral accelerations of $S_{Ds} = 2g$, $S_{D1} = 0.6g$.

Given that location of the Ordinary Standard Bridge is not provided, the distance to the earthquake epicenter and the possible earthquake moment magnitude are unknown. Both of these two parameters are required to obtain synthetic ground motions in the

program TARSCTHS. Therefore, a few combinations of earthquake epicentral distances and moment magnitudes were used in TARSCTHS to generate the synthetic ground motions. The resulting motions that yielded an acceleration response spectrum that best matched the target one were chosen.

The final set of nine spectral-compatible ground motions generated in TARSCTHS is shown in Figure 4-1. The lengths of the synthetic time histories are all 25 seconds. The numbers in the parenthesis above each ground motion correspond to earthquake moment magnitude, epicentral distance, and an identifier for each individual run of this combination. For example, (7 5-2) is the second ground motion generated for a site located 5km from a magnitude 7 earthquake.

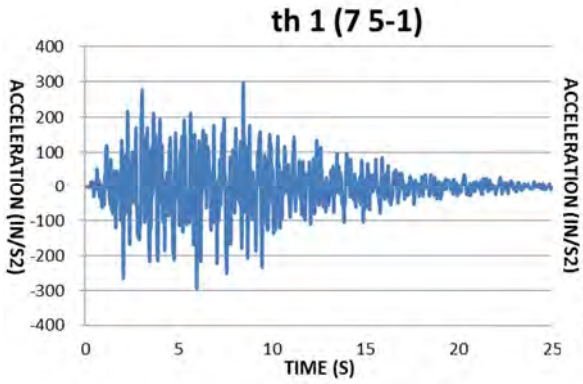


(1)

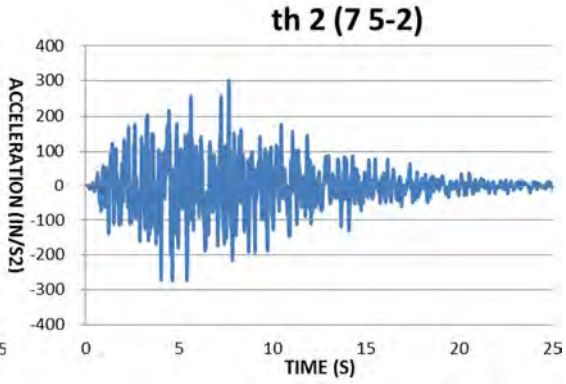


(2)

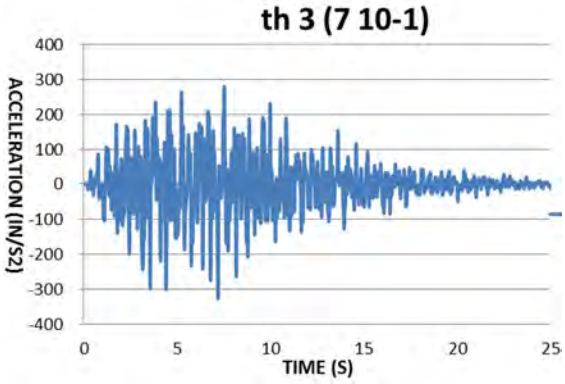


(3)

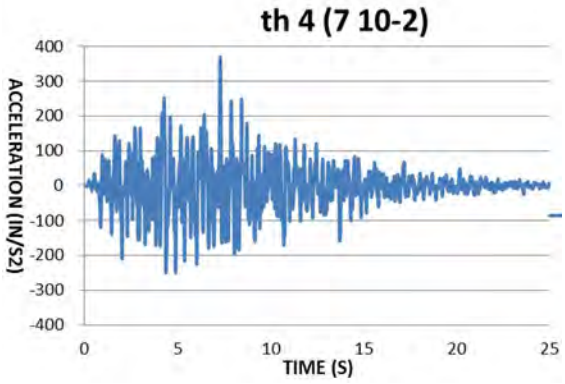


(4)

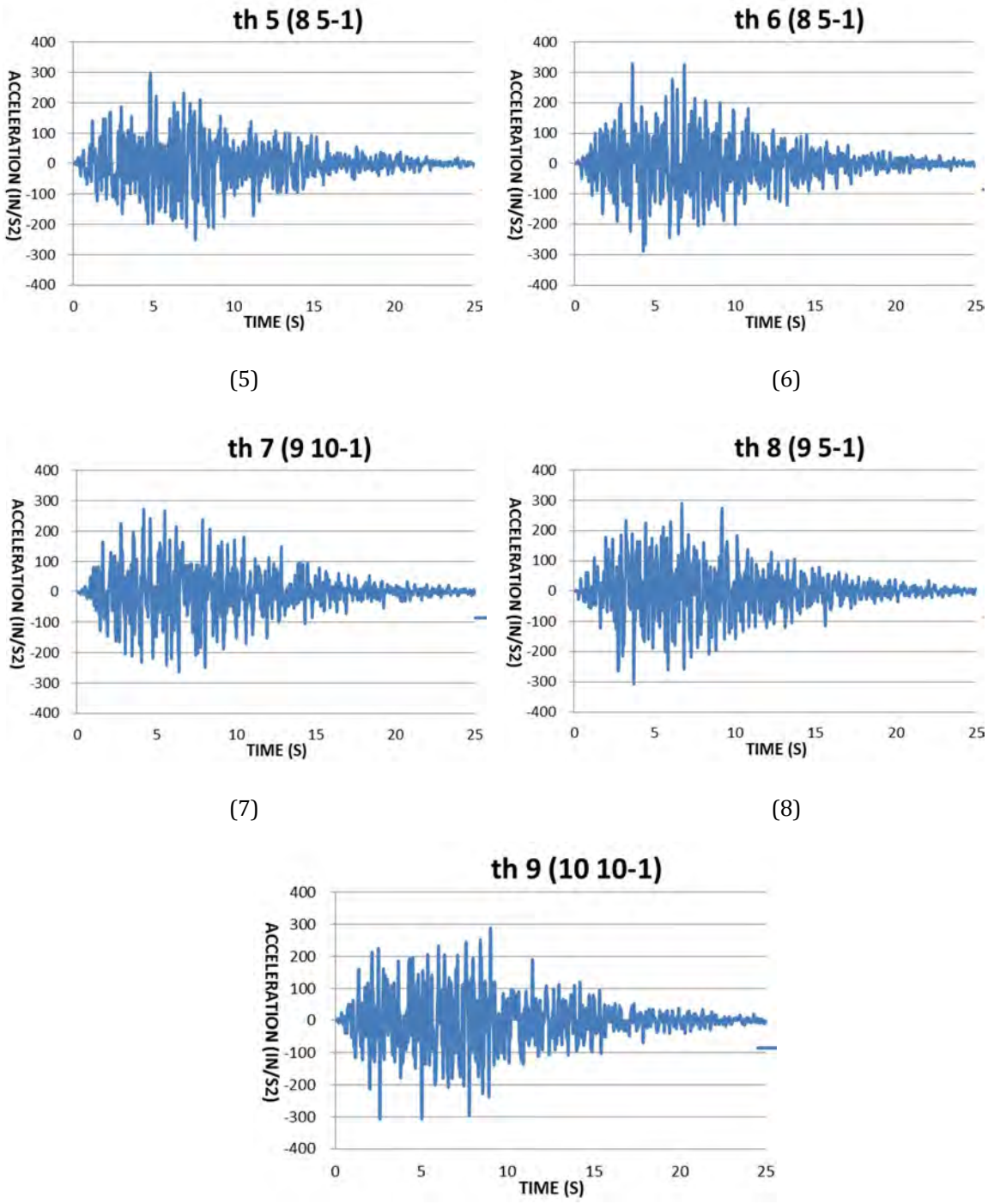


(5) (6)

(7) (8)

(9)

Figure 4-1 Nine ground motions used in the nonlinear time history analysis

Section 2.1.5 of Caltrans SDC (2010) requires that a 5% elastic response spectrum be used for determining seismic demand in Ordinary Standard Concrete Bridges. In Figure 4-2, the acceleration spectra of the nine ground motions are shown to match

with the target response spectrum with 5% damping.

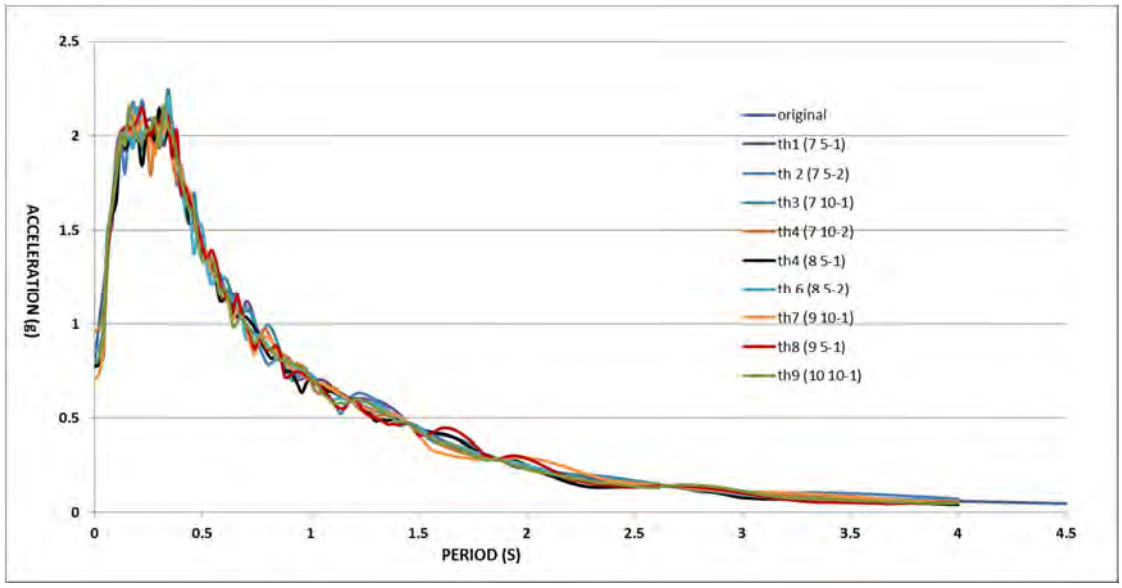


Figure 4-2 Acceleration response spectra of the nine synthetic ground motions (damping = 5%)

### 4.1.2. Nonlinear Time History Analysis Setting

The nonlinear time history analysis has been performed for the 2-D bridge bent instead of the 3-D entire bridge. The 2-D bent analysis makes it easier to compare with the pushover analysis results for the same bent. Out-of-plane displacements of the bent are restrained in this model. The mass of the bridge is assigned as a linearly distributed mass on the cap beam. The self-weight of the assigned mass is not accounted into the dead load since the mass is only used to apply the lateral seismic load to the bridge bent. The dead load is applied directly to the column before nonlinear time history analysis is conducted. Hinge properties and assignments are defined the same way as done for the pushover analysis (see Section 3.4 and 3.5).

In the nonlinear time history analysis, direct integration was used to solve the dynamic equilibrium equations for the bridge bent at discrete time steps. The selection of the integration method was based on the desire for stability and accuracy of the results. Direct implicit integration was chosen. It is computational

demanding, since it requires iteration at each time step to achieve equilibrium, but it allows consideration of any type of damping and nonlinearity. Certain parameters, if chosen well, can make the direct implicit integration tolerate larger time step due to unconditional stability. Among all implicit integration methods, the Hilbert-Hughes-Taylor (HHT) method was used for this direct integration time history analysis (SAP2000 reference manual, 2010). In these analyses, ground acceleration was applied in the bridge's transverse direction, which corresponds to excitations applied in the plane of the 2-D bridge bent model. The output time step is 0.002 second. P-delta or second order effect is not considered in the analysis. From the modal analysis, the mass participating ratio is more than 90% for the first two modes. Rayleigh damping was used, with coefficients corresponding to 5% damping for the first and second modal periods here.

## 4.2 Analysis Results

### 4.2.1. Two-CFT-Column Bent

The two-CFT-column bridge bent with BRBs have two configurations: single inclined BRB and inverted-V chevron BRBs. Referring to Appendix B, the theoretical fundamental period of the two-CFT-column bent designed with BRBs is 0.19 s. The bare bridge bent without BRBs is also analyzed to compare with the two designed bridge bents with BRBs. The first two periods of the three bridge bent are presented in the Table 4-1 (these were the periods used to setting the Rayleigh damping coefficients). The modal shapes of the bridge bents are shown in Figure 4-3. The first modal periods of the two designed bridge bents with BRBs are close to the theoretical period of 0.19 s, and substantially smaller than the bare bent without BRBs. The first modal shape of all the bridge bents considered corresponds to a sway mode of vibration (i.e. bents moving laterally). The second modal shape of the bridge bents with BRBs have the columns elongating on one side and compressing on the

other, while the bare bridge bent without BRBs have both columns elongating and compressing at the same time.

Table 4-1 First and second modal periods of the two-CFT-column bent

| Period (s) | Single inclined BRB | Inverted-V BRBs | No BRB |
|---|---|---|---|
| First mode | 0.225 | 0.202 | 0.406 |
| Second mode | 0.089 | 0.097 | 0.080 |

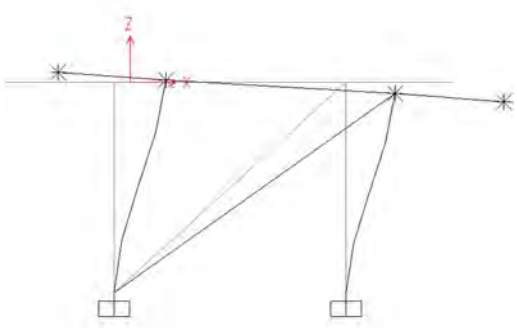

(1) Single inclined BRB first mode

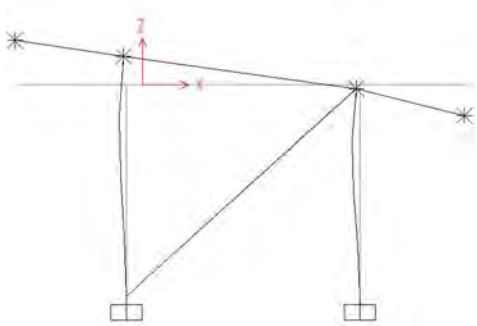

(2) Single inclined BRB second mode

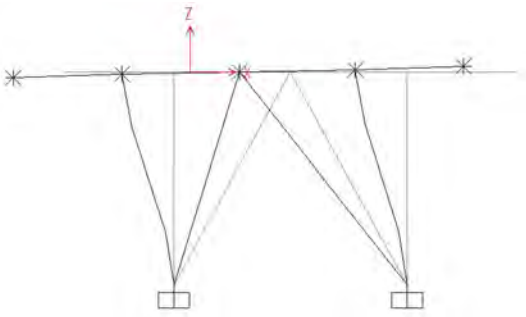

(3) Inverted –V chevron BRBs first mode

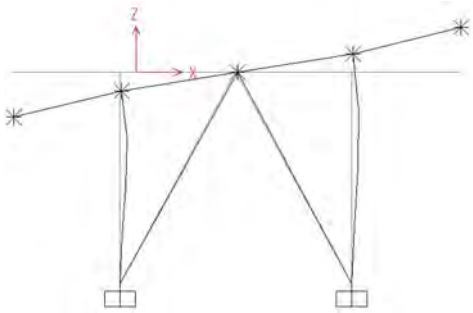

(4) Inverted –V chevron BRBs second mode

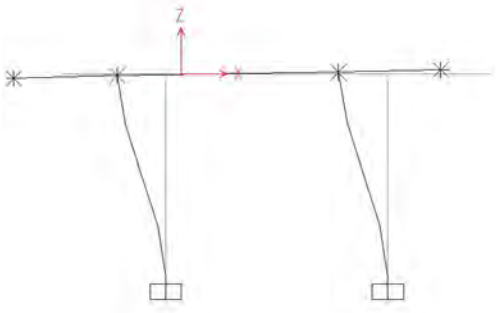

(5) No BRB first mode

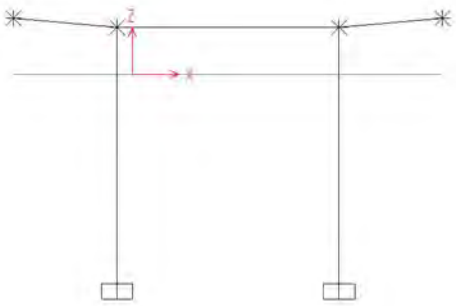

(6) No BRB second mode

Figure 4-3 The mode shapes of the two-CFT-column bent with and without BRBs

The maximum displacements in positive and negative in-plane transverse directions

(X directions) of all the two-CFT-column bents resulting from the nine ground motions are presented in Table 4-2. The averages of the maximum displacements are in bold.

Table 4-2 Displacement demands at top of the two-CFT-column bents

| | | th1 | th2 | th3 | th4 | th5 | th6 | th7 | th8 | th9 | **Ave.** |
|---|---|---|---|---|---|---|---|---|---|---|---|
| Single inclined BRB (in) | max | 1.012 | 1.123 | 1.122 | 1.117 | 0.851 | 0.991 | 1.047 | 1.160 | 1.000 | **1.130** |
| | min | -1.117 | -1.075 | -1.116 | -0.992 | -1.138 | -1.208 | -0.977 | -1.297 | -0.829 | |
| Inverted-V chevron BRBs (in) | max | 0.999 | 1.076 | 1.051 | 1.064 | 0.808 | 0.933 | 0.982 | 1.085 | 0.944 | **1.095** |
| | min | -1.085 | -1.017 | -1.092 | -0.965 | -1.124 | -1.229 | -0.919 | -1.262 | -0.815 | |
| Bare bent with no BRB (in) | max | 3.175 | 1.880 | 1.766 | 1.584 | 1.957 | 1.315 | 1.101 | 1.759 | 1.941 | **2.139** |
| | min | -1.495 | -1.757 | -1.716 | -1.744 | -2.099 | -2.399 | -2.218 | -2.027 | -1.385 | |

The average maximum absolute lateral displacement of the two-CFT-column bent with no BRB is 2.139 in. The bridge bent with single inclined BRB has an average maximum displacement of 1.13 in, which corresponds to 52.8% of the bare bridge bent value. The bridge bent with inverted-V chevron BRBs case has an average maximum displacement of 1.095 in, equal to 51.2% of the bare bridge bent value.

The base shear forces for the three bridge bents are compared in Table 4-3. The average maximum absolute base shear forces of the bridge bents with single inclined BRB and the inverted-V chevron BRBs case are 3916.5 kips and 3904.7 kips, respectively, which are 20.7% and 20.3% higher than the no BRB case of 3245.8 kips. Note that this 20% increase in base shear strength produced a reduction of approximately 50% of the lateral displacement for the designed two-CFT-column bents with structural fuses, which is a significant gain in drift reduction for a relatively modest increase in base shear demands.

Table 4-3 Base shear demands of the two-CFT-column bents

| | | th1 | th2 | th3 | th4 | th5 | th6 | th7 | th8 | th9 | Ave. |
|---|---|---|---|---|---|---|---|---|---|---|---|
| Single inclined BRB (kips) | max | 3917.1 | 3827.7 | 3936.6 | 3689.0 | 3969.4 | 4035.1 | 3628.9 | 4139.4 | 3234.0 | **3916.5** |
| | min | -3763.3 | -3880.9 | -3911.7 | -3918.5 | -3378.8 | -3725.8 | -3787.9 | -3964.9 | -3663.4 | |
| Inverted-V chevron BRBs (kips) | max | 3902.0 | 3750.6 | 3912.8 | 3656.5 | 3973.9 | 4106.5 | 3628.9 | 4135.1 | 3251.9 | **3904.7** |
| | min | -3732.8 | -3866.8 | -3846.8 | -3869.3 | -3326.5 | -3681.2 | -3787.9 | -3916.7 | -3588.1 | |
| Bare bent with no BRB (kips) | max | 3160.1 | 3164.2 | 3242.5 | 3219.7 | 3249.8 | 3258.7 | 3237.4 | 3264.7 | 3039.5 | **3245.8** |
| | min | -3290.2 | -3209.5 | -3143.4 | -3207.3 | -3195.0 | -3149.3 | -2947.5 | -3260.4 | -3240.1 | |

The nonlinear response of the two bridge bents under ground motion TH5 (Figure 4-1) are shown below as examples. Displacement time histories at top of the cap beam are plotted in Figure 4-4 for the two-CFT-column bent with (1) no BRB, (2) single inclined BRB, and (3) inverted-V chevron BRBs. The yield displacement of the CFT column is 0.71 in, marked by the horizontal red lines. The elastic yielding demand is not marked for each case here. Note that all three bridge bents reach a maximum displacement larger than yield displacement of the columns, meaning that columns undergo inelastic deformations. As shown in Table 4-2, for that particular ground motion, the two-CFT-column bent with a single inclined BRB has a maximum displacement of 1.14 in, which is equal to 54.3% of the corresponding value for the two-CFT-column bent with no BRB case. For the inverted-V chevron BRBs case, the displacement demand is 1.12", i.e., 53.3% of that for the two-CFT- column bent with no BRB case.

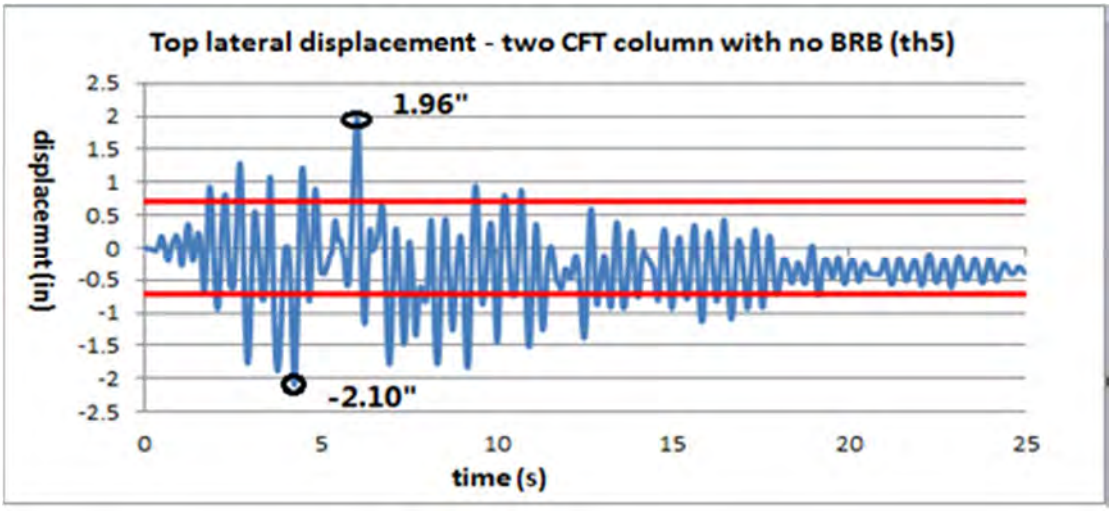


(1)

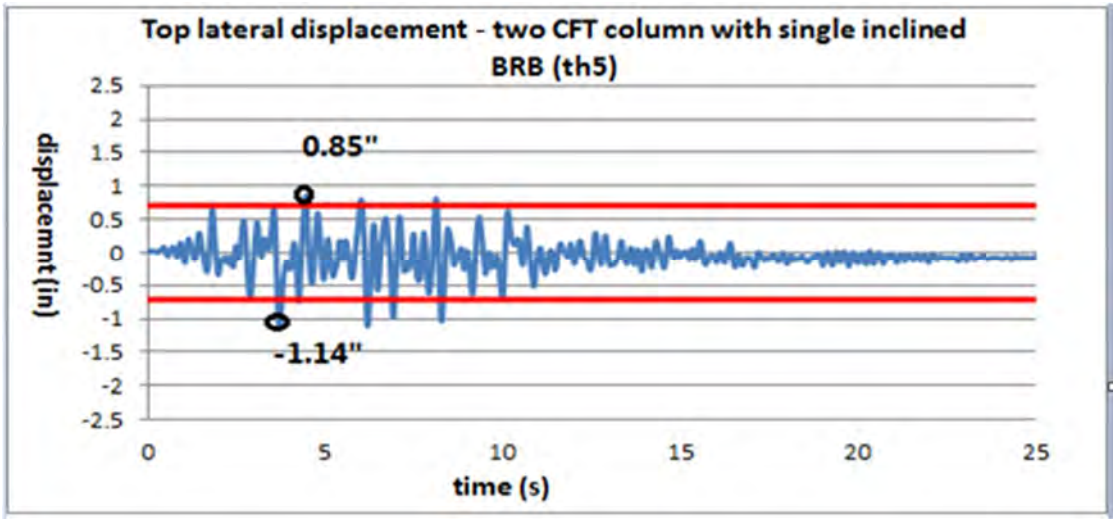


(2)

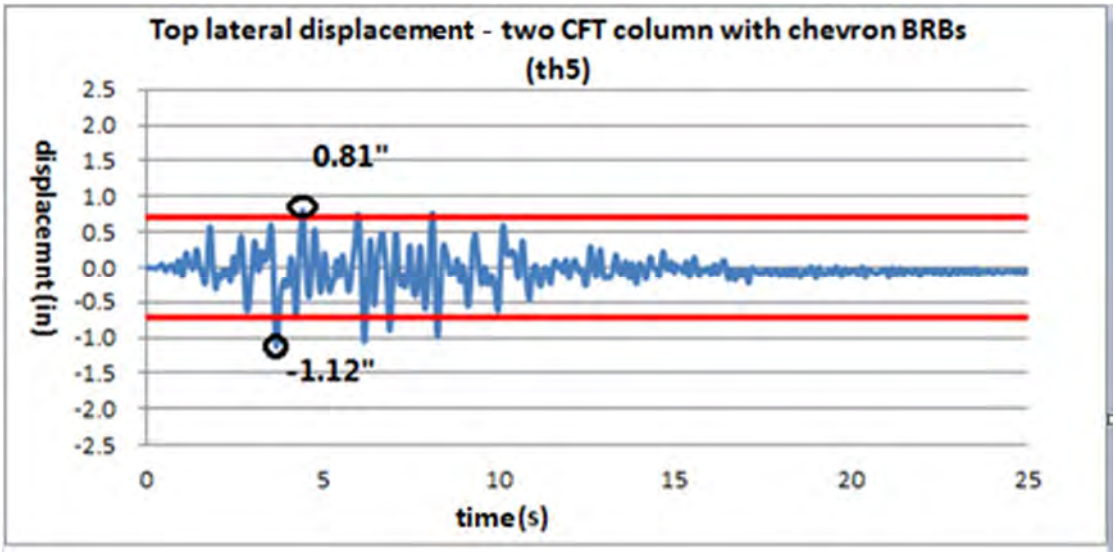


(3)

Figure 4-4 Displacement demands of the two column bridge bents under ground motion TH5

The base shear force time histories resisted by the three bents are plotted in Figure 4-5. Note that, the maximum base shear forces are 21.1% and 22.3% larger, respectively, for the single inclined BRB and the inverted-V chevron BRBs case, compared to the no BRB case.

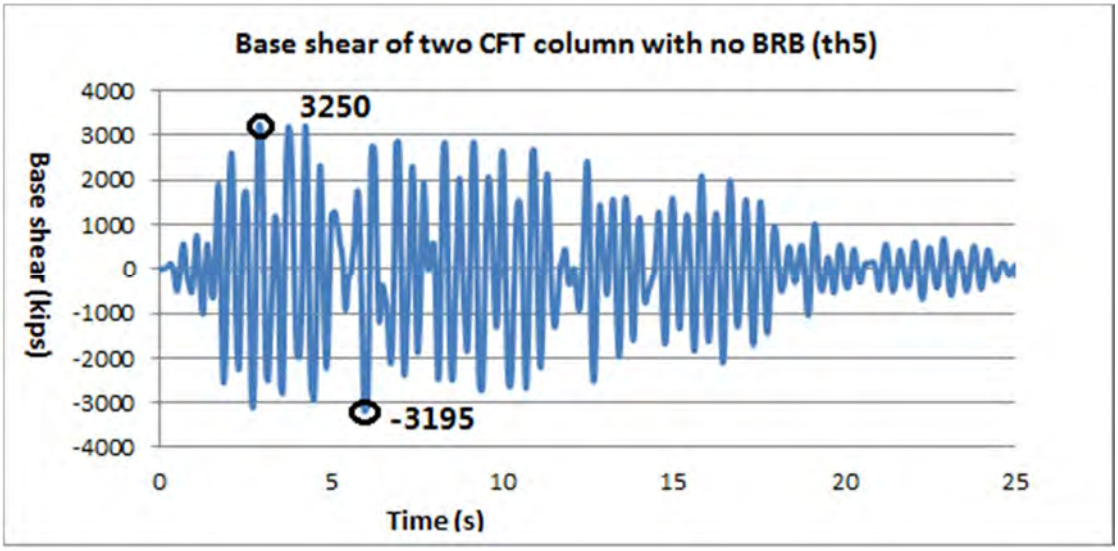


(1)

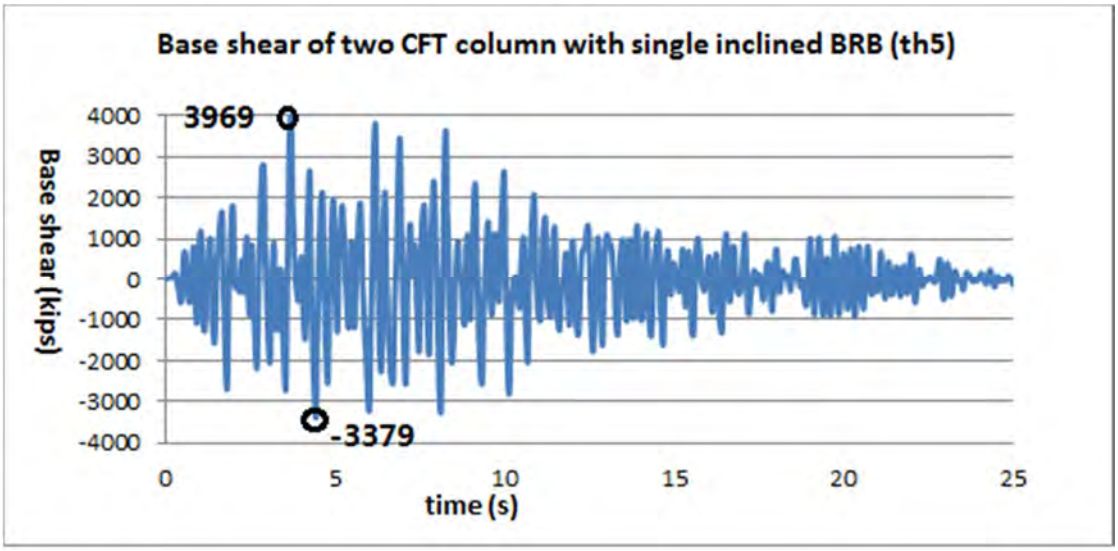


(2)

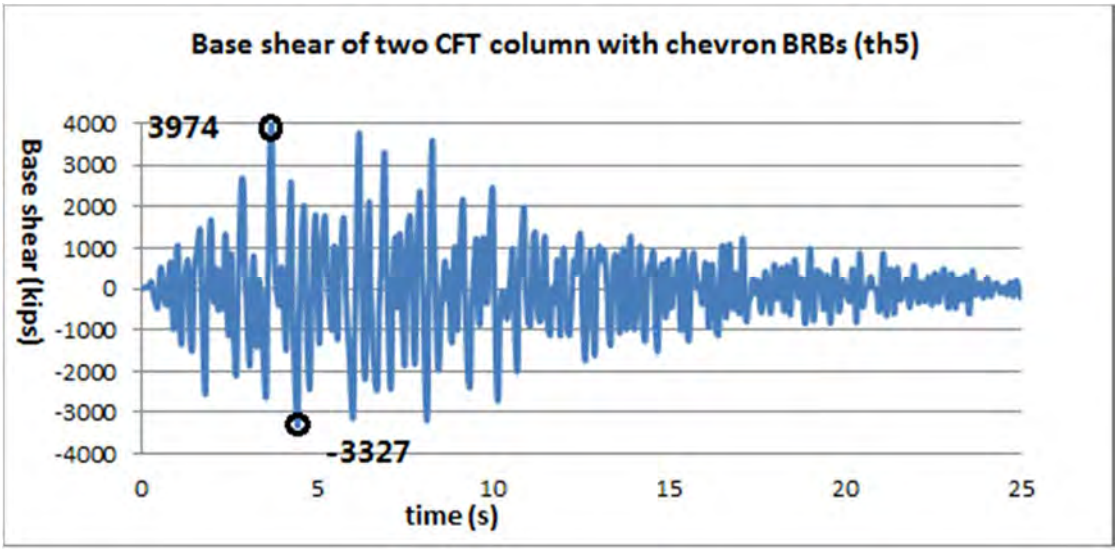


(3)

Figure 4-5 Base shear demands of the two column bridge bents under ground motion TH5

In all cases considered, P-$M_2$-$M_3$ fiber hinges (as defined in Section 3.3.1.1.3) were located at top and bottom of the CFT columns. Moment rotation history for the hinge at bottom of the right column, found to develop the maximum rotation, is shown in Figure 4-6. The maximum rotation for the single BRB case and the inverted-V chevron BRBs case is 0.0013 rad and 0.00092 rad, respectively, which is only about 20% of the corresponding value for the no BRB case which has a 0.005 rad maximum rotation. Note that, from Figure 4-6, the yield rotation for the column (under its specific axial loads) is graphically estimated to be approximately 0.0005 rad. The yielding in the column is deemed acceptable.

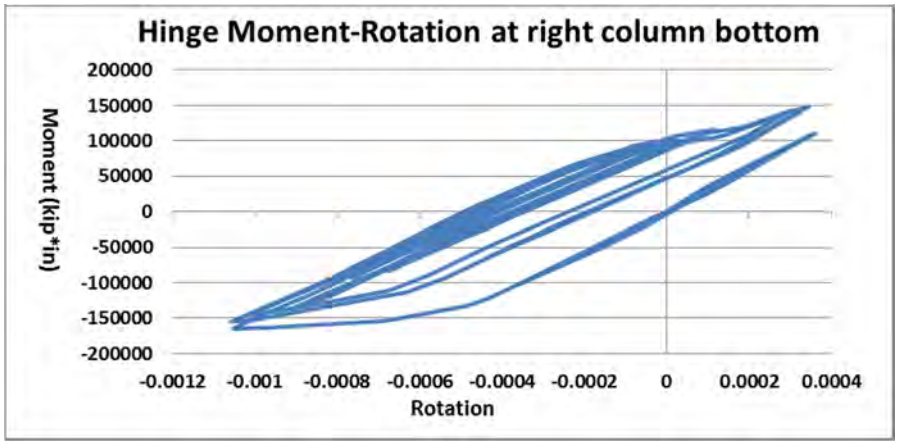


(1)

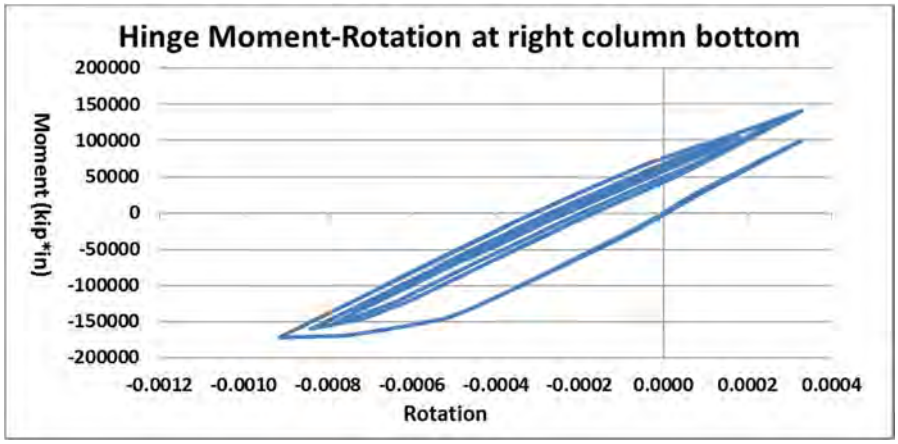


(2)

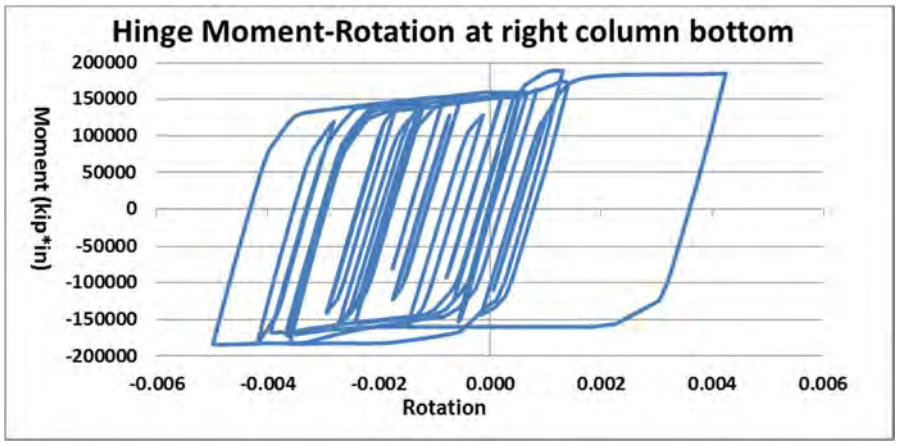


(3)

Figure 4-6 Moment-rotation plot of the $PM_2M_3$ hinge at bottom of the right column for : (1) single inclined BRB case (2) inverted-V chevron BRBs case, and (3) no BRB case

In Figure 4-7, the BRBs in the (1) single inclined BRB case have reached a compressive strength of 1411 kips and tensile strength of 1270 kips (after strain hardening). Also, BRBs in the (2) inverted-V chevron BRBs case have reached a compressive strength of 1082 kips and tensile strength of 973 kips (after strain hardening). This corresponds to maximum ductility of 10 and 15.2, respectively, for the single inclined BRB case and inverted-V chevron BRBs case.

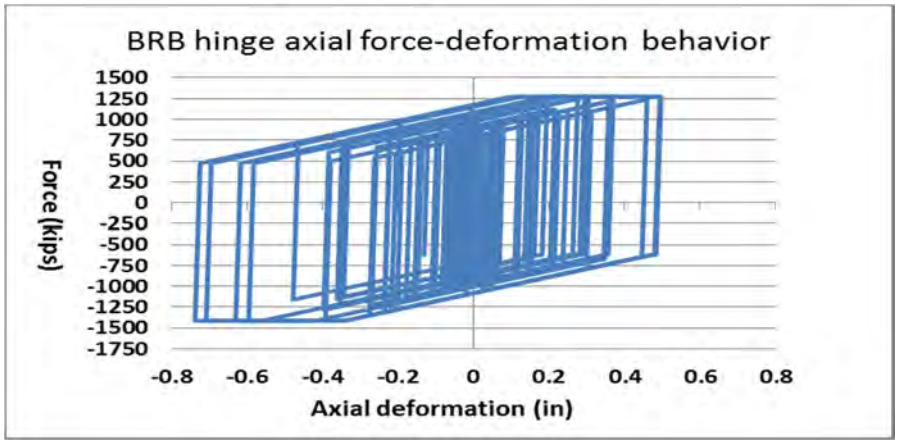


(1)

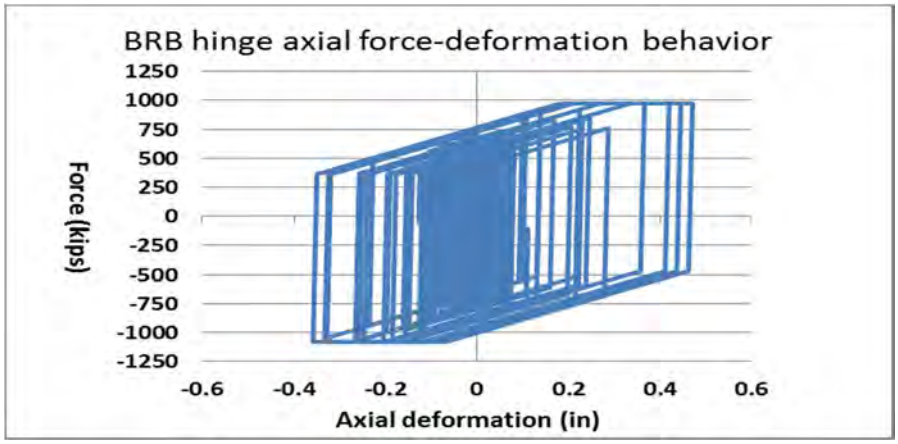


(2)

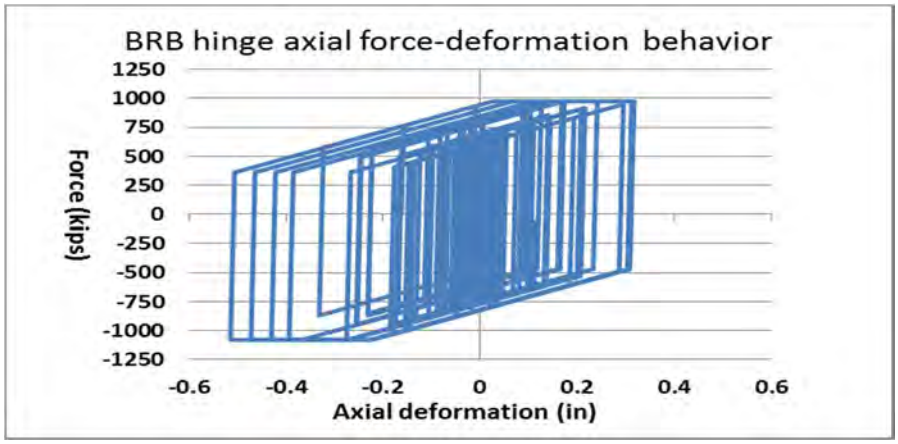


(3)

Figure 4-7 BRB hinge axial force-deformation plot for the bridge bents: (1) single inclined BRB case (2) left BRB in the inverted-V chevron BRBs, and (3) right BRB in the inverted-V chevron BRBs

### 4.2.2. Box-Pier Bent

The box-pier bridge bent was analyzed separately in the transverse and longitudinal direction. Referring to Appendix B, the theoretical fundamental period of the bridge

bent with BRBs in both the transverse and longitudinal direction is 0.23 s. The bare bridge bent was also analyzed to compare with box-pier bent with BRBs in both directions. To note, the bare bent for the box-pier configuration is purely academic because the box-pier system would never be used without BRBs. The first two periods of the box-pier bents with and without BRBs are presented in the Table 4-4 (these are the periods used in setting the Rayleigh damping coefficients). The modal shapes of the bridge bents are shown in Figure 4-8. The first modal periods of the box-pier bridge bents with BRBs are close to the theoretical period of 0.23 s, i.e., smaller than the period of the bare bent without BRBs. The first modal shape of all the bridge bents considered corresponds to a sway mode of vibration. The second modal period of the box-pier bent with BRBs does not differ much from the no-BRB case in each direction. The second modal shape of the bridge bents in the transverse direction have one side compressed and the other elongated; the same behavior is observed in the longitudinal direction.

Table 4-4 First and second modal periods of the box-pier bents

| Period (s) | Transverse with BRBs | Transverse no BRBs | Longitudinal with BRBs | Longitudinal no BRBs |
|---|---|---|---|---|
| First mode | 0.256 | 0.455 | 0.244 | 0.444 |
| Second mode | 0.062 | 0.063 | 0.059 | 0.059 |

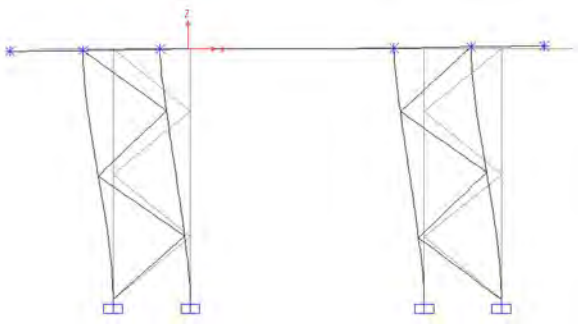

(1) Transverse with BRBs first mode

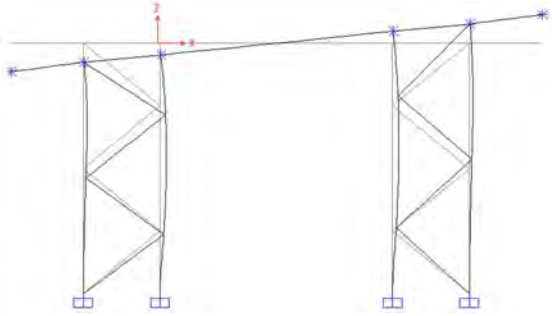

(2) Transverse with BRBs second mode

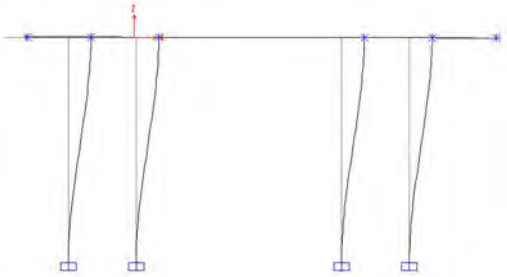

(3) Transverse no BRBs first mode

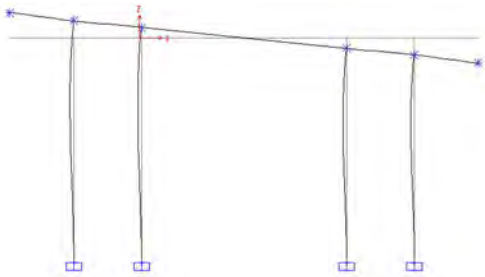

(4) Transverse no BRBs second mode

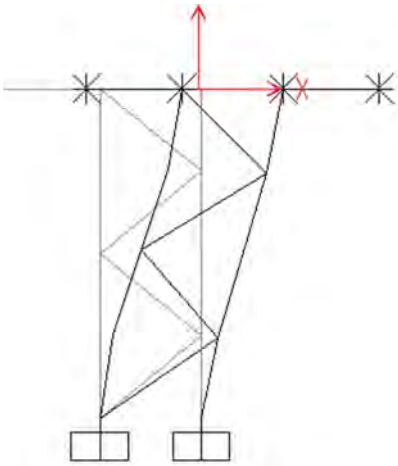


(5) Longitudinal with BRBs first mode

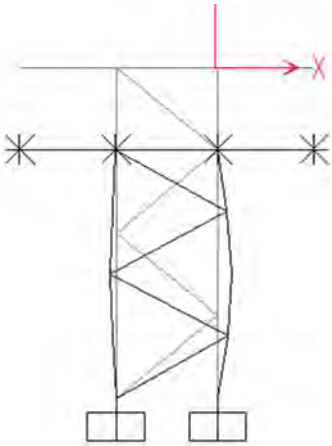


(6) Longitudinal with BRBs second mode

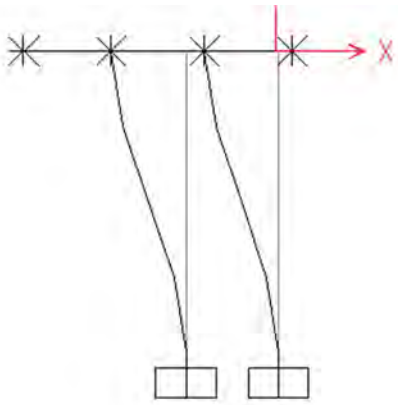


(7) Longitudinal no BRBs first mode

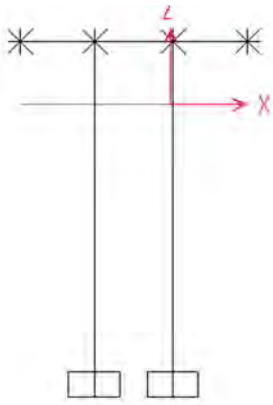


(8) Longitudinal no BRBs second mode

Figure 4-8 The mode shapes of three two-CFT-column bents

The maximum displacements in positive and negative in-plane transverse directions (X directions) of the box-pier bents with and without BRBs are presented in Table 4-5. The averages of the maximum displacements are in bold.

Table 4-5 Displacement demands at top of the box-pier bents

| | | th1 | th2 | th3 | th4 | th5 | th6 | th7 | th8 | th9 | **Ave** |
|---|---|---|---|---|---|---|---|---|---|---|---|
| Transverse with BRBs (in) | max | 1.256 | 1.340 | 1.397 | 1.301 | 1.084 | 1.184 | 1.241 | 1.234 | 1.052 | **1.317** |
| | min | -1.314 | -1.369 | -1.247 | -1.212 | -1.270 | -1.308 | -1.181 | -1.601 | -1.049 | |
| Transverse no BRBs (in) | max | 2.789 | 2.893 | 1.558 | 2.116 | 2.758 | 1.421 | 1.298 | 1.756 | 1.943 | **2.617** |
| | min | -2.109 | -1.892 | -2.800 | -1.556 | -1.897 | -3.110 | -2.724 | -2.417 | -1.688 | |
| Longitudinal with BRBs (in) | max | 1.154 | 1.302 | 1.323 | 1.255 | 1.157 | 1.022 | 1.149 | 1.194 | 1.024 | **1.259** |
| | min | -1.250 | -1.260 | -1.220 | -1.157 | -1.277 | -1.227 | -1.095 | -1.520 | -0.969 | |
| Longitudinal no BRBs (in) | max | 2.747 | 2.738 | 1.610 | 2.149 | 1.365 | 2.549 | 1.396 | 1.890 | 2.049 | **2.505** |
| | min | -2.020 | -1.874 | -2.710 | -1.467 | -2.666 | -1.953 | -2.572 | -2.364 | -1.554 | |

The average maximum absolute lateral displacement of the box-pier bent with no BRB in the transverse direction is 2.617 in. The average maximum displacement of the box-pier bent with BRBs in the transverse direction is 1.317 in, which corresponds to 50.3% of the bare bridge bent value. The box-pier bent with no BRB in the longitudinal direction has an average maximum displacement of 2.505 in. The average maximum displacement of the box-pier bent with BRBs in the longitudinal direction is 1.259 in, equal to 50.3% of the bare bridge bent value.

The base shear forces for the four bridge bents are compared in Table 4-6. The average maximum absolute base shear forces of the box-pier bent are 1930.2 kips and 950.6 kips in the transverse and longitudinal direction, which are 10.2% and 7.8% higher than the no-BRB case in both directions. Note that this 10% increase in base shear strength produced a reduction of approximately 50% of the lateral displacement for the designed box-pier bents with BRBs. Similar to the two column bridge bents with BRBs, a significant gain is also observed in drift reduction for a relatively modest increase in base shear demands.

Table 4-6 Base shear forces of the box-pier bents

| | | th1 | th2 | th3 | th4 | th5 | th6 | th7 | th8 | th9 | **Ave.** |
|---|---|---|---|---|---|---|---|---|---|---|---|
| Transverse with BRBs (kips) | max | 1946.1 | 1970.0 | 1885.1 | 1842.9 | 1896.5 | 1933.6 | 1804.5 | 2135.7 | 1644.5 | **1930.2** |
| | min | -1900.9 | -1958.3 | -2015.2 | -1929.4 | -1698.5 | -1821.7 | -1879.1 | -1862.4 | -1666.1 | |
| Transverse no BRBs (kips) | max | 1750.1 | 1600.7 | 1738.5 | 1613.7 | 1716.0 | 1785.0 | 1771.5 | 1758.1 | 1674.1 | **1750.9** |
| | min | -1749.1 | -1747.0 | -1605.0 | -1737.5 | -1762.6 | -1556.0 | -1486.3 | -1710.8 | -1708.2 | |
| Longitudinal with BRBs (kips) | max | 954.7 | 951.7 | 941.2 | 906.5 | 961.5 | 940.5 | 868.1 | 1063.2 | 789.5 | **950.6** |
| | min | -912.3 | -969.1 | -988.1 | -953.2 | -905.0 | -824.0 | -902.7 | -923.5 | -822.8 | |
| Longitudinal no BRBs (kips) | max | 875.2 | 821.5 | 876.7 | 811.1 | 891.6 | 867.7 | 887.4 | 884.7 | 817.8 | **882.0** |
| | min | -893.8 | -878.5 | -835.7 | -875.2 | -760.0 | -884.1 | -763.5 | -867.3 | -865.6 | |

The nonlinear response of the box-pier bridge bents under ground motion TH5 (Figure 4-1) are shown below as an example. Displacement time histories at top of the cap beam are plotted in Figure 4-9 for the box-pier bent cases (1) transverse with BRBs, (2) transverse no BRBs, (3) longitudinal with BRBs, and (4) longitudinal no BRBs. The yield displacement of the frame is 1.05 in, marked by the horizontal red lines. The elastic yielding demand is not marked for each case here. Note that the CFT columns of all four bridge bents undergo inelastic deformations since the largest lateral deformations are all larger than 1.05". As shown in Table 4-5, for that particular ground motion, the box-pier bent with BRBs in the transverse direction has a maximum displacement of 1.27 in, which is reduced to 46% from the box-pier bent with no BRB case of 2.76 in. For the longitudinal direction, the displacement demand is 1.28", i.e., 48% of that for the box-pier bent with no-BRB case of 2.67 in.

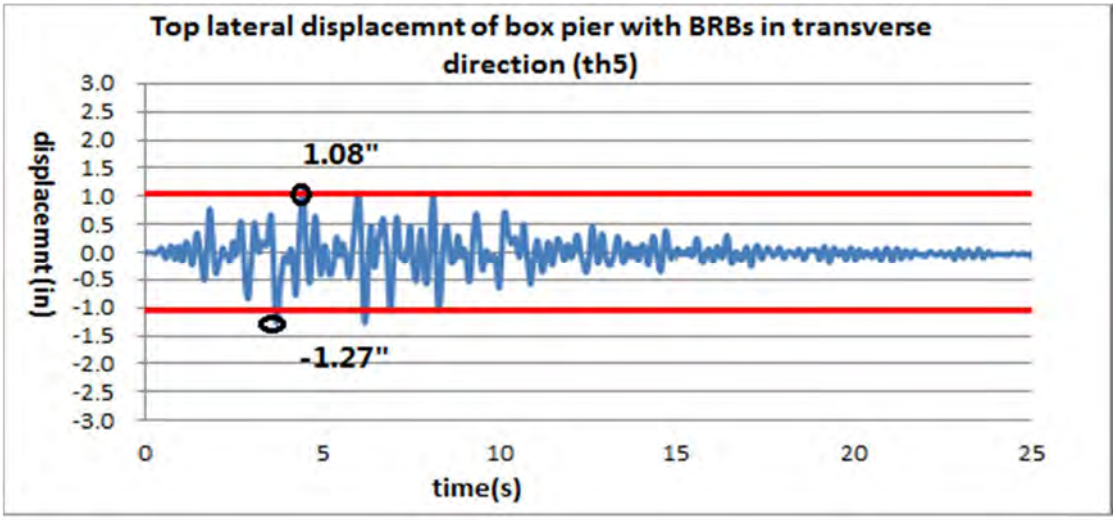
Top lateral displacemnt of box pier with BRBs in transverse direction (th5)
displacemnt (in)
time(s)
1.08"
-1.27"

(1)

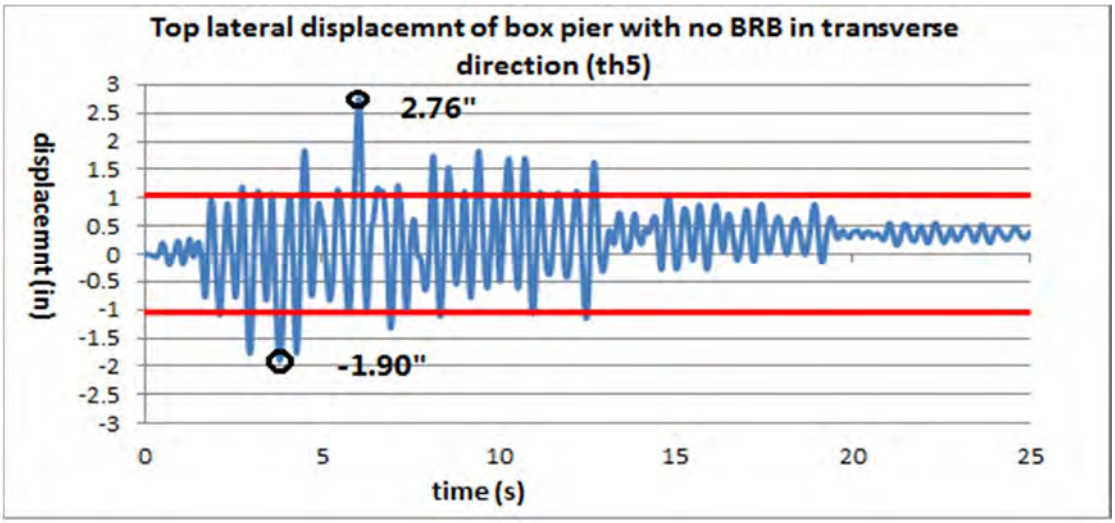
Top lateral displacemnt of box pier with no BRB in transverse direction (th5)
displacemnt (in)
time (s)
2.76"
-1.90"

(2)

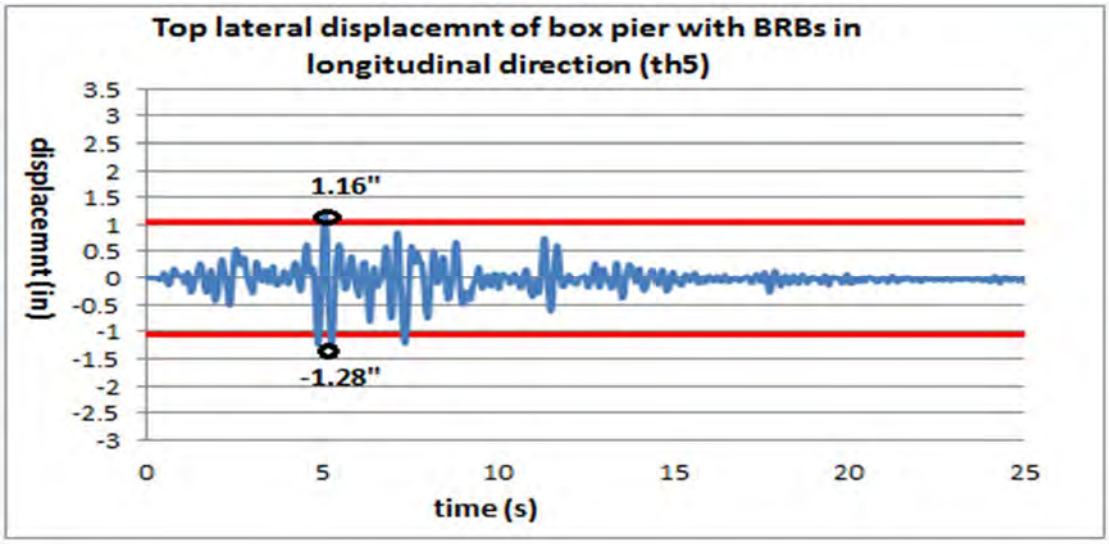
Top lateral displacemnt of box pier with BRBs in longitudinal direction (th5)
displacemnt (in)
time (s)
1.16"
-1.28"

(3)

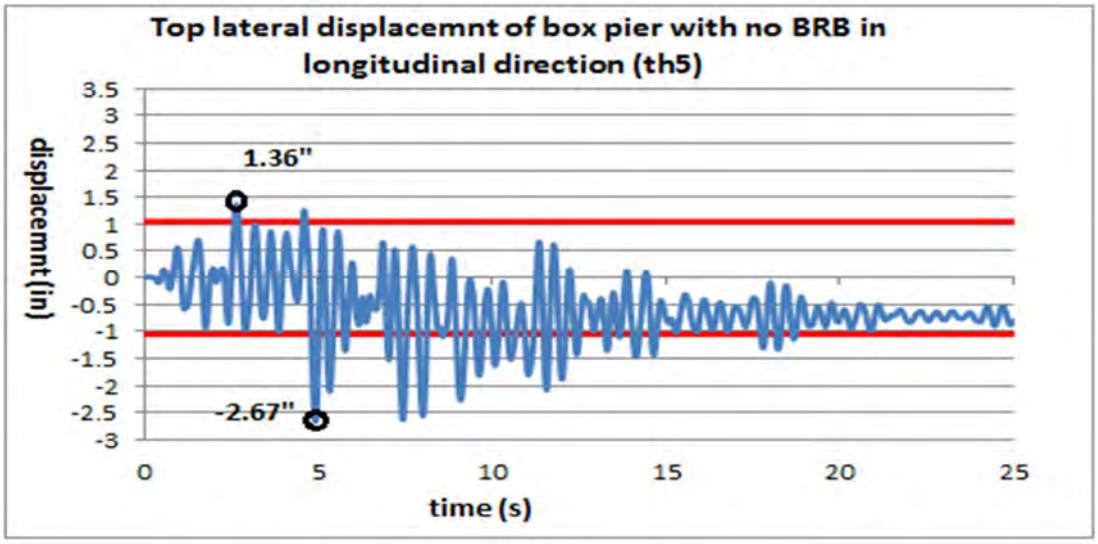


(4)

Figure 4-9 Displacement demands of the two column bridge bents under ground motion TH5

The base shear force time histories resisted by box-pier bents are plotted in Figure 4-10. Note that, the maximum base shear forces are only increased by 7.6% and 7.8% for the box-pier in the transverse and longitudinal directions, if comparing them with the no-BRB case.

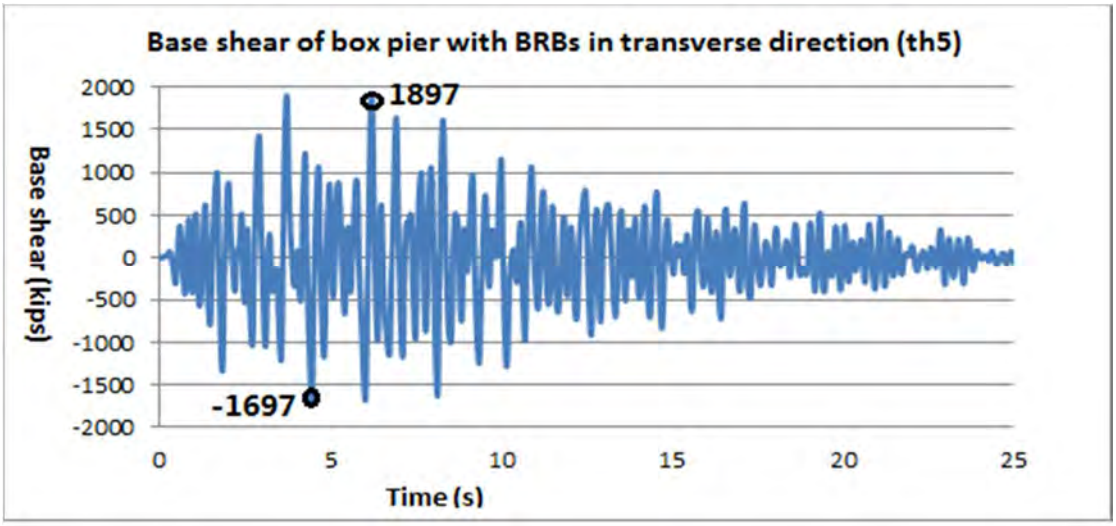


(1)

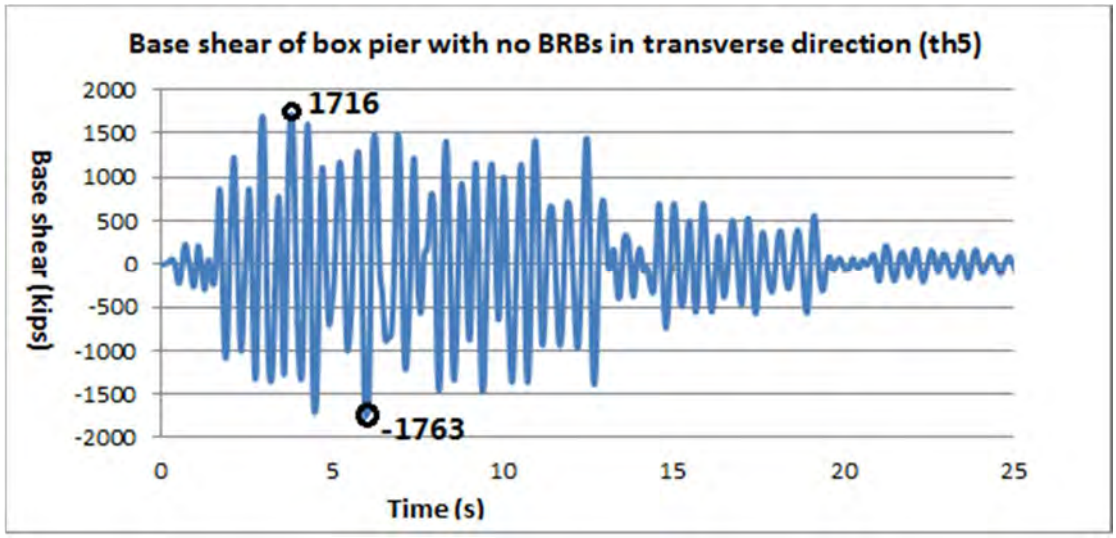


(2)

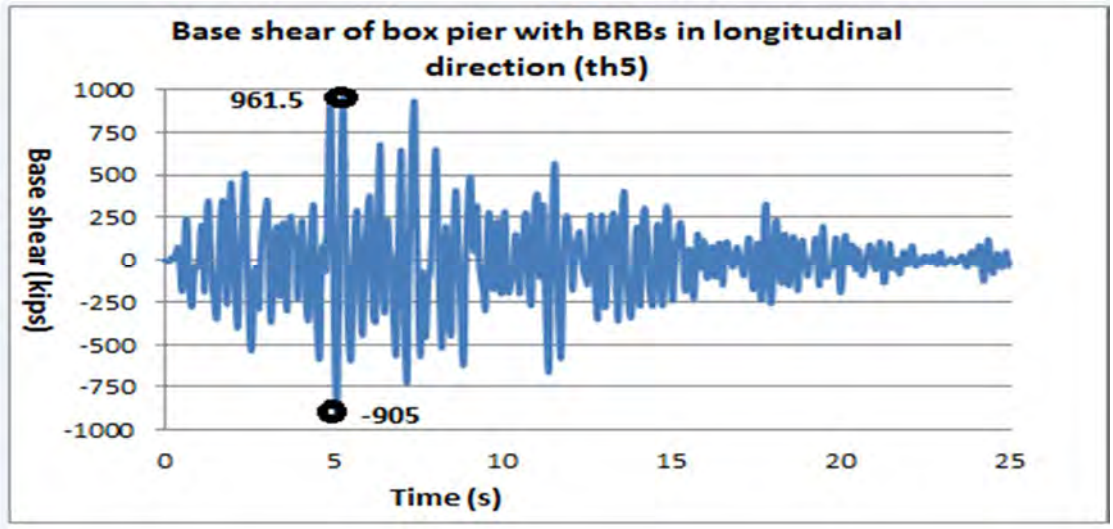


(3)

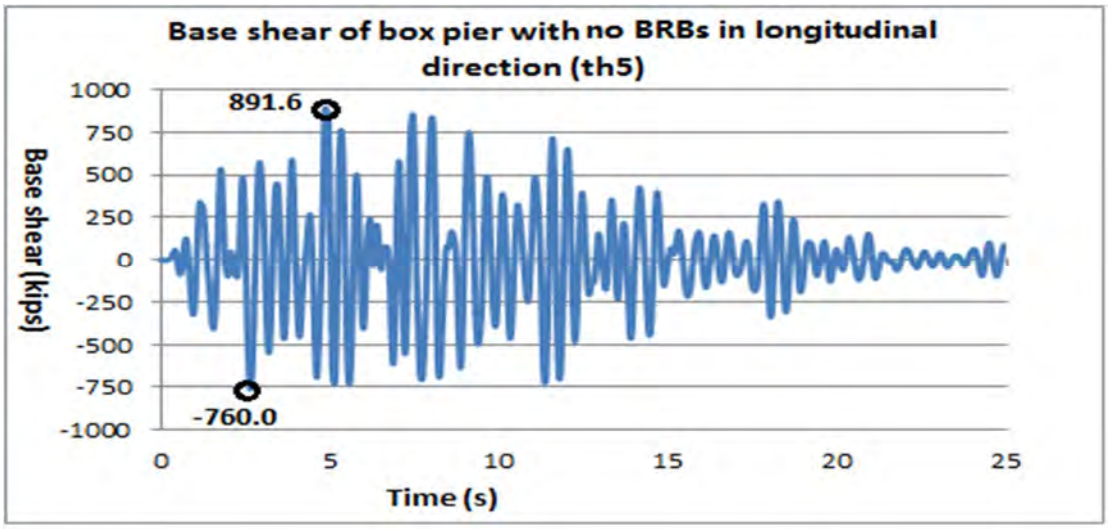


(4)

Figure 4-10 Base shear demands of the box-pier bents under ground motion TH5

For all the box-pier bent cases considered, P-$M_2$-$M_3$ fiber hinges (as defined in Section 3.3.1.1.3) are located at top and bottom of the CFT columns. Moment rotation history for the hinge at bottom of the right column, found to develop the maximum rotation, is shown in Figure 4-11.

The hinge behaviors in the transverse box-pier bent with and without BRBs are shown in Figures 4-12 (1) and (2). The maximum rotation of the hinge is 0.001 rad, which is only about 15% of the no-BRB case which has a 0.0065 rad maximum rotation. For the box-pier bent with and without BRBs in the longitudinal direction, the hinge behaviors at bottom of the rightmost column are shown in Figures 4-12 (3) and (4). The maximum rotation of the hinge is 0.0008 rad, which is only about 14% of the no-BRB case, which has a 0.0058 rad maximum rotation. Note that, from Figure 4-12, the yield rotation for the column (under its specific axial loads) is graphically estimated to be approximately 0.0006 rad. The yielding in the column is deemed acceptable for the box-pier bent with BRB in both directions.

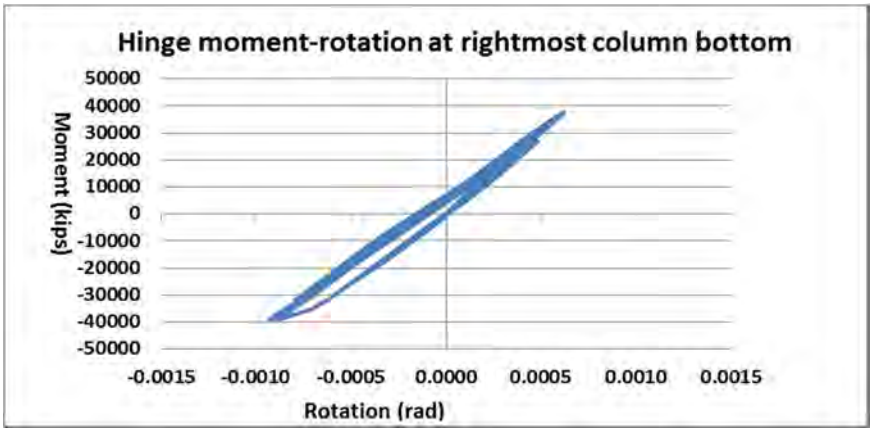


(1)

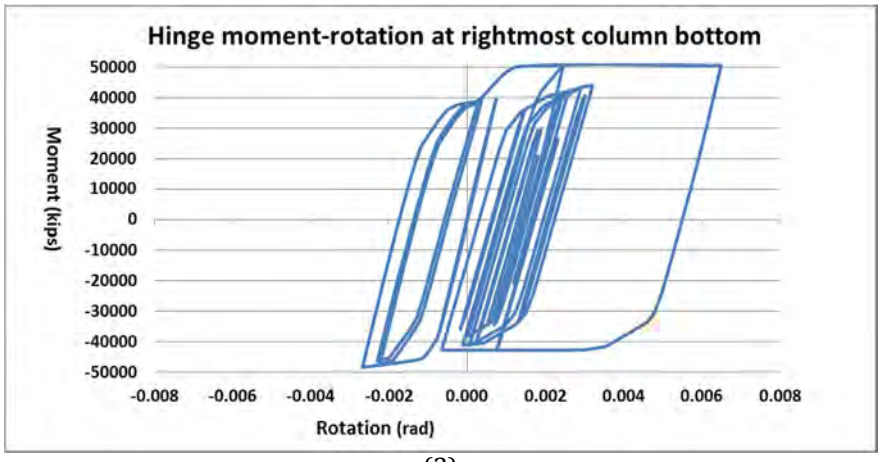


(2)

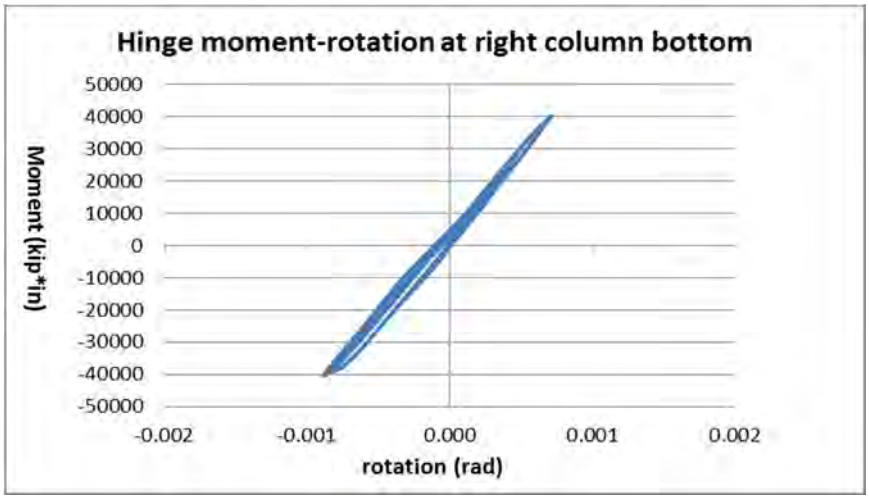


(3)

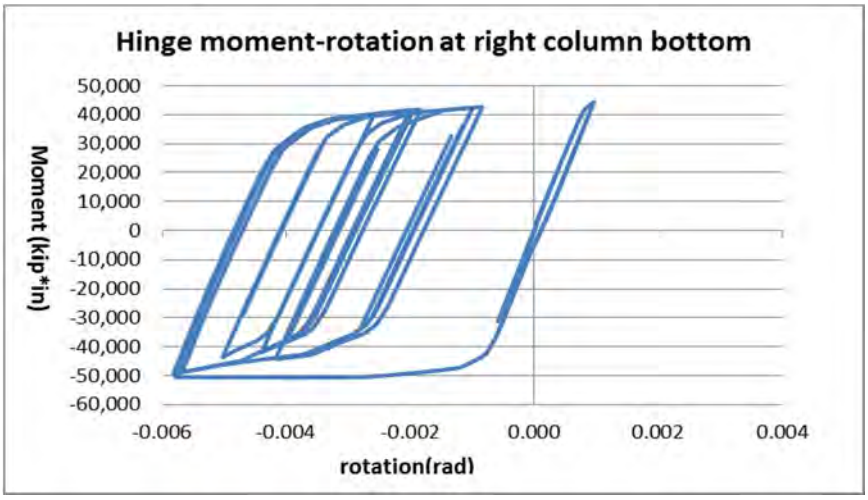


(4)

Figure 4-11 The hinge behaviors at bottom of the rightmost column of the box-pier bent (1) transverse with BRB, (2) transverse no BRB, (3) longitudinal with BRB and (4) longitudinal no BRB

Figure 4-12 shows the hinge axial force-deformation behavior for the four BRBs located between the left two columns in the transverse direction box-pier model. The BRBs between the right two columns have similar behaviors. For the box-pier bent in the longitudinal direction, the axial force-deformation plots are shown in Figure 4-13. In both directions, the BRBs did not yield to the same extent. The middle two BRBs have developed more ductility than the top and bottom ones. Note that a compressive strength of 332 kips and tensile strength of 299 kips (after strain hardening) developed in the BRBs at maximum ductility of 15 and 12.5, respectively, for the box-pier bent in the transverse and longitudinal direction, respectively.

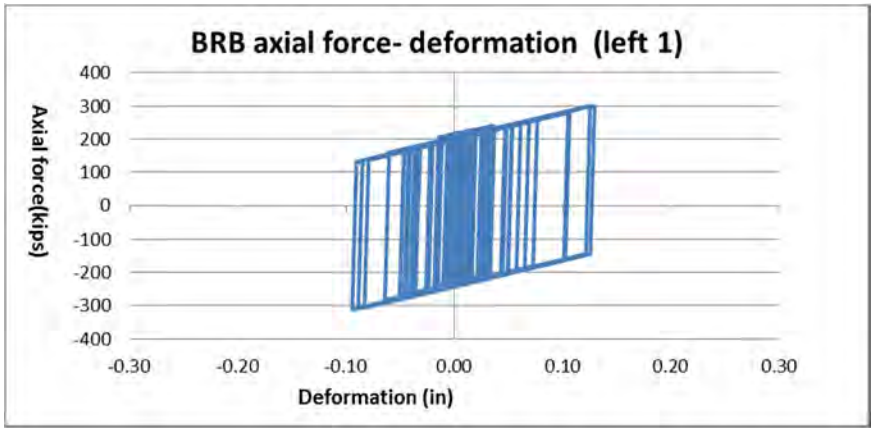


(1)

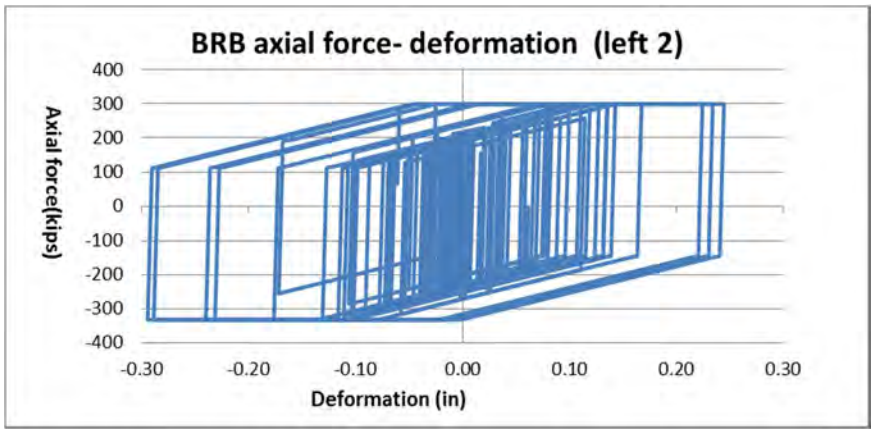


(2)

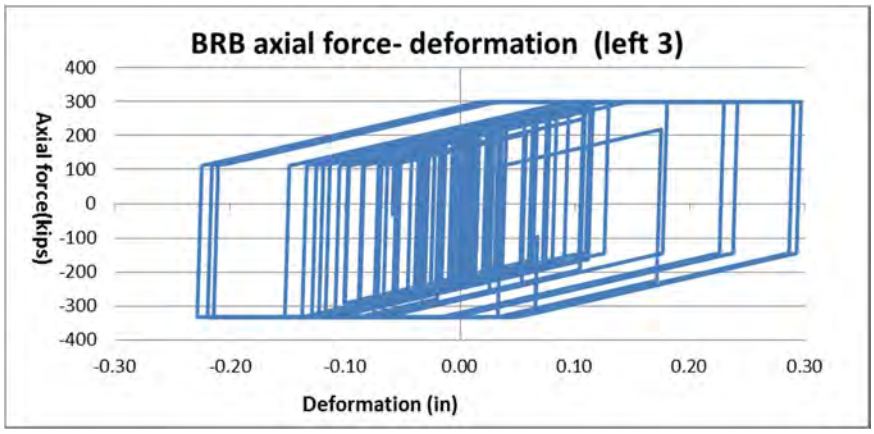


(3)

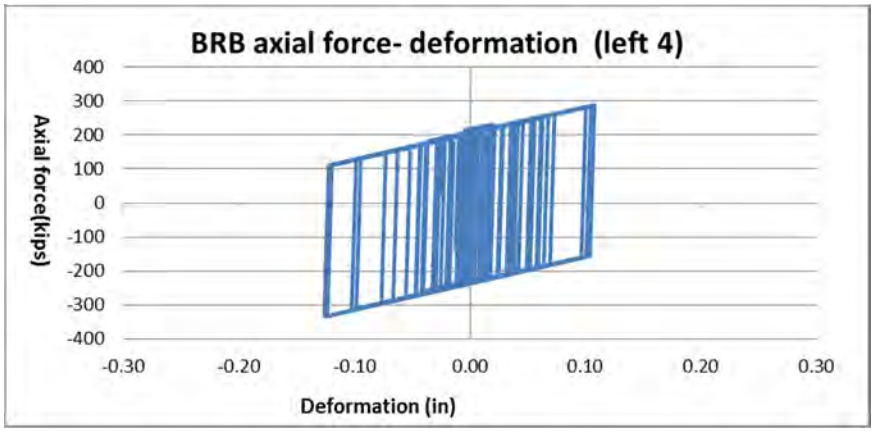


(4)

Figure 4-12 BRB hinge axial force-deformation plot for the box-pier bridge bent in the transverse direction (between left two columns, numbered from 1 to 4 top to bottom)

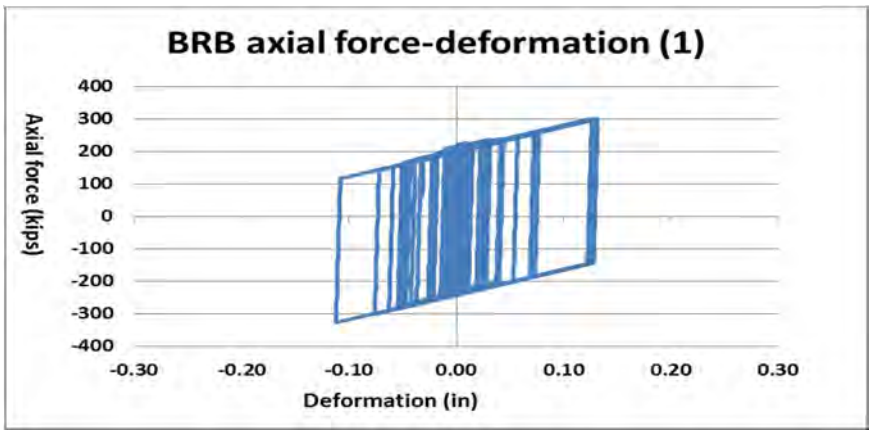


(1)

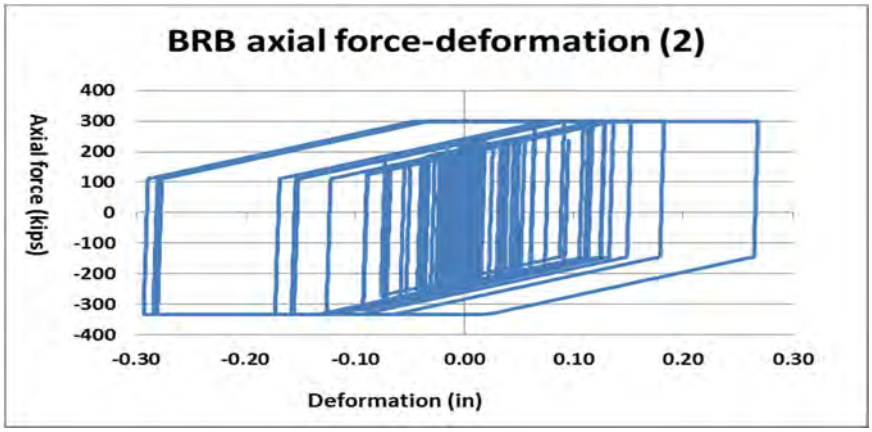


(2)

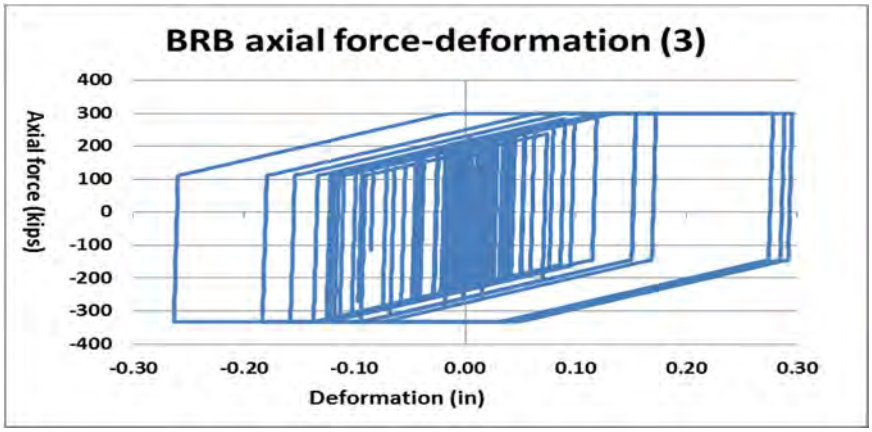


(3)

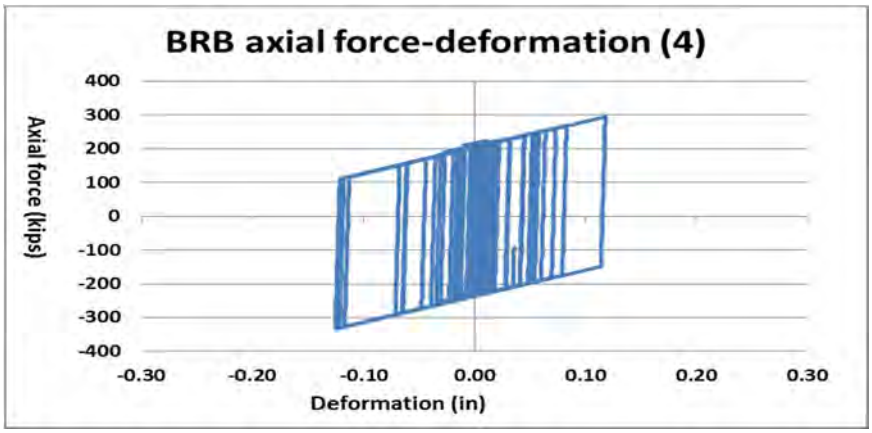


(4)

Figure 4-13 BRB hinge axial force-deformation plot for the box-pier bridge bent in the longitudinal direction (numbered from 1 to 4 top to bottom)

### 4.2.3. Verification with SDOF Nonlinear Time History Analysis

Vargas and Bruneau (2006a, 2006b) described the Structural Fuse (SF) concept in a

parametric formulation, considering the behavior of nonlinear Single Degree Of Freedom (SDOF) systems subjected to synthetic ground motions. A systematic and simplified design procedure was developed to achieve and implement the SF concept in generic buildings, in a way that ensure that damage only occurs in disposable structural elements. The procedure, intended to eliminate the need for complex analyses, relied on the use of regions of admissible solutions for the SF concept, pre-determined using nonlinear time history analyses. Response of a Single Degree of Freedom (SDOF) system with structural fuses was presented in terms of normalized parameters, as shown in Figure 4-14. These dimensionless charts are normalized with respect to a number of key parameters, namely, the stiffness ratio $\alpha$ (equal to the ratio between the frame stiffness $K_f$ and the total initial stiffness $K_t$), maximum displacement ductility ratio $\mu_{\max}$ (i.e., the ratio of the frame yielding displacement $\Delta_{yf}$ and the fuse yielding displacement $\Delta_{yb}$), frame ductility $\mu_f$, fuse ductility $\mu$, and the strength-ratio $\eta$ defined as the ratio of the yielding strength of the system $V_y$ over the maximum ground force applied during the ground motion $m\ddot{u}_{g\max}$.

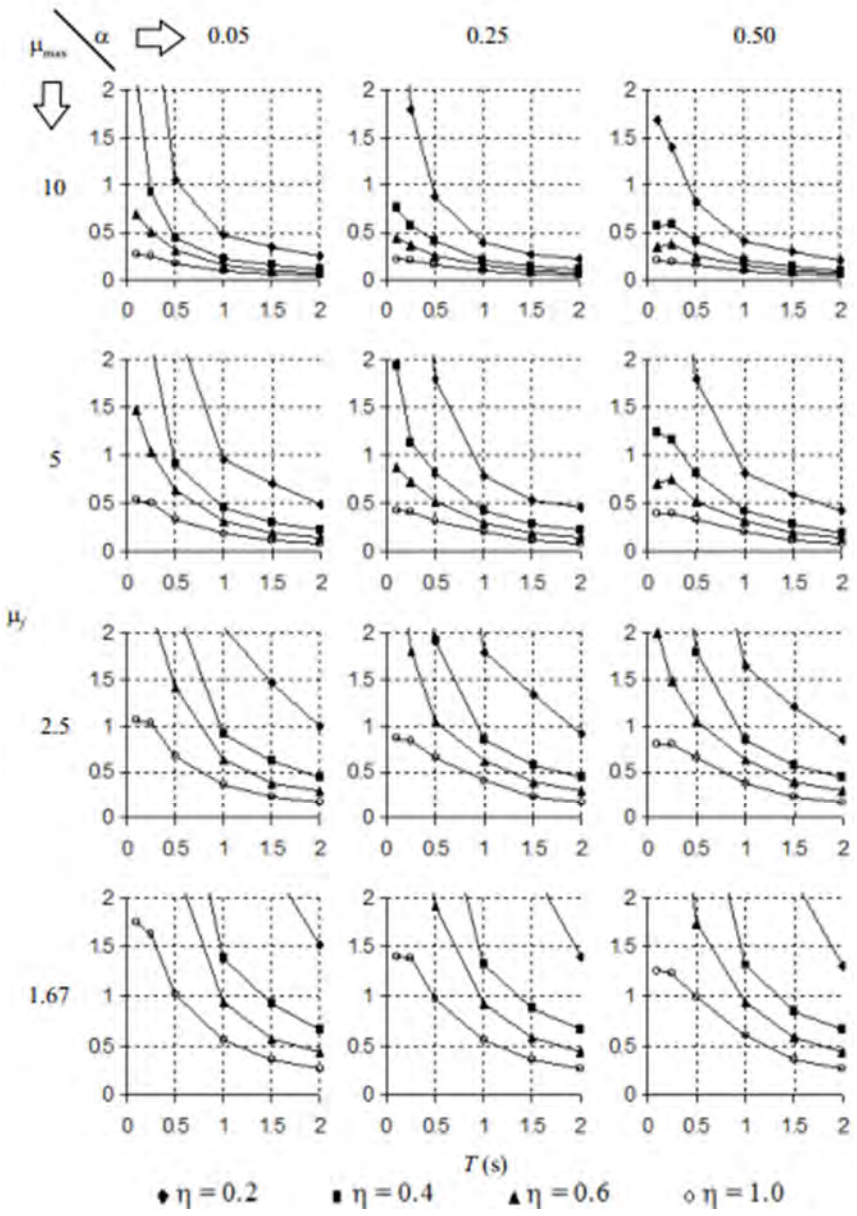


(1)

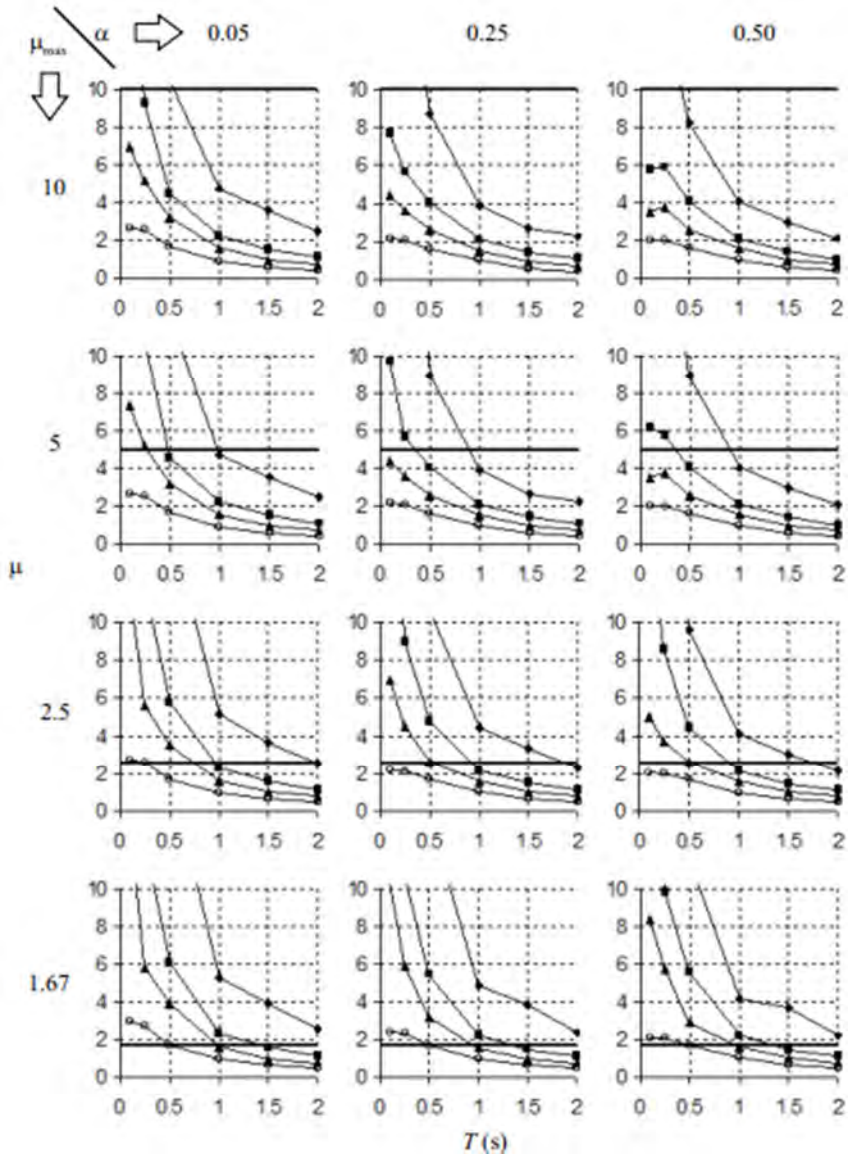


(2)

Figure 4-14 Nonlinear time history analysis response plots of a Single Degree of Freedom (SDOF) system with structural fuses

Referring to Chapter 2 for the two-CFT-column bent with BRBs systems considered, the period is 0.19 second. The stiffness ratio $\alpha$, the maximum displacement ductility ratio $\mu_{\max}$ and the yielding strength of the system $V_y$ are:

$$\alpha = \frac{K_f}{K_t} = 0.231 \tag{4-1}$$

$$\mu_{\max} = \frac{\Delta_{yf}}{\Delta_{yb}} = 10.29 \tag{4-2}$$

$$V_y = (K_f + K_b)\Delta_y = 912.18 kips \tag{4-3}$$

Table 4-7 shows the strength ratio $\eta$ , the frame ductility $\mu$ , and the fuse ductility $\mu$ under for the nine ground motions considered for the two-CFT-column bents with BRBs.

Table 4-7 Strength ratios of the two-CFT-column bent with BRBs under the nine ground motions

| | | TH1 | TH2 | TH3 | TH4 | TH5 | TH6 | TH7 | TH8 | TH9 | Ave |
|---|---|---|---|---|---|---|---|---|---|---|---|
| $\ddot{u}_{g\max}$ (in/s$^2$) | | 117.3 | 118.6 | 110.4 | 145.7 | 117.5 | 129.7 | 107.4 | 114.4 | 113.5 | 119.4 |
| $\eta$ | | 0.25 | 0.25 | 0.27 | 0.20 | 0.25 | 0.23 | 0.28 | 0.26 | 0.26 | 0.25 |
| Single BRB | $\mu_f$ | 1.53 | 1.52 | 1.54 | 1.50 | 1.58 | 1.73 | 1.38 | 1.78 | 1.33 | 1.54 |
| | $\mu$ | 15.72 | 15.59 | 15.83 | 15.42 | 16.29 | 17.81 | 14.23 | 18.29 | 13.68 | 15.87 |
| Chevron BRBs | $\mu_f$ | 1.57 | 1.58 | 1.58 | 1.57 | 1.60 | 1.70 | 1.47 | 1.83 | 1.41 | 1.59 |
| | $\mu$ | 16.18 | 16.28 | 16.26 | 16.18 | 16.50 | 17.51 | 15.18 | 18.79 | 14.49 | 16.37 |

With the stiffness ratio $\alpha$ of 0.23 and the maximum displacement ductility ratio $\mu_{\max}$ of 10.3, the charts in Figure 4-15 can be consulted to obtain an estimate of expected response. Note that the closest SDOF system corresponding to the two-CFT-column bent with BRBs would be the one whose behavior is represented by the second chart in the first row of Figure 4-15. Here, the average strength ratio $\eta$ for the bridge bents with BRBs is 0.25, i.e., between 0.2 and 0.4 (which would require interpolation). The frame ductility $\mu_f$ of 1.54 for the single inclined BRB case and 1.59 for the inverted-V chevron BRBs case are both between the 0.65 and 2.0 cases in Figure 4-15 (1). And it is hard to verify if the previously calculated fuse ductility $\mu$

of 15.87 for the single inclined BRB case and 16.37 for the inverted-V chevron BRBs case can be predicted by the data in Figure 4-15 (2), since the value to be read would be out of range.

The second case considered in this section is the box-pier bent. The period of the box-pier bent with BRBs is 0.23 second. The stiffness ratio $\alpha$, the maximum displacement ductility ratio $\mu_{\max}$ and the yielding strength of the system $V_y$ are:

$$\alpha = \frac{K_f}{K_t} = 0.25 \tag{4-4}$$

$$\mu_{\max} = \frac{\Delta_{yf}}{\Delta_{yb}} = 10.41 \tag{4-5}$$

$$V_y = (K_f + K_b)\Delta_y = 901.93 kips \tag{4-6}$$

Table 4-8 shows the strength ratio $\eta$, the frame ductility $\mu$, and the fuse ductility $\mu$, for the nine ground motions considered for the box-pier bents with BRBs in both transverse and longitudinal directions.

Table 4-8 Strength ratios of the box-pier bents with BRBs under the nine ground motions

| | | TH1 | TH2 | TH3 | TH4 | TH5 | TH6 | TH7 | TH8 | TH9 | Ave |
|---|---|---|---|---|---|---|---|---|---|---|---|
| $\ddot{u}_{g\max}$ (in/s$^2$) | | 117.3 | 118.6 | 110.4 | 145.7 | 117.5 | 129.7 | 107.4 | 114.4 | 113.5 | 119.4 |
| $\eta$ | | 0.25 | 0.25 | 0.26 | 0.20 | 0.25 | 0.23 | 0.27 | 0.26 | 0.26 | 0.25 |
| Transverse direction | $\mu_f$ | 1.25 | 1.30 | 1.33 | 1.24 | 1.21 | 1.24 | 1.18 | 1.52 | 1.00 | 1.25 |
| | $\mu$ | 13.01 | 13.56 | 13.83 | 12.88 | 12.58 | 12.95 | 12.29 | 15.85 | 10.41 | 13.04 |
| Longitudinal direction | $\mu_f$ | 1.62 | 1.54 | 1.42 | 1.38 | 1.43 | 1.58 | 1.40 | 1.76 | 1.32 | 1.49 |
| | $\mu$ | 16.81 | 16.00 | 14.74 | 14.38 | 14.86 | 16.48 | 14.61 | 18.30 | 13.76 | 15.55 |

With the stiffness ratio $\alpha$ of 0.25 and the maximum displacement ductility ratio

$\mu_{max}$ of 10.4, the closest SDOF system corresponding to the box-pier bent with BRBs would also be the one whose behavior is represented by the second chart in the first row of Figure 4-15. Here, the average strength ratio $\eta$ for the bridge bents with BRBs is 0.25, i.e., between 0.2 and 0.4 (which would require interpolation). The frame ductility $\mu_f$ of 1.25 for the transverse direction and 1.49 for the longitudinal direction is between the 0.55 and 2.0 case in Figure 4-15 (1). This makes it hard to verify if the previously calculated fuse ductility $\mu$ of 13.04 for the transverse direction and 15.55 for the longitudinal direction can be predicted by the data in Figure 4-15 (2), since the value is out of the range.

Note that the above examples illustrate that, in some instances, structural fuse implementations in bridges could have combination of parameters that fall outside the range covered in Figure 4-15. This could be even more so for bridge with different fuse and column designs, or subjected to different severity of earthquake ground motions. Therefore, a broader parametric study of SDOF structures with fuses may be required to obtain charts to predict the behavior of bridge systems with fuses.

## 4.3 Bridge Performance Comparison

### 4.3.1. Displacement

The displacement demand at top of the column obtained by the design hand calculation (yielding displacement of the column), the elastic response spectrum analysis, and the inelastic nonlinear time history analysis, are compared in Table 4-9. Due to the smaller stiffness in the SAP2000 model for the columns (their restraint being less than for the fixed end condition assumed in the design hand calculation), the elastic displacement demand in the response spectrum analysis is larger than the design hand calculation.

Nonlinear time history analysis results are also tabulated in Table 4-9. The inelastic displacement demands of the bridge bents are larger than the elastic response spectrum demand. This is due to the fact that design was based on the "equal displacement" assumption (i.e., assuming that displacements resulting from inelastic analysis are approximately equal to those obtained from a linear elastic analysis). This is usually a reasonable assumption, except for short period structures for which it is not conservative (AASHTO Seismic Design Specification, 2009). Recognizing this exception, a modification factor $R_d$ is typically prescribed to magnify the maximum elastic displacements of short-period structures and estimate the actual maximum inelastic response. $R_d$ as defined by MCEER-ATC 49, is equal to:

$$R_d = \frac{\Delta_{inelastic}}{\Delta_{elastic}} \tag{4-7}$$

Table 4-9 Displacement demand comparison at top of the column

| | | Displacement at top of column | | |
|---|---|---|---|---|
| | | Hand Calculation | Response Spectrum | Time history |
| Two-CFT-Column bent | single inclined BRB | 0.71" | 0.94" | 1.13" |
| | inverted-V BRBs | 0.71" | 0.81" | 1.10" |
| Box-pier bent | Transverse with BRB | 1.05" | 1.28" | 1.32" |
| | Transverse with BRB | 1.05" | 1.28" | 1.32" |

The modification factor $R_d$ when the bridge period is smaller than $1.25T_s$ is given by Equation 4-10, from the MCEER-ATC 49 (similar to AASHTO 2009):

$$R_d = (1-\frac{1}{R})\frac{1.25T_s}{T} + \frac{1}{R} \geq 1 \tag{4-10}$$

where: $T$ is the period of the bridge bent;

$T_s$ is the period at the end of the acceleration response spectrum plateau;

$R$ is the ratio between design elastic lateral force and the lateral strength of the bent, which is conceptually similar to the maximum local displacement ductility demand, $\mu_D$,in AASHTO 2011 (conservatively, the upper limits for $\mu_D$ in AASHTO could have been used here instead of the actual value of this ratio, but this would have resulted in larger values of $R_d$ ).

The ratio $R$ in Table 4-11 is the ratio from the bilinear pushover curve assumed in the design process, as illustrated in Figure 4-15. The value $R_d$ calculated from Equation 4-10, using $T_s$ of 0.35s from the acceleration response spectrum in Figure 3-10. The periods $T$ of the different bents are listed in Table 4-11. For comparison, the actual $R_d$ values computed directly from the non-linear inelastic time history analysis results (i.e., actual inelastic over elastic deformation values) are also presented in Table 4-9. Note that these actual values are smaller than the value predicted by the Equation 4-10, which indicates that Equation 4-10 is conservative for this particular application.

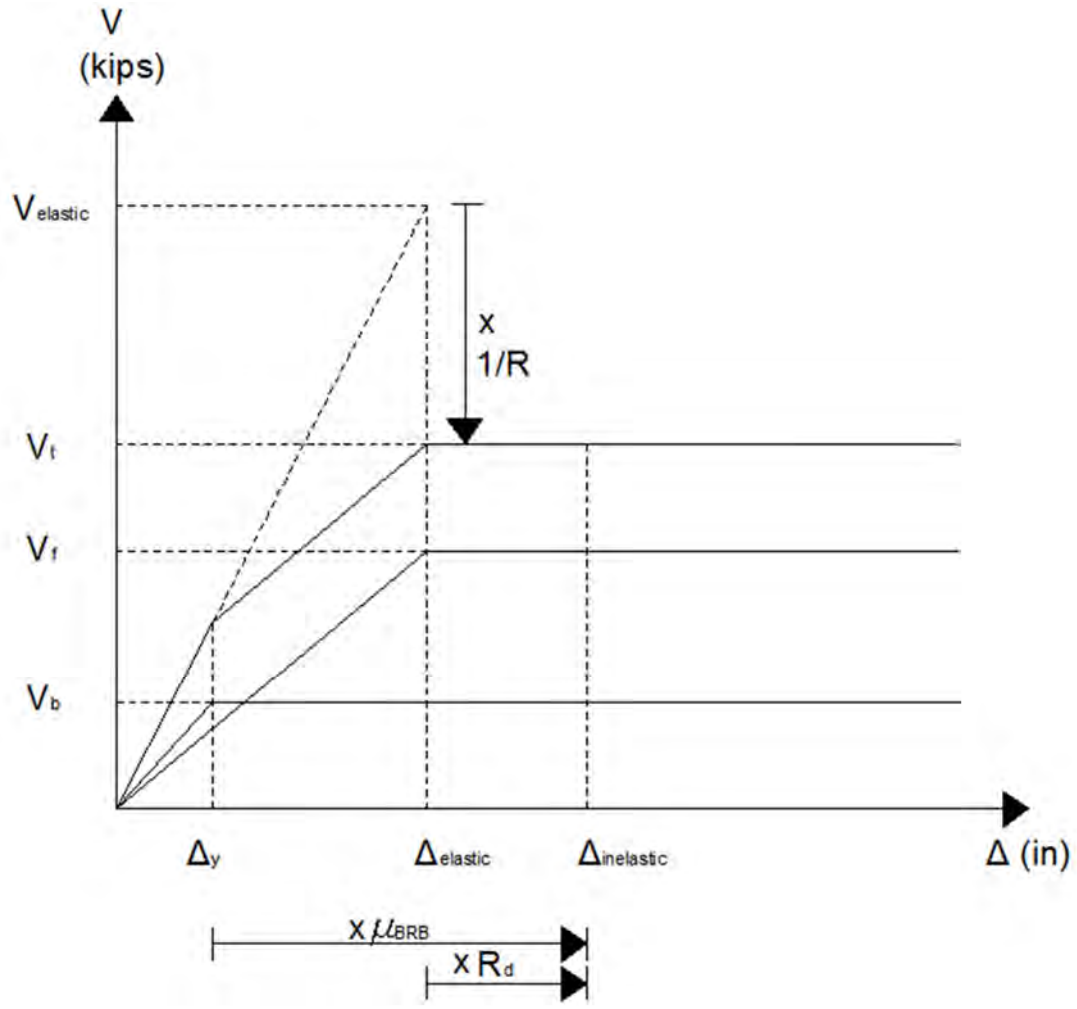


Figure 4-15 Lateral strength vs displacement plot for trilinear system

Table 4-10 Elastic and inelastic base shear demand ratio and displacement amplification factor

| | $R$ | $R_d$ (analysis) | $R_d$ (equation) | $T$ (s) |
|---|---|---|---|---|
| Two-CFT-Column bent with single inclined BRB | 2.90 | 1.20 | 1.62 | 0.225 |
| Two-CFT-Column bent with inverted-V BRBs | 2.90 | 1.36 | 1.76 | 0.202 |
| Transverse box-pier bent with BRBs | 2.84 | 1.03 | 1.46 | 0.256 |
| Longitudinal box-pier bent with BRBs | 2.84 | 1.08 | 1.51 | 0.244 |

The validation of Equation 4-10 remains for the trilinear system to be investigated, since it has been originally developed based on nonlinear time history results for of bilinear system for assumptions as shown in Figure 4-16.

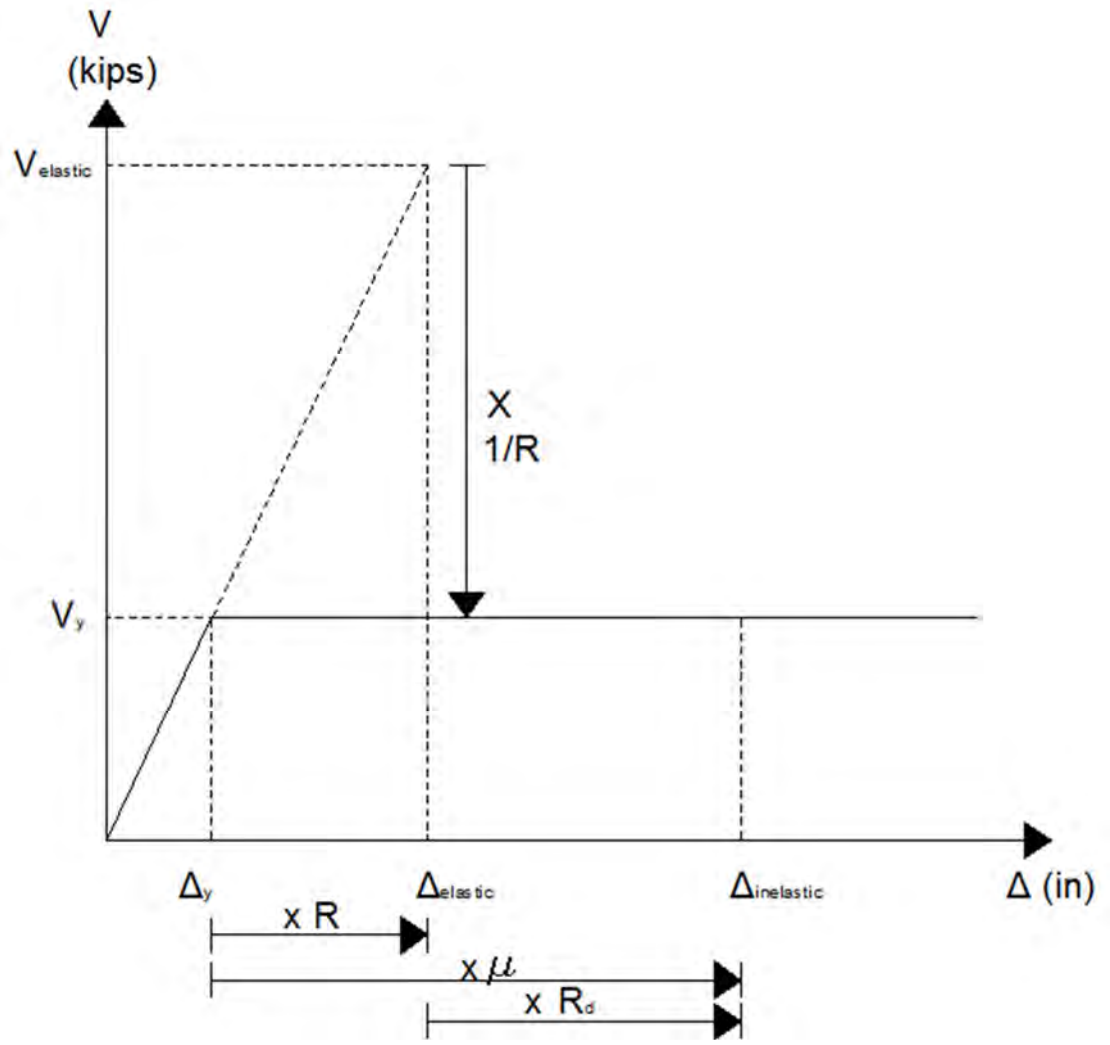


Figure 4-16 Displacement modification factor for bilinear system

## 4.3.2. Base Shear Force

The base shear forces for the frame base shear from the bent pushover analysis at the target elastic displacement of response spectrum analysis, as well as the base shear demand from elastic response spectrum analysis and the inelastic nonlinear time history analyses, are compared in Table 4-11. The elastic response spectrum over the inelastic pushover base shear force is also shown in Table 4-11.

Table 4-11 Elastic and inelastic base shear force demand

| | | Base Shear | | | Base Shear |
|---|---|---|---|---|---|
| | | Pushover | Response Spectrum | $R_{real}$ | Time history |
| Two-CFT-Column bent | single inclined BRB | 3504.3 | 9334.4 | 2.66 | 3916.5 |
| | inverted-V BRBs | 3247.7 | 9445.6 | 2.91 | 3904.7 |
| Box-pier bent | Transverse with BRB | 3786.2 | 9534.4 | 2.52 | 3860.4 |
| | Longitudinal with BRB | 3599.9 | 8778.4 | 2.44 | 3802.4 |

# Chapter 5 Connections

Given that BRBs are to be added to a bridge bent to implement the structural fuse concept, it is important to investigate how BRBs could potentially be connected to transfer their loads. It is recognized that various transportation agencies may implement connection details that are completely different than those investigated below; the purpose of the information presented here is to ensure that there exists at least one satisfactory solution. For structural fuses connections to reinforced concrete columns, three types of connections have already been briefly introduced. In this chapter, primary focus is on connection to CFT columns by welding of the gusset plate of the BRB to the steel shell of a CFT (Section 5.1). For BRBs' connections to the cap beam or foundation, steel headed studs (Section 5.2) and anchor rods (Section 5.3) embedded in concrete, are considered. Connection details will be developed and the capacity of these three kinds of connections will be identified.

## 5.1 Welding to the Steel Shell

### 5.1.1. Model Description

As described in Chapter 2, a SAP2000 model of the cross-section having a steel shell (same as the steel jacketing) around a concrete infill was built to investigate the load carrying capacity of the steel shell to transfer the applied tensile loads, as a means of connecting BRBs to columns.

To the capture development of plastic hinges at any location in the steel shell due to the applied tensile load, the arch was divided into 50 beam elements as shown in Figure 5-1. Using more frame members along the perimeter will provide more resolution as to the possible location of plastic hinges and actual strength of the

system, because such hinges were located at two ends of members in the model; results were found to converge when using 50 elements. In addition, at each joint between frame elements, a gap link was used to account for the concrete resistance to inward displacements of the shell. The gap link was set to have zero stiffness when the gap became larger than zero, thus allowing the steel to separate from the concrete under tensile load. The stiffness of the gap link in contact was specified a large value when the gap closed, to keep the steel from moving inward into the concrete. That stiffness was set as 100,000 kip/in, which was found to be sufficient to simulate the condition of concrete restraint provided to the steel.

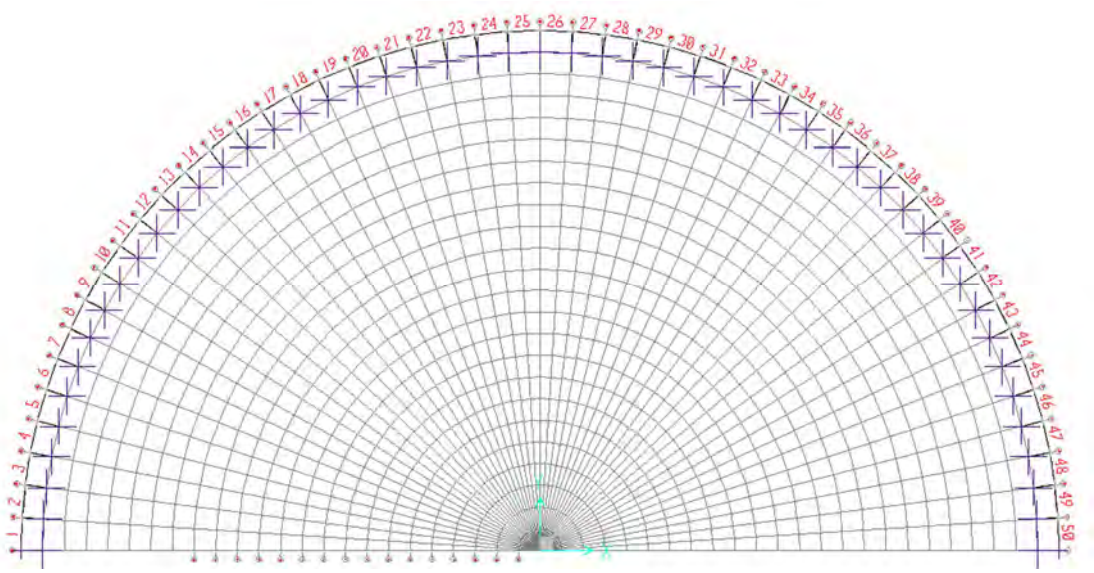

Figure 5-1 Steel jacketing plate model in Sap2000

The purpose of this analysis was to obtain the capacity of the CFT in resisting a tensile load applied perpendicularly to its surface, when a plastic hinge mechanism develops in the steel shell plates. Since locations of the plastic hinges are unknown at the onset, the SAP2000 pushover analysis was conducted (by displacing the load application point away from the CFT surface) to determine this plastic mechanism, as well as the tensile force resisted by the CFT at the development of the first hinge, which is actually more important when the intent is to keep the CFT column elastic.

The CFT column for the two-column bent with BRBs case (which is 4 ft diameter column having a steel shell thickness of 1.25 in) was first studied. The above SAP2000 model is set for a 1 in. segment of column length, for expediency, to get the axial tensile load capacity per unit length of the connection. As a result, this model neglects the possible contribution of yield lines extending along the steel shell beyond the end of the gusset plate, which is slightly conservative for long gussets.

The steel shell model has a diameter of 4 ft, with a rectangular cross section of 1.25 in (thickness) by 1 in (unit length). The steel grade used was A572Gr60. The stress-strain curve for that material is shown in Figure 5-2. SAP2000 beam elements were used, with fiber P-$M_2$-$M_3$ hinges at both ends of each element, to account for the interaction of axial and flexural forces in plastic hinges. The nonlinear static pushover analysis using displacement control was performed.

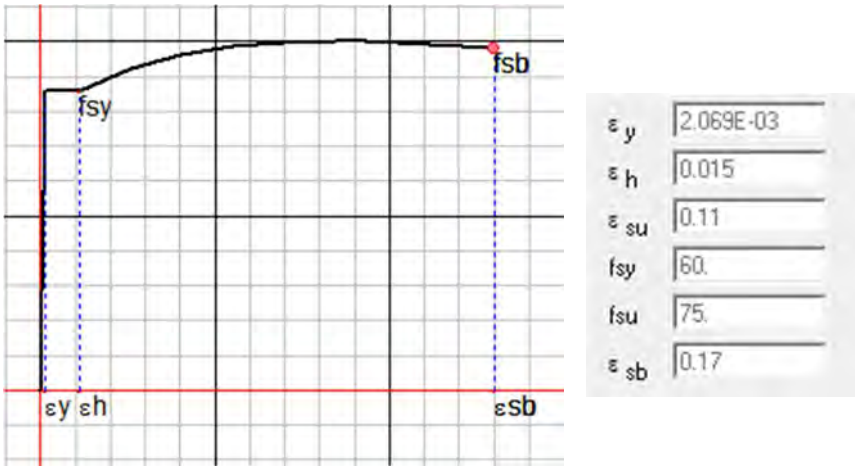


Figure 5-2 Steel stress-strain curve considering the strain hardening

For the box-pier bent with smaller CFT columns, the model has 32 in diameter, with a rectangular cross section of 0.75 in (thickness) by 1 in (unit length). All the other modeling aspects for that CFT column were taken to be the same as for the two-CFT-column bent with BRB.

## 5.1.2. Pushover Analysis

Before using the material of the steel shell considering strain hardening, a pushover analysis was first conducted for a bi-linear elasto-plastic material (i.e. for the steel stress-strain curve shown in Figure 5-3). The development of the plastic hinges along the steel arch was examined. And then strain hardening was introduced to get the pulling strength of the steel shell. The steel shell model analysis for the CFT column with 4 ft diameter and 1.25 in thickness was first carried out. Following the same procedure, the result for the box-pier bent using CFT column with 32 in diameter and 0.75 in thickness was presented.

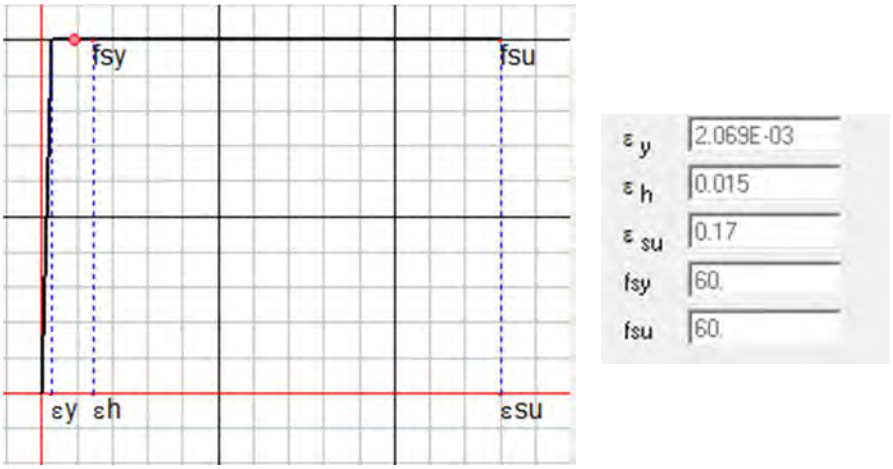


Figure 5-3 The bilinear model of the steel stress-strain curve

**1) CFT column with 4 ft diameter and 1.25 in thickness**

The force versus displacement at the load point resulting from the pushover analysis of the arch model with 50 frame element is shown in Figure 5-4. Since the pushover analysis is a displacement applied to the load point, the corresponding force is obtained by summing the vertical reactions for the model (labeled “base reaction” in Figure 5-2). The maximum load that can be applied to the structure under this condition is 19.61 kips/in, reached at a displacement at the loading point of 0.29 in.

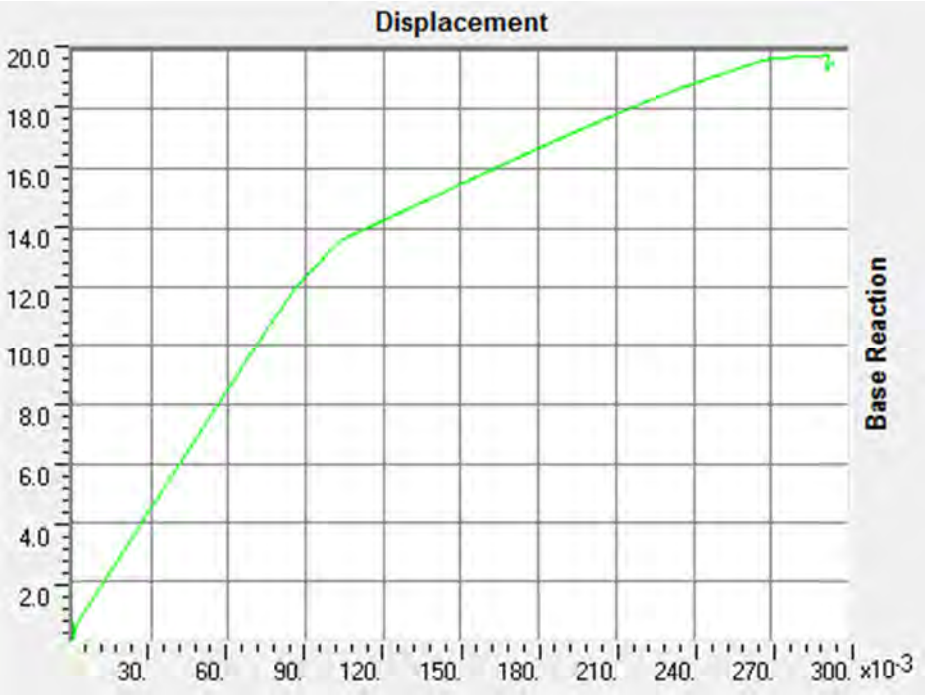


Figure 5-4 Pushover curve of the arch structure for bilinear steel material

The moment diagram shown in Figure 5-5a corresponds to the case when first plastic hinges develop. The plastic hinges locate at the apex of the arch, where frame members 25 and 26 meet (frame element numbers are labeled in Figure 5-1). Note that significant moments only develop in nine frame elements on each side from the point where the load is applied (the moment in the other frame elements is negligible). The corresponding force applied to the arch is 13.55 kips, with a displacement at the loading point of 0.10 in when the largest moment is reached at the first hinges. Upon increased loading, the next plastic hinges occur at the intersection of frame elements 19 and 20, and, symmetrically, frame elements 31 and 32, as shown in Figure 5-5b. The corresponding force applied to the arch is 19.72 kips, with a displacement at the loading point of 0.27 in. The analysis stopped at an applied force of 19.61 kips and corresponding displacement at the loading point of 0.29", when the strain limit of 0.17 (specified in the steel stress-strain material properties) was reached. The corresponding moment diagram is shown in Figure 5-5c.

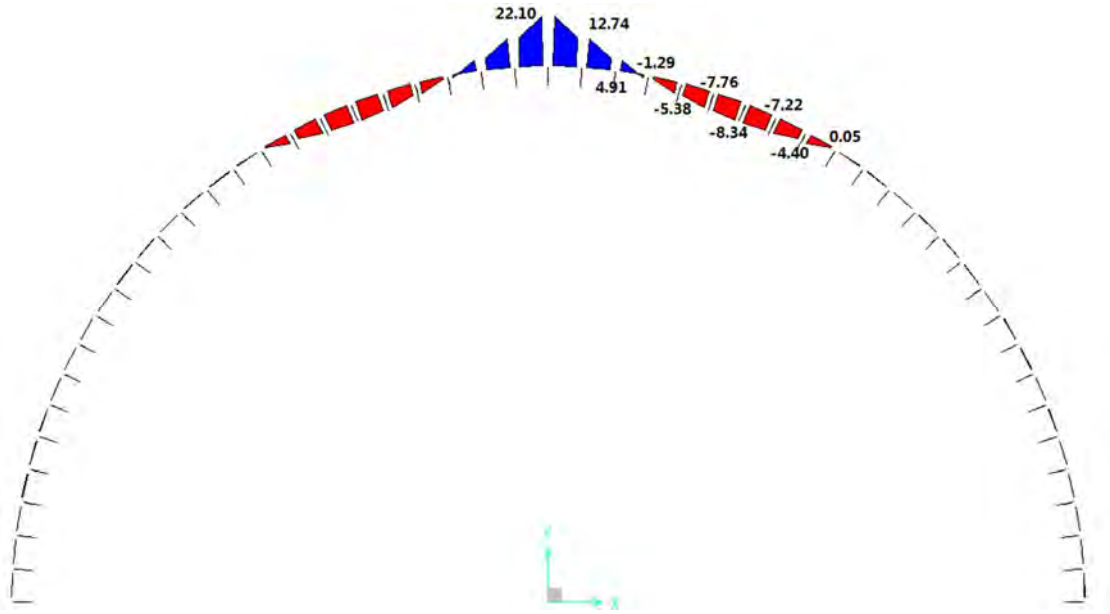


Figure 5-5 (a) Moment diagram of the arch model corresponding to the maximum moment at the first hinge

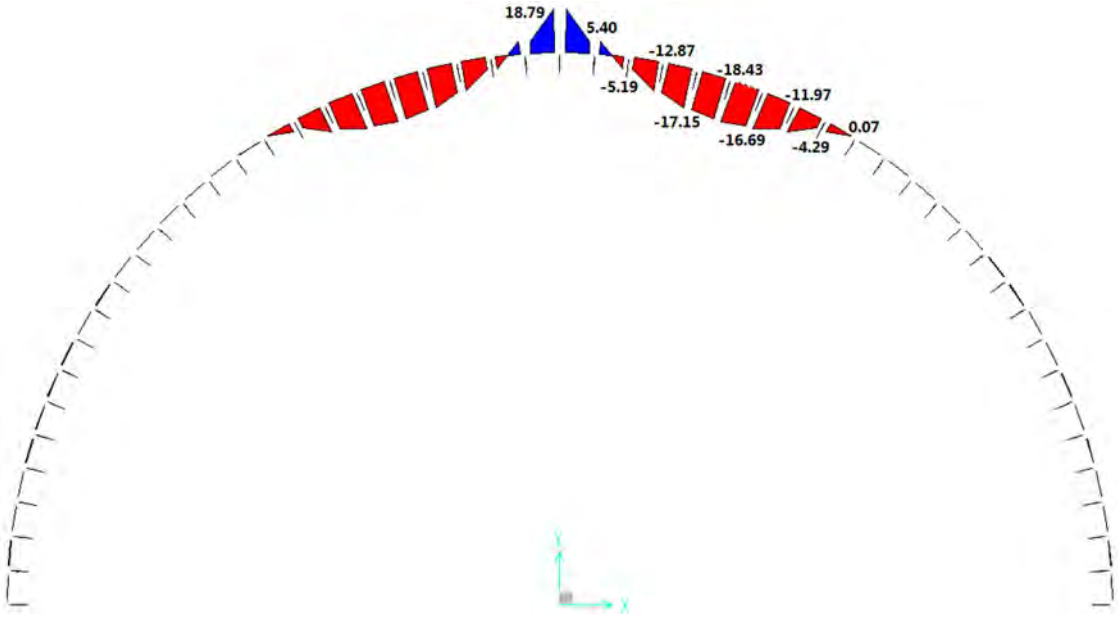


Figure 5-5 (b) Moment diagram of the arch model corresponding to the maximum hinge at the second hinge

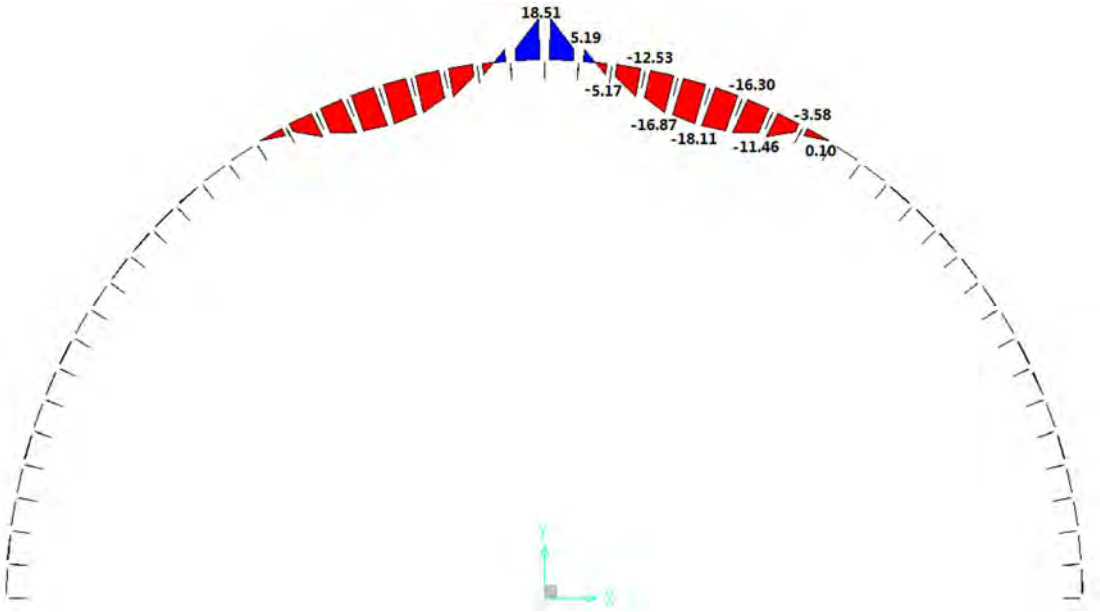


Figure 5-5 (c) Moment diagram of the arch model corresponding to the the end of the pushover analysis

Note that the small decrease in the value of the plastic moment in the first hinge was due to moment-axial force interaction and changes in axial forces in the arch (this phenomenon can be observed by comparing the plastic moment values in Figures 5-5a, b and c). To illustrate this phenomenon, the moment-rotation relationship of the first hinge is shown in Figure 5-6. A decrease of the hinge moment capacity is observed to occur as the applied load increases after the section has reached its moment capacity.

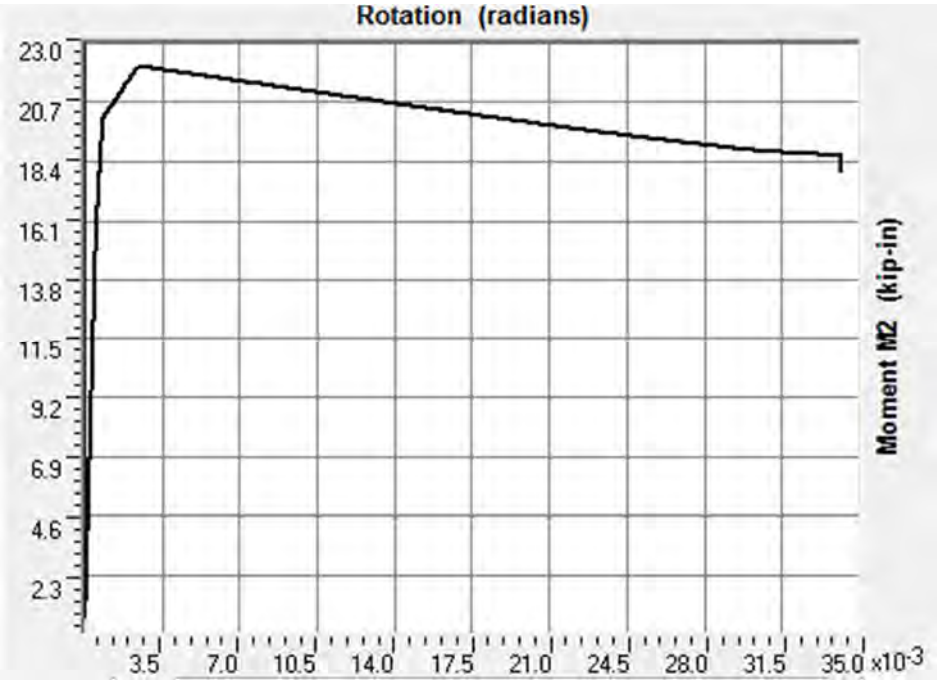


(a)

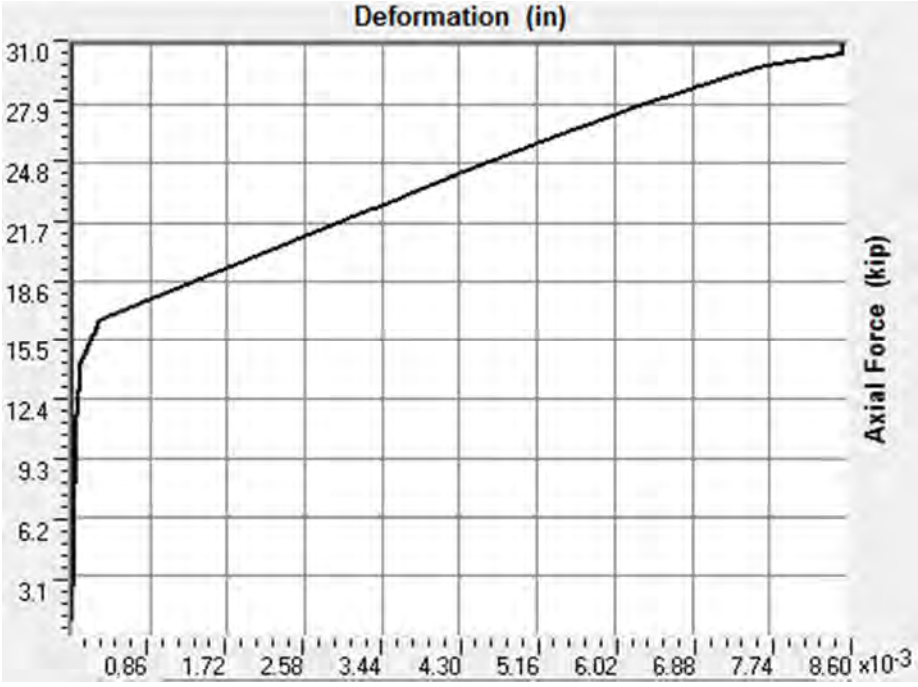


Figure 5-6 (a) Moment-rotation relationship of the plastic fiber hinge at apex of arch; (b) Corresponding axial load in the hinge

When stain hardening of the steel was considered, the pushover curve changed to that shown in Figure 5-7; the yield plateau, for the applied forces that existed at

development of the plastic mechanism in Figure 5-4, no longer exists. The force can be applied before the strain hardening in the hinge happens is 13.8 kips with a displacement of 0.11 in. The moment diagram shown in Figure 5-8 corresponds to the point when the largest moment in the first hinge was reached. The force applied to the arch for Figure 5-8 was 20.2 kips, with a corresponding displacement at the loading point of 0.23 in. Note that this strength is 49.6% more than what was obtained in the analysis considering an elasto-plastic steel material (compared with the largest moment reached in the first hinges in the bilinear model).

Figure 5-9 shows the moment-rotation relationship of the first hinge in the middle of the arch model. The analysis stops when the specified maximum strain of 0.17 was reached in the hinge at the apex of the arch (no other plastic hinges had yet developed in the rest of the arch at that point).

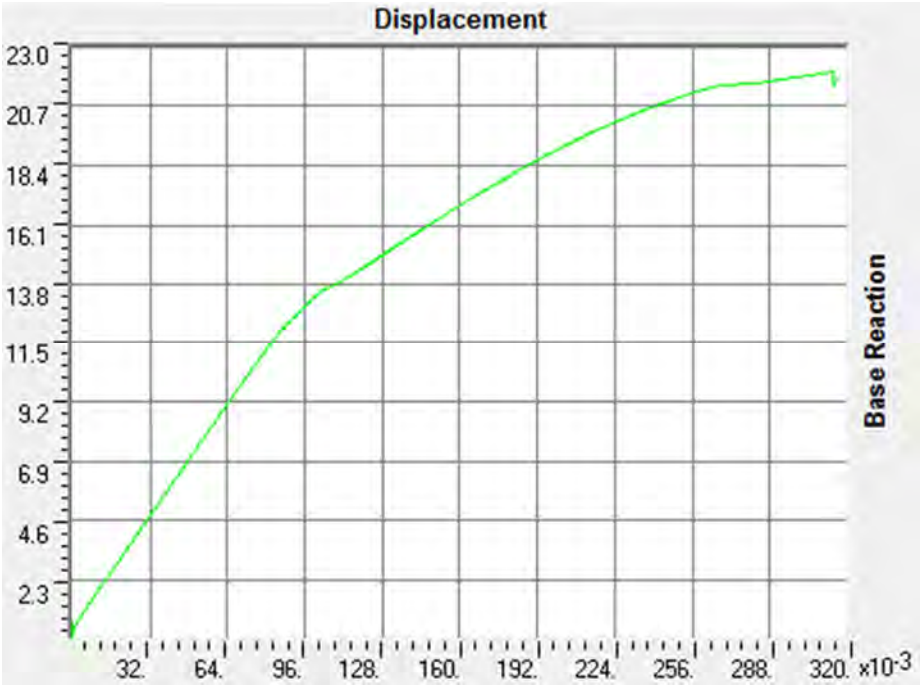


Figure 5-7 Pushover curve of the arch structure

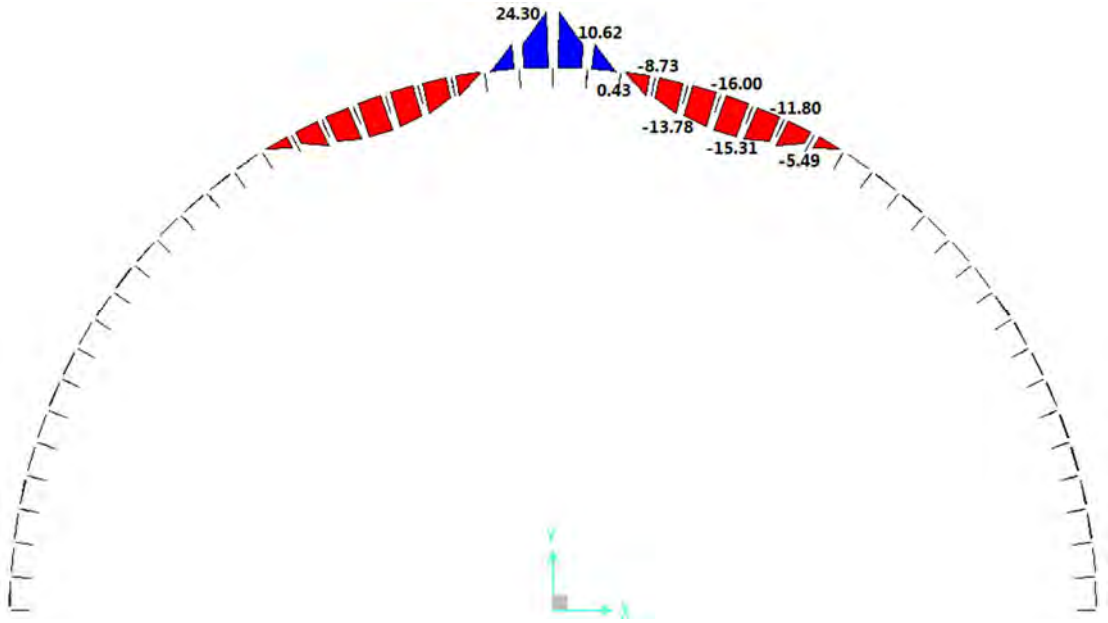


Figure 5-8 Moment diagram of the arch model corresponding to the maximum moment happened in the first hinge

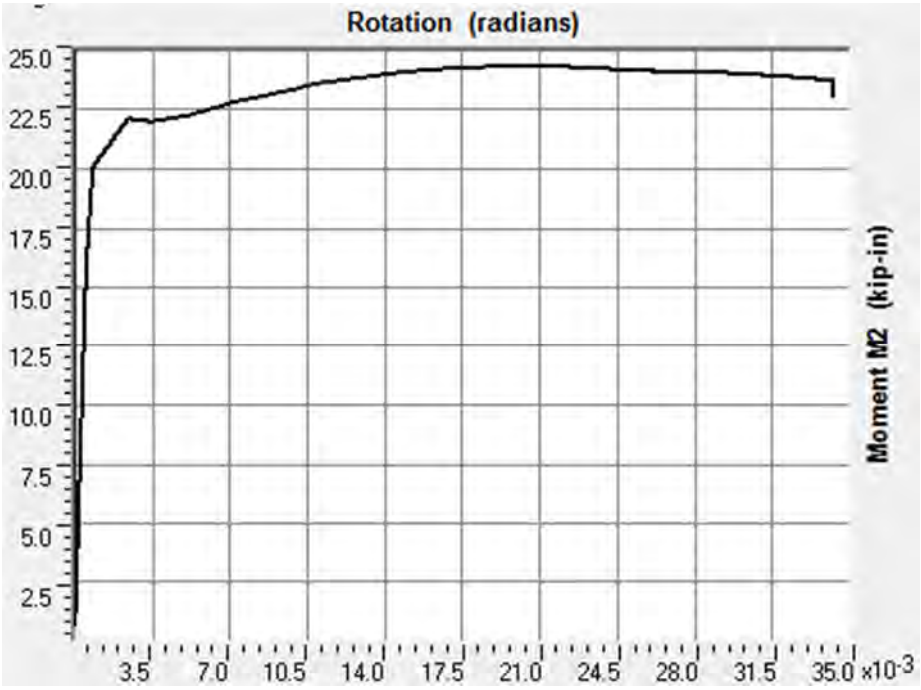


Figure 5-9 Moment-rotation relationship of the first plastic fiber hinge at the center of the arch model

**2) CFT column with 32 in diameter and 0.75 in thickness**

The arch model with a diameter of 32 in diameter, and a rectangular section of 0.75 in

(thickness) by 1 in (unit length) is built to have 50 frame elements, similar to the previous example. The bilinear properties of the steel shell are used (Figure 5-3), and the force versus displacement at the load point resulting from the pushover analysis, is shown in Figure 5-10. The maximum load that can be applied to the structure under this condition is 10.86 kips/in, corresponding to a displacement at the loading point of 0.215 in.

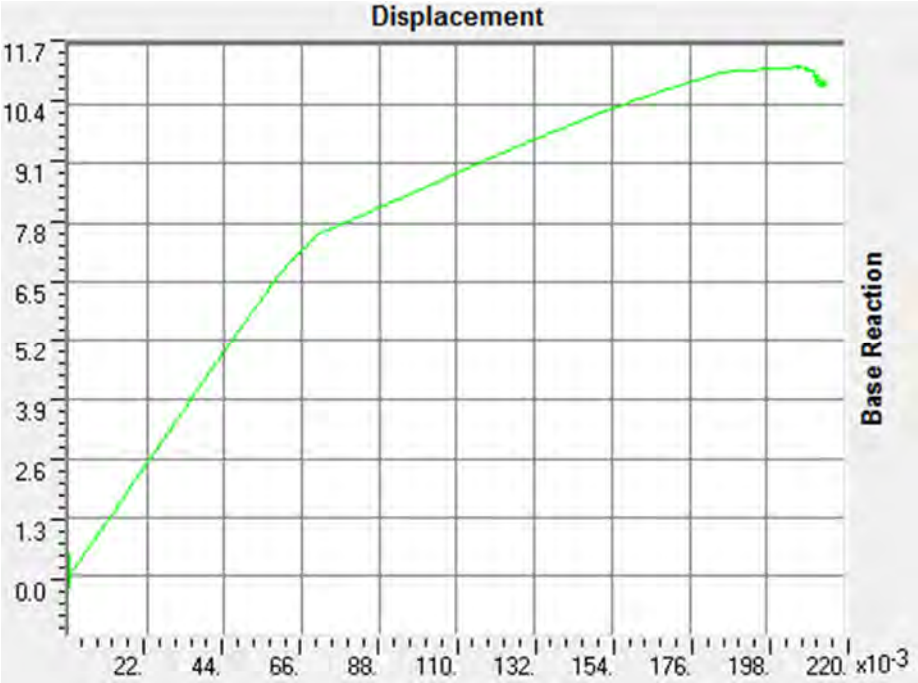


Figure 5-10 Pushover curve of the arch structure for bilinear steel material

The moment diagram shown in Figure 5-11a corresponds to the case when first plastic hinges develop. The plastic hinges also locate at the apex of the arch, where frame members 25 and 26 meet (frame element numbers are labeled in Figure 5-1). Significant moments also only develop in nine frame elements on each side from the point where the load is applied (the moment in the other frame elements is negligible). The corresponding force applied to the arch is 7.65 kips, with a displacement at the loading point of 0.074 in when the largest moment is reached at the first hinges. Upon increased loading, the next plastic hinges to form occur at the intersection of frame elements 19 and 20, and, symmetrically frame elements 31 and 32, as shown in Figure 5-11b. The corresponding force applied to the arch is 11.10 kips, with a

displacement at the loading point of 0.186 in. The analysis stopped at an applied force of 10.86 kips and corresponding displacement at the loading point of 0.215 in, when the strain limit of 0.17 (specified in the steel stress-strain material properties) was reached. The corresponding moment diagram is shown in Figure 5-11c.

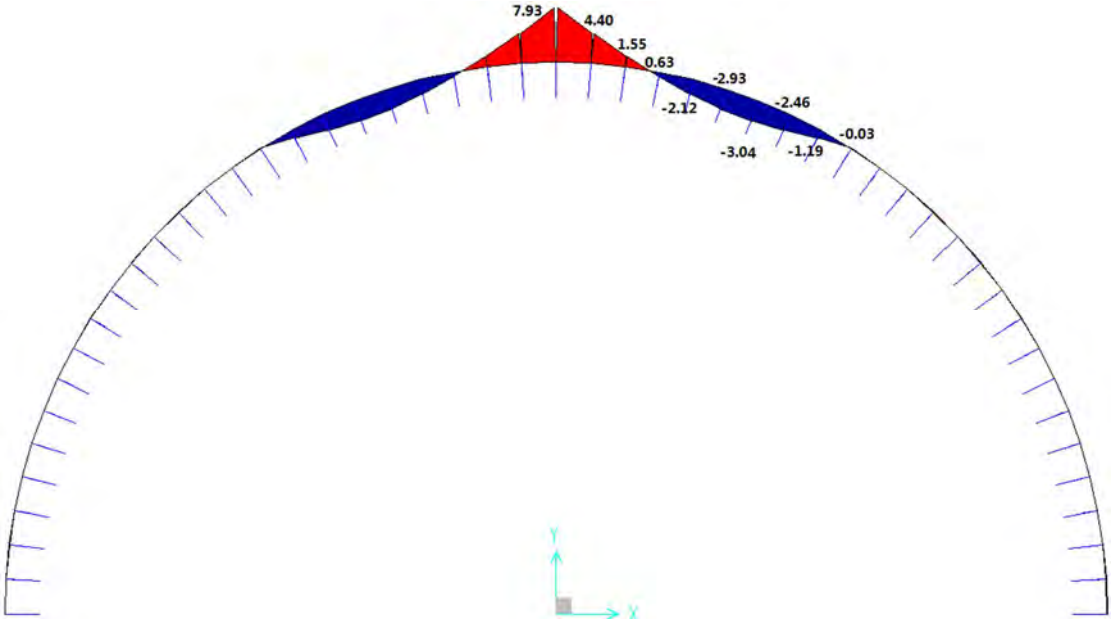


Figure 5-11 (a) Moment diagram of the arch model corresponding to the maximum moment at the first hinge93

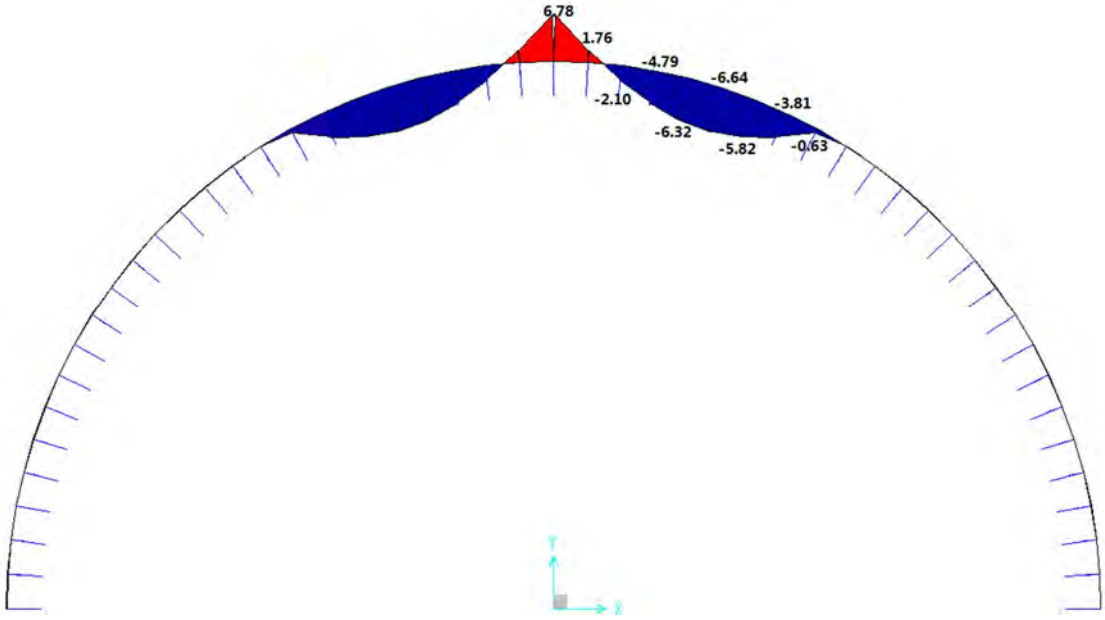


Figure 5-11 (b) Moment diagram of the arch model corresponding to the maximum hinge at the second hinge 233

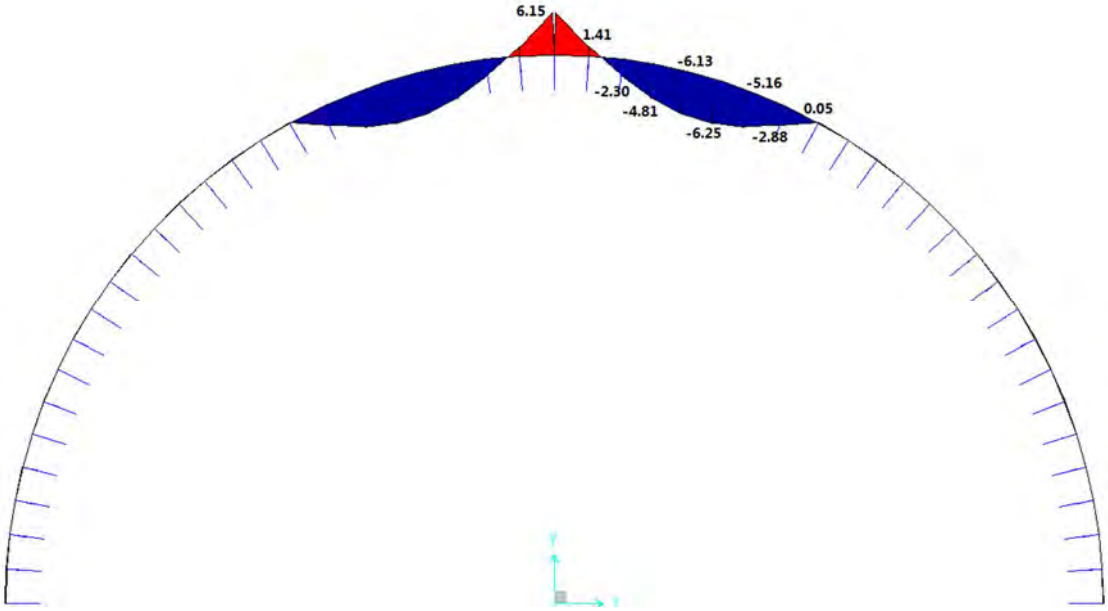


Figure 5-11 (c) Moment diagram of the arch model corresponding to the end of pushover analysis

Small decrease value of the plastic moment in the first hinge was due to moment-axial force interaction and changes in axial forces in the arch (this phenomenon can be observed by comparing the plastic moment values in Figures 5-11a, b and c). The moment-rotation relationship of the first hinge is shown in Figure 5-12. A decrease of the hinge moment capacity is observed to occur as the applied load increases after the section has reached its moment capacity.

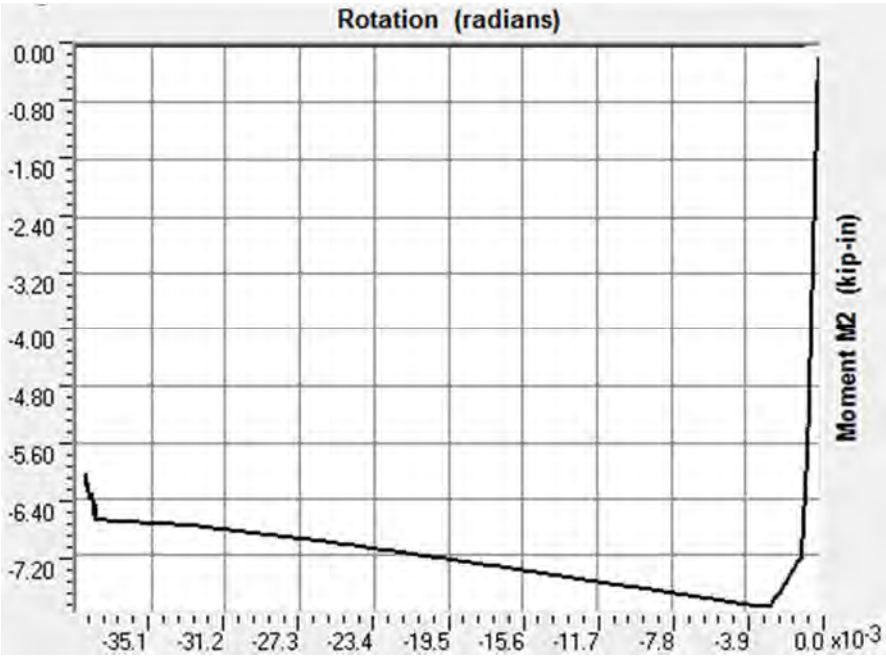


(a)

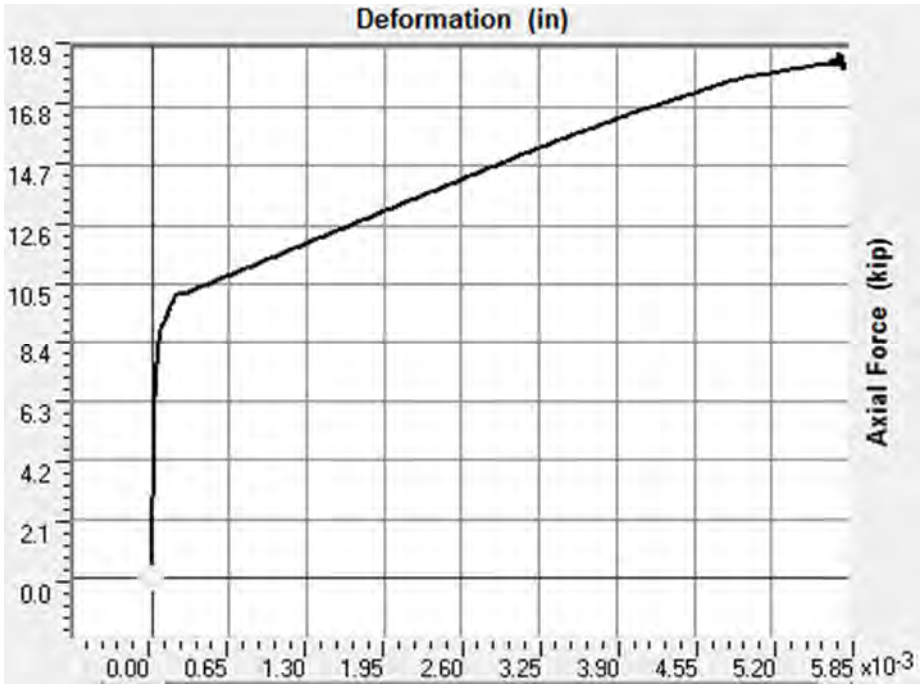


Figure 5-12 (a) Moment-rotation relationship of the plastic fiber hinge at apex of arch; (b) Corresponding axial load in the hinge

When stain hardening of the steel was considered, the pushover curve changed to that shown in Figure 5-13; the yielding plateau for the applied forces that existed at development of the plastic mechanism in Figure 5-10, no longer exists. The moment diagram shown in Figure 5-14 corresponds to the point when the largest moment was reached, as the first plastic hinge developed in the middle of the arch. The force applied to the arch is 11.61 kips with corresponding displacement at the loading point of 0.165 in for Figure 5-13. Note that this strength is 51.7% more than what was obtained in the analysis considering an elasto-plastic steel material (compared with the largest moment reached in the first hinges in the bilinear model).

Figure 5-15 shows the moment-rotation relationship of the first hinge in the middle of the arch model. The analysis also stops when the specified maximum strain of 0.17 was reached in the hinge at the apex of the arch (no other plastic hinges had yet

developed in the rest of the arch at that point).

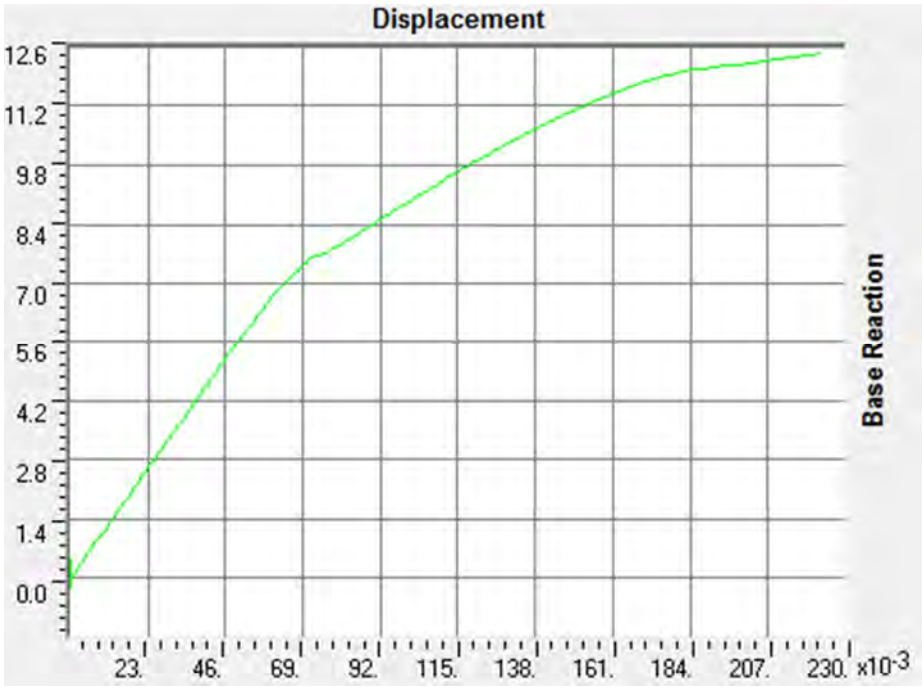


Figure 5-13 Pushover curve of the arch structure

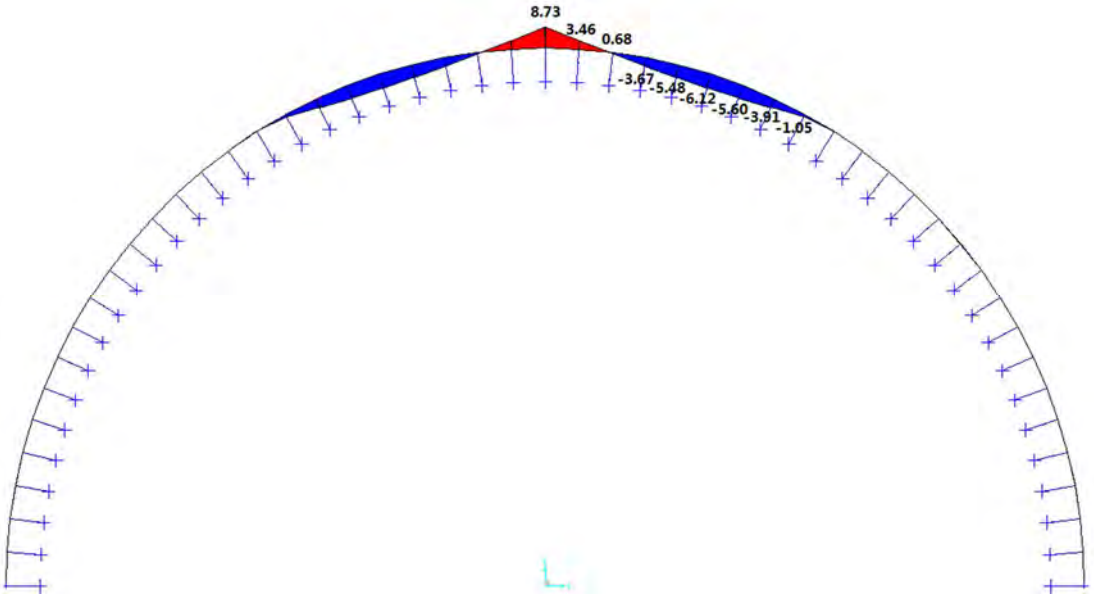


Figure 5-14 Moment diagram of the arch model corresponding to the maximum moment happened in the first hinge

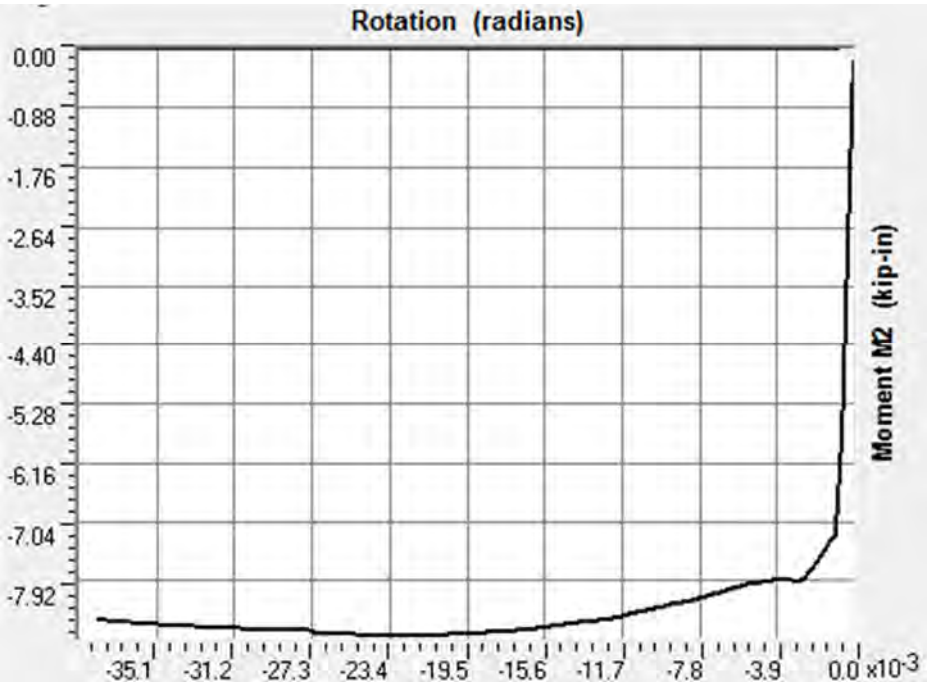


Figure 5-15 Moment-rotation relationship of the first plastic fiber hinge at the center of the arch model

Note that the analyses presented neglect the presence of axial stresses simultaneously acting along the longitudinal axis of the CFT column. This is a reasonable assumption provided that the steel shell of the CFT columns is not near yielding in that longitudinal direction (based on the von Mises yield criteria). This assumption could be revisited in future studies.

### 5.1.3. Connection Design

Connection of a BRB to a column could be done by transferring the load to the column, to the foundation, or both. The connection of the BRB to the CFT column considered here is assumed to be entirely accomplished through a gusset plate, welded to the CFT column, and schematically circled in red as shown in Figure 5-16.

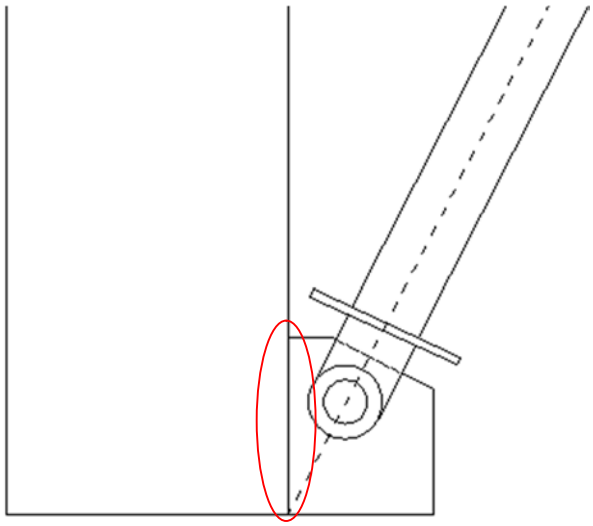

Figure 5-16 BRB connected with the CFT column through the gusset plate

(1) Two-CFT-column bent with BRBs

For the single inclined BRB case, the largest tensile force produced by the BRB is 1270 kips. The corresponding horizontal and vertical force components are 941.07 kips and 853.44 kips. For the distributed strength of 20.2 kip/in calculated above for tension perpendicular to the steel shell (at first plastic hinging considering strain hardening), a gusset plate of 47 in would be required to resist the above forces.

Note that the model presented in the previous section only accounted for a tensile load applied to the CFT. For the gusset connection described above, the steel shell would also be subjected to shear forces. To account for the presence of the shear stress caused by the vertical component of the force from the gusset plate, the tensile strength of the steel shell needs to be reduced. For a thickness of the steel shell of 1.25 in, assuming a shear failure surface in the CFT around the perimeter of the gusset, the area of the steel shell subjected to the shear force from the gusset plate is 117.5 $in^2$. The corresponding shear stress in the steel shell is 7.26 ksi. According to the von Mises yielding criterion, the tensile strength of the steel shell is reduced from 60 ksi to 58.67 ksi. Such a slight reduction is negligible.

For the two columns with chevron BRB case, the largest tension force in the BRB is 973.97 kips. The corresponding horizontal and vertical force components are 470.43 kips and 853.44 kips. A corresponding gusset plate should have a length of 24 in.

(2) Box-pier bent with BRBs

The largest tensile force produced by the BRB is 295.8 kips. The corresponding horizontal and vertical force components are 229.54 kips and 186.65kips. Based on the distributed strength of 11.61 kip/in calculated above for tension perpendicular to the steel shell (at first plastic hinging considering strain hardening), a gusset plate of 20 in would be required to resist the above forces. For the gusset connection described above, the steel shell would also be subjected to shear forces. To account for the presence of the shear stress caused by the vertical component of the force from the gusset plate, the tensile strength of the steel shell needs to be reduced. For a thickness of the steel shell of 0.75 in, assuming a shear failure surface in the CFT around the perimeter of the gusset, the area of the steel shell subjected to the shear force from the gusset plate is 30 $in^2$. The corresponding shear stress in the steel shell is 6.22 ksi. According to the von Mises yielding criterion, the tensile strength of the steel shell is reduced from 60 ksi to 59.02 ksi. Such a slight reduction is negligible.

## 5.2 Anchor Bolts

First the strength of the head studs connection under tensile and shear loading is shown respectively. The numbers of headed studs are calculated for a specific connection, to investigate the applicability of this form of connection for the situation at hand.

Note that headed studs can be designed in accordance with ACI 318-08 Appendix D, PCI design handbook (2004) or AISC (2010). ACI 318-08 does not apply to

reinforcement used as part of embedment, therefore the strength calculated is based on the resistance from the concrete surroundings and the strength of the anchor itself.

### 5.2.1. General

There are mainly two types of headed studs. PCI (2004) specifies minimum tensile and yield strength for headed studs in Table 5-1. Type A headed studs are for general purpose of any type and size. Type A studs cannot be used in shear transfer of composite beam design and construction because of their lower capacity. The available diameters of type A headed-studs are 1/4" and 3/8". The shank diameters of type B shear studs are available in the range from 1/4" to 7/8". Dimensions of example anchor studs are shown in Table 5-2.

The respective tensile and shear force capacity of single cast-in-place headed stud is first calculated, according to ACI 318-08 and PCI (2004). In order to get the largest capacity of one single anchor, the largest shank diameter $d_0$ of 7/8" of type B headed stud in Table 5-2 is used. The area of that steel stud is 0.6 $in^2$. The design compressive strength of normal weight, uncracked concrete $f_c^{'}$ is taken here as 5000 psi. The concrete density factor $\lambda$ is 1. The headed studs are installed without supplementary reinforcements. The design ultimate strength of the anchor steel $F_{ut}$ is 65 ksi, and the yield strength $F_y$ is 51 ksi.

Table 5-1 Minimum Mechanical Property Requirements for Headed Studs (PCI Design Handbook, 2004)

| **Property** (Diameter) | **Type A** (1/4 and 3/8 in.) | **Type B** (1/2 to 1 in.) |
|---|---|---|
| Tensile Strength (min.) | 61,000 psi | 65,000 psi |
| Yield Strength (0.2% offset) | 49,000 psi | 51,000 psi |
| Elongation (min. % in 2 in.) | 17% | 20% |
| Reduction of area (min.) | 50% | 50% |

Table 5-2 Dimensions of headed studs (PCI Design Handbook, 2004)

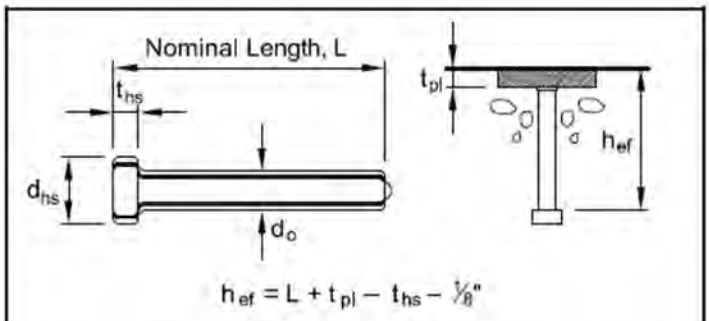


| Shank Diameter, $d_o$ (in.) | Shank Area, $A_{se}$ ($in.^2$) | Head Diameter, $d_{hs}$ (in.) | Head Thickness, $t_{hs}$ (in.) | Bearing Area, $A_{brg}$ ($in.^2$) |
|---|---|---|---|---|
| 1/4 | 0.05 | 1/2 | 3/16 | 0.15 |
| 3/8 | 0.11 | 3/4 | 9/32 | 0.33 |
| 1/2 | 0.20 | 1 | 5/16 | 0.59 |
| 5/8 | 0.31 | 1 1/4 | 5/16 | 0.92 |
| 3/4 | 0.44 | 1 1/4 | 3/8 | 0.79 |
| 7/8 | 0.60 | 1 3/8 | 3/8 | 0.88 |

## 5.2.2. Strength Calculation

Effective embedment length is used as a controlled parameter to compare different strengths calculated below. The headed stud can be considered "in the field" for the current application. The tensile and shear force are assumed to be applied

concentrically to the single headed stud. Equations using approaches from ACI318 and PCI (2004) are calculated and compared. Different strength calculated below corresponds to the various types of steel and concrete failure modes defined in ACI 318 Appendix D for a single anchor shown in Figure 2-14.

(1) Steel anchor strength

$$F_s = A_{se} F_{ut} = 0.6 \times 65 = 39\,\text{ksi}$$

The reduction factors for steel failure are 0.75 for tension, and 0.65 for shear respectively. Therefore, the corresponding tensile and shear strength of the anchor failing in steel shank is 29.25 kips and 25.35 kips, respectively.

(2) Concrete breakout strength in tension per ACI 318-08

$$N_b = k_c \lambda \sqrt{f_c'} h_{ef}^{1.5} = 24 \times \sqrt{5000} \times h_{ef}^{1.5} = 1.70 h_{ef}^{1.5}$$

where: $k_c$ = 24 for cast-in anchors

(3) Concrete breakout strength in shear per ACI 318-08

$$V_b = 2 \times 7 \times \left( \frac{l_e}{d_0} \right)^{0.2} \sqrt{d_0} \times \lambda \times \sqrt{f_c'} \times (c_{a1})^{1.5} = 14 \times (h_{ef})^{0.2} \times \left( 7/8 \right)^{0.3} \times \sqrt{5000} \times (12)^{1.5}$$

$$= 39.54 h_{ef}^{0.2}$$

where: $l_e$ = the load-bearing length of the anchor for shear, equal to $h_{ef}$ for anchors with a constant stiffness over the full length of embedded sections

(4) Concrete pullout strength in tension per ACI 318-08

$$N_{pn} = 8 A_{brg} f_c' = 8 \times 0.88 \times 5000 = 35.20 kips$$

where: $A_{brg}$ =the bearing area of the headed stud head in tension, as listed in Table 5-2;

(5) Pryout strength for anchors in shear per ACI 318-08

$$V_{cp} = k_{cp} N_b$$

where: $k_{cp}$ =1.0 for $h_{ef} < 2.5$ in;

=2.0 for $h_{ef} \geq 2.5$ in.

(6) Concrete breakout strength in tension per PCI (2004)

$$N_b = 3.33\lambda\sqrt{\frac{f_c^{'}}{h_{ef}}}\times 9h_{ef}^2 = 3.33\times\sqrt{\frac{5000}{h_{ef}}}\times 9h_{ef}^2 = 2.12h_{ef}^{1.5}$$

(7) Concrete breakout strength in shear per PCI (2004)

$$V_b = 87\lambda\sqrt{f_c^{'}}\left(c_{a1}\right)^{1.33}\left(d_0\right)^{0.75} = 87\times\sqrt{5000}\times\left(12\right)^{0.75}\times\left(7/8\right)^{0.75} = 35.88kips$$

The side to edge distance of anchors loaded in shear parallel to the edge $c_{a1}$ is taken as $6d_0 = 5.25"$.

(8) Concrete pullout strength in tension per PCI (2004)

$$N_{pn} = 11.2A_{brg}f_c^{'} = 11.2\times 0.88\times 5000 = 49.28kips$$

(9) Pryout strength for anchors in shear per PCI (2004)

$$V_{cp} = 215\sqrt{f_c^{'}}\times\psi_y\times\left(d_0\right)^{1.5}\times\left(h_{ef}\right)^{0.5} = 215\times\sqrt{5000}\times 0.53\times\left(7/8\right)^{1.5}h_{ef}^{0.5}$$

$$= 6.59h_{ef}^{0.5}$$

$$h_{ef} \le 4.5d_0$$

where: $\psi_y = \frac{\sqrt{y}}{4d_0}$ for $\frac{y}{d_0} \le 20$, or =1.0 for y =0; y = center-to-center spacing of studs in direction of load, which is the minimum center-to-center distance of the headed stud, taken as $4d_0 = 3.5"$

Figure 5-17 plots the steel and concrete strength calculated per the above equations, for embedment lengths ranging from 0 to 8.75 in (10 times of the shank diameter). The steel strength of the anchor remains the same no matter how large $h_{ef}$ is, while the concrete strength increases when the anchor is embedded deeper. The concrete strength shown are for a strength reduction factor ($\phi$) of 0.7. The steel strength reduction factor is already included in the calculation.

For anchors strengths calculated per PCI (2004), the anchor is certain to fail in the steel shank if the embedment length is larger than 7.375 in under tensile force. Per ACI 318-08, the concrete breakout strength controls the strength for anchors loaded under tensile force for embedment length less than 7.75 in. Otherwise, the concrete

pullout strength controls no matter how deep the embedment length is beyond 7.75 in. Anchors would fail in steel shank under shear forces, if the embedment length is larger than 4.875 in and 4 in per ACI 318-08 and PCI (2004), respectively.

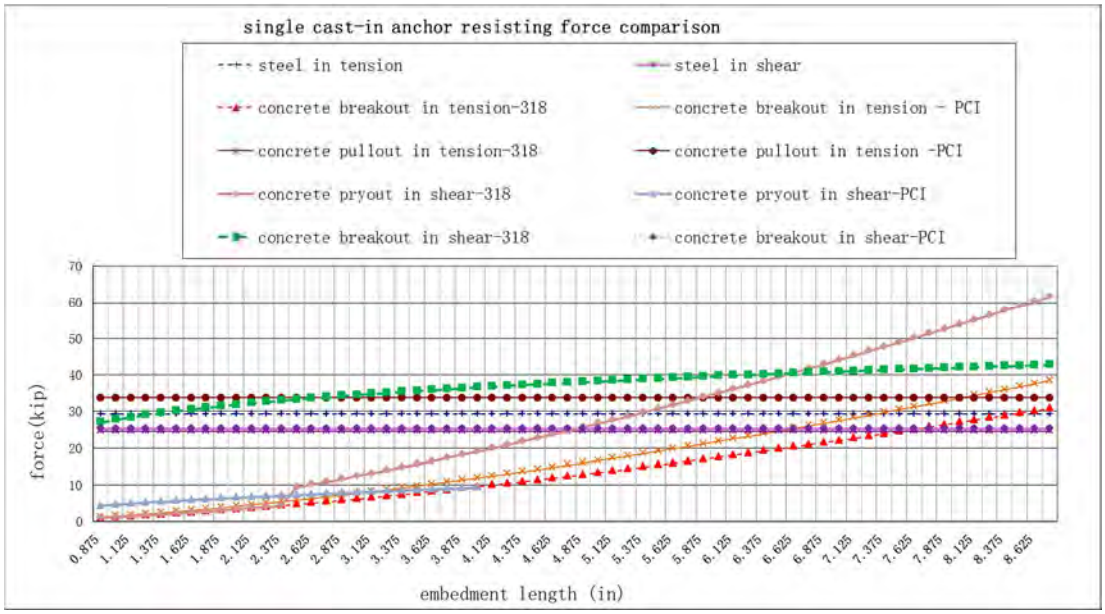


Figure 5-17 Single headed studs resisting strength comparison

Based on the values shown in Figure 5-17, the strength of a single stud with 7/8 in diameter is summarized in Table 5-3 if the embedment length is larger than the specified length in the brackets in the table header. For ACI 318-08, the tension and shear strength of a single stud having embedment length greater than 7.75" is 24.64 kips and 25.35 kips. For PCI (2004), the single stud with embedment length larger than 7.375" has the tensile and shear strength of 29.25 kips and 25.35 kips. The strengths from PCI (2004) will be used to design the layout of the headed studs.

Table 5-3 Shear and tension force sustained by headed-studs

| | ACI 318-08 (Embedment length larger than 7.75 in) | PCI (2004) (Embedment length larger than 7.375 in) |
|---|---|---|
| Tension strength | 24.64 kips | 29.25 kips |
| Shear strength | 25.35 kips | 25.35 kips |

## 5.2.3. Connection Evaluation

This section illustrates sample BRB connection designs using headed studs. The case of two columns with chevron BRBs and box-pier bent with BRBs are presented. The layout and geometry of the resulting connection is shown at the end of the connection design process. The evaluation is for BRBs under tensile force, since the tension and shear force design for the connection with the foundation or the cap beam governs, rather than the combined compression and shear force.

**(1) Two-CFT-column bent with chevron BRBs**

a. Bottom BRB connection with the footing (BRB in tension)

The tensile force in the BRB to transfer is 973.97 kips. The corresponding horizontal and vertical force components are 470.43 kips and 853.44 kips, which would exert tensile and shear forces of 853.44 kips and 470 kips, respectively, on the footing. It assumes that the entire force is to be transferred to the footing (e.g. none transferred to the column).

From the precious section, the tension and shear strength of individual headed stud are 29.25 kips and 25.35 kips, respectively. The interaction equation for tensile and shear forces acting on a headed stud in both ACI318-08 and PCI(2004) , is:

$$\left(\frac{N_u}{\phi N_n}\right)^{\frac{5}{3}} + \left(\frac{V_u}{\phi V_n}\right)^{\frac{5}{3}} \leq 1.0 \qquad (5\text{-}1)$$

where: $N_u$ is the applied tension force; $V_u$ is the applied shear force; $\phi N_n$ is the reduced tension force capacity; $\phi V_n$ is the reduced shear force capacity

The resulting total number of headed studs needed to transfer the forces is calculated to be 40. Figure 5-18a illustrates the headed studs configuration at the connections, from a top view. A side view is shown in Figure 5-18b. Note that the distance

between the headed studs and the minimum side distance with the footing are identified in Figure 5-18. The center-to-center stud distance is chosen based on the ACI 318-08 requirement of at least 3 times of the embedment length (to exclude the group effect of the headed studs). The side distance is 1.5 times of the embedment length.

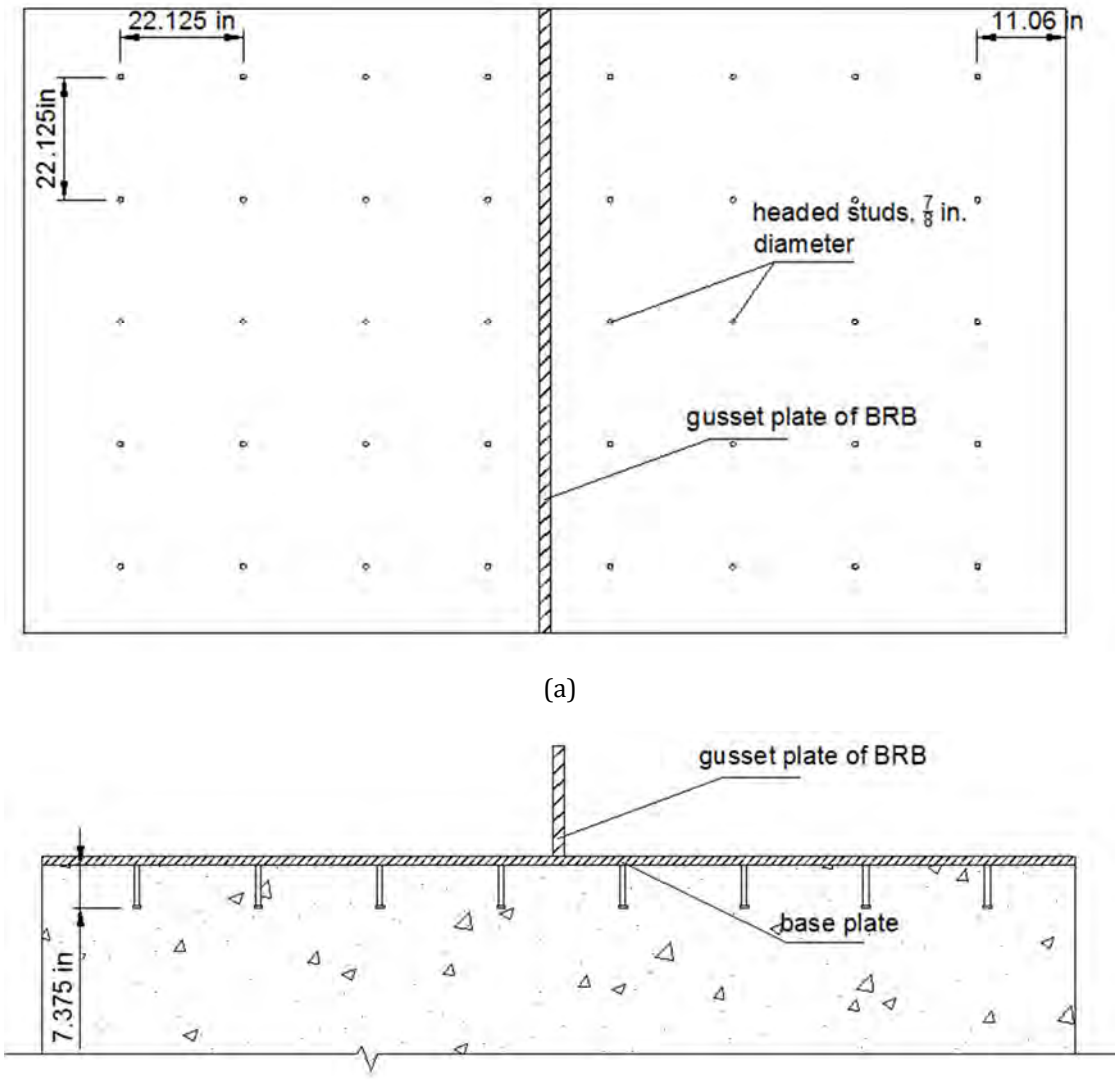


Figure 5-18 (a) Top view of BRB gusset plate connected with foundation (b) Side view

The eccentricity of the loading to the headed studs is not considered here. The base plate is not designed. The welding between the BRB gusset plate and the base plate is not evaluated either.

The detail shown in Figure 5-18 indicate that an unrealistically high number of studs would be needed to transfer the BRB forces, making the use of headed studs impractical for connections in this application.

b. BRB connections with cap beam

The largest tensile and shear forces in the BRBs are 973.97 kips and 1083 kips, respectively. The resultant of these forces acting simultaneously at the point where both BRB meet at the underside of the bent cap would exert compression and shear forces of 95 kips and 992 kips, respectively. The compressive force is transferred to the bent cap directly without mobilizing the studs. Therefore, the connection need only resist the resultant shear force, and is designed based on the shear capacity of the headed studs of 25.35 kips.

The total number of headed studs needed is again 40, resulting in the same layout of the studs shown in Figure 5-18. Again, for this connection design, the large a number of headed studs required for the connection design to work make it not feasible to implement.

**(2) Box-pier bent with BRBs**

The largest tensile force in the BRB to transfer is 295.8 kips. The corresponding horizontal and vertical force component is 229.54 kips and 186.65kips, which would exert tensile and shear force of 186.65 kips and 229.54 kips, respectively on the footing. It assumes that the entire force is to be transferred to the footing (e.g. none transferred to the column).

Again, the tension and shear capacity of a single headed stud of 29.25 kips and 25.35 kips is used. Using the same interaction Equation 5-1, the total number of headed studs needed to transfer the forces is calculated to be 12. Figure 5-19a illustrates the

headed studs configuration at the connections, from top view. A side view is shown in Figure 5-19b. Note that the distance between the headed studs and the minimum side distance with the footing are identified in Figure 5-19. The center-to-center stud distance is chosen based on the ACI 318-08 requirement of at least 3 times of the embedment length (to exclude the group effect of the headed studs). The side distance is 1.5 times of the embedment length.

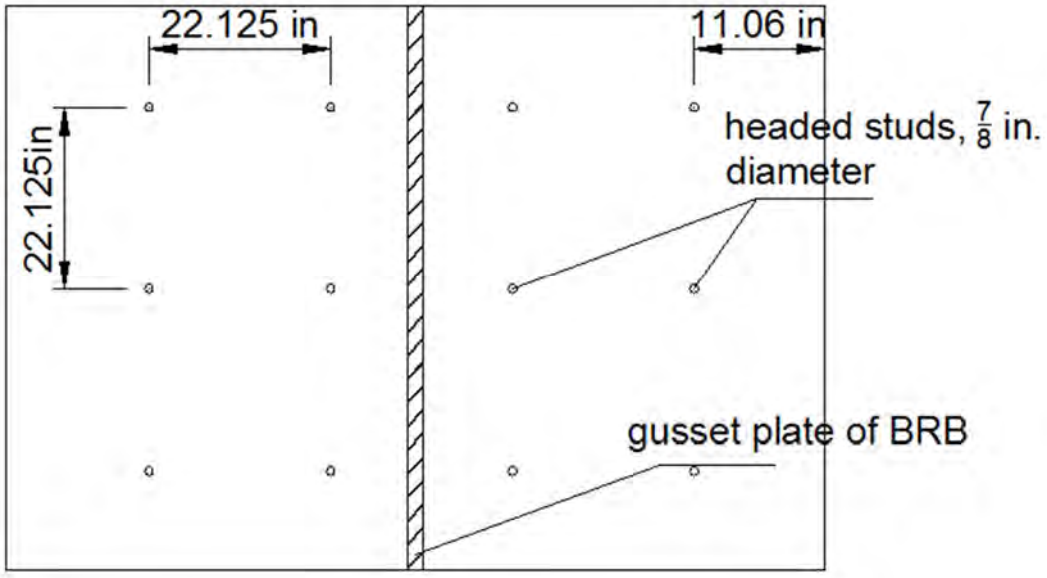


(a)

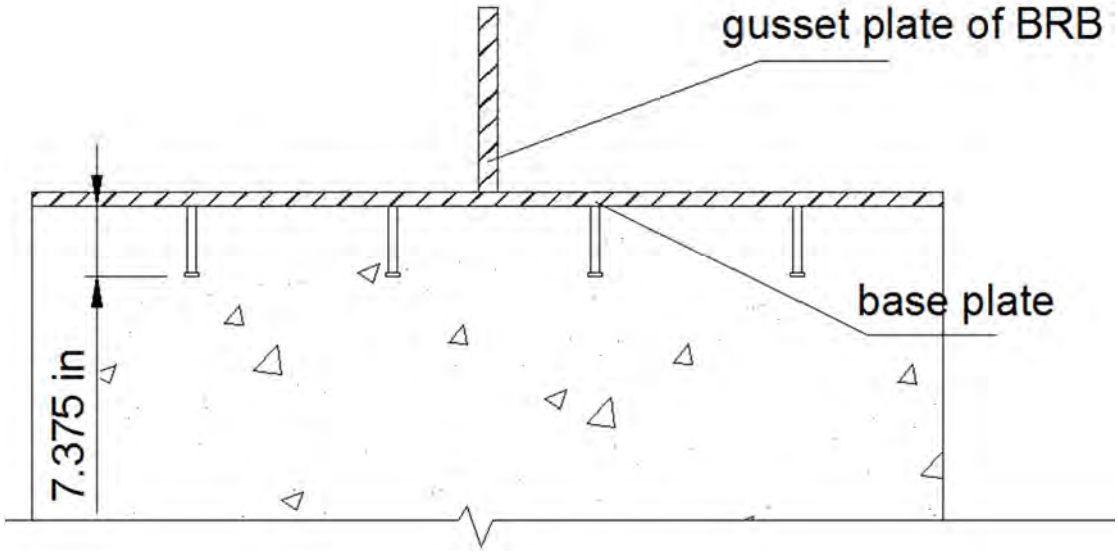


(b)

Figure 5-19 (a) Top view of BRB gusset plate connected with foundation (b) Side view

The eccentricity of the loading to the headed studs is not considered here. The base plate is not designed. The welding between the BRB gusset plate and the base plate is not evaluated either. The design is shown for the footing connection. For the cap beam connection, the design remains the same but upside down.

For this connection design, the headed studs design works. However, the design is not complete, as the connection between the CFT column and the footing has not considered yet. Depending on the detail used, it might require adjusting the locations of the headed studs, leaving less space for the headed studs to be installed.

## 5.3 Anchor Rods

The connections of steel plates with concrete footing or cap beam can be accomplished with embedded anchor rods. This is similar to what is done with column base plate connection, when connecting a steel structure to its concrete foundation (as shown in Figure 5-20).

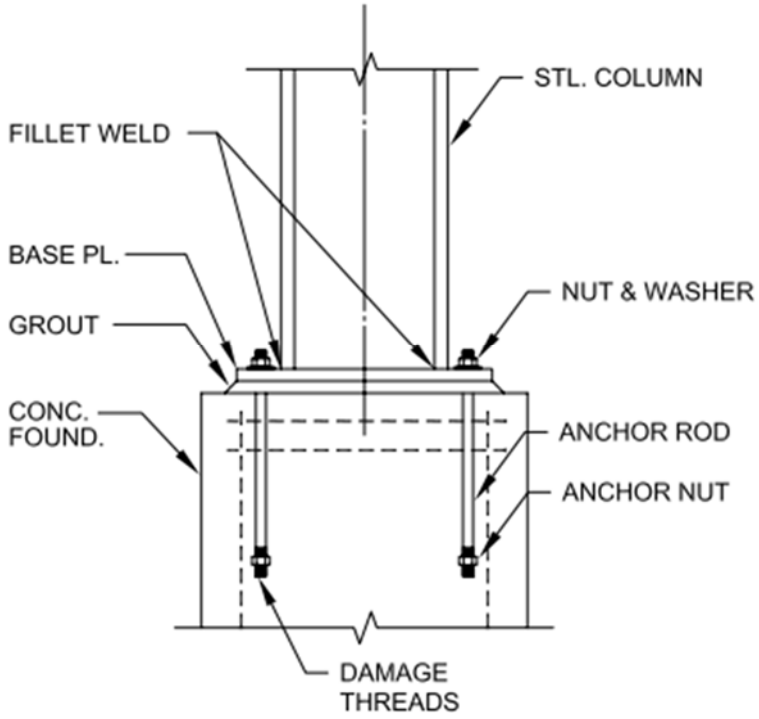


Figure 5-20 Column base connection components (Fisher, J.M. and Kloiber, L.A., 2006)

### 5.3.1. Materials and Types

Anchor rods are supplied in conformance with ASTM F1554 "Standard Specification for Anchor Bolts, Steel, 36, 55, and 105 ksi Yield Strength." ASTM F1554 provides for three different grades of anchor rods: Grade 36, Grade 55, and Grade 105. The specified minimum yield strength ($F_y$) and specified minimum tensile strength ($F_u$) for each grade are given in Table 5-4.

Table 5-4 Tensile Properties for Anchor Rods

| Tensile Property | ASTM F15544 Rod Grade 36 | ASTM F15544 Rod Grade 55 | ASTM F15544 Rod Grade 105 |
|---|---|---|---|
| Minimum Yield Strength $F_y$ (ksi) | 36 | 55 | 105 |
| Minimum Tensile Strength $F_u$ (ksi) | 58 | 75 | 125 |

The ASTM F 1554 Grade 36 rod of ¾ in diameter is recommended for most common applications. When more strength is required, increasing rod diameter up to about 2 in for ASTM F1554 Grade 36 is common practice before switching to a higher-strength material grade (Fisher and Kloiber, 2006). Anchor rod details typically provide ample threaded length, and it is recommended that threaded lengths be specified to be at least 3 in. The most common threaded anchor rods with nuts are used in this section to design the connections.

### 5.3.2. Connection Evaluation

This section illustrates simple design of BRBs connections using anchor rods for two cases: the two-column bent with chevron BRBs (with BRB force demand smaller than for the case of two-column bent with single BRB) and the box-pier bent with BRBs. Similar to the headed stud design, the design is only performed for the BRB in tension

connected to the foundation, and for the top BRB in tension connected with the cap beam.

Note that the connection of the CFT column to the footing or bent cap beam can be designed in many different ways to ensure that the force demand can be achieved. Examples can be found in Roeder and Lehman (2008), Fujikura, Bruneau, and Lopez-Garcia (2008).

**(1) Two-CFT-column bent with chevron BRBs**

a. Bottom BRB connection only with the footing (BRB in tension)

For the chevron BRB case, the tensile force applied by the BRB is 973.97 kips. The corresponding horizontal and vertical force components are 470.43 kips and 853.44 kips, respectively. This corresponds to tensile and shear force on the foundation of 853.44 kips and 470 kips, respectively.

Appendix D presents detailed calculations for the design of anchor rods according to the equations provided in ACI318-08 and AISC (2010). The resulting layout and geometry of the connection is shown in Figures 5-21a and b. Note that the plate thickness to allow engaging all anchor rods remains to be sized and would have to be much thicker than schematically shown in Figure 5-21.

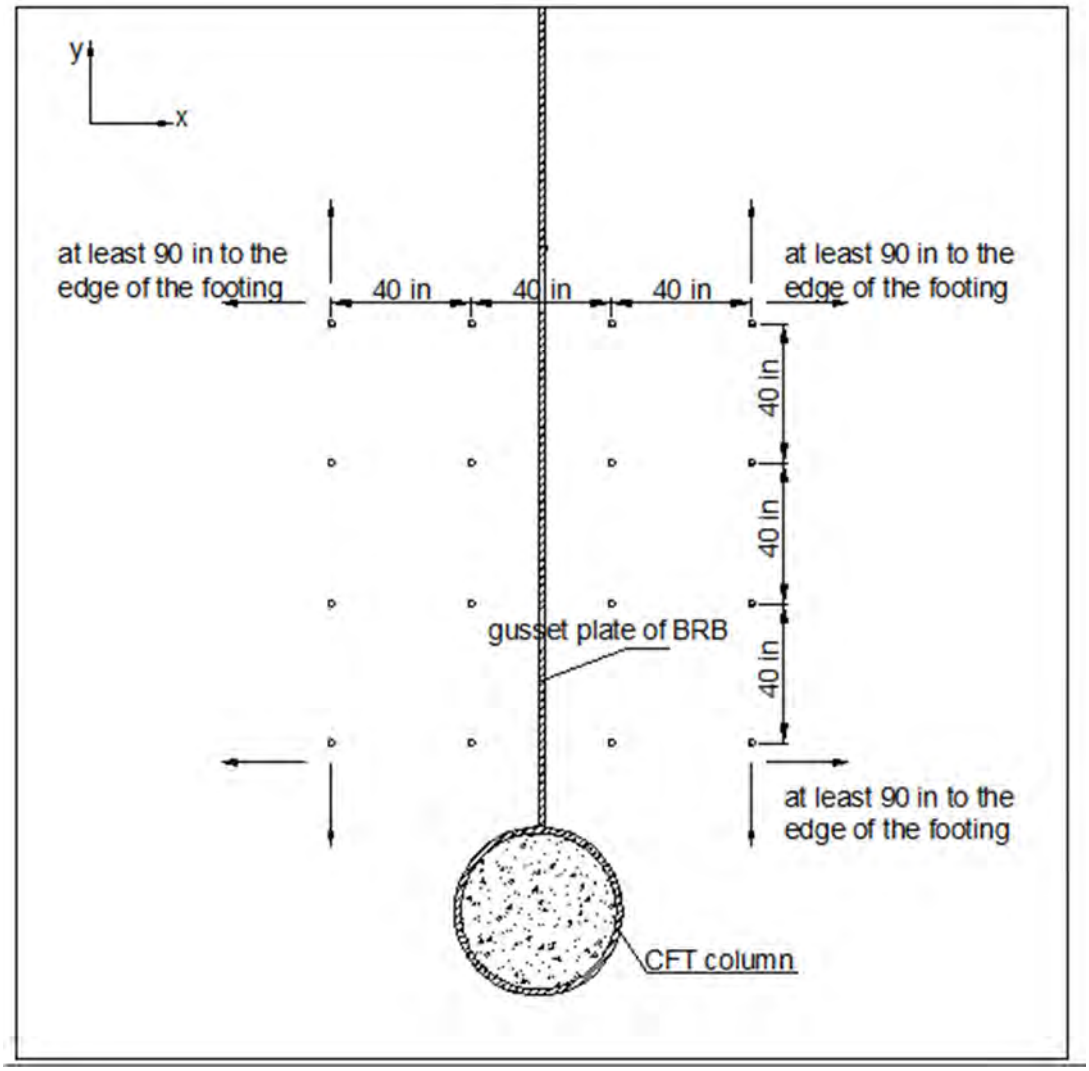


(a)

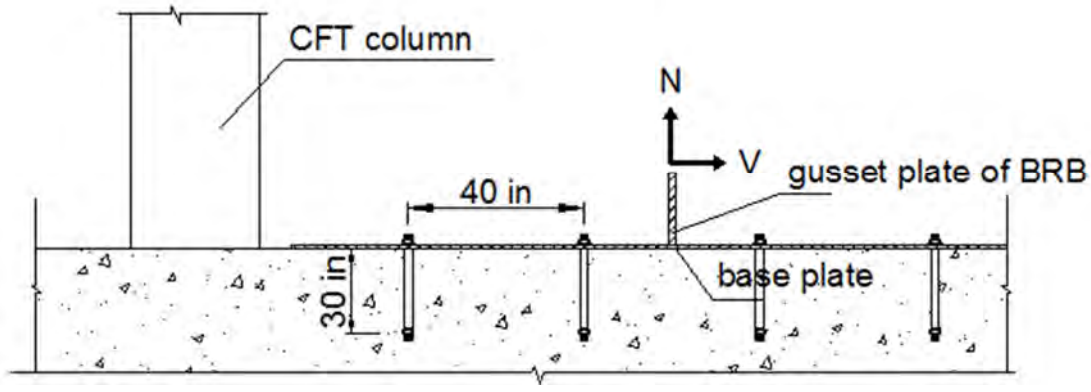


(b)

Figure 5-21 (a) Top view of BRB gusset plate connected with foundation (b) Side view

b. BRB connections with cap beam

The largest tensile and compressive forces in the BRBs are 973.97 kips and 1083 kips, respectively. The resultant of these forces acting simultaneously at the point where both BRB meet at the underside of the bent cap would exert compression and shear forces of 95 kips and 992 kips, respectively. The compression force is transferred to the bent cap directly without mobilizing the studs. Therefore, the connection need only resist the resultant shear force.

The calculation in Appendix D shows that the same anchor rod configuration as the BRB connected with the footing would be used, except that the distance of the anchor rod to the any edge would be 100 in instead of 90 in.

**(2) Box-pier bent with BRBs**

Similar to the headed stud design, the design is only performed for the BRB in tension connected to the foundation, and for the top BRBs in tension connected with the cap beam. The layout and geometry of the connection is shown in Figure 5-22 for the BRB and footing connection. For the cap beam connection, the design remains the same but upside down.

The tensile force applied by the BRB is 295.8 kips. The corresponding horizontal and vertical force components are 229.54 kips and 186.65kips, respectively. This corresponds to tensile and shear force on the foundation of 186.65 kips and 229.54 kips, respectively.

Appendix D presented detailed calculation for the design of anchor rods according to the equations provided in ACI318-08 and AISC (2010). The resulting layout and geometry of the connection is shown in Figures 5-22a and b.

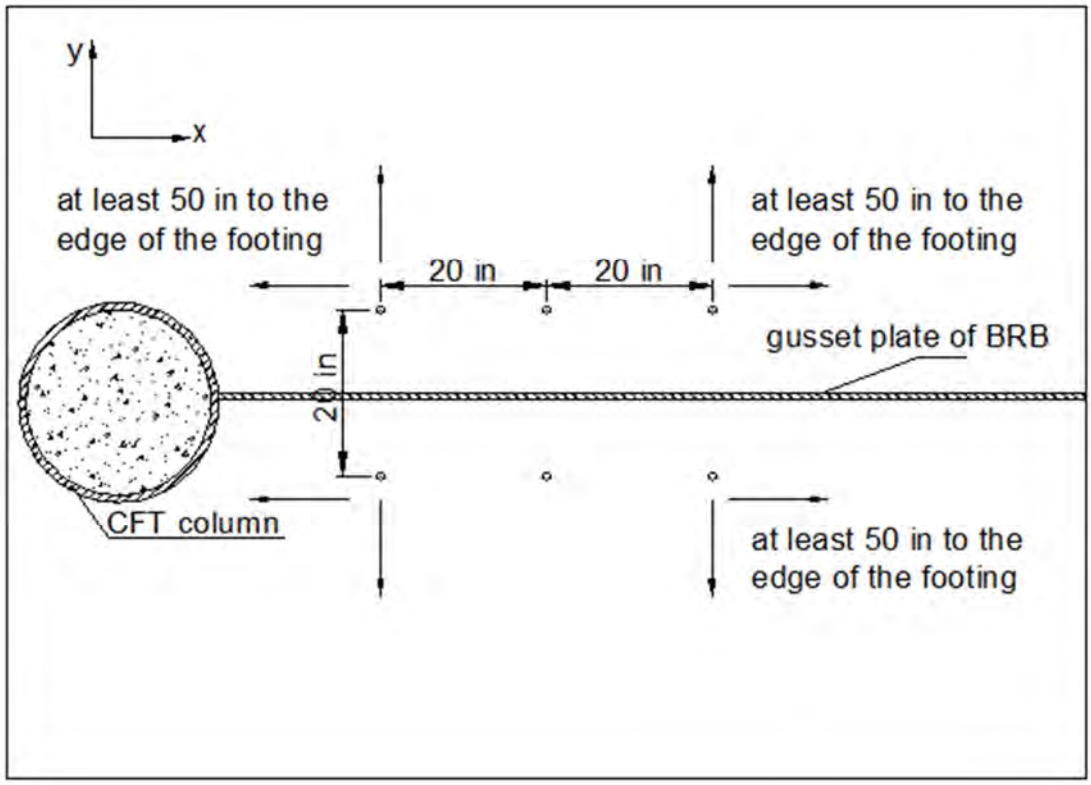


(a)

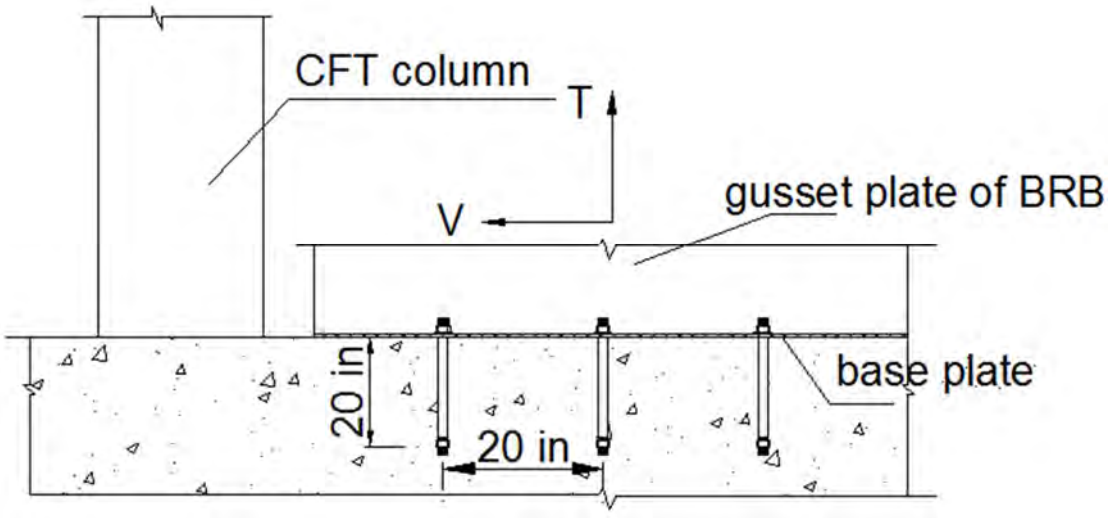


(b)

Figure 5-22 (a) Top view of BRB gusset plate connected with foundation (b) Side view

Note that for both cases, the plate thickness to allow engaging all anchor rods remains to be sized and would have to be thicker than schematically shown in Figures 5-21

and 5-22. The possibility of eccentricity of the loading to the anchor rods group is not considered here. The base plate has not been designed either. The welding between the BRB gusset plate and the base plate is not sized either. Not to mention that the above design is incomplete, as the connection between the CFT column and the footing has not been considered yet. Depending on the detail used, it might require adjusting the locations of the headed studs, leaving even less space for the anchor rods to be installed.

## 5.4 Conclusion

Three types of connections were used in this chapter to connect the BRB to different members of the bridge bent.

For the connection directly welding to the shell of the CFT, yield line analysis of the steel shell under the pulling force gave an estimate of the required length of the gusset plate of the BRB. The resulting design was found to be workable for both the two-column bent case and the box-pier case.

The headed studs and anchor bolts were designed for BRBs to be connected to the foundation or the cap beam. Note that results were derived for the case of chevron BRB configuration. It was found that an unrealistically high number of headed studs was required to transfer the BRB forces, making the use of headed studs impractical for connections in this application. Since the forces for the case of a single inclined BRB are larger than for the chevron BRBs for the two-CFT-column bent case, connections were not designed for that case. However, a headed stud connection was possible for the BRBs between the box pier columns due to the smaller BRB forces.

Using anchor rods to connect the BRB to the CFT column and the footing or cap

beam was found to be workable for both the chevron BRBs in the two-CFT-column bent case and box-pier bent case. Note that, the possibility of eccentricity of the loading to the headed studs or anchor rods group was not considered.

The connection designs considered in this chapter serve as examples to explore possible connection details that can work. The design was incomplete, as the connection between the CFT column and the footing has not been considered yet.

# Chapter 6 Conclusions

## 6.1 Conclusion

Research results presented in this report demonstrate that bridge bents using BRBs as SFs can be designed and be effective in improving seismic behavior. A conservative design objective of full elastic column response was considered in this study by limiting demands in columns to their yield moment ($M_y$). While this made design of the structural fuses more challenging, it remained possible to implement SFs in the cases considered.

Pushover analyses were performed using fundamental capacity design principles to investigate seismic demands on the columns for two proposed bridge bent configurations.

First, a two-column bent (considering single inclined BRB and inverted-V BRBs configurations) was studied. For that case, the SF concept modifies response of the bent to seismic excitation only in the transverse direction, which can be used in retrofitting of old bridges or new bridge constructions. This would have to be coupled with another system in the longitudinal direction (which could be SFs in series with Lock-up Devices connecting the bridge deck to the abutments, for example). While satisfactory design could be obtained for both BRB layouts considered, the difference between the single BRB case and the inverted-V BRBs case lies in the resulting smaller BRB sizes needed in the latter case (and correspondingly, smaller force demands on the connections). Compared with the single inclined BRB case, the force demand in the BRBs is reduced by 24% in the inverted-V BRBs case. Besides, the inverted-V brace configuration was found to be more beneficial since the forces developed in the BRBs are not transferred to the columns, thus resulting in smaller

column sizes (unless column sizes is governed by non-seismic load conditions). The BRB forces still have to be resisted by the foundations. The force demand on the foundation in the inverted-V BRBs case is smaller than that in the single inclined BRB case.

Second, a box-pier configuration with BRBs was considered. This design concept, applicable to new bridges, allows implementing SFs to resist earthquake excitations in both the longitudinal and transverse directions. Smaller BRBs were designed and installed between closely spaced columns.

The seismic demands on the CFT columns were checked for the interaction of axial and flexural strength, which gave ratios of less than 1.0 and indicated that the columns were sufficient to resist the force demand at the target elastic displacement from response spectrum analysis. Note that the reaction at the bottom of the column was used for that calculation, which conservatively considered the eccentricity between the foundation and the intersection of the worklines of the BRB and CFT column. To verify that the design of the BRB and bridge bent was governed by the seismic loads, the bridge bents were also analyzed for service loads, including dead load, live load and wind load.

Comparison of theoretical and actual pushover curves in both the two-CFT-column and box-pier column cases showed good results, and indicated that bridge bent behavior was consistent with that predicted by the structural fuse concept.

Nonlinear time history analysis was also performed to verify the behavior of the bridge bents compared to the response predicted by the design procedure, elastic response spectrum and pushover analysis. The displacement at bent cap beam level and base shear force demand were compared for the bridge bents with BRBs in each case with

their corresponding bare bent. The two-CFT-column with BRBs case has a 20% larger base shear strength, together with an approximately 50% lower bent lateral displacement, than for the bare bent case. For the case of the box-pier bent in both transverse and longitudinal direction, the base shear strength is 10% larger and displacement are approximately 50% smaller than for the case without BRBs (although that latter comparison is purely academic because the box-pier system would never be used without BRBs). For all the bents designed with BRBs, a significant gain in drift reduction for a relatively modest increase in base shear demands is achieved. Displacement demands were found to slightly exceed predictions. This was a consequence of using a constant strength reduction factor as part of the design procedure (which is a known phenomenon to result in greater inelastic displacement for structures having short periods). Recommendations have been provided to modify the design procedure to account for this effect. Nonetheless, in spite of this, it remains that displacement of the bridge bents with BRBs cases were still significantly reduced from that for the bare bridge bents.

Finally, details have been designed for connecting BRBs to other members of the bridge bent (to establish feasibility for at least one connection type, recognizing that other details are also possible). Welding of the gusset plate of the BRB to the steel shell of a CFT emerged as the preferred approach, particularly for large BRBs. Design of BRBs to the cap beam and foundation using anchor bolts or anchor rods were also investigated, and found to be practical only for small BRBs.

## 6.2 Future Work

Future research on the design and analysis of SFs for application in Caltrans type bridges should investigate the following issues. First, seismic performance of designs using the proposed modified strength reduction factors (applicable in short period range of design spectra) must be determined, to verify that it better controls

predictions of maximum column deformations. Second, as structural fuses become smaller, their contribution to the initial stiffness becomes less dominant, and the design procedure may need to be revisited to ensure that maximum displacements predicted based on initial stiffness can still be achieved (or are corrected accordingly). Third, measures to reduce total base shear must be investigated, which can be achieved by allowing limited inelastic deformation of columns, by allowing BRBs to develop up to 3% strain in their yielding core, or both. Fourth, long-term performance of BRBs exposed to various harsh environments in sustained service, and immediately after an earthquake, should be investigated. Finally, the proposed connections details needs to be validated through tests to ensure satisfactory performance of BRBs in the bridge bent.

# Reference

AASHTO Guide Specifications for LRFD Seismic Bridge Design (2009), AASHTO, Washington DC, 2009

AASHTO LRFD Bridge Design Specifications (2010), AASHTO, Washington DC, 2010

ACI 318-08, building Code Requirements for Structural Concrete and Commentary. American Concrete Institute: Detroit, MI, 2007

Aiken, I.D., Clark, P.W., Tajirian, F.F., Kasai, K., Kimura, I., and Ko, E. (2000), "Unbonded Braces in the United States — Design Studies, Large-Scale Testing and the First Building Application," Proceedings, Japan Passive Control Symposium, Tokyo Institute of Technology, Japan

AISC. (2010). "Seismic Provisions for Structural Steel Buildings" American Institute of Steel Consctruction, Inc., Chicago, IL

ASTM F1554 "Standard Specification for Anchor Bolts, Steel, 36, 55, and 105 ksi Yield Strength." ,ASTM International, PA, 2007

Aviram A., Markie K.R. and Stojadinovic B. (2008), "Guidelines for Nonlinear Analysis of Bridge Structures in California" , PEER Report 2008/03, University of California, Berkeley, CA

Chai Y.H., Priestley M.J.N., and Seible F. (1994), "Analytical Model for Steel-jacketed RC Circular Bridge Columns," Journal of Structural Engineering, Vol.120,No.8, August, 1994

"Caltrans Bridge Design Specifications" (2012), California Department of Transportation, CA, 2012

"Caltrans. Seismic Design Criteria" (2010), California Department of Transportation, CA, 2010

El-Bahey, S., Bruneau, M., (2010). "Analytical Development and Experimental Validation of a Structural-Fuse Bridge Pier Concept", Technical Report MCEER-10-0005, MCEER, University at Buffalo, Buffalo, NY.

Fisher, J.M. and Kloiber, L.A. (2006) "Base Plate and Anchor Rod Design," American Institute of Steel Construction Inc, Second Edition

Fujikura S., Bruneau M, and Lopez-Garcia D. (2008), "Experimental Investigation of

Multihazard Resistant Bridge Piers Having Concrete-filled Steel Tube under Blast Loading", Journal of Bridge Engineering, Vol.13, No.6, pp.586-594

Ghobarah A, Abou Elfath H. (2001), "Rehabilitation of a Reinforced Concrete Frame using Eccentric Steel Bracing" Engineering Structures, 23, 745-755

Hogan, T.J. and Thomas, I.R., "Design of structural connections," Fourth Edition, Australian Institute of Steel Construction, 1994

Hu H.T., Huang C.S. and Chen Z.L. (2005), "Finite element analysis of CFT columns subjected to an axial compressive force and bending moment in combination", Journal of Constructional Steel Research, Vol. 61, Issue 12, Page 1692-1712,

Keller, D. and Bruneau, M. (2008), "Development of a Steel Plate Shear Wall Bridge Pier System Conceived from A Multi-hazard Perspective" Technical Report MCEER-08-0030, MCEER, University at Buffalo, Buffalo, NY.

Keller, D. and Bruneau, M. (2009), "Multi-hazard resistant steel plate shear wall bridge pier concept" Taylor & Francis Group, London, ISBN 978-0-415-56326-0

López, W.A., and Sabelli, R. (2004). "Seismic Design of Buckling-Restrained Braced Frames." Steel Tips Report. Structural Steel Educational Council.

MCEER ATC 49, "Recommended LRFD Guidelines for the Seismic Design of Highway Bridges" MCEER-03-SP03, MCEER, University at Buffalo, Buffalo, NY.

PCI design handbook, 6th ed. Chicago (I1): Prestressed Concrete Institute PCI,2004

Priestley M.J.N., Seible F., Calvi G.M. (1996) "Seismic Design and Retrofit of Bridges", Wiley-Intersceience, 1 Edition

Priestley M.J.N., Seible F., Calvi G.M. (1996) "Seismic Design and Retrofit of Bridges", Wiley-Intersceience, 1 Edition

Priestley M.J.N., Seible F., Calvi G.M. and Kowalsky M.J. (2007) "Displacement-Based Seismic Design of Structures", IUSS Press, Pavia, Italy, ISBN 978-88-6198-000-6

Roeder C.W. and Lehman D.E. (2008), "An Economical and Efficient Foundation Connection for Concrete Filled Steel Tube Piers and Columns", The 2008 Composite Construction in Steel and Concrete Conference VI, Tabernash CO, 2008

Sahoo D.R.and Chao S.H. (2010) “Performance-based Plastic Design Method For Buckling-Restrained Braced Frames” Engineering Structures, 32, page 2950-2958

SAP 2000 Reference Manual (2010), Computers and Structures, Inc, CA, 2010

Papageorgious A., Halldorsson B. and Dong G., “Target Acceleration Spectra Compatible Time Histories (TARSCTHS) User’s Manual”, Version 1.0

Vargas, R., Bruneau, M. (2006a), “Experimental Investigation of the Structural Fuse Concept”, Technical Report MCEER-06-0005, Multidisciplinary Center for Earthquake Engineering Research, State University of New York at Buffalo, Buffalo, NY, 2006.

Vargas, R., Bruneau, M. (2006b), “Analytical Investigation of the Structural Fuse Concept”, Technical Report MCEER-06-0004, Multidisciplinary Center for Earthquake Engineering Research, State University of New York at Buffalo, Buffalo, NY, 2006.

Wardenier J., Kurobane Y., Packer J.A. etc. (2008), “Design guide for circular hollow section (CHS) joints under predominantly static loading,” CIDECT, Section Edition

Zhang G., Unjoh S., Hoshikuma J., and Sakai J. (2009), “Seismic Retrofit Techniques for Reinforced Concrete Bridge Columns with Combination of FRP Sheet and Steel Jacketing,” the 25th U.S.-Japan Bridge Engineering Workshop Proceeding, Oct, 2009

# Appendix A Literature Review of Structural Fuses

## A.1 General

The terminology "ductile fuse" has long been used in the literature, going back at least to Roeder and Popov (1977) who used this term to describe the links of Eccentrically Braced Frames (EBF), promoted at that time as a mean to increase the hysteretic energy dissipation capacity of steel frames by concentrating energy dissipation primarily in specially detailed shear links that are integral to the frame itself. In other examples, Fintel and Ghosh (1981) used the term "structural fuse" to describe the capacity design concept in which beams are intentionally designed as weaker members that would yield by plastic hinging, to protect columns and walls which are considered more crucial for the structure to remain elastic.

The above examples use the terminology "fuses generically for system designed in compliance with capacity design principles. However, for the case of interest here, "fuses" is a term used when damage is controlled by using parallel systems, as discussed below.

Wada et al. (1992) proposed the concept of "damage-controlled structures" schematically explained in figure A-1. Such a structure consists of two separate primary components, namely the main moment frame structure and a system of passive energy dissipation elements. In this cited study, the moment frame resists 80% of the lateral loads while the secondary fuse system withstands the loads resulting from strong ground motions (various ratios have been considered in other studies). This damage-controlled concept was further investigated and improved following the 1995 Northridge and 1995 Hyogoken-Nabu earthquake by Conner et al. (1997). The study demonstrated that by adjusting the distribution of stiffness and hysteretic damping, it is possible to control the seismic response of a building to limit repair costs. A schematic relationship between repair cost and earthquake intensity for conventional and damage-controlled structures is presented in figure A-2. Damage-controlled structures were deemed more efficient in terms of cost reduction for larger earthquakes. Relevant extensive studies about this concept can also be found in Shimizu et al. (1998), Wada and Huang (1999), and Huang et al. (2002).

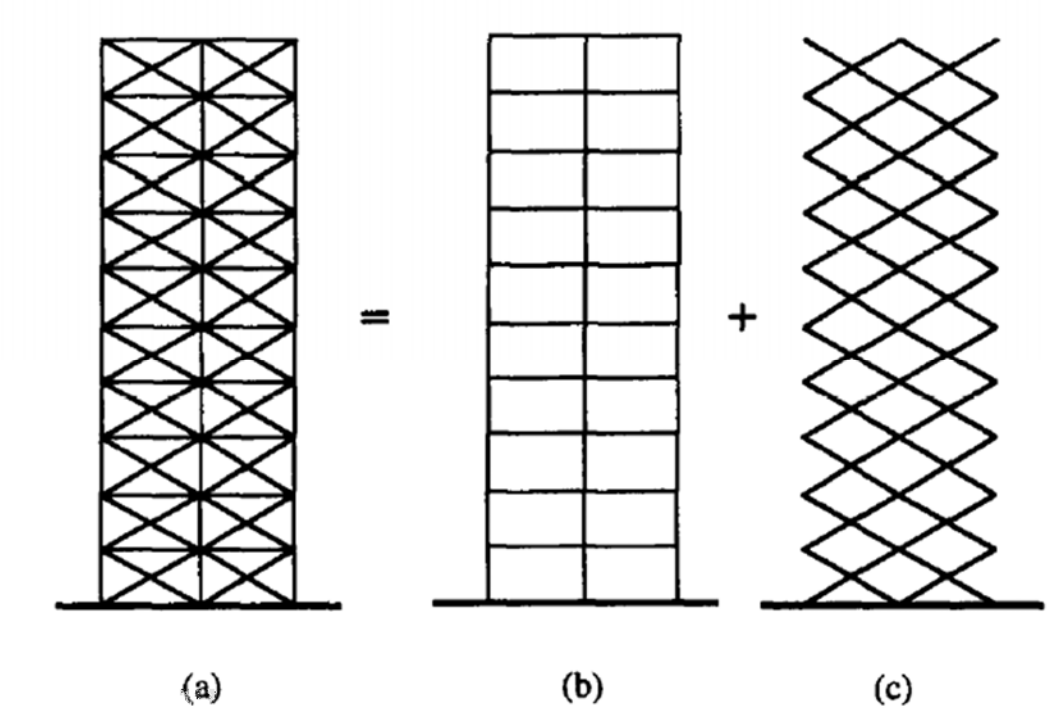


Figure A-1 Damage-controlled Structure: (a) Total Structure; (b) Gravity Support Structure; (c) Seismic-Resistant Structure (Wada et al., 1992)

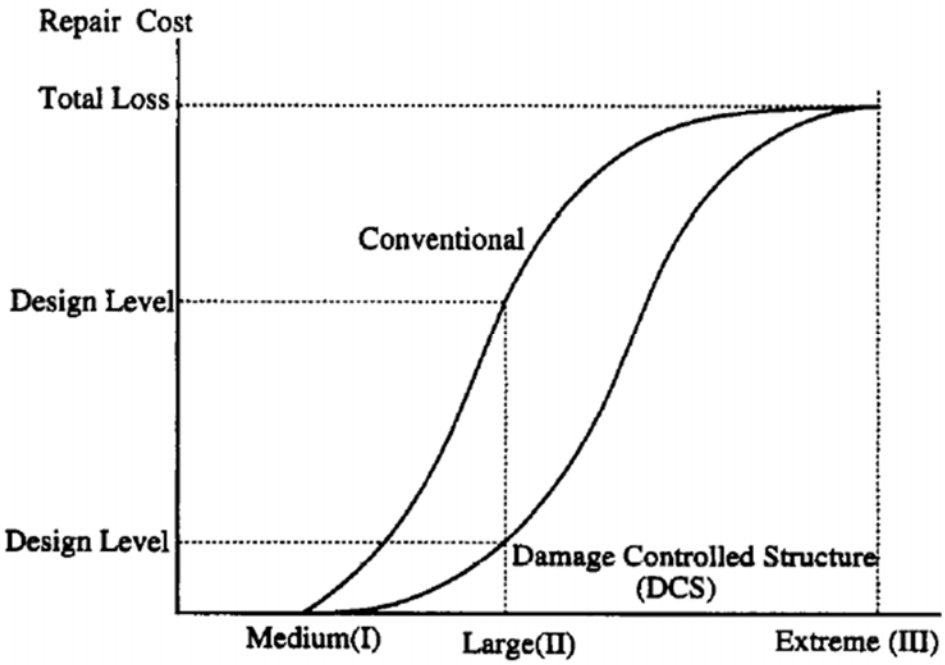


Figure A-2 Repair Cost vs Earthquake Intensity (Conner et al., 1997)

The ideal Structure Fuse (SF) implementation would be one in which the fuse a disposable and replaceable structural element introduced into the structure system

specifically to provide all of the needed seismic energy dissipation. Only limited research to date has focused on achieving this ideal objective, particularly with regard to easy replaceability (and thus expedient repairs) following the earthquakes.

Vargas and Bruneau (2006a, 2006b) described the SF concept in a parametric formulation, considering the behavior of nonlinear Single Degree Of Freedom (SDOF) systems subjected to synthetic ground motions. A general pushover curves for a SDOF structure is shown in figure 2-3. The SF concept requires that yield deformation of the damping system $\Delta_{ya}$ be less than the yielding deformation corresponding to the bare frame $\Delta_{yf}$. A systematic and simplified design procedure was put forward to achieve and implement SF concept that would limit damage to disposable structural elements for any general building. The procedure without the need for complex analyses was based on identifying regions of admissible solutions for the SF concept using nonlinear time history analyses. Metallic dampers such as BRBs, Triangular Added Damping and Stiffness (TADAS) and Shear Panels were implemented in both SDOF and Multi-Degree-of-Freedom (MDOF) systems to ensure the adequate seismic performance. A following experimental project tested a three-story building frame designed with BRBs as a proof of concept of the developed design procedure. Furthermore, the research reported the impact of introducing SF on floor accelerations and velocities (which has impact on seismic performance of nonstructural components).

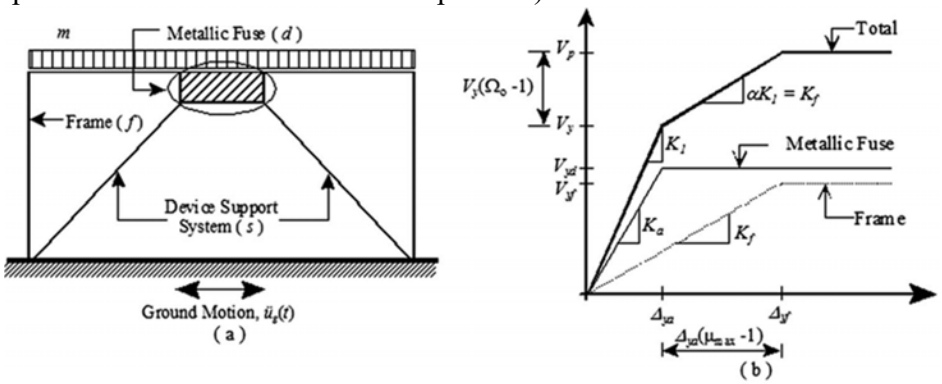


Figure A-3 (a) Sample Model of a SDOF System with Metallic Fuses; (b) General Pushover Curve (Vargas and Bruneau, 2006a)

A wide range of passive hysteretic energy dissipation devices can be used to enhance the stiffness and strength of the structure to meet the structural fuse concept. Focus here is on, metallic yielding members of various types and configurations. Section 2.2 provides an overview of some types of hysteretic energy dissipation schemes that could be adapted to serve as structural fuses in bridge applications. Note that hysteretic energy dissipation systems are sometimes called metallic yielding dampers if their only purpose is to provide hysteretic behavior of metals in the inelastic range. These are also called “rate or displacement dependent dampers” because their response is not sensitive to the frequency of loading. The resisting force of such dampers, therefore, depends on the nonlinear stress-strain characteristics of the materials. The amount of damping they provide is somewhat proportional to the magnitude of their inelastic deformations. However, in the present context, the perspective taken includes any solution that can achieve the structural fuse objectives stated above, and consequently, the design procedure followed is not

based on structural damping analogies but rather on conventional stiffness and strength analyses.

A partial list of possible type of SF elements that could be constructed for potential use in bridge applications, includes standard Buckling Restrained Braces (BRBs) (Wada et al. 1992, AISC 2010), short specialty BRBs (El-Bahey and Bruneau 2010), shear links (Nakashima M. 1995, Tanaka et al. 1998, Goodyear & Sun 2003), flexural links (Kelly et al. 1972, Whittaker et al. 1989, Tsai et al. 1993), Steel Plate Shear Link (El-Bahey and Bruneau 2010), to name a few. Different types of fuses may work best for different bridge topologies. Some development and applications of SF in seismic resisting structures are briefly provided at first. More existing building and bridge examples would be given later as details of various SF are reviewed.

# A.2 Metallic Hysteretic Damping Devices

## A.2.1 Buckling Restrained Braces (BRBs)

### A.2.1.1 General

BRBs were initially developed in Japan by the Nippon Steel Corporation in the mid-1980s, and were then called as Unbounded Braces (UBs). Watanabe et al. (1988) presented a summary of some of the early development of BRBs. This system has been well received by Japanese designers after the 1995 Kobe Earthquake and implemented in numerous buildings. In North America, BRBs have been studied and implemented since the late 1990's and are becoming widely used in steel buildings, with at least three commercial suppliers of BRBs in the United States. However, there have been only a implementations of BRBs in concrete buildings to date, and (to the best of the authors' knowledge at the time of this writing) no application in concrete bridges.

A BRB generally consists of a central core surrounded by a tube that restrains the core from axially buckling in compression. The space between the core and the tube is filled with mortar. Unbonded material covers the steel core to isolate it and allow it to deform freely in the axial direction. The unbonding material should be thin enough to avoid local buckling of the core, and yet thick enough to accommodate lateral expansion of the core due to Poison's effects. The steel core is usually of rectangular or cruciform cross section shapes. Figure A-4 shows the components of a typical BRB and some detailed configurations.

Since BRBs prevent global buckling of the steel core by encasing it over its length, they exhibit a better force-displacement hysteretic behavior and can overcome many of the problems associated with the hysteretic behavior of concentrically braced special frames. A description of the mechanics of the BRBs with fully detailed design examples are presented in Lopez and Sabelli (2004). Most importantly, BRBs have a superior resistance to low-cycle fatigue, being typically able to sustain a large significant number of hysteretic cycles at large ductility demands. The large maximum ductility $\mu_{max}$ (BRB

maximum deformation divided by BRB yield deformation) and cumulative ductility $\mu_c$ (sum of BRB plastic deformation over BRB yield deformation) capability can be observed in table A-1.

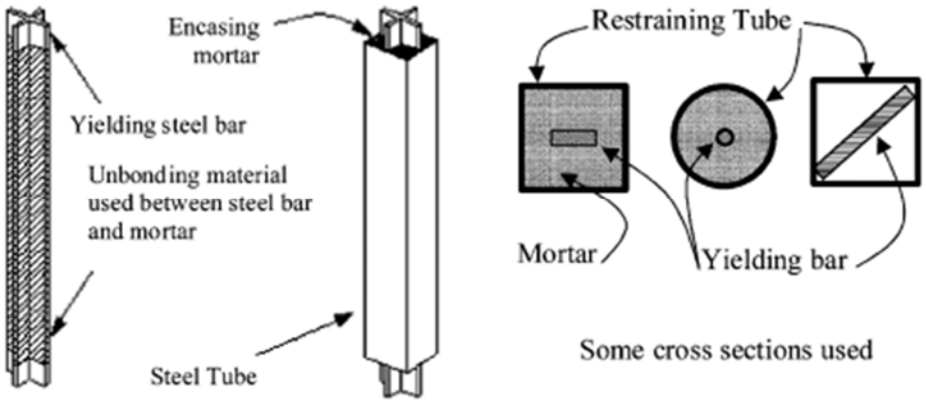


Figure A-4 Some Schematic Details Used For BRB by Sabelli (Sabelli et al., 2003)

Table A-1 Ductility Demands for Isolated BRB Tests (Fahnestock et al.,2007)

| Reference | Designation | $\mu_{max}$ | $\mu_c$ |
|---|---|---|---|
| Watanabe et al. (1988) | [a] | 10[b] | 50[b] |
| Black et al. (2002) | 99-1 | 20 | 324 |
| | 99-2 | 10 | 879[c] |
| | 99-3 | 10 | 279 |
| | 00-11 | 15 | 1,045 |
| | 00-12 | 15 | 538 |
| Merritt et al. (2003) | 1 | 15 | 900[c] |
| | 2 | 15 | 600[c] |
| | 3 | 10 | 1,600 |
| | 4 | 15 | 1,100 |
| | 5 | 15 | 1,300 |
| | 6 | 15 | 800 |
| | 7 | 10 | 1,000 |
| | 8 | 10 | 1,000 |
| Usami et al. (2003) | [a] | 25[b] | 400[b] |
| Tsai et al. (2003a) | T2_420SN_A | 48.4[d] | a,c |
| | T3_350 | 42.3[d] | a,c |

[a]Not reported.
[b]Estimated from published plot.
[c]Core fracture due to low-cycle fatigue.
[d]Tension only.

## A.2.1.2 Analytical and Experimental Research

A comprehensive study of 3-D frames with and without Buckling Restrained Braces (BRBs) was carried out by Wada et al. (2000). Dynamic analysis and experimental studies of a number of moment resisting frames validated the ability of BRBs to dissipate

energy through hysteretic behavior and protect beams and columns from yielding. Actual projects of application of BRBs in tall buildings were also presented.

Aiken et al. (2000) presented a comprehensive study of BRBs in the United States (US) context, and a design case study for a multi-story steel structure having BRBs working as hysteretic dampers. The details of the first building application of BRBs in US were also shown. The study, focusing on BRBs with having their core restrained by grout and unbonding material, showed an ability to sustain stable cycles of hysteretic behavior up to large displacements.

Clark et al.(2000) performed a series of large-scale tests on BRBs using cyclic loading protocol. The BRBs exhibited stable cyclic behavior with no degradation of strength or stiffness for all of the loading cycles up to failure. Figure A-5 shows the force vs. displacement curve of one of the BRBs being tested during basic cyclic loading protocol consistent with what is used for steel beam-to-column connections.

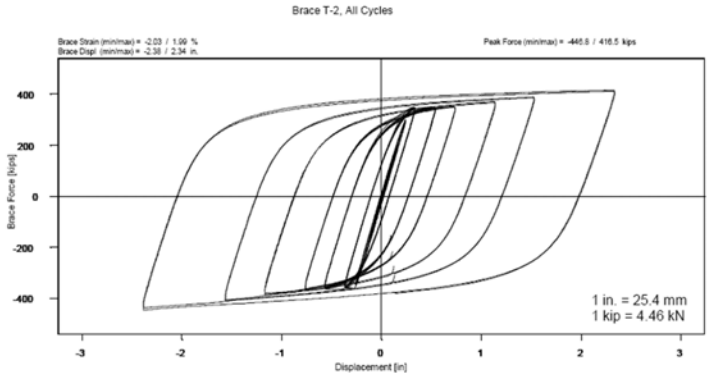


Figure A-5 Force-Displacement Behavior of Specimen During Basic Loading History (Clark et al., 2000)

Lopez et al. (2002) conducted a series of tests in support of the design of a new laboratory building. The BRBs were tested in a subassembly to confirm the behavior under frame loading conditions. This study focused on the behavior of the braces under frame-induced axial and rotational deformation. The BRBs' hysteretic and elongation behavior was proven not to be influenced by the combined axial and flexural demands associated with loading in the frame configuration.

The above-mentioned research focus on BRBs more used in the context of reducing the inelastic deformations of the existing building frames. There are also a lot of work has been done to study the application of BRBs in bridges. Usami et al. (2005) studied the implementation of BRBs in steel arch bridges for seismic upgrading. The bridge was composed of reinforced concrete deck slab, steel girders and arch ribs as shown in figure A-6. Nonlinear time-history analysis of the bridge showed that its seismic performance in the transverse direction was inadequate. Two retrofit plans considered replacing some lateral members and diagonals by BRBs. In figure A-7, lateral braces of the pier as well as twelve diagonals near the two arch rib bases were replaced by BRBs. The addition of

BRBs at the arch ribs decreases the strain demand at the arch rib base to elastic range. The maximum strain demand in BRBs is below the capacity and stable behavior is ensured.

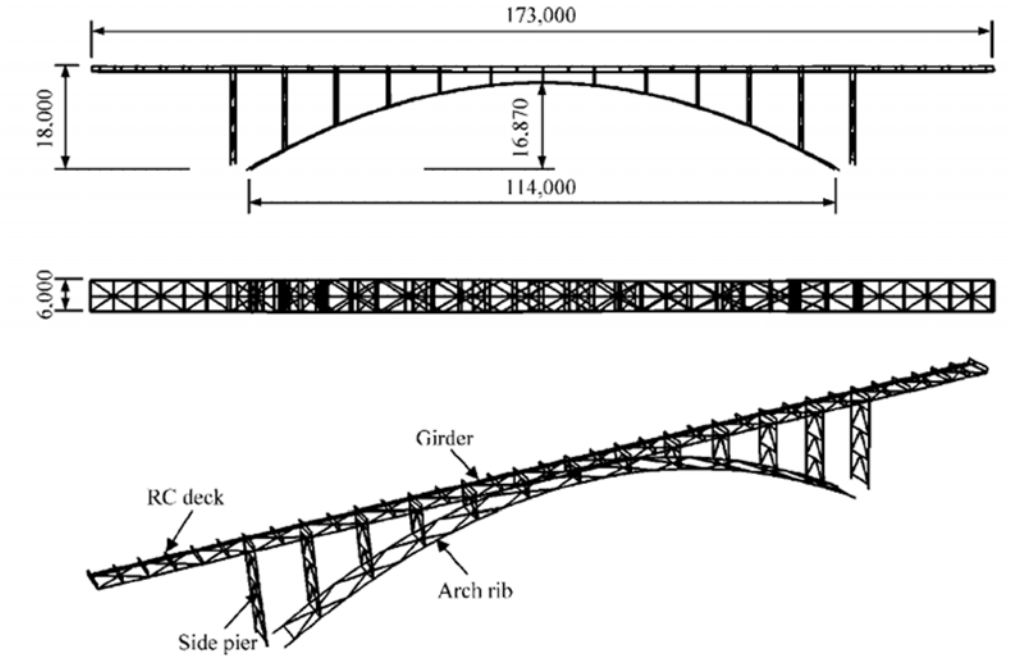


Figure A-6 Layout of the Steel Arch Bridge to be retrofitted: (a) Elevation; (b) Plan; and (c) 3-D View (Usami et al., 2005) (Unit:mm) (Usami et al., 2005)

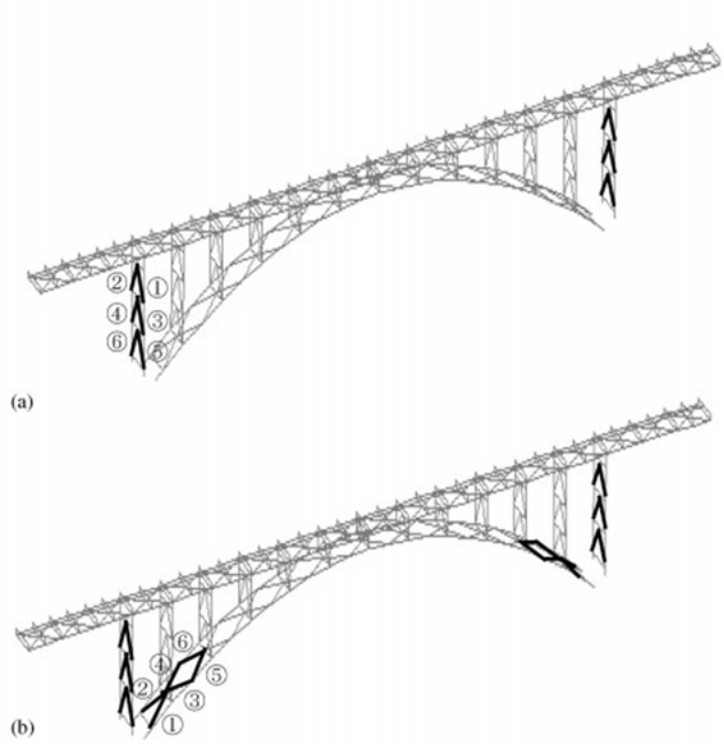


Figure A-7 Location of BRBs in the Two Retrofit Proposals (Usami et al., 2005)

The behavior of ductile end cross frames with BRBs was studied by Carden et al. (2006) using an 18m long single span model of a two-girder bridge. The prototype by a factor of 0.4 is an implementation of the ductile diaphragm concept developed by Zahrai and Bruneau (1999). BRBs at end cross frames were designed with both pin-ended connections and fixed-end connections. Figure A-8 shows a typical BRB used in the specimen for the large shake table experiment. The bridge specimen, with BRBs as end cross frames at each end, was subjected to increasing amplitudes of transverse excitation using the 1940 El-Centro earthquake ground. Despite slippage, the pin-ended connections were considered more effective as flexural action in the relatively short braces was prevented. The relatively large deformation capacity of the BRBs, although not as great as the X-braces, was necessary to achieve a significant reduction in the base shear.

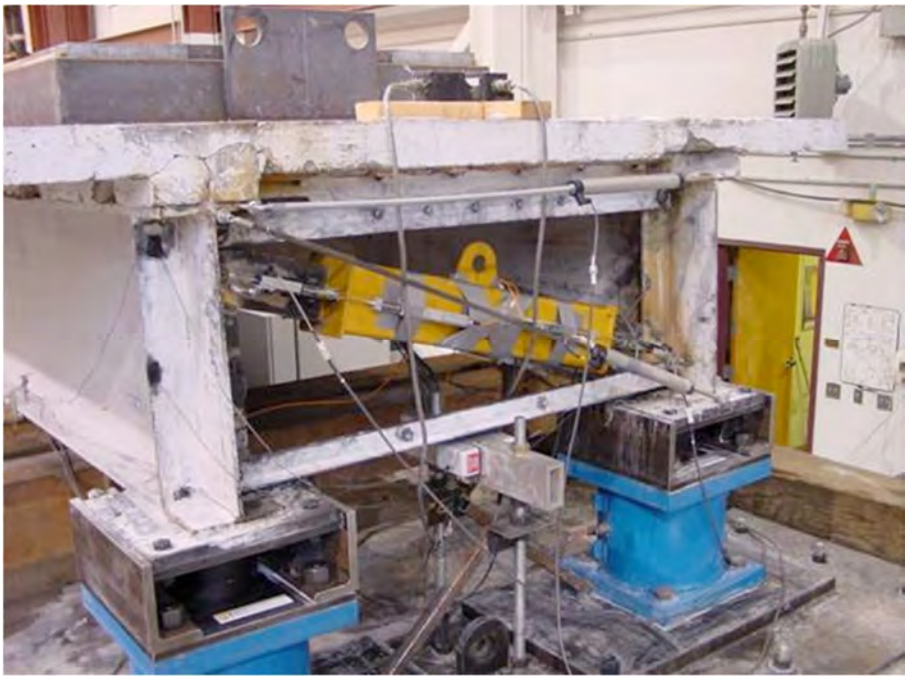

Figure A-8 View of BRB at the End Cross Frame of the Plate Girder Bridge (http://www.unr.edu/engineering/cee/faculty/itani/bridgeComponents.html)

El-Bahey and Bruneau (2010) considered using an inverted chevron BRB brace system to retrofit general RC bridge bents. Governing parameters defining the behavior and design of the fuse system were identified. Seismic response was verified through parametric analyses of the studied systems and the results were refined and validated using non-linear time history analyses. A step-by-step design procedure was also proposed. That study was analytical and assumed that connection of the BRBs to concrete columns was possible.

In related experiment, although using composite columns, special purpose short BRBs were inserted between twin closely-spaced segmental columns and over the whole height of the columns, as shown in the configuration in figure A-9. The twin columns were

subjected to a series of quasi-static cyclic tests. Analytical investigation was also conducted to replicate the experimental results. Hysteretic curves obtained during the full bridge column specimen tests reflected the behavior of the entire system, and were complemented by uniaxial BRB tests to verify the effectiveness of the newly proposed BRB device developed for this application.

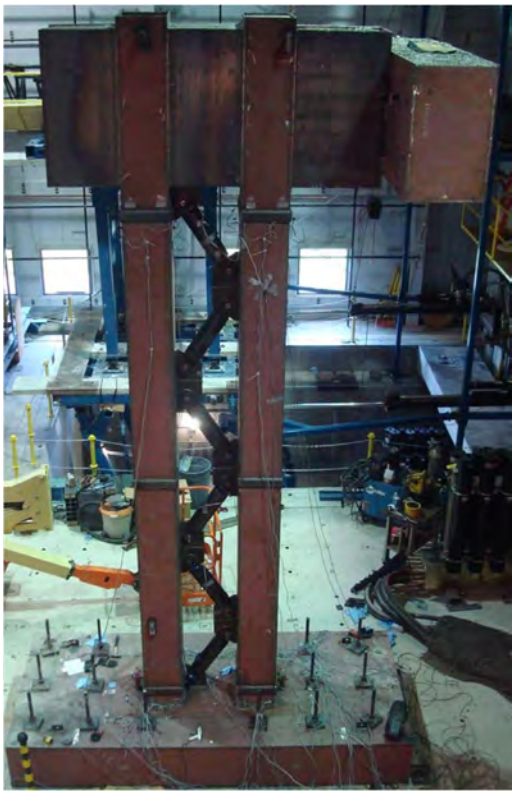

Figure A-9 Twin Column Specimen S2-1 with BRBs Prior to Testing (El-Bahey and Bruneau, 2010)

### A.2.1.3 Application and Installation in RC Buildings in the US

The BRBs have been used extensively used in Japan since 1987 in nearly 200 buildings. The first installation of BRBs in US is the Plant and Environmental Science Building at the University of California, Davis, which is a new steel structure. As to Given that BRBs implemented in RC bridge bents are likely to be connected to RC columns, the known BRB implementations in RC buildings are summarized below. Note that the first three of those implementation examples described above used a secondary steel frame attached to the RC frame or columns.

(1) Martin County Civic Center, San Rafael, CA

The Martin County Civic Center locates in San Rafael California. This long and narrow building had the original lateral load resisting system comprised of concrete diaphragms, collectors and shear walls. Seismic deficiencies were found in particular in the transverse direction where the stairs and elevator walls were insufficient to carry the seismic

demanded forces. The diaphragm and collectors were not capable to transfer seismic forces to existing resisting elements due to weak connections. Shaw et al. (2000) described a BRBs and shear wall retrofit scheme: thirteen locations were chosen as lateral resisting elements in the transverse directions, and nine locations in the longitudinal direction. In total, 44 BRBs were installed. Figure A-10a shows a section in the building with new BRBs and shear walls; and figure A-10b shows the BRBs' connection details.

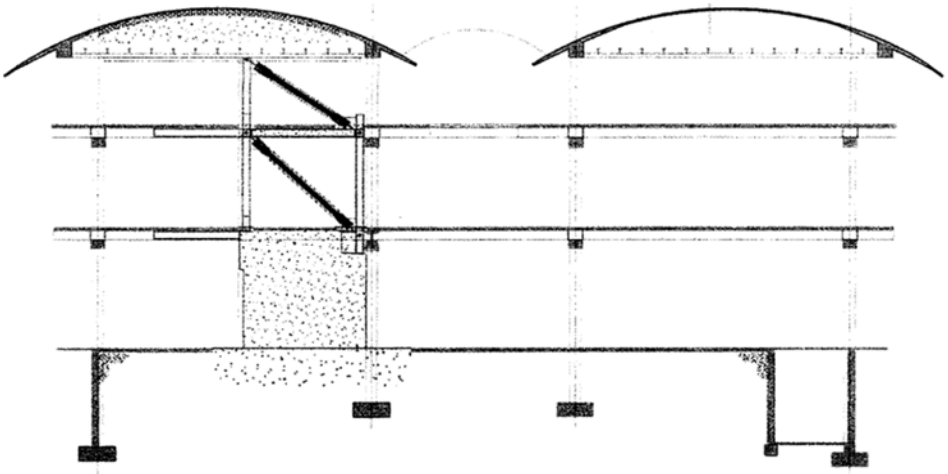

(a)

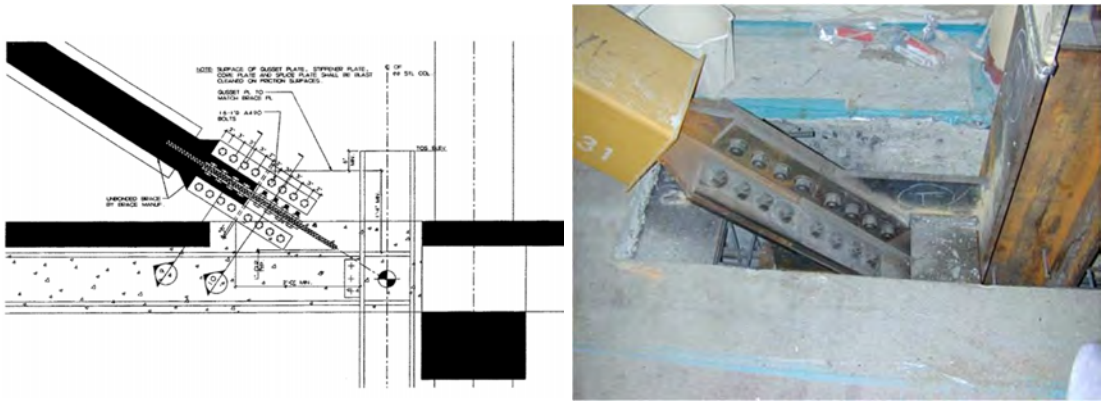

(b)

Figure A-10 Martin County Hall of Justice Building a) Section Drawing of Retrofit Plan with BRBs and Shear Walls; b) BRB Connection Details (Shaw et al. ,2000)

(2) Wallace F. Bennett Federal Building, Salt Lake City, Utah

The Wallace F. Bennett Federal Building located in Salt Lake City, Utah, was constructed in the early 1960s as an 8-storey office building. The RC structure was constructed of 8" thick two-way flat plate floors, spirally-reinforced rectangular columns and pile foundations. It was deemed incapable of resisting the large magnitude earthquake that nearby Wasatch Fault might generate.

Aiken et al. (2001) described the structural steel framework to be connected to the

existing RC frame, and to which the 344 BRBs were connected to become the seismic lateral force resisting system for the upgrading building. The frame was designed to remain safely below the yield stress level for the maximum forces delivered by BRBs. Figure A-11 shows a photograph of the building prior to rehabilitation and an architectural rendering of the upgraded building. Details of BRBs connected to the frame structure are shown in figure A-12.

Figure A-11 Wallace F. Bennett Building Prior and Post Rehabilitation (Aiken et al., 2001)

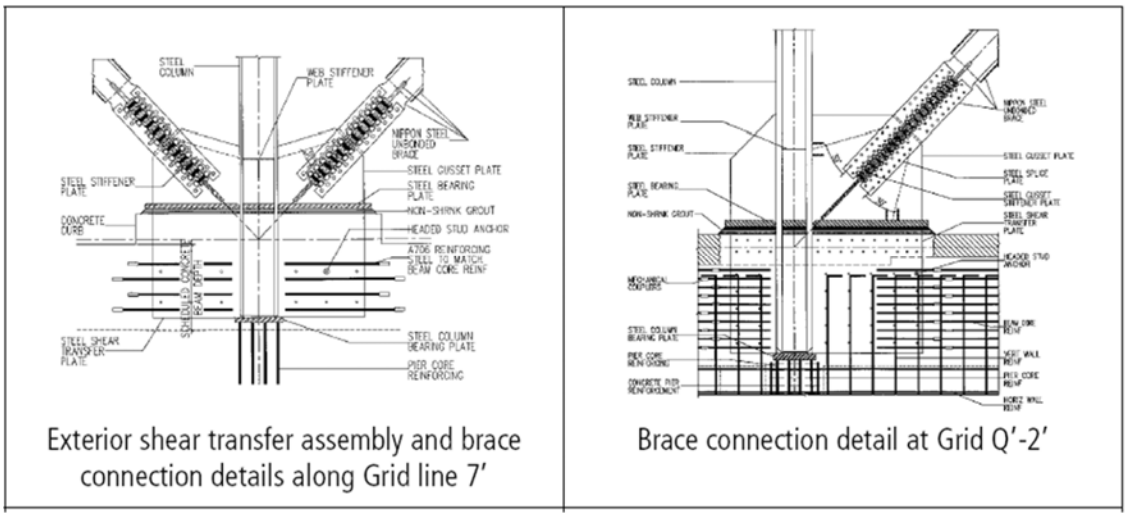


Figure A-12 BRBs Connection Details (Aiken et al., 2001)

(3) Hildebrand Hall University of California, Berkeley, CA

This Hilbebrand hall Building, constructed in 1963, is a three-story tower structure atop an expanded two-story basement. The tower structure roof and floor framing systems are post-tensioned lightweight concrete slabs supported directly on concrete columns and bearing walls. There are no beams, column capitals or drop panels beneath the slab. Floor slabs acting as diaphragms transfer loads to the stair and elevator core concrete walls and four large concrete box columns located at the corners of the structure. However the columns and slabs are not detailed to behave in frame-action and therefore provided negligible lateral strength. Two frames consisting of multiple BRBs, as shown in figure A-13, were added to the north and south ends of the building in the transverse

direction. The retrofit plan of north elevation is shown in figure A-14. Details of BRBs connected to the added steel frames are also provided (figure A-15). The existing concrete box columns adjacent to the steel braces were thickened to provide the frames with continuous chord action for seismic overturning considerations. The capacity curve for the braces frame direction is shown in figure A-16.

Figure A-13 Hildebrand Hall University of California Prior and Post Rehabilitation (Morgan et al., 2004)

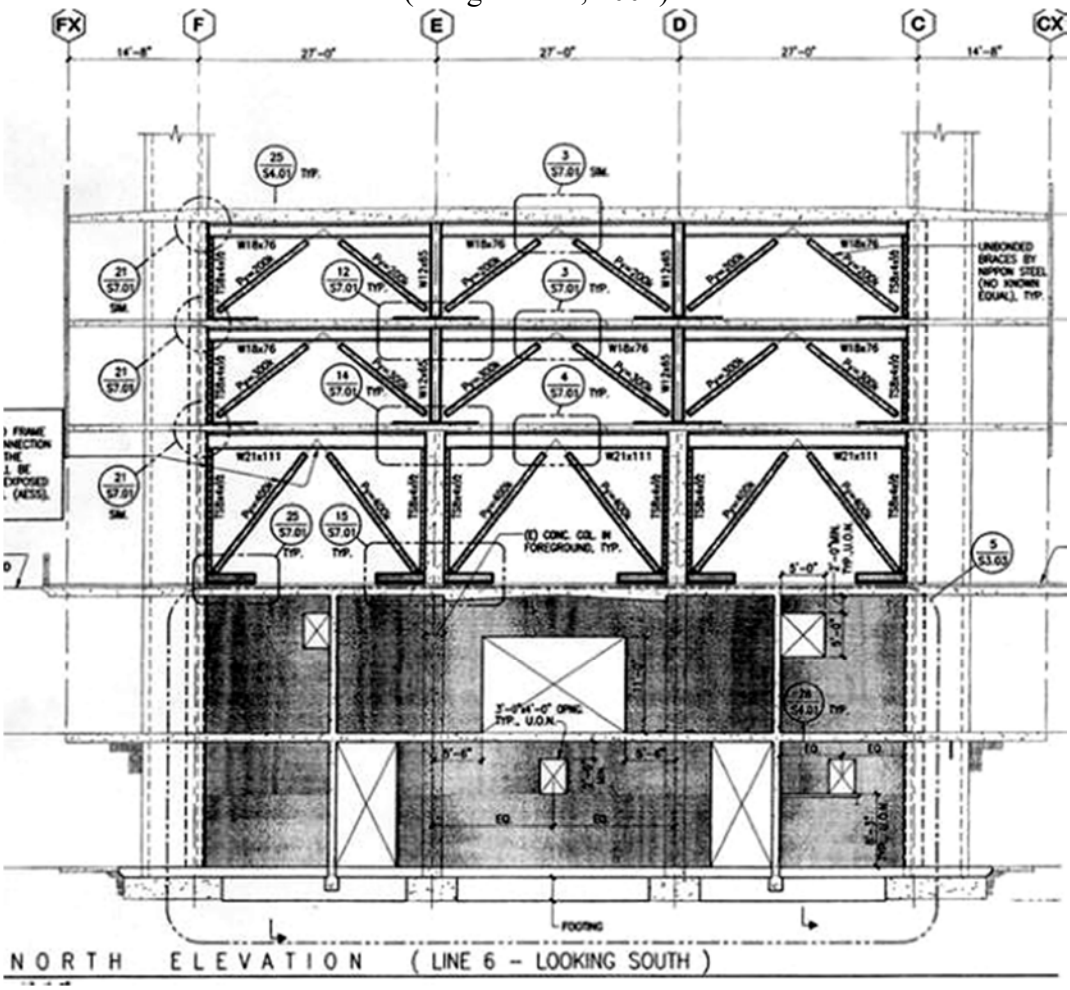


Figure A-14 North Elevation Retrofit Plan with BRBs (Anagnos T., 2011)

Figure A-15 BRB Connection Details (Anagnos T., 2011)

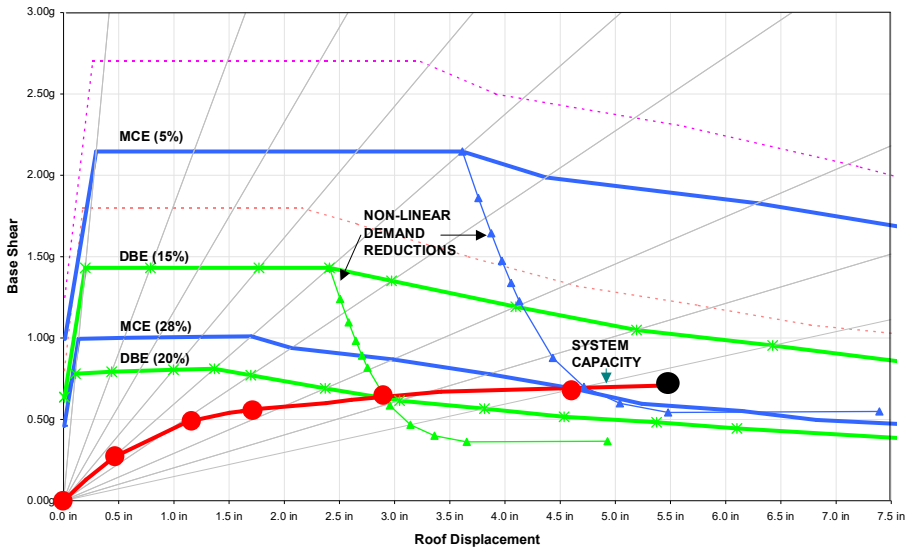


Figure A-16: Demand-Capacity Spectrum for Buckling-Restrained Brace Frame Retrofit Direction (Morgan et al., 2004)

(4) Webb Tower in University of Southern California in Los Angeles

A retrofit plan using BRBs for the Webb Tower, a 14-story residential RC structure, was proposed by Islam et al. (2006). The building constructed in 1972 had a lateral system composed of perimeter post-tensioned concrete moment frames with non-ductile beams

and columns. Several seismic deficiencies were discovered, such as non-ductile detailing, excessive building deflection and joint shear overstress. BRBs were used to retrofit the structure. The proposed seismic upgrade consists of adding new exterior BRBF's to improve the overall lateral load resisting capability of the building, as well as its stiffness against deflection. A typical perimeter frame elevation is shown in figure A-17, with one bay of BRBs in combination with a RC beam-column frame. BRBs (manufactured by Nippon Steel) having a design axial capacity of between 230 kips and 700 kips and connected to the new concrete beams and columns. The seismic performance verification was based on a series of nonlinear time history analysis using the seven acceleration time history records for the EQ-III (475 year) and EQ-IV (2500 year) seismic hazard levels. The interstory drift ratio response of the building for the EQ-III and EQ-IV is shown in figure 2-18 for the east-west direction of the building.

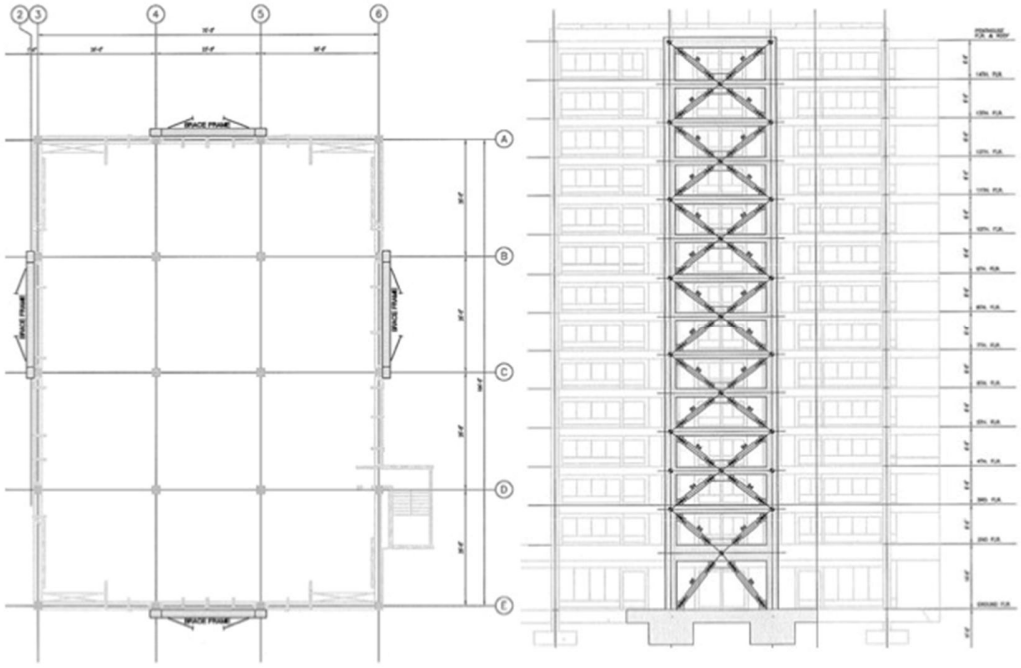

Figure A-17 Typical floor plan and one facade of retrofitted building (Islam et al. ,2006)

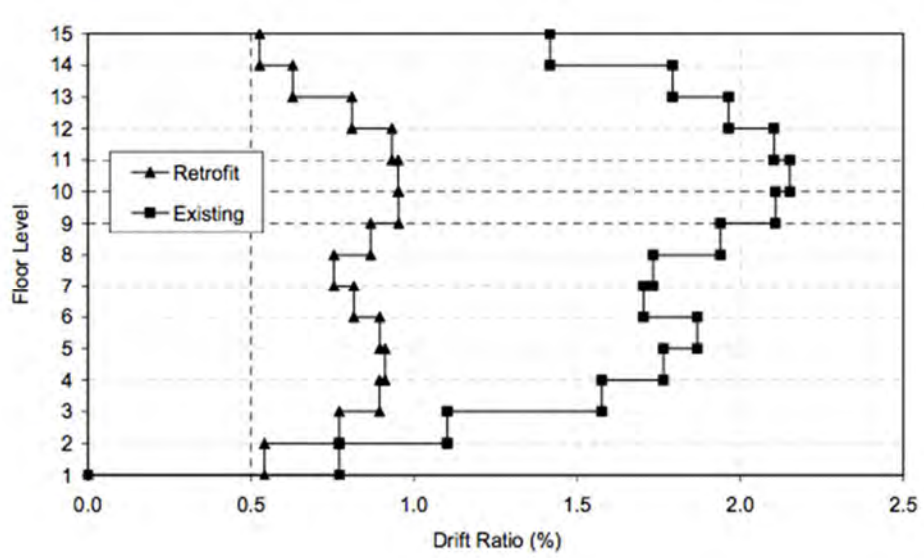


Figure A-18 Interstory Drift Response of Retrofit Building in East-West Direction (Average of 7 Ground Motions) (Islam Et Al., 2006)

## A.2.1.4 Application and installation in Bridges

Applications of BRBs in bridges have been recently contemplated, and in a few cases implemented. Following are two examples applications of BRBs in bridges to improve their seismic performance.

(1) Minato Bridge, Osaka, Japan

The Minato Bridge is a long-span truss bridge whose center span length is 510m, ranked as the world's 3rd truss bridges (Hamada et al., 2007). The bridge needed to be retrofitted in order to accommodate the Japanese seismic performance level 2, described in table 2-2. This was achieved by installing BRBs on the cross frames of the main tower and on the lower lateral bracing near the main tower, as shown in figure A-20. In addition, one of the lower lateral bracing panels on the side of the center span was also replaced with BRBs. In order to use BRBs in this bridge retrofit, BRBs used mainly in retrofitting buildings were modified to make them lighter members and suitable to coupled with the existing gussets. Kanaji et al. (2005) reported that analyses of the retrofitted bridge proved that BRBs were effective to reduce the strain energy of lower chord members near the tower. Adequate damping to the entire bridge was provided by BRBs and buckling or yielding of main members can be avoided.

**Table A-2 Functions Required for Bridge and Performances Required for Members**

| Level | Functions required for bridge (Basic performances required for bridge) | Performances required for members |
|---|---|---|
| Performance level 1 | To protect human lives (to alleviate bridge collapse)<br>To allow transport of emergency and general vehicles (to necessitate inspection after earthquake but in principle not to necessitate repair) | Elastic behavior of all members<br>Demonstration of hysteretic damping by damage-control members and devices |
| Performance level 2 | To protect human lives (to alleviate collapse)<br>To allow transport of emergency and general vehicles (to necessitate reinforcement of non-main frame and inspection and monitoring during reinforcement period) | Elastic behavior of main members<br>Allowance of damage of non-main members<br>Demonstration of hysteretic damping by damage-control members and devices |
| Performance level 3 | To protect human lives (to alleviate collapse but to allow large-scale repair and reinforcement) | Allowance of damage of main frames within the range in which they do not lead to collapse<br>Allowance of damage of non-main members<br>Demonstration of hysteretic damping by damage-control members and devices |

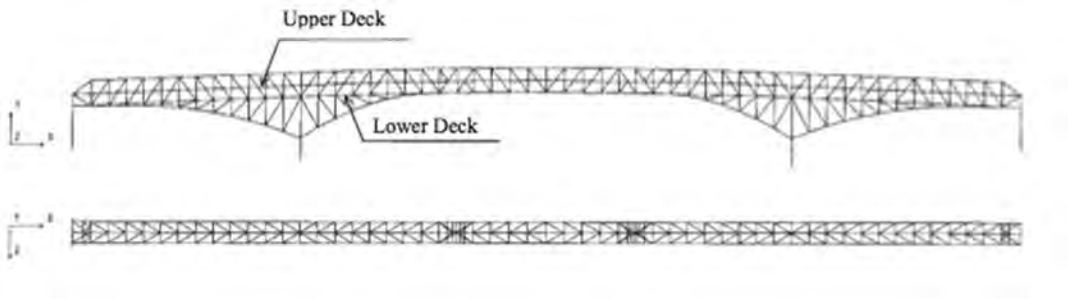


Figure A-19 Analytical Model of Minato Bridge (Kanaji et al. ,2005)

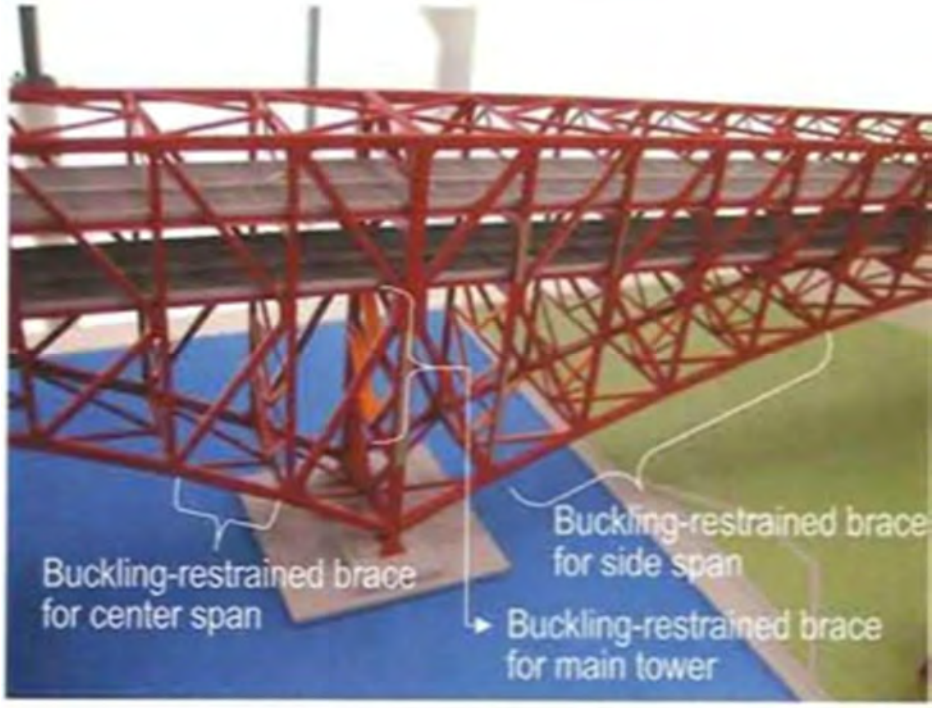


Figure A-20 Location of BRBs in the Bridge (Hamada et al., 2007)

Figure A-21 BRB Installed in the Bridge (Hamada et al., 2007)

(2) Auburn-Foresthill Road Bridge, Northern California

The Auburn-Foresthill Road Bridge, in northern California (figure A-22), was built by the Bureau of Reclamation in 1973. The superstructure is a parabolic haunched deck truss bridge that has fracture-critical, high-strength steel (100ksi) main members. There are two locations of the BRBs being installed.

Longitudinal anchor plates at abutments were attached with link plates, as shown in figures A-23 and A-24. These longitudinal anchor plates will experience forces and strains that significantly exceed their capacity, which leads to longitudinal instability of the bridge. Yielding and damage in the anchor plates anchored in the concrete at the abutment was also not desirable because of the irreplaceability. So the geometry of the link plates at the abutment was changed to reduce their capacity so that yielding occurs in the link plates rather than the anchor bars. And then BRBs were added at the abutment about the centerline of the bridge to provide longitudinal stability. When the link plates fail at the prescribed strain 0.4 during earthquake events, BRBs will take over the load so that the system can stabilize and later the bridge be inspected and repaired. Figure A-25 shows the plan view of the planned BRBs installation.

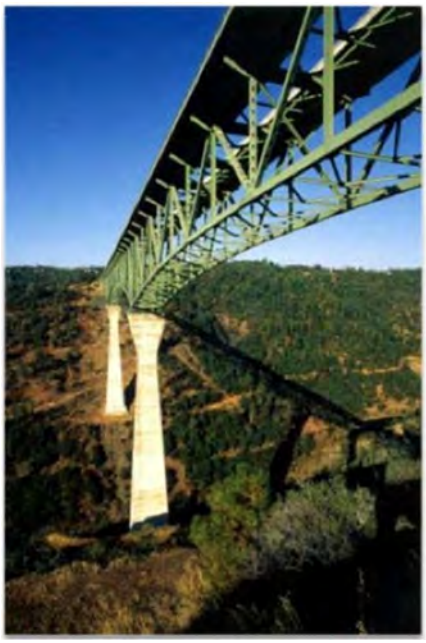

Figure A-22 Auburn-Foresthill Road Bridge View

Figure A-23 Abutment of the Bridge

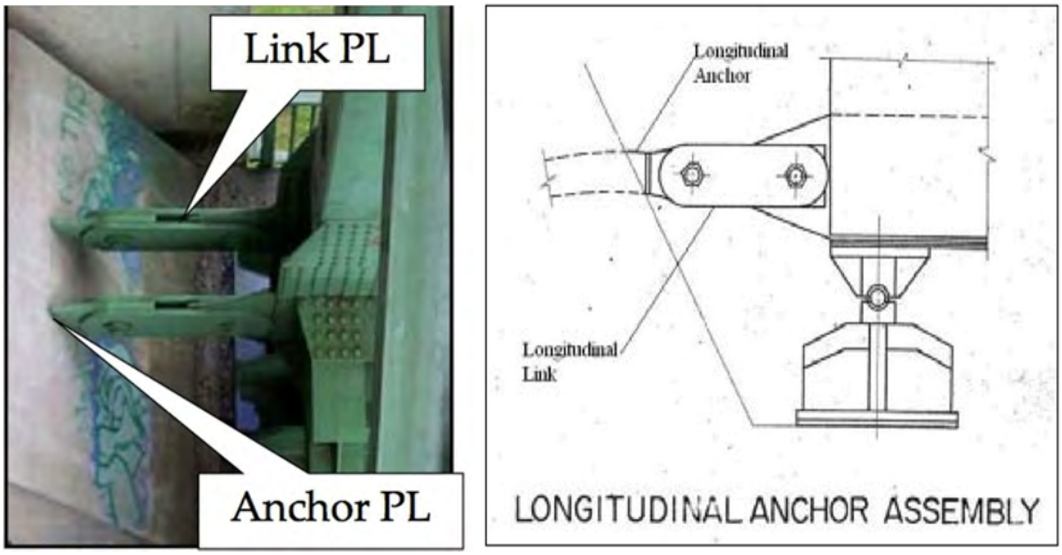


(a) (b)

Figure A-24 Longitudinal Anchors Assembly to the Abutment

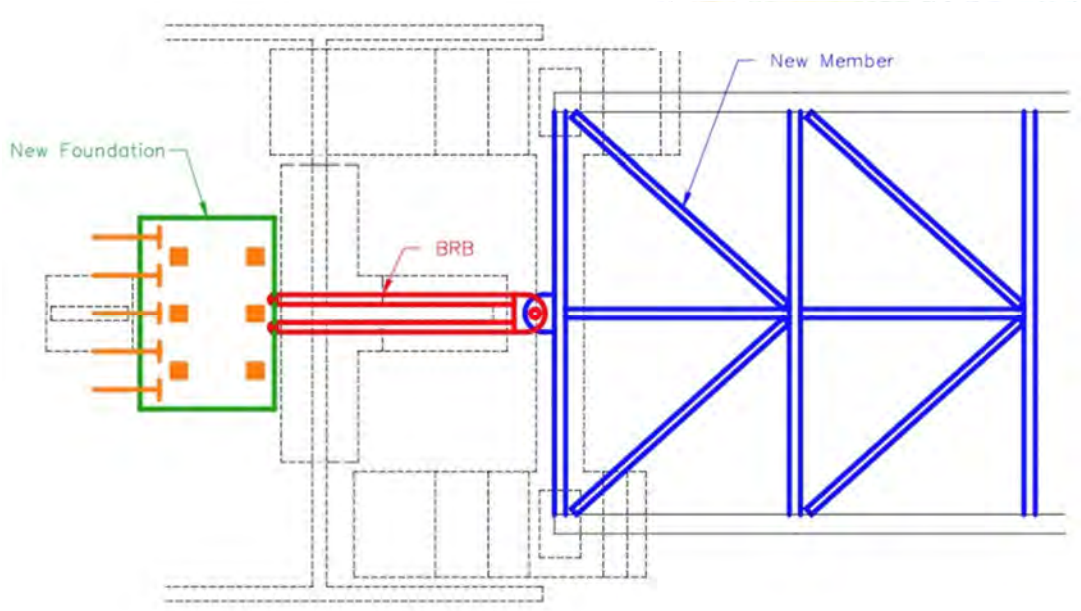


Figure A-25 Plan View of BRB Installed at Location 1

Horizontal chevron bracing members near the abutment have strain demands surpass the design criteria, as shown in figure A-26. The members were replaced by BRBs, together with new longitudinal struts, in order to take conservative loads into the critical load path system. Proof tests were conducted at the University of California, San Diego to quantify the right type of BRBs supplied by the manufacturer. The loading cycles history was not as severe as those tests of BRBs used in buildings. The figures about the Auburn-Foresthill Road Bridge retrofit project all come from the following link.
http://foresthillbridgerenewal.com/images/docs/Pre-Bid%20Mtg%208-9-10_low.pdf.

Figure A-26 Lower Horizontal Bracing Near Abutment

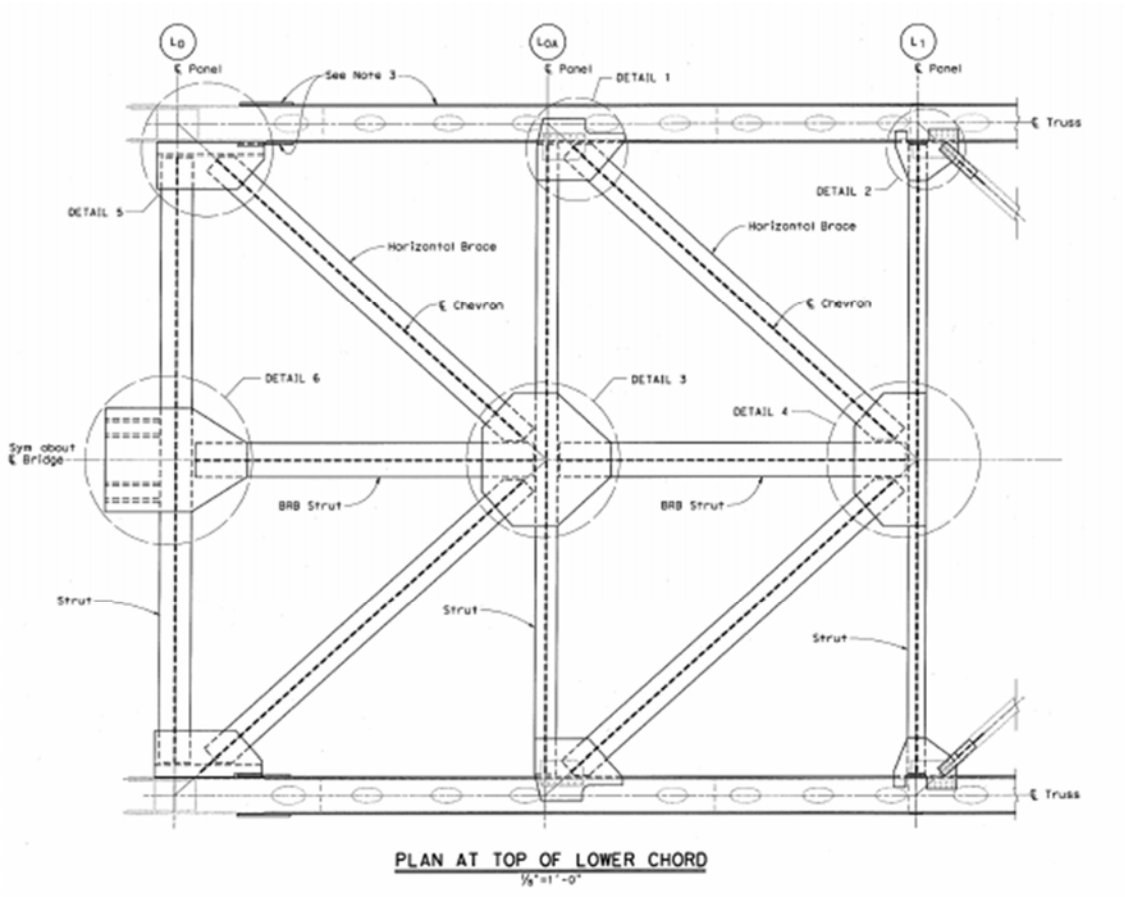


Figure A-27 Plan View of BRBs Installed in Location 2

(3) Araku-bashi Bridge, Japan

The Araku-bashi Bridge is a rigid frame bridge with knee brace. The length of the bridge

is 80.0 m. The distance between the fulcrums in figure 2-28 is 28.0 m. A new type of BRBs, which using two steel mortar planks welded together as the buckling restraining parts to keep the core plate being under axial forces and exhibit plastic behavior, were implemented (figure A-29).

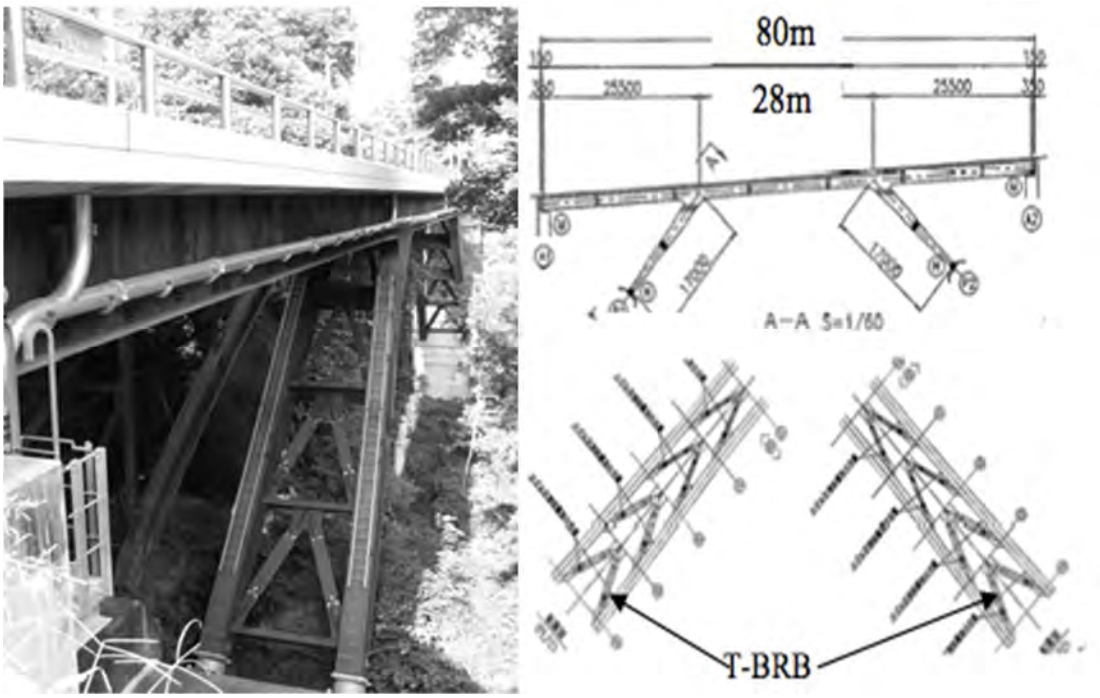


Figure A-28 Layout of BRBs Installed in the Bridge (Oya et al., 2009)

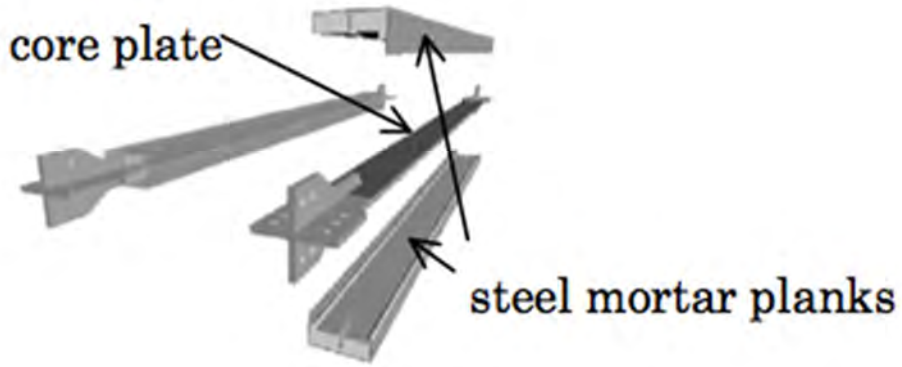


Figure A-29 T-BRB Configuration (Oya et al., 2009)

## A.2.1.5 Application and Installation in Other Structures

Mircowave communication towers usually been placed on the top of buildings. These high-rise steel truss structures with pipe sections have been basically designed to withstand wind forces. Such structures would also be likely to undergo serious damage

when subjected to large seismic forces. Some seismic retrofit projects have been carried out that the critical truss members are replaced with BRBs to avoid the structure collapse due to buckling of members. The BRBs installed exposed to the elements are shown in figure A-30 and A-31.

Figure A-30 A Telecommunication Tower in Japan (Courtesy of Ian Aiken, Seismic Isolation Engineering, Emeryville, California)

Figure A-31 Close Look of BRBs Installed in the Communication Tower (Courtesy of Ian Aiken, Seismic Isolation Engineering, Emeryville, California)

Many exterior installations of BRBs have been completed in the US. The following table A-3 is a brief summary of where they have been used and how the BRBs are protected against harsh environmental problems by StarSeismic. Figure A-32 and A-33 show the pictures of some of the BRB applications in the table A-3.

Table A-3 Exterior Applications of BRBs by StarSeismic (Courtesy of Steve Powell, StarSeismic, Park City, Utah)

| Project Name | Location | Industry | Protection of BRBs |
|---|---|---|---|
| John Wane Airport Parking Garage | Tustin, Orange County, CA | Transportation | Galvanized |
| Casad Dam | Bremerton, WA | Utility, Power & Water | Stainless Steel |
| Rio Tinto Soccer Stadium | Salt Lake City, Utah | Stadium | Painted |
| BART Dublin Transit Station | San Francisco, CA | Transportation | Painted |
| Harborside Pedestrian Bridge | San Diego, CA | Transportation | Painted |
| San Francisco International Airport, Terminal 2 Renovation | San Francisco, CA | Transportation | Painted |

Figure A-32 Configuration of BRBs in Parking Building of John Wayne Airport (http://www.airportimprovement.com/content/story.php?article=00258)

Figure A-33 BRBs Installed in Casad Dam (http://www.starseismic.net/projects.html)

## A.2.2 Steel Shear Panel Links

Shear links have been used in eccentric braced frames (EBF) since the mid-1970s (Roeder & Popov 1977). The reliability of EBFs to resist large earthquake lateral loads has been confirmed by research that extensively focused on new buildings (Kasai & Popov 1983, Popov & Malley 1983, Hjelmstad & Popov 1986, Ricles & Popov 1987, Engelhardt & Popov 1989). EBFs in buildings typically rely on shear links, which are sections of beams that yield and plastically deform in shear (rather than flexure) to provide a stiff and ductile lateral load resisting system.

For shear links, the shear force is constant over its length. This allows for the development of large plastic deformations without the excessive local strain that normally occur in flexural yielding. Shear yielding is considered to provide more efficient energy dissipation than flexural yielding. Such links are built using a web-stiffened W section. If the link and braces were to be directly connected to an RC members, it would require steel plates, bolts and epoxy gouting, or the link can be connected to a collector steel beam attached to the concrete cap beam and the brace via steel plates to the RC member.

A noteworthy implementation of shear links as SF is provided by the built-up wide-flange shear links implemented in the tower of the new San Francisco-Oakland Bay (SFOBB) suspension cable bridge. The main bridge tower in figure A-34 consists of four closely spaced columns connected by a series of steel shear links designed per AISC seismic provisions. Details of the shear links installed between the columns are shown in figure A-35. Each column is a hollow, semi-elliptical cross section with an interior steel liner

that tapers from the tower head to the base. The shear links help form a transverse structural frame system with a greater number of redundant ductile elements. Goodyear and Sun (2003) compared the capacity of the tower with and without links by using nonlinear pushover analysis as shown in figure A-36. The pushover curve of the tower with shear links showed no inelastic demand in the concrete tower element until well beyond the Safety Evaluation Earthquake (SEE) demand displacement. And all inelastic demand for the single tower was confined to the steel links.

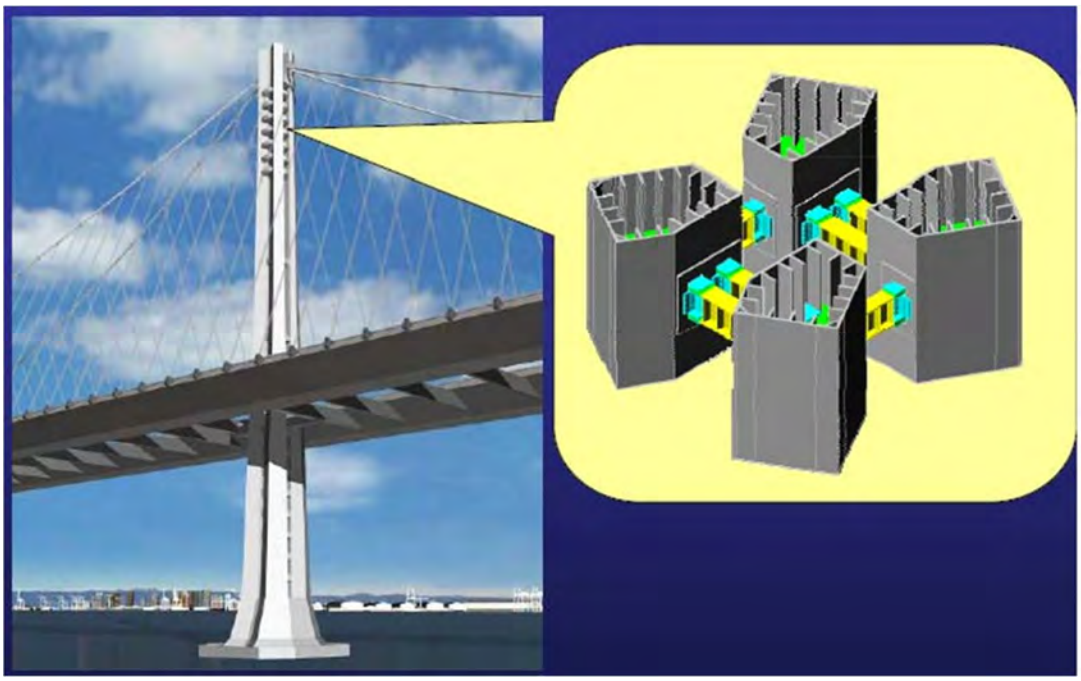

Figure A-34 Bay Bridge Towers with Shear Links (Bahey and Bruneau, 2010)

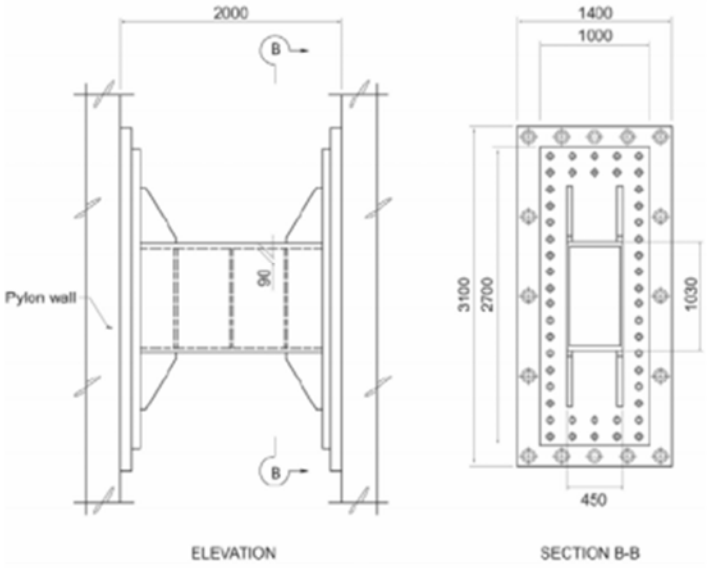


Figure A-35 Shear Link Dimensions in SFOBB (Goodyear and Sun , 2003)

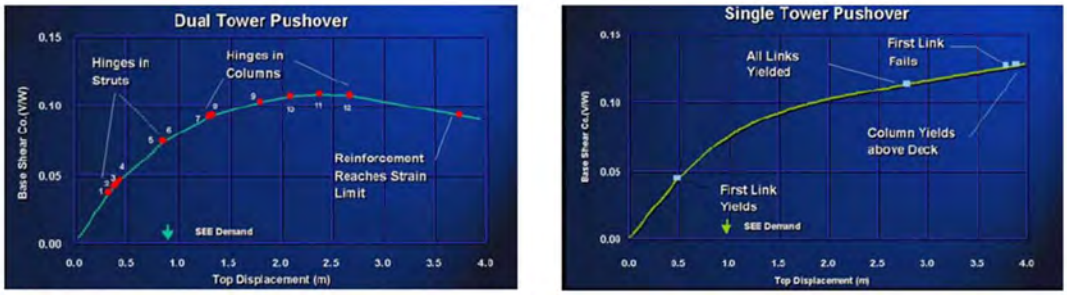


Figure A-36 Pushover Curves for the Tower: a) With Shear Links; b) Without Shear Links (Goodyear and Sun, 2003)

Main factors that affect the energy dissipation performance of shear links are plate buckling and strength degradation. Chen Z. et al. (2006) proposed a two-way stiffened (both in longitudinal and transverse directions) shear link. These shear links were supposed to sustain large deformation without pinching and consequent strength degradation. A series of inelastic large deformation analyses using a simple hysteretic model were performed, taking into account geometric and material imperfection of the components. Effects of several structural parameters, e.g. the web slenderness, are investigated through sensitivity studies and suitable ranges for these parameters were also suggested for design purposes.

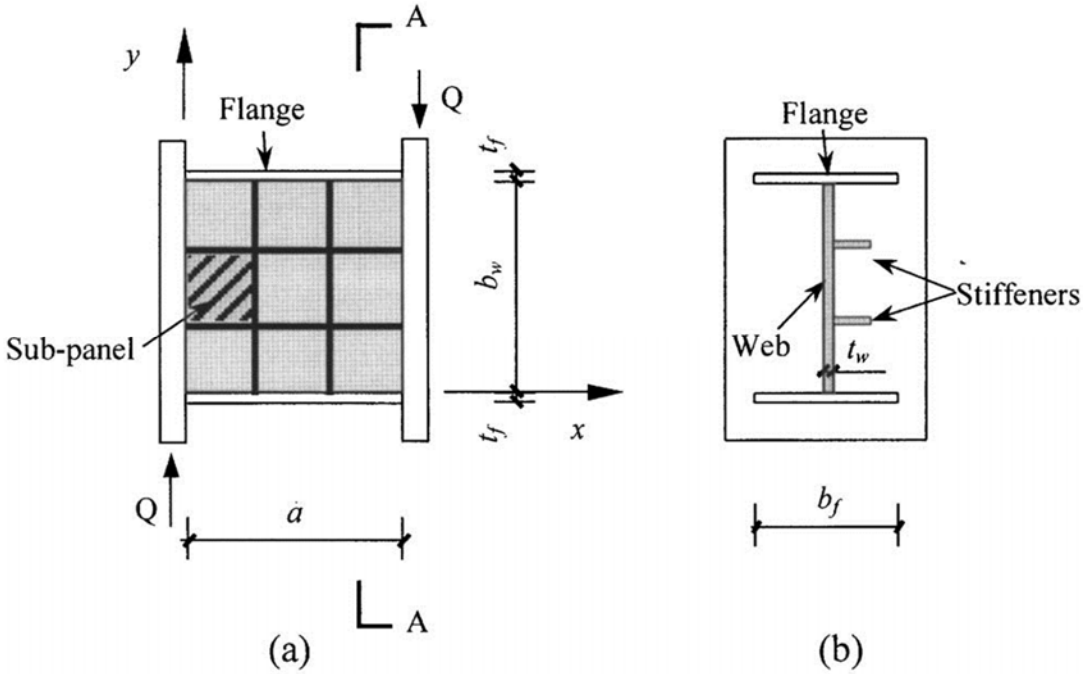


Figure A-37 Stiffened Shear Link with Two Pairs of Longitudinal and Transverse Stiffeners: (a) Elevation and (b) View A-A (Chen Z. et al. ,2006)

Shear links different than those typically used in EBF has also been shown to be effective hysteretic energy dissipators. A sketch of a prototype building into which a shear panel

links with low-yield steel were incorporated is shown in figure A-38 (Nakashima M., 1995). In that prototype, the story height and shear panel links height were taken to be 4m and 1.2 m, respectively. Inelastic dynamic response analyses revealed that the shear panel links seldom exceeded 0.01 rad as the maximum drift angle under ground motions equivalent to the ultimate earthquake design forces. Analytical models proposed were in good agreement with experimental results of systems having variable loading conditions and width-to-thickness ratio. The models can accurately predict strain-hardening behavior and stiffness degradation of these shear panel links. Figure A-40 shows the normalized horizontal forces vs deformation relationship obtained from the cyclic loaded tests of the detailed specimens. Significant strain hardening was observed during cycles at the same deformation amplitude as well as under increasing deformations.

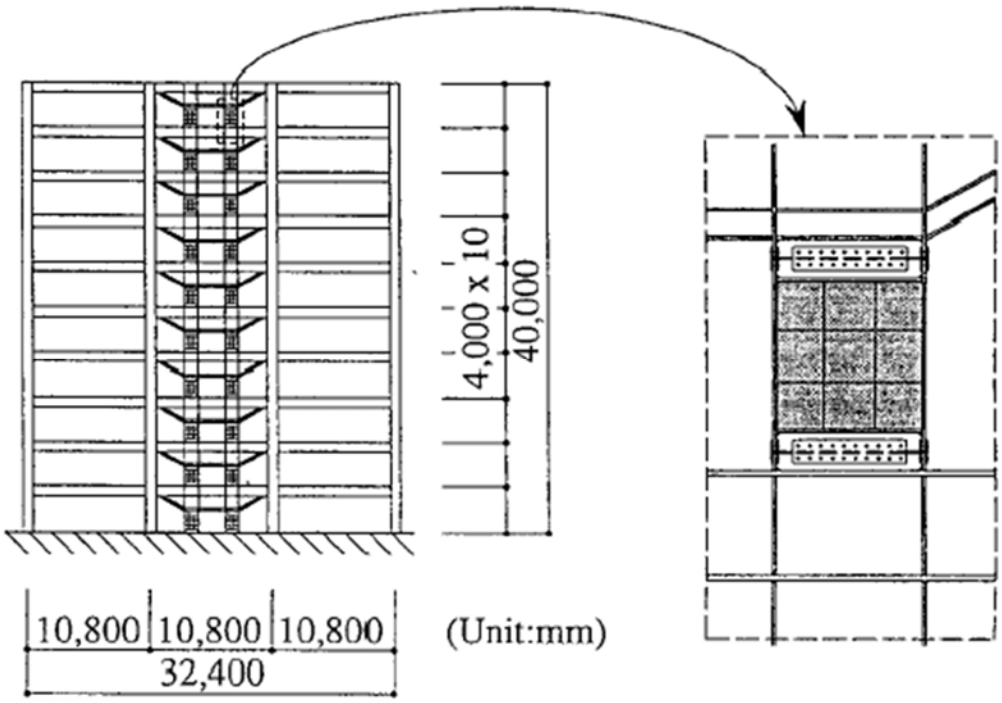


Figure A-38 Prototype Building Including Shear Panel Links With Low-Yield Steel (Nakashima M.,1995)

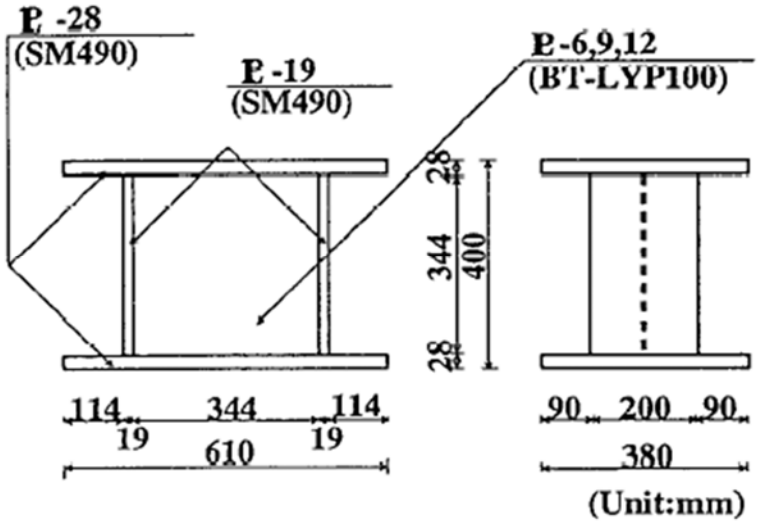


Figure A-39 Shear Panel Links Details And Dimensions Of Test Specimens (Nakashima M.,1995)

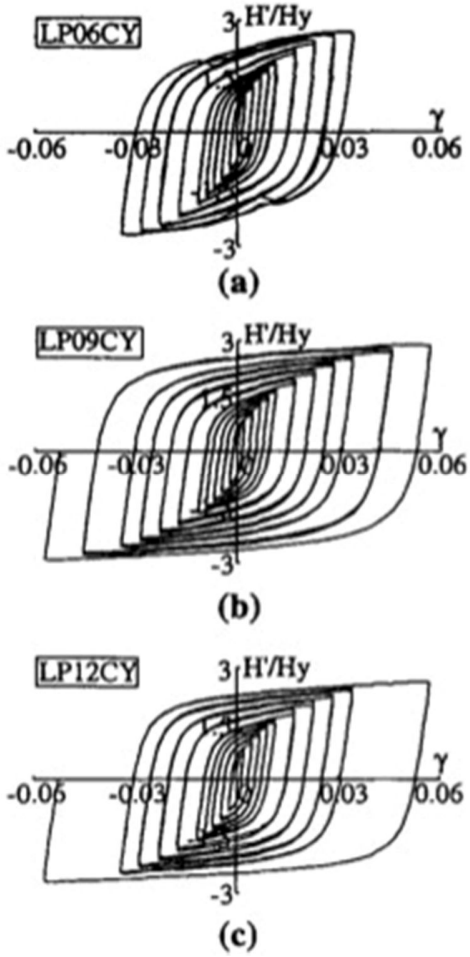


Figure A-40 Normalized Horizontal Forces Vs Shear Deformation Relationships In The Cyclic Loaded Tests (Nakashima M.,1995)

Shear links was places vertically and used in the ductile end-diaphragms as a seismic retrofit strategy to protect the substructures of existing steel slab-on-girder bridges from damage during earthquakes (Zahrai and Bruneau, 1999). Simplified analytical models as well as step-by-step design procedures were developed using shear links (as steel panel in this literature) in the inverted Y-bracing configuration as shown in figure A-41. Zahrai and Bruneau (2000) presented experiments results on the steel link specimen. The resulting hysteretic curves showed good energy dissipation. Link rotation angle of 0.08 to 0.11 rad corresponded to average ductility of 8 to 10 before failure. Shear links visibly deformed as a parallelogram bounded by the end plates and flanges at large drifts of 1.5% (figure A-42).

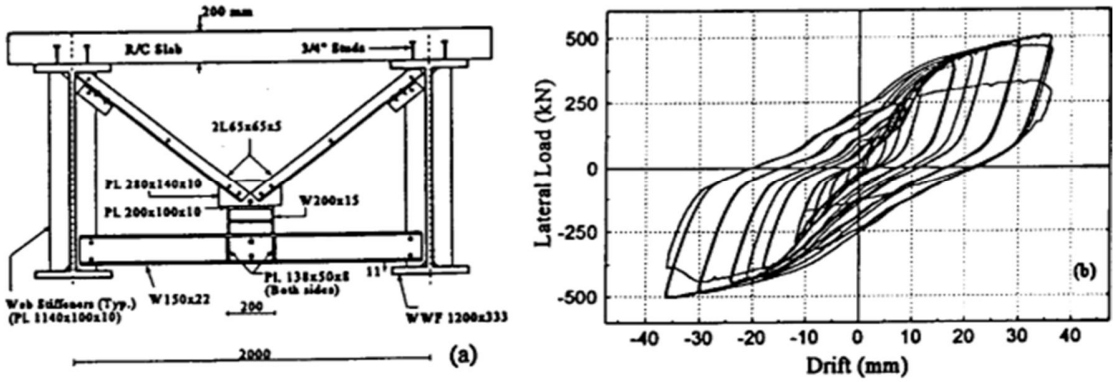


Figure A-41 Ductile End-diaphragm Specimen Having Shear Links: (a) Elevation; (b) Hysteretic Curves (Zahrai and Bruneau, 2000)

Figure A-42 Deflected Shear Links and Visible Buckling in the Flanges (Zahrai and Bruneau, 2000)

An experimental and numerical study of using shear links in the inverted Y-bracing configuration for the seismic protection of existing RC structures was carried out by Mazzolani, F.M. (2008). Figure A-43 and A-44 show the tested structure configuration. Three tests have been conducted on the same RC frame of shear links with changed cross

sections and connection details. Shear links without accounting for capacity design criteria had the failure occurred due to the bolted joint, accompanied by large flexural deformation in the flanges. The base shear –interstorey drift relationship at the first level of the structure is presented in figure A-45. When overstrength coefficient for the shear links and capacity design criteria were both considered, the cyclic behavior was extremely stable with good energy dissipation due to the large shear yielding in the link (figure A-46), though shear failure in the bolts still happened. The finite element analysis of the structure matched the experimental results with good approximation.

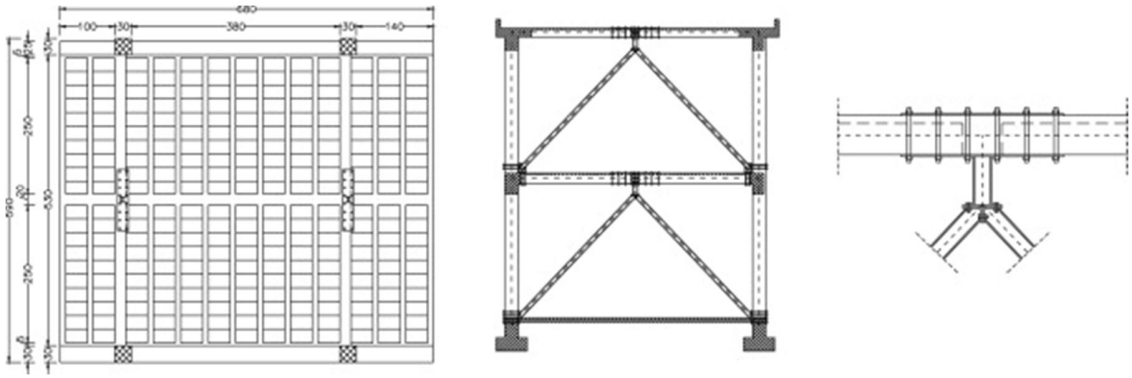

Figure A-43 Basic Geometry of the RC Structure and Typology of the Eccentric Bracing Retroffing System (Mazzolani, F.M., 2008)

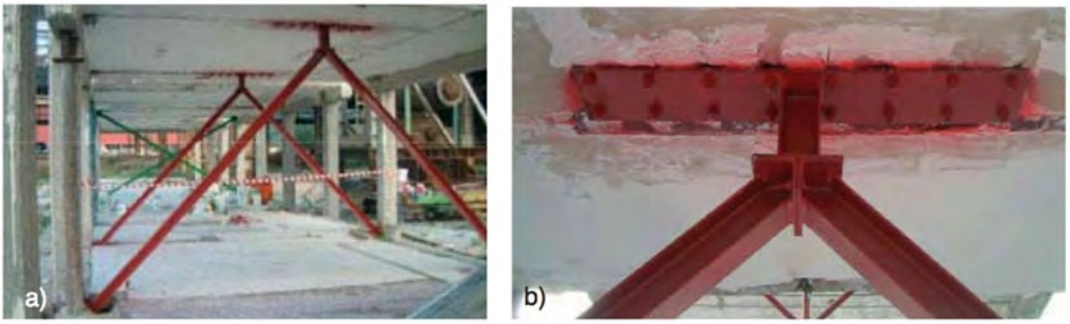


Figure A-44 Structure Configuration of Shear Links Used in the system: (a) Combination with the Braces; (b) Detail of Connections (Mazzolani, F.M., 2009)

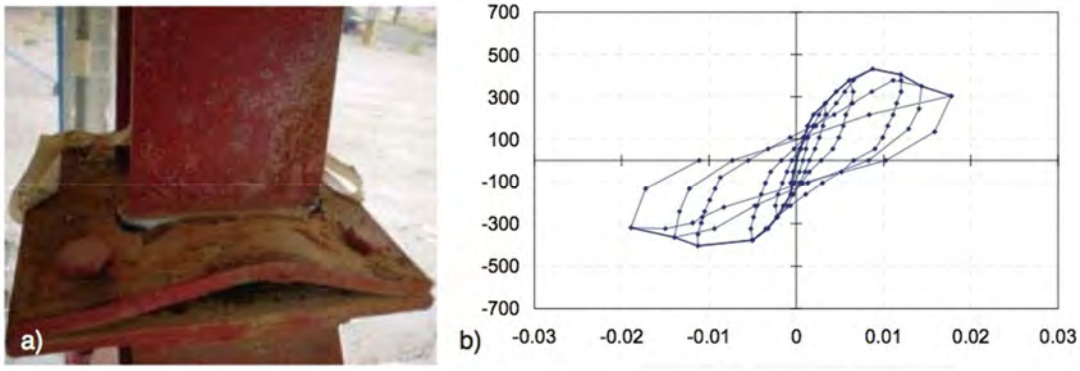


Figure A-45 First Test (a) Failure Mode; (b) Experimental Response in terms of "Base Shear- Interstorey Drift" Curve (Mazzolani, F.M., 2009)

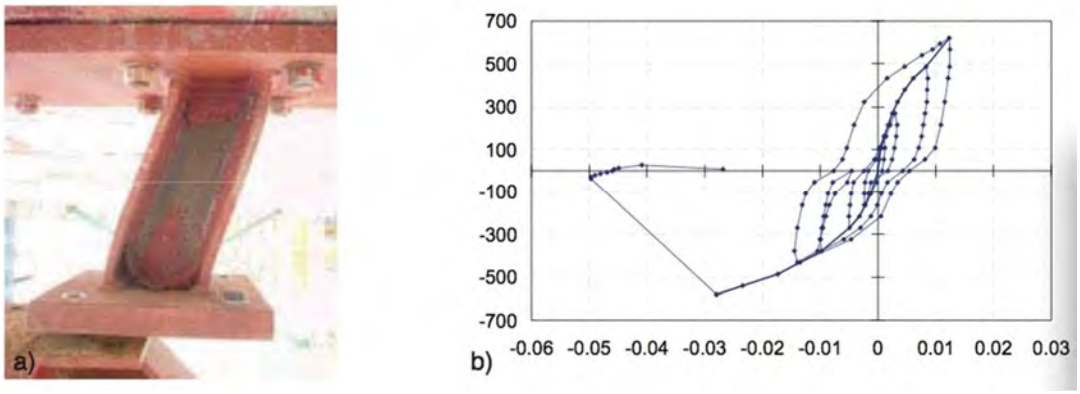


Figure A-46 Third test (a) failure mode; (b) experimental response in terms of "base shear- interstorey drift" curve (Mazzolani, F.M., 2009)

## A.2.3 Steel Plates Added Damping and Stiffness Device

### A.2.3.1 Triangular Plate Added Damping and Stiffness Device (TADAS)

Triangular plate energy dissipaters were originally developed in New Zealand and used as damping elements in several base isolation application (Boardman et al 1983). Later, they were used in buildings in the form of tapered or triangular damping and stiffness devices. TADAS consists of a number of identical triangular structural steel plates positioned in parallel. The base of each triangular plate is welded into a rigid base plate to approximate a fixed end condition, while a slotted pin connection is employed at the apex to ensure free movement in the axial direction. There would not be rotational restraint at the top of the brace connection, and potential instability of the triangular plates due to excessive axial load. Figure A-48 shows the details of TADAS devices studied by Tsai et al. (1993).

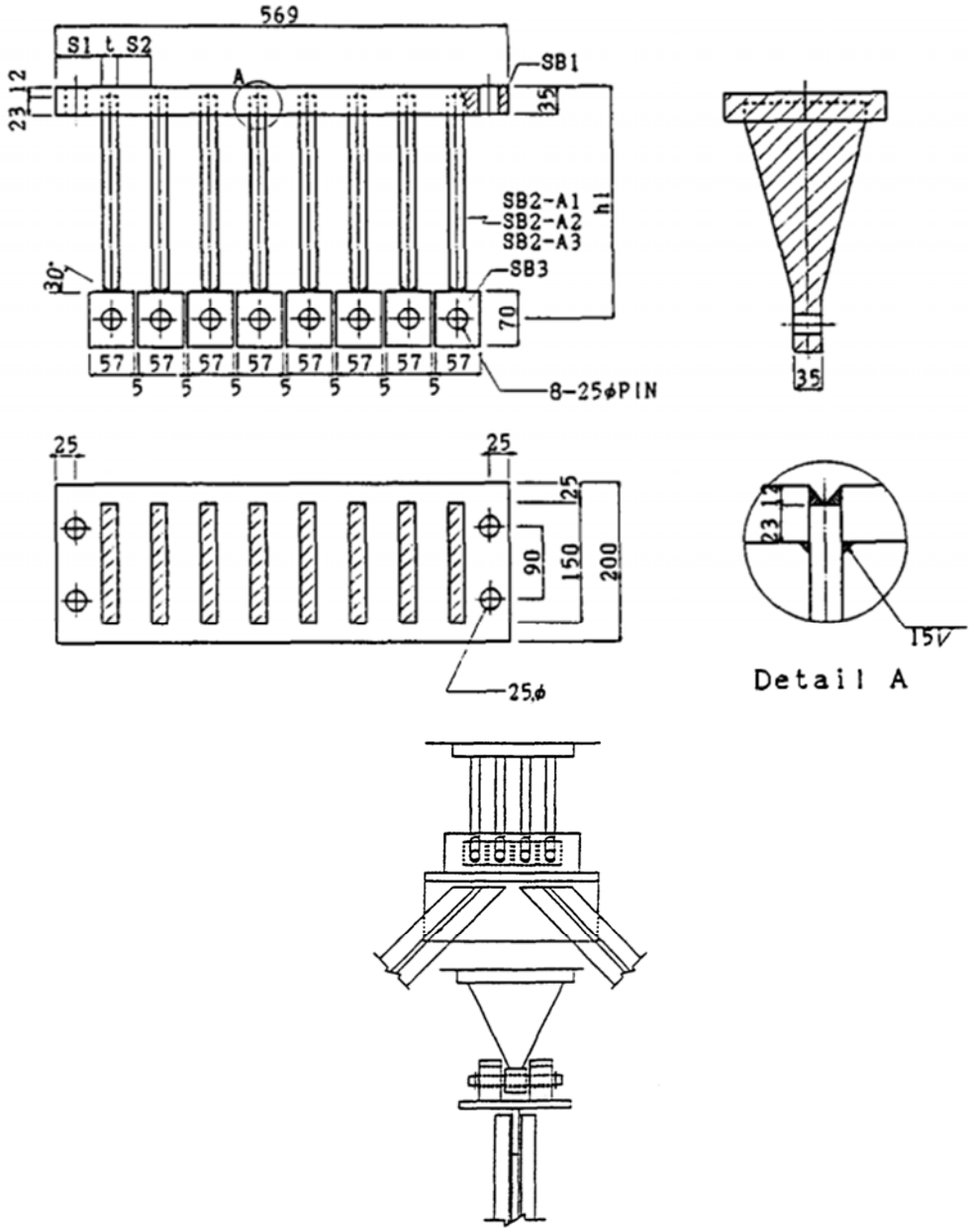


Figure A-47 Details of Steel Welded TADAS devices (unit in mm) (Tsai et al. ,1993)

Tsai et al. (1993) described the mechanical properties of the TADAS devices, and compared their analytical characteristics with experimental results obtained from pseudo-dynamic tests of a two-story TADAS frame. A properly welded TADAS can sustain a large number of yielding reversals without any stiffness or strength degradation. The plastic rotational capacity of the TADAS system could exceed 0.25 radians. Typical hysteretic loops for TADAS elements are shown in figure A-48. A design methodology example was developed for TADAS application in earthquake-resistant building constructions.

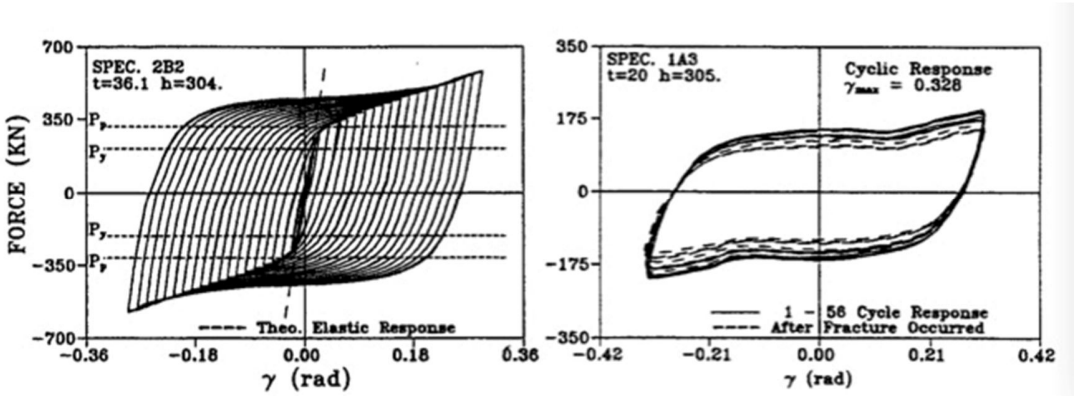


Figure A-48 Force Versus Deformation Relationships of the Tested Welded TADAS Devices (Tsai et al., 1993)

Besides the shear links mentioned in section A.2.2 used in the ductile steel bridge end-diaphragms by Zahrai and Bruneau (1999, 2000), TADAS system was also developed and tested. Full-scale ductile diaphragm specimens were constructed and tested using conventional reversed cyclic inelastic loading as well as pseudo-dynamic testing as the specimen with shear links. The TADAS specimen was subjected to 21 cycles of lateral loading before failure occurred at 4% drift. The specimen and its lateral load-deflection curves are shown in figure A-49. The hysteretic loops experience pinching due to connection slippage and existing gaps between the top of TADAS plates and reaction points.

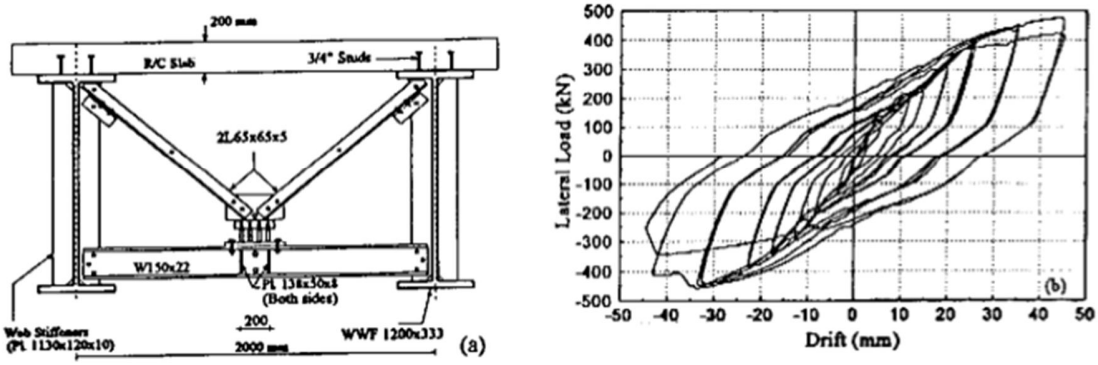


Figure A-49 Ductile End-diaphragm Specimen Having TADAS: (a) Elevation; (b) Hysteretic Curves (Zahrai and Bruneau, 2000)

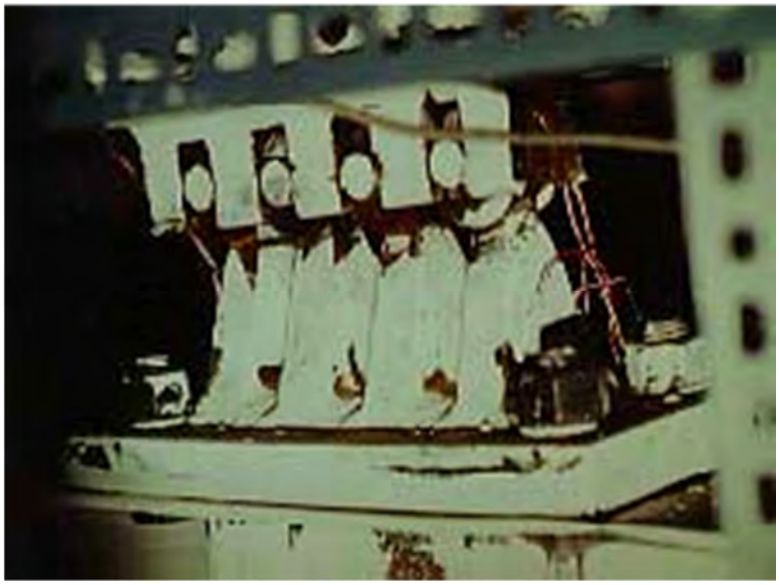

Figure A-50 TADAS Plates under Huge Flexure at 2% Drift (Zahrai and Bruneau, 2000)

### A.2.3.2 Steel Plate Added Damping and Stiffness Device (ADAS)

ADAS devices were introduced by Bechtel Power Corporation and CounterQuake Corporation. It features X-shaped individual plates which are bolted together at both ends to approximate a fixed-fixed support condition. A typical ADAS device is presented in Figure A-51. ADAS resist the force by deflecting and yielding in double curvature through the entire plate surface. ADAS can sustain repeated inelastic deformation by avoiding concentrations of yielding and premature failure.

Extensive experimental studies have been carried out to investigate the behavior of ADAS elements in dissipating energy (Bergman and Goel, 1987; Whittaker et al., 1991). Shake table tests of a three-story moment-resisting steel frame demonstrated that the presence of ADAS element improved the behavior of the frame by increasing its stiffness, strength, and ability to dissipate energy. The inter-story drifts in the frame were reduced by 30 to 70 percent with the addition of ADAS elements. The ratio of base shears in the structure with ADAS elements to those without ADAS ranged from 0.6 to 1.25. Shear forces were primarily resisted by ADAS elements and their supporting braces. The ADAS elements yield in a predetermined manner and relieve the frame from excessive ductility demands.

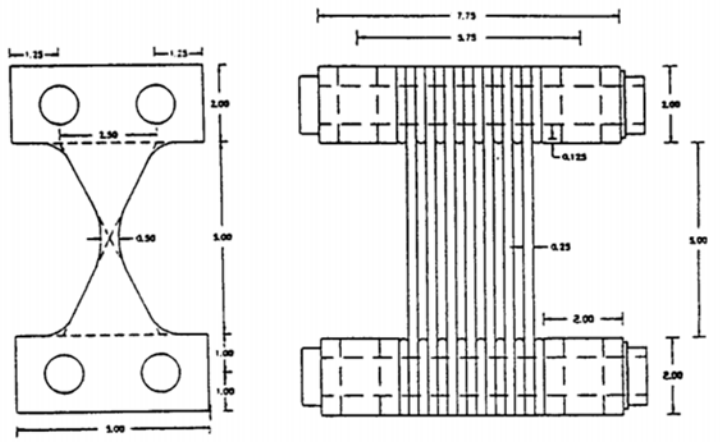

Figure A-51 ADAS device (Whittaker et al., 1991)

Xia (1992) showed that the energy dissipation capacity of a building could be substantially increased by ADAS while the demand on the framing members of the structure was reduced. ADAS can exhibit stable hysteresis for displacement amplitudes as large as 14 times the yield displacement of the device. In the displacement range of 6 times the yield displacement of the device, and extremely large number of yielding reversals (over 100 cycles in the tests) can be sustained.

Alehashem et al. (2008) investigated the behavior and performance of steel structures equipped with ADAS and TADAS metallic dampers and compared them with conventional earthquake-resisting steel structures such as CBF, CHEVRON and EBF systems. A series of numerical simulations of a multi-story steel building was performed using DRAIN-2DX program. Results show suitable behavior of systems equipped with ADAS and TADAS and main damage occur in metallic dampers to keep the main structure safe.

Table A-4 below shows the early structural application of ADAS in North America (Soong, 1995). The Wells Fargo Bank Building in San Francisco, CA was retrofitted with ADAS (Perry et al., 1993). The building was constructed in 1967 as a two-story nonductile concrete frame structure and got damaged in the 1989 Loma Prieta earthquake. Seven ADAS devices were added to the retrofit plan along with the interior columns and a shear wall being strengthened. Equivalent linear approximate model of ADAS was used in a following 3-D response spectrum analyses. The final design was also verified by DRAIN-2D nonlinear time history analyses. It was indicated by both the linear and nonlinear analyses that the retrofit design was table and all the seismic design criteria were satisfied.

Table A-4 Structural Application of ADAS in North America (Soong, 1995)

| Name and type of structure | Country / City | Type and number of dampers | Date | Load | Additional information |
|---|---|---|---|---|---|
| Wells Fargo Bank<br>Nonductile RC frames<br>2-story building (1967) | USA / San Francisco | ADAS (yielding steel)<br>Total: 7<br>Design yield force: 150 kips | 1992 | seismic | Retrofit; damaged in 1989 Loma Prieta earthquake.<br>3D linear and 2D nonlinear analyses performed. |
| Izazaga #38-40<br>RC frames with brick infilled end walls.<br>12-story building + basement (1970s) | Mexico / Mexico City | ADAS (yielding steel)<br>Total: approx. 200 | 1990 | seismic | Retrofit; damaged in 1985, 1986, and 1989 earthquakes.<br>Retrofit complete during building occupation.<br>2D nonlinear time-history analysis performed.<br>Maximum inter-story drifts reduced by 40% |
| Cardiology Hospital Bldg.<br>RC frames<br>(1970s) | Mexico / Mexico City | ADAS (yielding steel)<br>Total: 90 | 1990 | seismic | Retrofit; damaged in 1985 earthquake.<br>Operational hospital while retrofitting.<br>Nonlinear time-history analysis performed. |
| Reforma #476 Bldg.<br>Mexican Institute for Social Security.<br>RC frames.<br>3 building complex,<br>10 stories + basement.<br>(1940s) | Mexico / Mexico City | ADAS (yielding steel)<br>Total: approx. 400 | 1992 | seismic | Retrofit; significant damage in 1957 earthquake.<br>2D nonlinear time-history analysis performed. |

## A.2.4 Steel Slit Dampers

Kajima Corporation developed yielding devices (a.k.a. honeycomb dampers) for in highrise buildings and large-scale structures. Steel plates with honeycomb-shaped openings are shown in figure A-52(a). Honeycomb dampers applied continuously between stories through the height of a 29 story hotel and apartment building were to function only for the loads acting within its installation plane. Cyclic load tests of specimen with 135 mm were capable of maximum deflection angles of 1/15 to ¼. The load-deformation curve under cyclic loading with increasing amplitude is presented in figure A-52(b). The vertical axis indicates the normalized load divided by the yielding load.

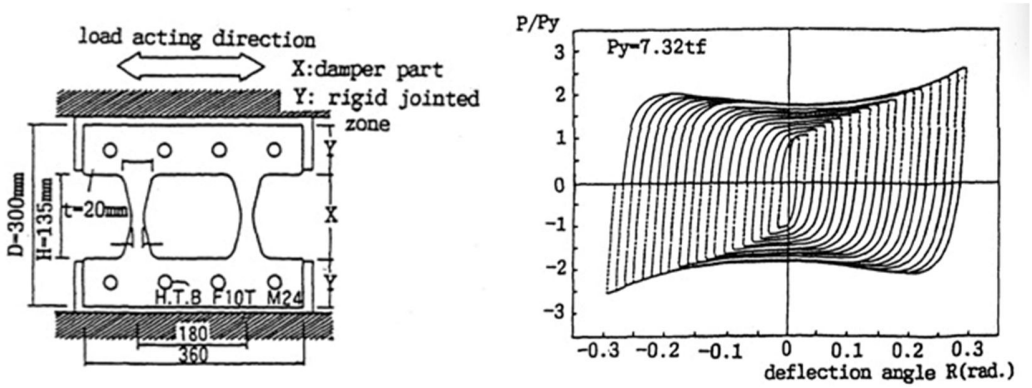


Figure A-52 (a) Test Specimen Of Honeycomb Damper And (b) Hysteretic Loops Under Cyclic Loading (Kobori Et Al. 1992)

Sugiyama (1998) presented a case study corresponding to a 26-storey building (98m in height) installed with Steel Slit Dampers (SSD). The fundamental period of the building reduced from 2.46s to 1.85s in the weak direction, along with reduction of lateral displacement. The frame response (in terms of energy dissipated) was found decreased,

but not eliminated.

The steel slit dampers similar to the honeycomb dampers described above are fabricated from standard structural wide-flange sections with a number of slits cut from the web and behave like the honeycomb dampers (figure A-53). A number of strips are left between the two flanges in a vierendeel truss arrangement. The slits can be rounded at their ends to reduce the stress concentration in reentrant-corners. Bolt holes are drilled on each flange for the connection to the parent structure. The device is a weld-free design, thus eliminating the uncertainties and imperfections associated with welding. The devices dissipate energy by flexural yielding of a series of strips as shown in figure A-54. A nonlinear finite element analysis studied by Chan et al. (2007) gave accurate predictions of the elastic and post-yield behavior of the devices. Strain-hardening made the ultimate strength larger than their respective yield strength by a factor of 2.0. Cyclic tests demonstrated stable hysteretic behavior. Large plastic strain concentrations at strip ends caused the specimens to fail by fracture.

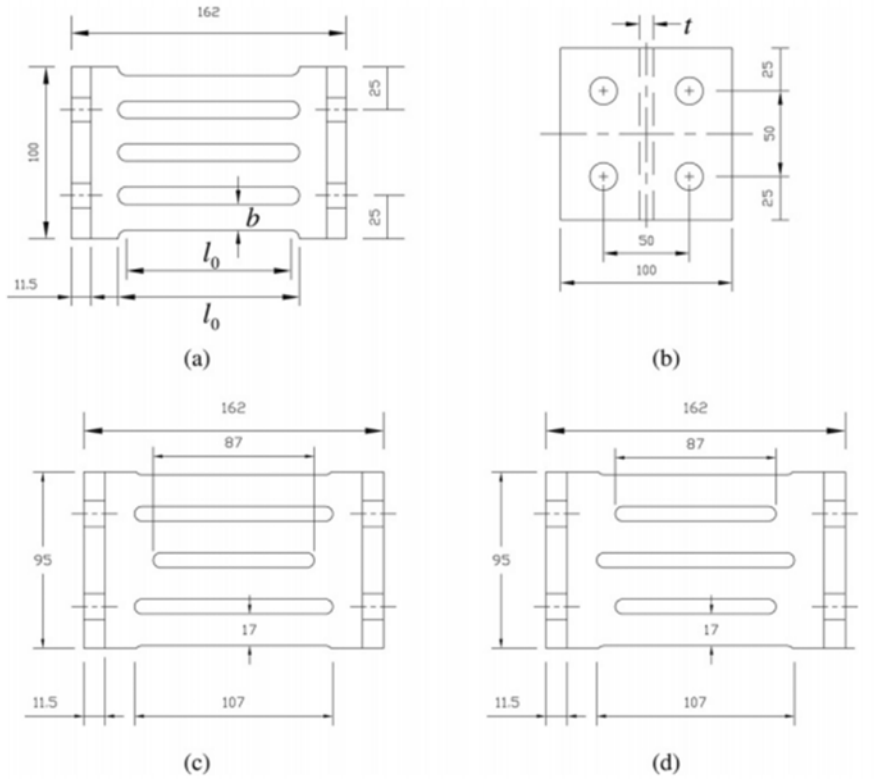


Figure A-53 Geometry of Steel Slit Dampers (Chan et al.,2007)

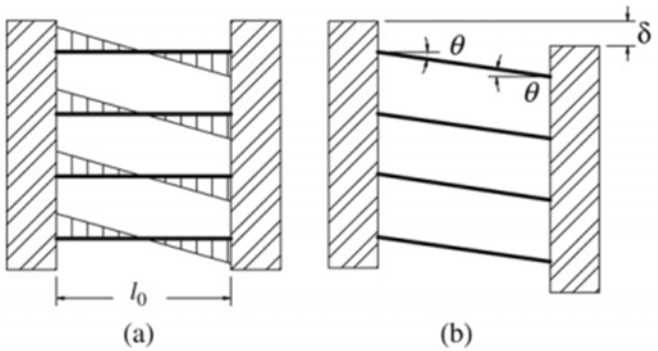

Figure A-54 (a) Bending Moment in SSD and (b) Deformed Shape of SSD (Chan et al., 2007)

## A.2.5 Steel Plate Shear Link (SPSL)

The SPSL proposed by El-Bahey and Bruneau (2010) composes of a steel plate and concrete encasement to restrain out-of-plane buckling. The steel plate is designed to yield in shear, at stress equal to 0.6 Fy. The configuration of the restrained SPSL is shown in figure A-55.

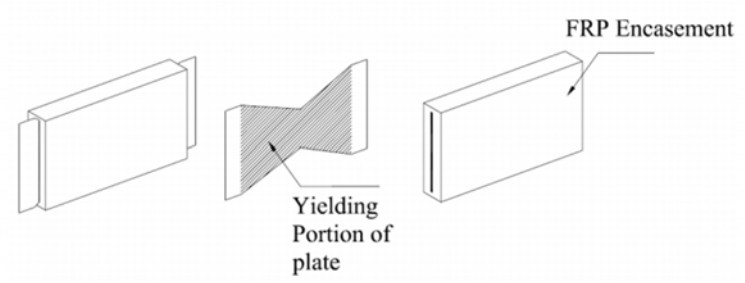

Figure A-55 Proposed SPSL Link Sketch (El-Bahey and Bruneau, 2010)

Shear yielding of SPSL is assumed to occur over a depth of $y_o$ shown in figure A-56. The effect of axial load and shear on the cross section plastic moment capacity is neglected. Shear yielding would occur across the middle part of the web accompanied by flexural yielding in the wedge parts for equilibrium.

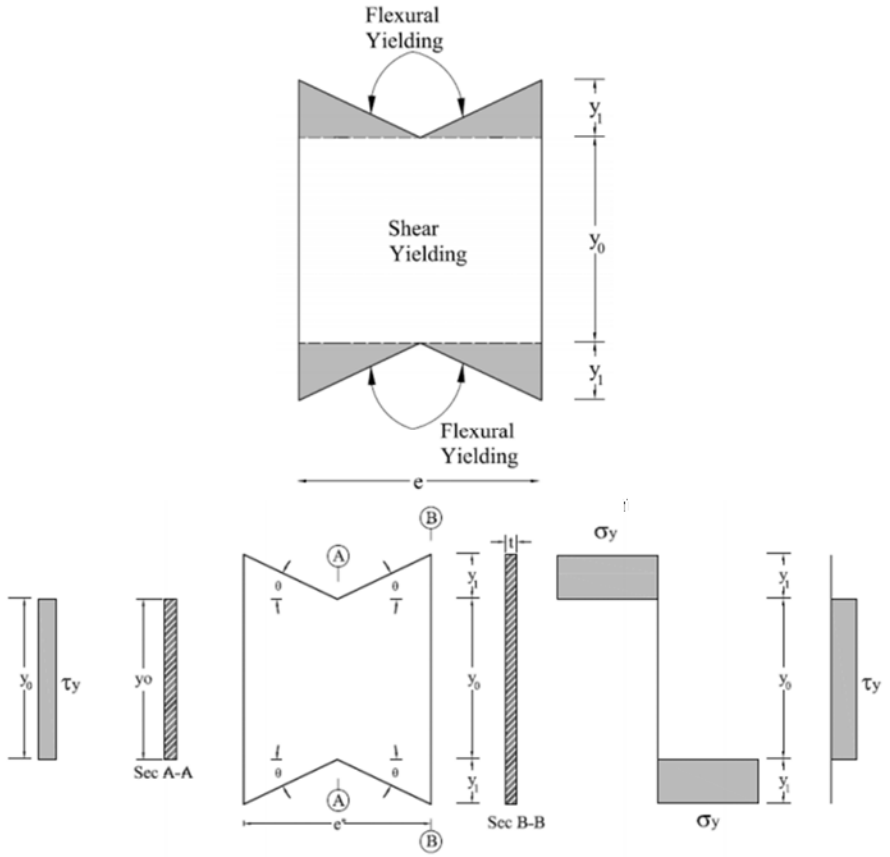


Figure A-56 Proposed Yielding in Steel Plate Shear Links (El-Bahey And Bruneau, 2010)

Steel plate shear links (SPSL) were then introduced between two bi-steel columns to act as a SF dissipating the seismic energy through inelastic shear deformation. The prototype bridge pier (figure A-57 and A-58) was subjected to quasi-static testing. Adding these SF increased stiffness and strength by about 40% and substantially increased the amount of hysteretic energy dissipated by the frame, while keeping the columns elastic up to the target design displacement. Uniaxial cyclic tests were performed on SPSLs with various geometry and lateral restraint conditions. Finite element model were also generated to replicate the observed hysteretic behavior of the SPSLs being tested.

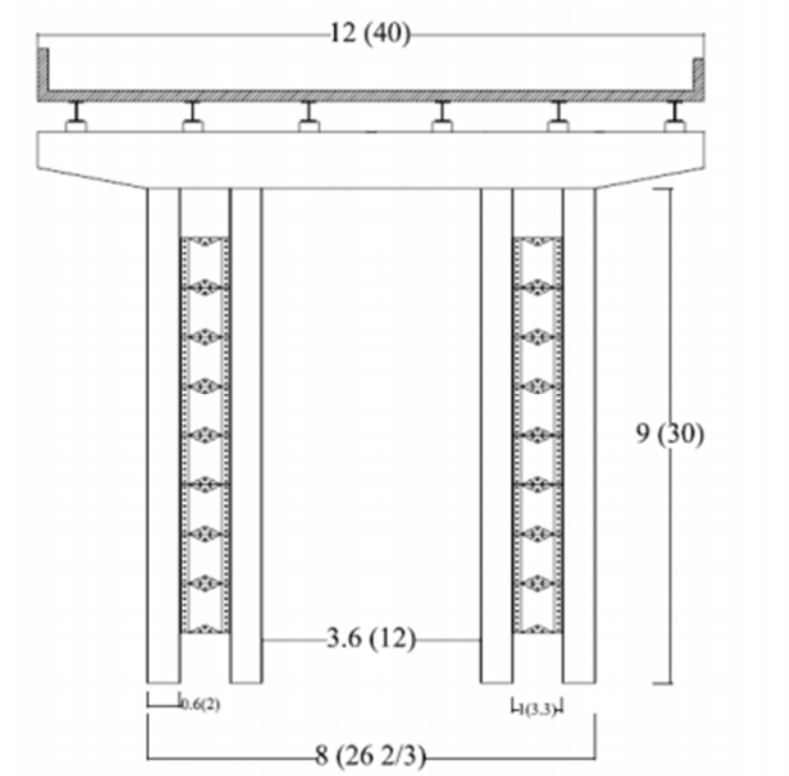


Figure A-57 Prototype RC Bridge Bent after Introducing SPSLs (El-Bahey and Bruneau, 2010)

Figure A-58 Specimen Setup With SPSLs (El-Bahey and Bruneau, 2010)

## A.2.6 Steel Plate Shear Wall (SPSW)

Steel Plate Shear Wall (SPSW) systems generally consist of a steel plate wall, two boundary columns and horizontal floor beams as shown in figure A-59. The main function of the steel plate shear wall is to resist the horizontal storey shear and overturning moments caused by lateral loads. A properly designed and detailed shear wall is very ductile and has a relatively large energy dissipation capacity. SPSW systems also have relatively high initial stiffness, and are thus very effective in limiting the lateral drift of structures.

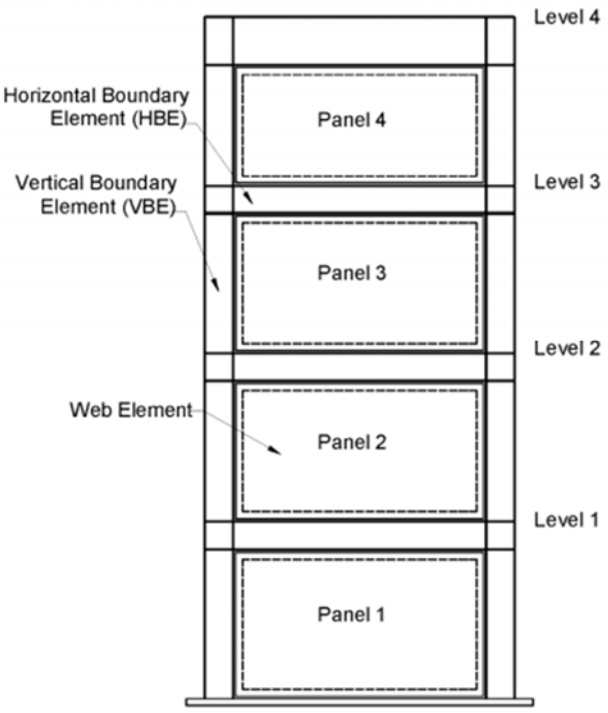


Figure A-59 Schematic of Special SPSW (AISC, 2005)

In the early applications of SPSW in US and Japan, the walls had numerous vertical and horizontal stiffeners. The stiffeners are there to prevent elastic and overall buckling; and to increase the shear buckling strength of the wall. Due to the high cost and time consumption of welding stiffeners in the steel fabrication shops, research and testing of SPSW have been indicated to use them alone due to the post-buckling loading capacity. A very ductile, desirable and efficient behavior of this unstiffened, slender-web SPSW has been observed.

There are numerous experimental and analytical studies investigating the behavior of unstiffened SPSW in the past 30 years. SPSW has been included as a “Basic Seismic Force Resisting System” in ASCE 7 and AISC 341. The web plate of SPSW has negligible compression strength and thus, shear buckling occurs at low levels of loading. Lateral loads are resisted through diagonal tension in the web plate rather than shear. Tension field are developed as shown in figure A-60. Boundary elements are designed to

permit the web plates to develop significant diagonal tension and reach their expected yield stress across the entire panel. Much of the research has focused on designing and modeling of the SPSW web plates, analysis methods, and validation of satisfactory cyclic inelastic and seismic performance. Alternate ways to analyze and design SPSW horizontal and vertical boundary elements (HBEs and VBEs) can also be found in Lopez-Garcia & Bruneau (2006), Berman & Bruneau (2008). An extensive summary of the research has been presented in Sabelli & Bruneau (2007).

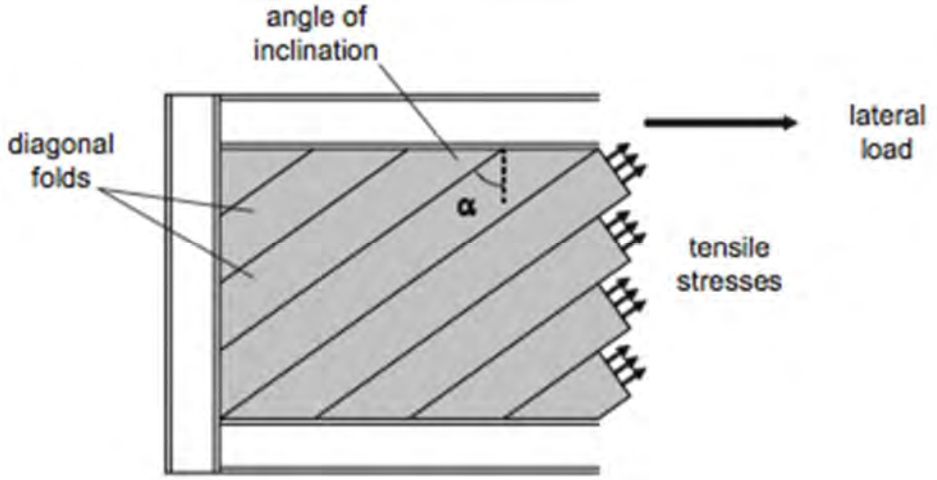


Figure A-60 Idealized Tension-Field Action in a Typical SPSW System (Sabelli & Bruneau, 2007)

SPSW have been used in a large number of buildings, including in the United States, Canada, Mexico and Japan. Building types range from single-family residential to high-rise construction (figure A-61 and A-62). In addition to new construction, SPSW with its large enormous stiffness and stiffness have been added to retrofit existing frame buildings, yet there is still no application in bridges.

(a)

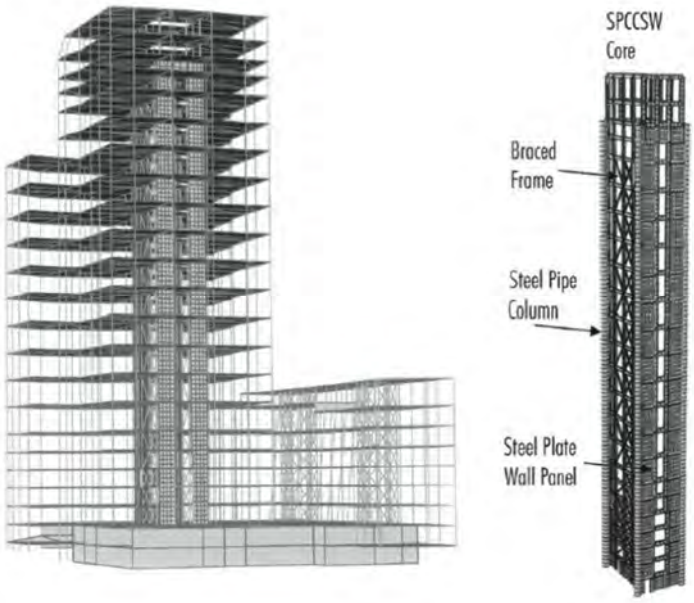


(b)

Figure A-61 U.S. Federal Courthouse, Seattle (Sabelli & Bruneau, 2007)

Figure A-62 Residential Building With SPSW In San Mateo County, CA (Sabelli & Bruneau, 2007)

Multi-hazard resistant Steel Plate Shear Wall (SPSW) bridge pier concept is put forward by Keller & Bruneau (2009). SPSW is introduced into bridge application to improve performance under multiple extreme hazards (earthquakes, vehicle collisions, tsunamis or storm surges, and blast). Steel plate shear walls between the bridge piers add redundancy

to the system because of their ductile nature, and also they are easy to repair (figure A-63). Following the development and design of a SPSW box pier concept that considered each hazard by use of simplified analyses, advanced nonlinear finite element analyses were conducted to verify and validate its behavior.

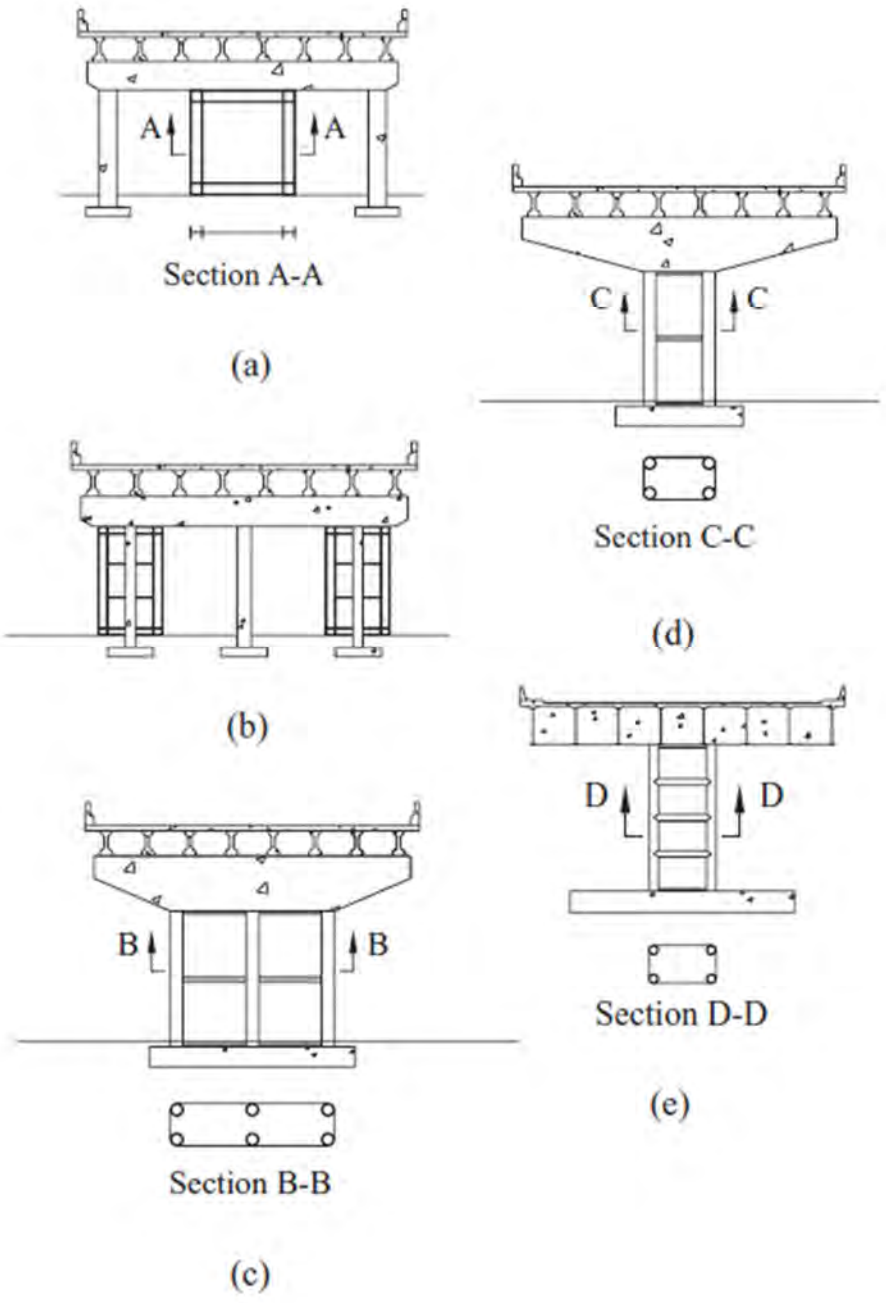


Figure A-63 Progression of Multi-Hazard Resistant SPSW Bridge Pier Concept (Keller And Bruneau, 2009)

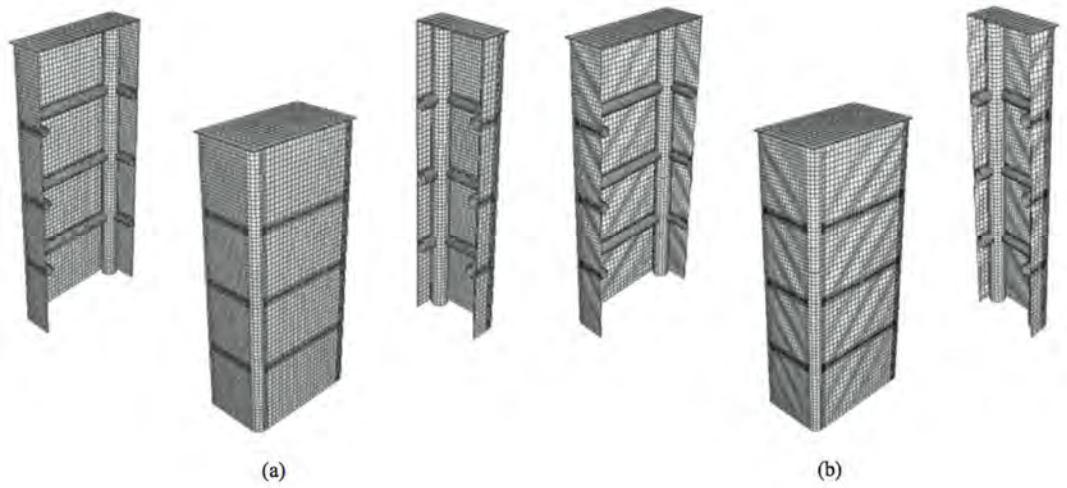


Figure A-64 Finite Element Model Showing (A) The Pier in its Undeformed State; And (B) The Pier After Being Laterally Loaded to its Capacity (Keller and Bruneau, 2009)

# Reference for the literature review:

Aiken, I.D., Clark, P.W., Tajirian, F.F., Kasai, K., Kimura, I., and Ko, E. (2000), "Unbonded Braces in the United States — Design Studies, Large-Scale Testing and the First Building Application," Proceedings, Japan Passive Control Symposium, Tokyo Institute of Technology, Japan

AISC (2005). "Seismic Provisions for Structural Steel Buildings." ANSI/AISC 341-05 and ANSI/AISC 341s1-05. American Institute of Steel Construction, Chicago, Illinois.

Alehashem S.M.S., Keyhani A., Pourmohammad H., (2008), "Behavior and performance of structures equipped with ADAS & TADAS Dampers," The 14th World Conference on Earthquake Engineering, Beijing, China, October, 2008

Anagnos T., (2011), "Risk Mitigation for older Concrete Buildings Presentation,", May 2, 2011

Bergman, D.M. and Goel, S.C. (1987), Evaluation of Cyclic Testing of Steel-Plate Devices for Added Damping and Stiffness, Report No. UMCE 87-10, The University of Michigan, Ann Arbor, MI.

Berman J.W., Bruneau M.(2008), "Capacity Design of Vertical Boundary Elements in Steel Plate Shear Walls," Engineering Journal, First Quarter, 57-71

Boardman, P.R., Wood, B.J., and Carr, A.J. (1983), "Union House- A Cross Brace Structure With Energy Dissipators," Bull. N.Z. Nat. Soc. For Earthquake Eng., 16(2), June

Carden, L., Itani, A., PE, F., and Buckle, I. (2006). "Seismic performance of steel girder bridges with ductile cross frames using buckling-restrained braces." Journal of Structural Engineering, 132, 338.

Chan R.W.K., Albermani F. (2007), "Experimental study of steel slit damper for passive energy dissipation," Engineering Structures, 30,1058-1066

Chan R.W.K., Albermani F., Williams M.S. (2009), "Evaluation of yielding shear panel device for passive energy dissipation," Journal of Constructional Steel Research, 65,260-268

Chen Z., Ge H., Usami T., (2006), “Hysteretic Model of Stiffened Shear Panel Dampers,” Journal of Structural Engineering, March, 2006

Clark, P., Aiken, I., Kasai, K., and Kimura, I. (2000) "Large-scale testing of steel unbonded braces for energy dissipation." Proceedings of the Structural Congress, Philadelphia, Pennsylvania.

Connor, J.J., Wada, A., Iwata, M., and Huang, Y.H. (1997). “Damage-Controlled Structures. I: Preliminary Design Methodology for Seismically Active Regions.” Journal of Structural Engineering, Volume 123, No. 4, ASCE, pp. 423-431.

Dargush G.F., Soong T.T. (1995) Behavior of metallic plate dampers in seismic passive energy dissipation systems. Earthquake Spectra, Volumn 11, No.4

El-Bahey, S., Bruneau, M., (2010). “Analytical Development and Experimental Validation of a Structural-Fuse Bridge Pier Concept”, Technical Report MCEER-10-0005, MCEER, University at Buffalo, Buffalo, NY.

Engelhardt, M.D. and Popov, E.P., (1989), "Behavior of Long Links in Eccentrically Braced Frames", Report No. UCB/EERC-89/01, Earthquake Engineering Research Center, Berkeley, CA.

FEMA (2000b), FEMA 356, Prestandard and Commentary for the Seismic Rehabilitation of Buildings, Building Seismic Safety Council for the Federal Emergency Management Agency, Washington, DC

Fintel, M., and Ghosh, S.K. (1981). “The Structural Fuse: an Inelastic Approach to Seismic Design of Buildings.” Civil Engineering. Volume 51, No. 1, ASCE, pp. 48-51.

Goodyear, D., and Sun, J. (2003). "New developments in cable-stayed bridge design, San Francisco." Structural Engineering International, 13(1), 59-63.

Ghobarah A, Abou Elfath H. (2001) Rehabilitation of a reinforced concrete frame using eccentric steel bracing. Engineering Structures, 23, 745-755

Hamada N., Nishioka T., and Kanaji H.,(2007), “Seismic Retrofitting of Long-span Truss Bridge-Minato Bridge Using Damage-control Technologies,” Steel Construction Today & Tomorrow, No.19, pp.12-16

Hjelmstad, K.D. and Popov, E.P., (1986), "Seismic Behavior of Active Beam Links in Eccentrically Braced Frames", Report No. UCB/EERC-86/01, Earthquake Engineering Research Center, Berkeley, CA.

Huang, Y.H., Wada, A., Iwata, M., Mahin, S.A., and Connor, J.J. (2002). “Design of Damage-controlled Structures.” Innovative Approaches to Earthquake Engineering, WIT Press, pp. 85-118.

Islam, S., Skokan, M., and Huang, S. (2006) "Innovative Hi-tech Solution for a Concrete Residential High Rise Tower."

Kanaji, H., Kitazawa, M., Suzuki, N., (2005). “Seismic Retrofit Strategy using Damage Control Design Concept and the Response Reduction Effect for a Long-span Truss Bridge”, US-Japan Bridge Workshop, 2005.

Kasai, I. and Popov, E.P., (1983), "A study of Seismically Resistant Eccentrically Braced Steel Frame Systems", Report No. UCB/EERC-83/15, Earthquake Engineering Research Center, Berkeley, CA.

Keller, D. and Bruneau, M. (2009), “Multi-hazard resistant steel plate shear wall bridge pier concept” Taylor & Francis Group, London, ISBN 978-0-415-56326-0

Kobori, T., Miura, Y., Fukuzawa, E. et al. (1992), “Development and application of hysteretic steel dampers.” 10th World Conference in Earthquake Engineering, Balkema, Rotterdam, ISBN 9054100605

Lopez-Garcia, D., Bruneau, M., Berman, J. and Vian, D. (2005), “Steel Plate Shear Wall Buildings: Design Requirements and Research,” Proceedings of 2005 North American Steel Construction Conference, Montreal, Canada

Lopez, W., Gwie, D., Saunders, M., and Lauck, T. (2002) "Lessons learned from large-scale tests of unbonded braced frame subassemblage." Proceedings 71st Annual Convention, Structural Engineers Association of California, Sacramento, California, 171-183.

López, W.A., and Sabelli, R. (2004). “Seismic Design of Buckling-Restrained Braced Frames.” Steel Tips Report. Structural Steel Educational Council.

Mazzaolani, F.M. (2008), “Innovative metal systems for seismic ungrading of RC structures,” Journal of Constructional Steel Research 64 (2008) 882-895

Morgan, T., and Walters, M. (2004). "Innovative Approaches to Performance-based Seismic Rehabilitation of Concrete Buildings." Pacific Earthquake Engineering Research Center, College of Engineering, University of California, Berkeley

Nakashima, M. (1995). “Strain-Hardening Behavior of Shear Panels Made of Low- Yield Steel. I: Test.” Journal of Structural Engineering, Volume 121, No. 12, ASCE, pp. 1742-1749.

Oya, T., Fukasawa, T. Fujiwara, M. et al. (2009). “Practical study on a new type Buckling-Retrained-Brace,” Proceeding of the International Association for Shell and Spatial Structure (IASS) Symposium 2009, Vlencia

Perry C.L., Fierro E.A., Sedarat H., Scholl R.E. (1993). Seismic upgrade in San Francisco using energy dissipation devices. Earthquake Spectra 1993;9(3):559–79.

Popov, E.P. and Malley, J.O., (1983), "Design of Links and Beam-to-column Connections for Eccentrically Braced Steel Frames", Report No. UCB/EERC-83/03, Earthquake Engineering Research Center, Berkeley, CA.

Ricles, J. and Popov, E. P., (1987), “Dynamic Analysis of Seismically Resistant EBFs”, Report No. UCB/EERC-87/07, Earthquake Engineering Research Center, Berkeley, CA.

Roeder, C., and Popov, E. (1977). “Inelastic Behavior of Eccentrically Braced Steel Frames under Cyclic Loadings.” Report No. UCB-77/17, Earthquake Engineering Research Center, University of California, Berkeley.

Sabelli, R., Mahin, S., and Chang, C. (2003). “Seismic Demands on Steel Braced Buildings with Buckling-Restrained Braces.” Engineering Structures, Elsevier Science Ltd., Volume 25, No. 5, pp. 655-666.

Sabelli, R., Bruneau, M., (2007). “Steel Plate Shear Walls (AISC Design Guide)”, American Institute of Steel Construction, Chicago, Illinois, 144 p.

Shaw, A., and Bouma, K. (2000) "Seismic Retrofit of the Marin County Hall of Justice Using Steel Buckling-Restrained Braced Frames." Proceedings, 69th Annual Convention, Structural Engineers Association of California, Sacramento, California.

Shimizu, K., Hashimoto, J., Kawai, H., and Wada, A. (1998). "Application of Damage Control Structure using Energy Absorption Panel." Paper No. T105-2, Structural Engineering World Wide 1998, Elsevier Science, Ltd.

Sugiyama, S. (1998). "Application of Hysteresis Steel Dampers to Tall Building." Paper No. T190-5, Structural Engineering World Wide 1998, Elsevier Science, Ltd.

Tanaka, K., Torii, T., Sasaki, Y., Miyama, T., Kawai, H., Iwata, M., and Wada, A. (1998). "Practical Application of Damage Tolerant Structures with Seismic Control Panel using Low-Yield-Point-Steel to a High-Rise Steel Building." Paper No. T190-4, Structural Engineering World Wide 1998, Elsevier Science, Ltd.

Tsai K.C., Chen H.W., Hong C.P., Su Y.F.(1993), "Design of Steel Triangular Plate Energy Absorbers for Seismic-Resistant Construction," Earthquake Spectra, Volumn 9, No.3

Usami, T., Lu, Z., and Ge, H. (2005). "A seismic upgrading method for steel arch bridges using buckling-restrained braces." Earthquake engineering & structural dynamics, 34(4-5), 471-496.

Vargas, R., Bruneau, M. (2006a), "Experimental Investigation of the Structural Fuse Concept", Technical Report MCEER-06-0005, Multidisciplinary Center for Earthquake Engineering Research, State University of New York at Buffalo, Buffalo, NY, 2006.

Vargas, R., Bruneau, M. (2006b), "Analytical Investigation of the Structural Fuse Concept", Technical Report MCEER-06-0004, Multidisciplinary Center for Earthquake Engineering Research, State University of New York at Buffalo, Buffalo, NY, 2006.

Wada, A., Connor, J.J., Kawai, H., Iwata, M., and Watanabe, A. (1992). "Damage Tolerant Structures." Proceedings of: Fifth U.S.-Japan Workshop on the Improvement of Structural Design and Construction Practices, ATC-15-4, Applied Technology Council, pp. 27-39.

Wada, A., and Huang, Y.H. (1999). "Damage-controlled Structures in Japan." U.S.- Japan Workshop on Performance-Based Earthquake Engineering Methodology for Reinforced Concrete Building Structures, PEER Report 1999, Volume 10, pp. 279-289.

Wada, A., Huang, Y.H., and Iwata, M. (2000). "Passive Damping Technology for Buildings in Japan." Progress in Structural Engineering and Materials, John Wiley & Sons, Ltd., Volume 2, No. 3, pp. 335-350.

Watanabe, A., Hitomi, Y., Saeki, E., Wada, A., and Fujimoto, M. (1988). "Properties of Brace Encased in Buckling Restraining Concrete and Steel Tube." Proceedings of Ninth World Conference on Earthquake Engineering, Tokyo-Kyoto, Japan, No. 6-7-4, Volume 4, pp. 719-724.

Whittaer,A.S., Bertero, V.V., Thompson, C.L. and Alonso, L.J.(1991), "seismic testing of steel plate energy dissipation devices." Earthquake Spectra, 7(4), 563-604

Zahrai S.M., Bruneau M. (1999), "Ductile end-dispharagms for seismic retrofit of slab-on-girder steel bridges," Journal of Structural Engineering, Vol. 125, No.1

Zahrai S.M., Bruneau M. (2000), "Seismic performance of diaphragms in slab-on-girder steel

bridges," 12th World Conference on Earthquake Engineering, Auckland, New Zealand, January 2000, on CD-ROM.

# Appendix B Design CFT column bent with BRBs

## B.1 Two CFT column bent with BRBs

This design example illustrates how BRBs are designed as structural fuses to limit damage to the bridge bent. The design procedure for two CFT columns with a single BRB, or BRBs in interted-V, is shown below. The capacity of the CFT columns is checked at the end of this example.

### CFT column properties

Start with a trial circular CFT column with the following properties

| | | |
|---|---|---|
| The height of the bent column | $h = 234$ | in |
| The diameter of the CFT column | $D = 48$ | in |
| The thickness of the steel tube | $t = 1.25$ | in |
| The inside diameter of the concrete infill | $D_c = D - 2 \cdot t = 45.5$ | in |
| The area of the steel tube | $A_s = \pi \cdot \frac{\left(D^2 - D_c^2\right)}{4} = 183.587$ | $in^2$ |
| The area of the concrete infill | $A_c = \frac{\pi \cdot D_c^2}{4} = 1.626 \times 10^3$ | $in^2$ |
| The area of the reinforcement in the infill concrete | $A_{sr} = 0$ | $in^2$ |
| The moment of inertia of the steel tube | $I_s = \pi \cdot \frac{\left(D^4 - D_c^4\right)}{64} = 5.019 \times 10^4$ | $in^4$ |
| The moment of inertia of the concrete infill | $I_c = \pi \cdot \frac{D^4}{64} = 2.606 \times 10^5$ | $in^4$ |
| The moment of inertia of the reinforcement in the concrete | $I_{sr} = 0$ | $in^4$ |
| The strength of the steel shell using A572 alloy steel plate Gr60 | $F_y = 60$ | ksi |
| | $F_u = 75$ | ksi |

The strength of the infill concrete $f_c = 4$ ksi

The elastic modulus of concrete $E_c = \frac{57000}{1000}\cdot\sqrt{f_c\cdot 1000} = 3.605\times 10^3$ ksi

The elastic modulus of steel $E_s = 29000$ ksi

EI of the CFT column $EI = E_s\cdot I_s + E_s\cdot I_c = 9.012\times 10^9$ $in^4$

## Strength calculation

### Axial Compressive and tensile strength

Per AISC 2010, the design compressive strength of the CFT section is calculated below using the LRFD approach. Additional information about why AISC equations instead of the AASHTO Bridge Design Specifications can be found in appendix A.

The stability limit using Width-to-thickness ratio is first checked according to table I1.1 A & B

$\frac{D}{t} = 38.4$ smaller than $\lambda p_1 = 0.15\cdot\frac{E_s}{F_y} = 72.5$ for compression

$\lambda p_2 = 0.09\cdot\frac{E_s}{F_y} = 43.5$ for flexure

The composite section is categorized as a compact section both under axial force and moment

To calculate the compressive strength, section I2.b is used per AISC2010

For circular section $C_2 = 0.95$

For compact section $P_p = F_y\cdot A_s + C_2\cdot f_c\cdot\left(A_c + A_{sr}\cdot\frac{E_s}{E_c}\right) = 1.719\times 10^4$ kips

$P_{n0} = P_p$

To get the effective stiffness of the CFT section, the coefficient C3 is calculated

$C_3 = 0.6 + 2\cdot\left(\frac{A_s}{A_c + A_s}\right) = 0.803$ smaller than 0.9, ok

The effective stiffness of the CFT section

$$EI_{eff} = E_s \cdot I_s + 0.5 \cdot E_s \cdot I_{sr} + C_3 \cdot E_c \cdot I_c = 2.21 \times 10^9 \quad in^4$$

Check global buckling of the CFT column under axial compression load

The CFT column is fixed at both ends $K_c = 0.5$

The elastic critical buckling load is determined by using equatioin I2-5 (AISC,2010)

$$P_e = \pi^2 \cdot \frac{EI_{eff}}{(K_c \cdot h)^2} = 1.593 \times 10^6 \quad kips$$

$$n_1 = \frac{P_{n0}}{P_e} = 0.011 \quad \text{smaller than 2.25, OK}$$

The axial compression strength of the CFT column is calculated according to equation I2-2 (AISC,2010)

$$P_n = P_{n0} \cdot 0.658^{n_1} = 1.712 \times 10^4 \quad kips \quad \phi_c = 0.75$$

The axial tension strength of the CFT column is determined based on I2-8

$$T_n = F_y \cdot A_s = 1.102 \times 10^4 \quad kips \quad \phi_t = 0.9$$

The strength reduction factor for design is listed on the right side, and not included into the strength calculations at this stage.

Per AISC 2010, shear strength for filled composite members can be determined using the available shear strength of the steel alone. The nominal shear strength for round HSS per AISC 2010 Chapter G, is calculated using the equations listed below. The limit states of shear yielding and buckling is considered. The same equation is provided in the AASHTO Bridge Design Specifications (2010) section 6.12.1.2.3c

The critical shear stress is calculated to be the smaller of

$$F_{cr1} = 1.60 \cdot \frac{E_s}{\sqrt{\frac{h}{D}} \cdot \left(\frac{D}{t}\right)^{\frac{5}{4}}} = 219.845$$

$$F_{cr2} = 0.78 \cdot \frac{E_s}{\left(\frac{D}{t}\right)^{\frac{3}{2}}} = 95.06$$

$F_{cr3} = 0.6 \cdot F_y = 36$

therefore, $F_{cr} = F_{cr3}$

The shear strength of the CFT section: $V_n = F_{cr} \cdot \frac{A_s}{2} = 3.305 \times 10^3$ kips

$$\phi_v = 0.9$$

## Flexural strength calculation

Two approaches are identified as appropriate to calculate the flexural strength in AISC (2010), namely, (1) the plastic stress distribution, (2) the strain compatibility method. Per AASHTO Guide Specifications for LRFD Seismic Bridge Design (2009) section 7.6 , the design flexural strength of the composite section is calculated below using a method similiar to the plastic distribution method.

β is the central angle formed between the neutral axis chord line and the center point of the steel shell found by the following recursive equation (unit: rad)

$$\beta = 2.443 \quad \frac{A_s \cdot F_y + 0.2 \cdot D^2 \cdot f_c \cdot \left[ \sin\left(\frac{\beta}{2}\right) - \left(\sin\left(\frac{\beta}{2}\right)\right)^2 \cdot \tan\left(\frac{\beta}{4}\right) \right]}{0.125 \cdot D^2 f_c + D \cdot t \cdot F_y} = \beta \qquad (7.6.2-8)$$

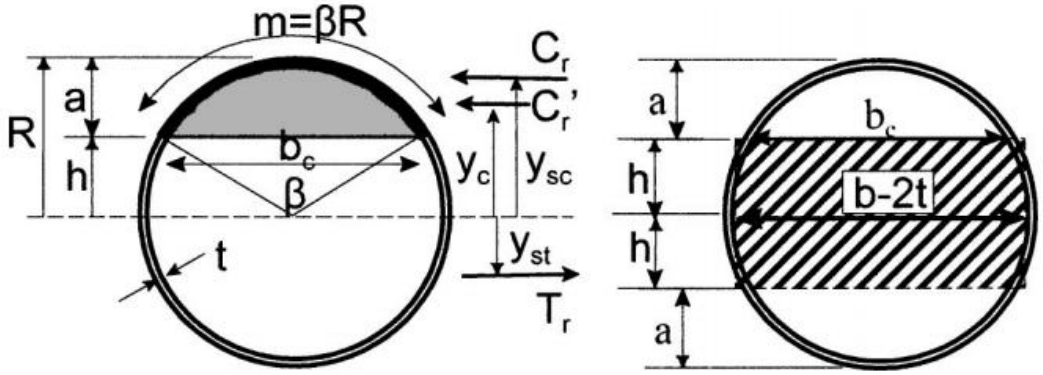


Figure B-1 Free body diagram to develop the flexural strength equation (Bruneau and Marson, 2004, similar to AASHTO Guide Specifications for LRFD Seismic Bridge Design (2009))

The following are parameters shown in figure 1-1 for calculating the flexural strength of the CFT section

$$b_c = D \cdot \sin\left(\frac{\beta}{2}\right) = 45.101 \qquad (7.6.2-7)$$

$$a = \frac{b_c \cdot \tan\left(\frac{\beta}{4}\right)}{2} = 15.786 \qquad (7.6.2-6)$$

$$e_1 = b_c \cdot \left(\frac{1}{2 \cdot \pi - \beta} + \frac{1}{\beta}\right) = 30.206 \qquad (7.6.2-4)$$

$$e_2 = b_c \cdot \left[\frac{1}{2 \cdot \pi - \beta} + \frac{{b_c}^2}{1.5 \cdot \beta \cdot D^2 - 6 \cdot b_c \cdot (0.5 \cdot D - a)}\right] = 26.494 \qquad (7.6.2-5)$$

$$C_{r1} = F_y \cdot \beta \cdot D \cdot \frac{t}{2} = 4.397 \times 10^3 \qquad (7.6.2-2)$$

$$C_{r2} = f_c \cdot \left[\beta \cdot \frac{D^2}{8} - \frac{b_c \cdot \left(\frac{D}{2} - a\right)}{2}\right] = 2.073 \times 10^3 \qquad (7.6.2-3)$$

$$\phi_f = 1.0$$

Therefore the plastic strength of the CFT section is

$$M_n = \phi_f \cdot \left(C_{r1} \cdot e_1 + C_{r2} \cdot e_2\right) = 1.878 \times 10^5 \quad \text{kips} \cdot \text{in}$$

## Flexural strength, yielding displacement, and stiffness

The yielding flexural strength is obtained when the extreme point in the steel shell reaches the yielding strain of 0.002. Hand calculation is not performed here; instead this value is obtained from SAP2000 Section Designer. Details are shown in Appendix C.

The yielding flexural strength of the section is $M_y = 126891$ kips·in

The yielding curvature of the CFT column $\phi_y = 0.00007776$ $\text{in}^{-1}$

The yielding displacement of the CFT column $\Delta_y = 2 \cdot \phi_y \cdot \frac{\left(\frac{h}{2}\right)^2}{3} = 0.71$ in

The effective stiffness of the CFT column $K_{col} = \frac{2 \cdot M_y}{h \cdot \Delta_y} = 1.528 \times 10^3$ $\frac{\text{kip}}{\text{in}}$

The gross stiffness of the CFT column based on the gross section properties $K_{gross} = 12 \cdot \frac{EI}{h^3} = 8.44 \times 10^3$ $\frac{\text{kip}}{\text{in}}$

The ratio of the effective stiffness over the gross stiffness is $\frac{K_{col}}{K_{gross}} = 0.181$

## Fuse stiffness calculation

There are two CFT columns in the bridge bent, so the total stiffness of the bridge bent is

$K_{bent} = 2 \cdot K_{col} = 3.057 \times 10^3 \quad \frac{kip}{in}$

Assuming the period of the bridge bent in the transverse direction is in the range of the design spectrum plateau, which is the largest value of the spectrum

$S_a = 2 \ g$

The relationship between the expected displacement of the bridge δe , the acceleration Sa, and the period T is

$$\delta_e = S_a \cdot T^2 \cdot \frac{g}{4 \cdot \pi^2}$$

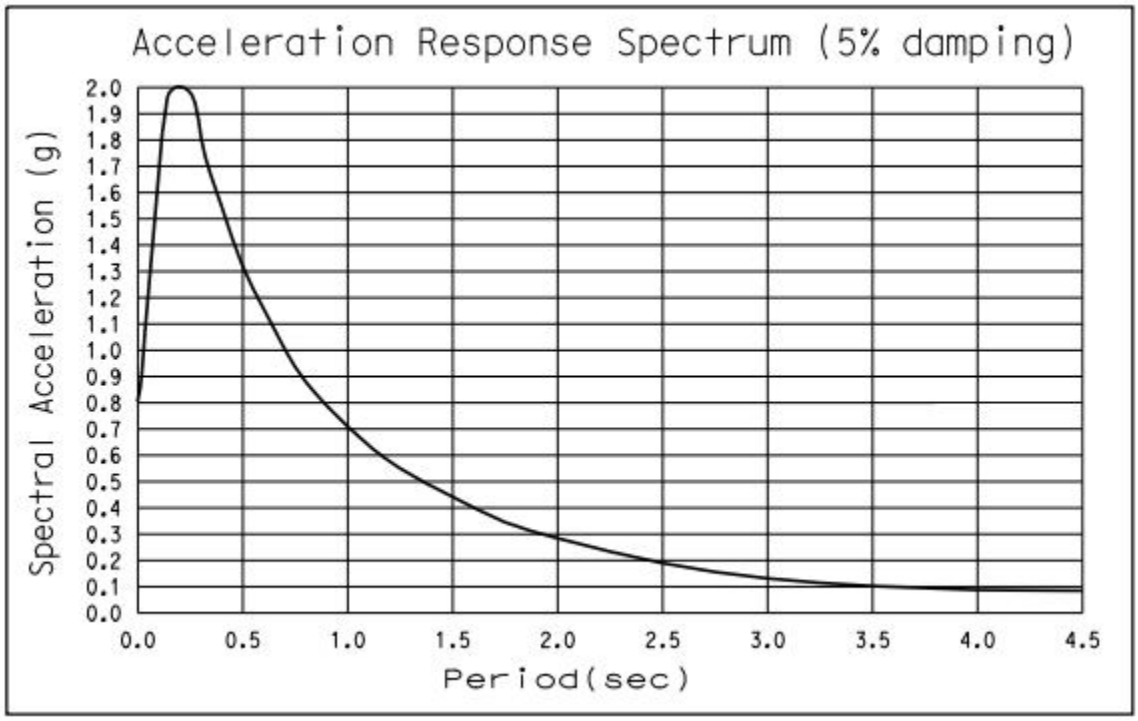


Figure B-2 Provided acceleration spectrum of OSB1 bridge

The period of the bridge bent combined with the fuse can be calculated, assuming the expected displacement of the bridge bent to be the yielding displacement of the CFT columns Δy.

$T_s = \sqrt{\Delta_y \cdot 4 \cdot \frac{\pi^2}{S_a \cdot 386}} = 0.19 \quad s$

The weight of the superstructure (includes all the dead loads calculated in chapter 3) is

$W_{super} = 4692$ kips

The total stiffness of the bridge required to make the period of the bridge in the transverse direction to be Ts is

$$K_t = \frac{W_{super} \cdot 4 \cdot \pi^2}{386 \cdot T_s^2} = 1.322 \times 10^4 \quad \frac{kip}{in}$$

The required stiffness of the fuse is obtained by substracting the stiffness of the bent columns

$$K_{fuse} = K_t - K_{bent} = 1.017 \times 10^4 \quad \frac{kip}{in}$$

The ratio of the stiffness of the fuse over the bent is

$$\frac{K_{fuse}}{K_{bent}} = 3.326$$

The following demonstrates the necessity of adding fuses to prevent column yielding

The period of the bridge for the bare bent alone is

$$T_b = 2 \cdot \pi \cdot \sqrt{\frac{W_{super}}{386 \cdot K_{bent}}} = 0.396 \quad s$$

From the acceleration spectrum in Figure B-2, the spectrum acceleration

$S_b = 1.5\ g$

The corresponding expected spectrum displacement is

$$\delta_t = S_b \cdot T_b^2 \cdot \frac{386}{4 \cdot \pi^2} = 2.303 \quad in$$

which is much larger than the expected displacement $\Delta y$

$$\frac{\delta_t}{\Delta_y} = 3.245$$

This shows that the added structural fuse is effective to prevent the yielding of the bent columns.

## Design of structural fuse for single BRB case

The configuration of the bridge bent with a single inclined BRB is shown in figure B-3 . Note that, the distance between the columns, the numbers of the BRBs, the columns size will vary from bridge to bridge.

The material used for BRB is A500Gr.B steel with yielding strength requirement of 42 ksi

$f_{ybrb} = 42$ ksi

The overhang of the bridge box girder is 6 ft, which is the same as the height of the box girder. The center-to-center distance between the two CFT columns is 25.5 ft. The clear distance between the CFT columns is 21.5 ft in this case.

$L_c = 21.5 \cdot 12 = 258$ in

The length of the BRB is

$L_{brb} = \sqrt{L_c^2 + h^2} = 348.31$ in

The inclination angle of the BRB with the horizontal axis is

$\theta = \operatorname{atan}\left(\frac{h}{L_c}\right) = 0.737$

$\cos(\theta) = 0.741 \quad \sin(\theta) = 0.672$

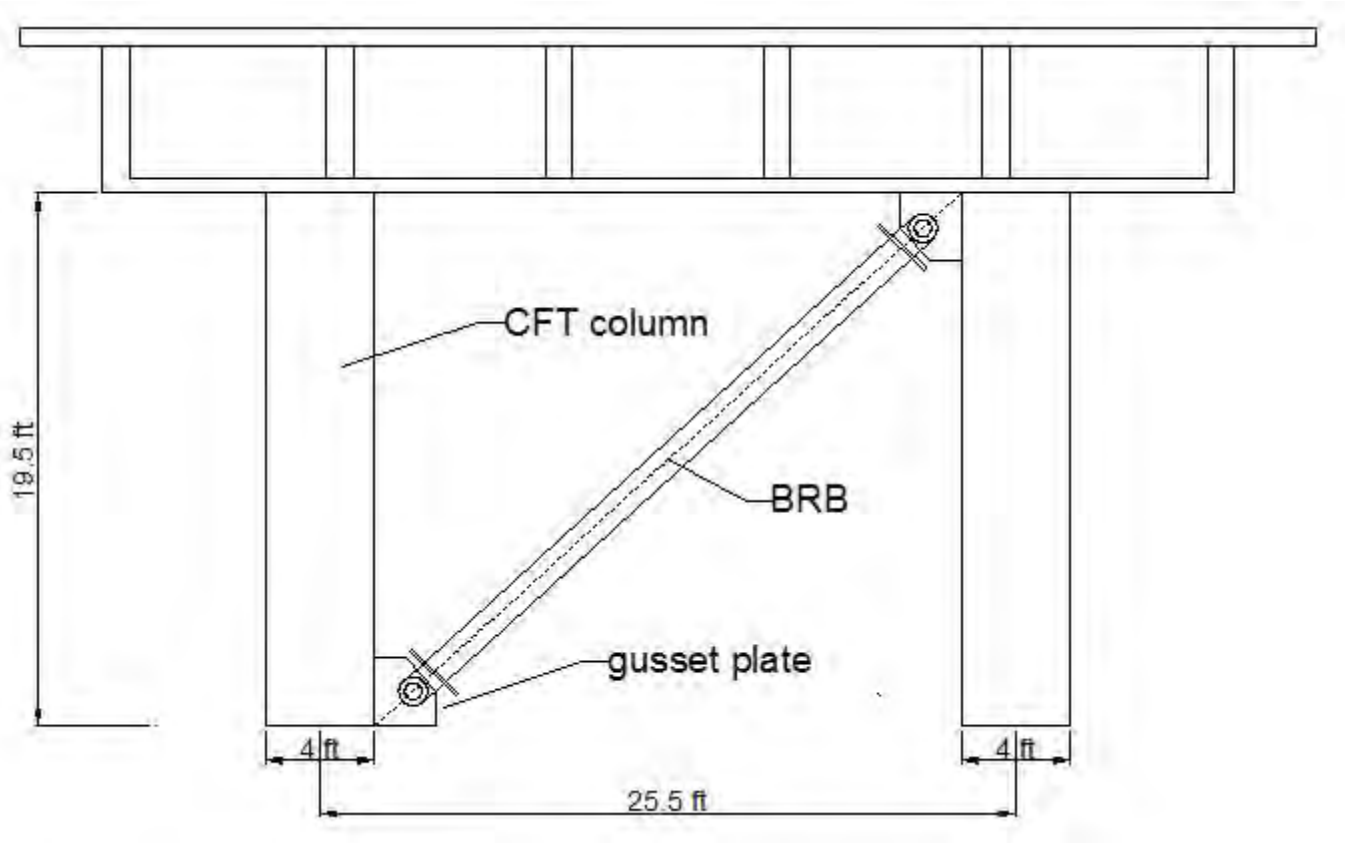


Figure B-3 The elevation of the bridge bent in the transverse direction with single BRB

A typical BRB consists of a yielding streel core encased to restrain buckling, non-yielding and buckling-restrained transition segments, and non-yielding and unrestrained end zones. When the BRB yields, yielding is limited to the buckling restrained yielding segment. The length of this yielding core is $c_{brb}$* $L_{brb}$, where $c_{brb}$ is the yielding length ratio, which needs to be calculated.

The yielding length ratio of the BRB is obtained here by having the BRB strain limit to be attained, when the expected spectrum displacement at the top of the bent reach Δy. The corresponding displacement of the BRB is $\Delta_y\cos\theta$. Noting that 1.5% strain limit is assumed to be conservative here, and larger strain limit can be used. A small strain limit can also be used, however, this would result in a longer yielding core and thus a larger brace section and yielding force to achieve the same target brace stiffness.

$$c_{brb} = \frac{\Delta_y}{0.015 \cdot L_{brb}} \cdot \cos(\theta) = 0.101$$

The corresponding displacement of the CFT column when the BRB yields is

$$\Delta_{fuse} = \frac{f_{ybrb} \cdot c_{brb} \cdot L_{brb}}{E_s \cdot \cos(\theta)} = 0.069 \quad \text{in}$$

The area of the BRB required to obtain the stiffness calculated above is

$$A_{brb} = \Delta_{fuse} \cdot \frac{K_{fuse}}{f_{ybrb} \cdot \cos(\theta)} = 22.392 \quad \text{in}^2$$

The yielding force in the BRB is

$$f_{ybrb} \cdot A_{brb} = 940.455 \quad \text{kips}$$

After the BRB yields, it will enter into the strain hardening stage. The axial force in the BRB will increase,and the strain hardening factors below are used to calculate the largest forces the BRB can develop under compression or tension forces. To note, strain hardening factors will vary with BRB size and suppliers.

$\omega\beta = 1.5 \quad \omega = 1.35$

The largest force that can be developed in the BRB subjected to compressive force is

$$\omega\beta \cdot f_{ybrb} \cdot A_{brb} = 1.411 \times 10^3 \quad \text{kips}$$

The largest force that can be developed in the BRB subjected to tensile force is

$$\omega \cdot f_{ybrb} \cdot A_{brb} = 1.27 \times 10^3 \quad \text{kips}$$

The largest lateral load resistance provided by the single inclined BRB when it is under compression is

$$V_{bc} = \omega\beta \cdot f_{ybrb} \cdot \cos(\theta) \cdot A_{brb} = 1.045 \times 10^3 \quad \text{kips}$$

The largest axial force added to the CFT columns by the single BRB under compression is

$P_{bc} = \omega\beta \cdot f_{ybrb} \cdot A_{brb} \cdot \sin(\theta) = 947.718$ kips

The largest lateral load resistance provided by the single inclined BRB when it is under tension is

$V_{bt} = \omega \cdot f_{ybrb} \cdot \cos(\theta) \cdot A_{brb} = 940.428$ kips

The largest axial force added to the CFT columns by the single BRB under tension is

$P_{bt} = \omega \cdot f_{ybrb} \cdot A_{brb} \cdot \sin(\theta) = 852.946$ kips

The lateral load resistance of the system in the transverse direction is provided by two parts: the shear resistance of the CFT columns and the horizontal component of the axial force in the single inclined BRB. When the expected displacement, a.k.a. the yielding displacement of the column, is reached, the shear force resistance from the CFT columns can be obtained. The moment at the end of the CFT columns are assumed to be the yielding strength of the column since the yielding displacement is reached. The frame action under the applied lateral seismic load will develop axial forces in the columns to resist the corresponding overturning moment. The axial force in the BRB would also adds to the column axial force. The axial strength of the columns are checked first. Then the shear strength of the CFT columns is also checked. The flexural strength of the section will be reduced because of the presence of additional axial force in the columns. The reduction of the flexural strength of the CFT section due to the presence of the larger axial force will be checked in chapter 3.

The lateral load resistance taken by the CFT columns is

$V_{bent} = 2 \cdot \frac{2M_y}{h} = 2.169 \times 10^3$ kips

The distance between the tension and compression resultant for the two CFT columns as in figure B-4 is

$x = 21.5 \cdot 12 = 258$ in

The resultant axial force $F_{re}$ resulting from the lateral load applied to the frame alone (in absence of the BRB) is

$F_{re} = \frac{\left(V_{bent} \cdot h - 2 \cdot M_y\right)}{x} = 983.651$ kips

Under the lateral load when the single chevron BRB is in compression, the largest reaction at the base of both columns is

$F_{oc} = F_{re} + P_{bc} = 1.931 \times 10^3$ kips

Under the lateral load when the single chevron BRB is in tension, the largest reaction at the base of both columns is

$F_{ot} = F_{re} + P_{bt} = 1.837 \times 10^3$ kips

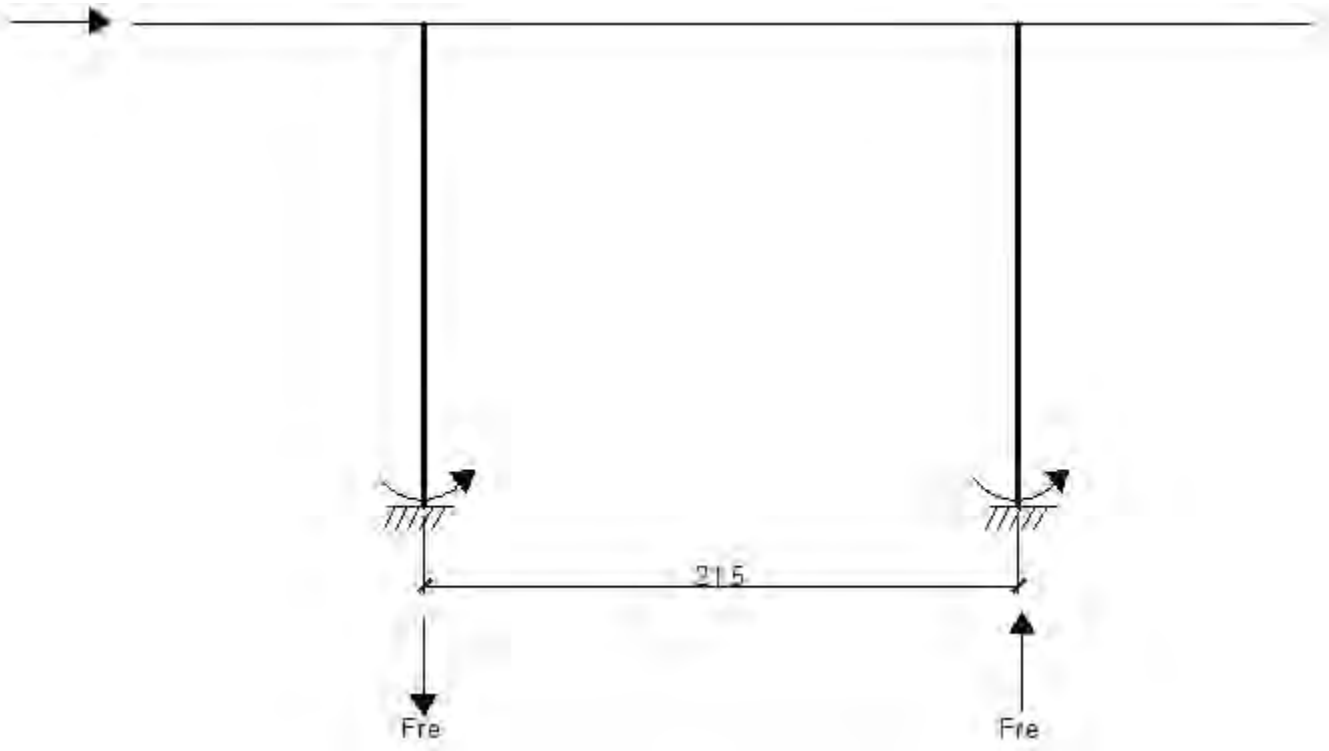


Figure B-4 Axial loads induced by the lateral loading on the bent in the transverse direction

The values resulting for the column axial force design due to the lateral load is shown in figure B-5a and B-5b, for the BRB in tension and compression respectively.

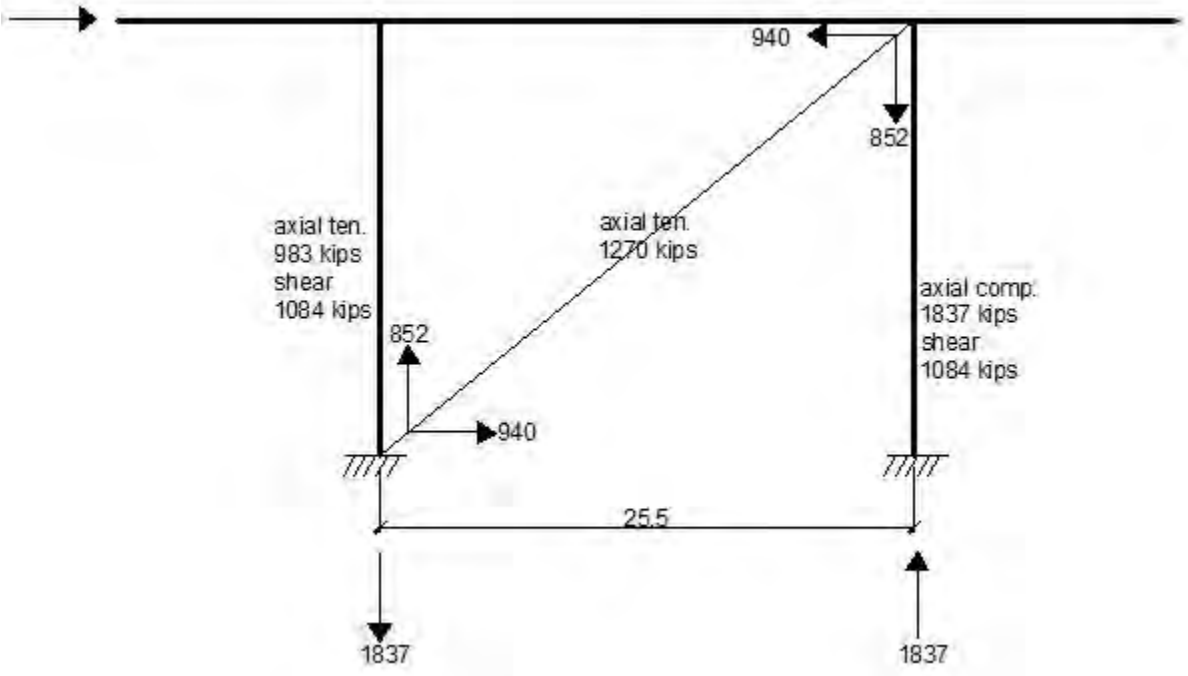


Figure B-5a Reactions at the base and forces in the bridge member when the BRB is in tension

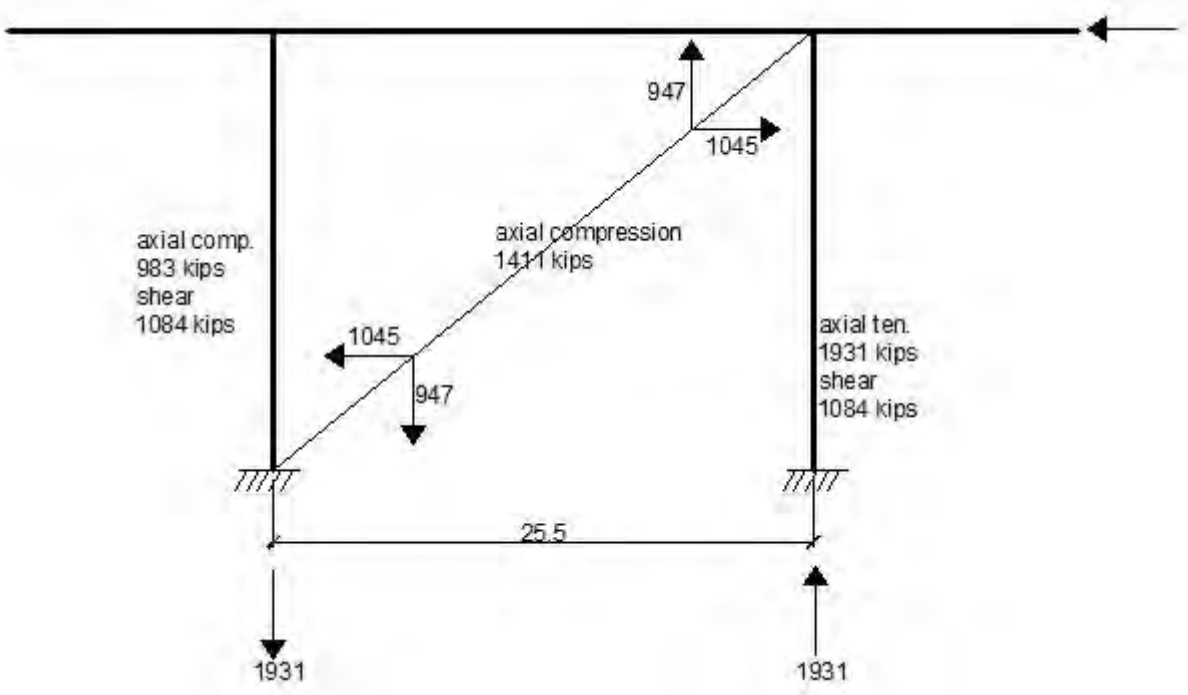


Figure B-5b Reactions at the base and forces in the bridge member when the BRB is in compression

Therefore, the design force for the column under the lateral load can be summarized in table B-1 below (govening cases are hignlighted by the box):

Table B-1 Design force for the column under lateral load

| case | column | M(kips*in) | P(kips) | V(kips) |
|---|---|---|---|---|
| BRB in ten. | left | 126891 | 983 | 1084 |
| | right | 126891 | -1837 | 1084 |
| BRB in comp. | left | 126891 | -983 | 1084 |
| | right | 126891 | 1931 | 1084 |

To note, the model assumes that the force from the BRB goes directly into the foundation as shown in figure B-6a. However, if there is an eccentricity between the point where the brace and the column workline meet around the foundation, the segment of the column over the length of that eccentricity could be subjected to forces equal to the value of the reactions shown in figure B-6a and B-6b. Therefore,the design forces for the columns would change to the values in table B-2.

Table B-2 Design force for the column under lateral load considering the eccentricity

| case | column | M(kips*in) | P(kips) | V(kips) |
|---|---|---|---|---|
| BRB in ten. | left | 126891 | 1837 | 2024 |
| | right | 126891 | -1837 | 2024 |
| BRB in comp. | left | 126891 | -1931 | 2128 |
| | right | 126891 | 1931 | 2128 |

The governing design forces for the column is highlighted in the box. To be conservative, the force from table B-2 will be used.

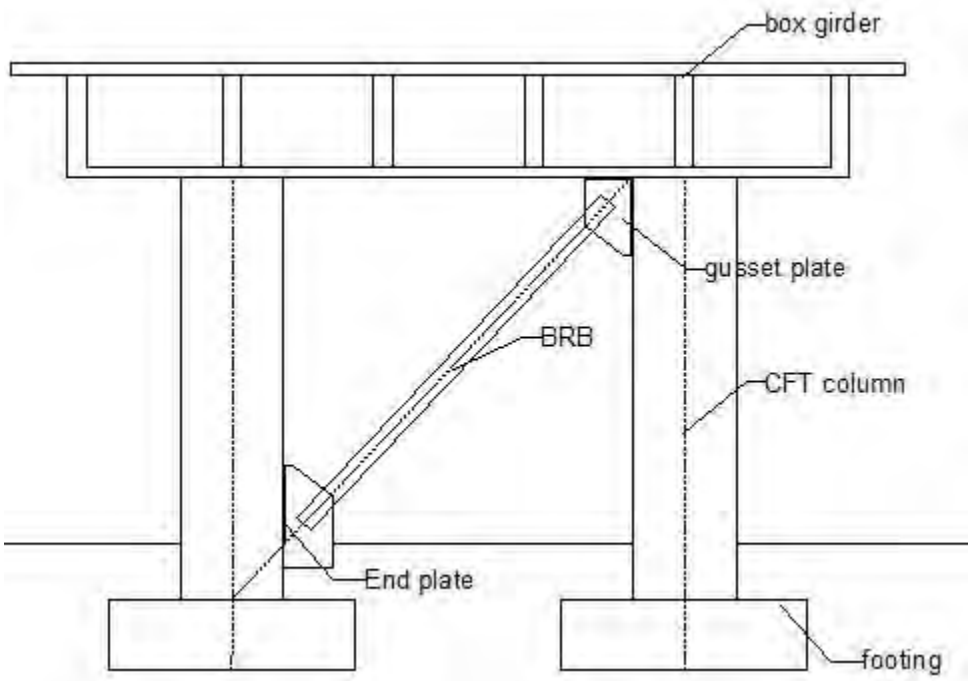


Figure B-6a Idealized geometry of the bridge bent with single inclined braces in the transverse direction

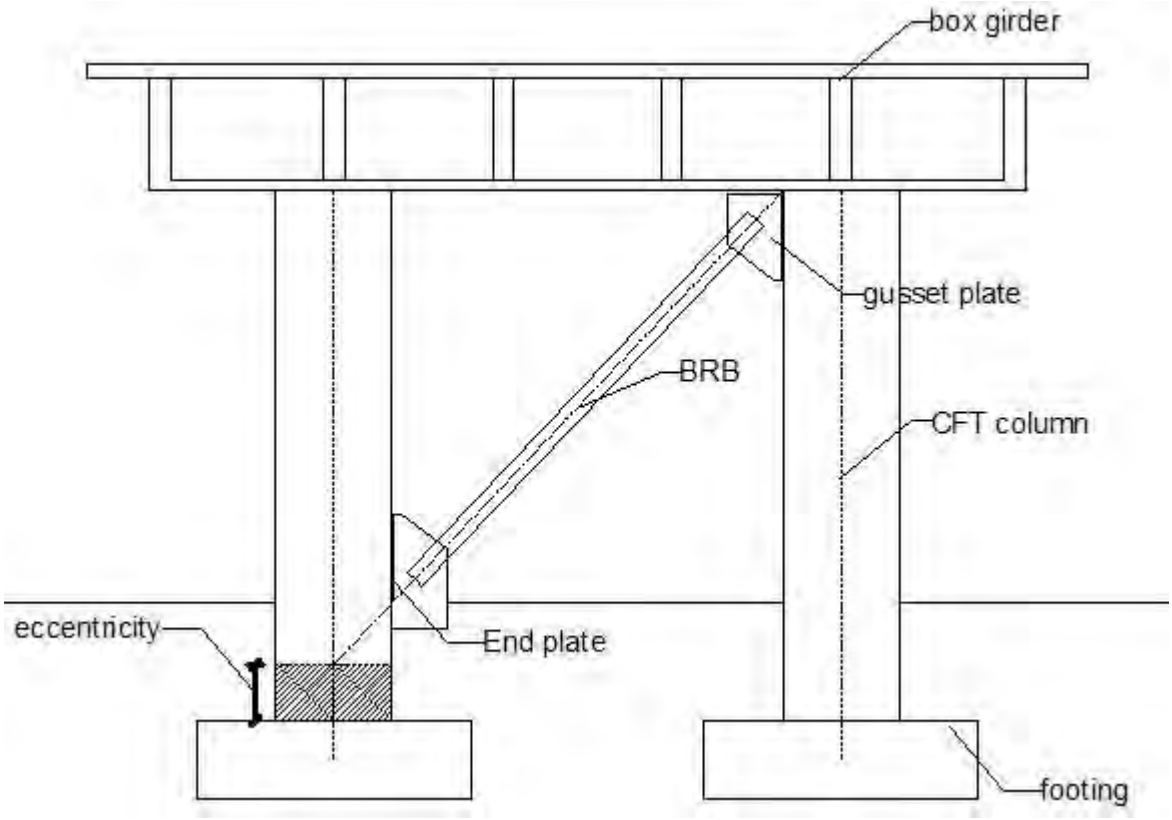


Figure B-6b The bridge bent with single inclined braces in the transverse direction considering a possible eccentricity,e

The load that is present in the columns would also need to consider the dead load effect. The distributed dead loads is 15.64 kip/ft, applied on the entire length of the bridge in the longitudinal direction.

An estimation of the dead load reaction at the bent is

$R_b = 2994.68$ kips

The axial force should be obtained by applying the dead load on the cap beam at the locations of the girders. Here a simplified analysis is done and the force is directly distributed to in the two columns. The BRB is assumed not to take any dead loads.

$$P_d = \frac{R_b}{2} = 1.497 \times 10^3 \quad \text{kips}$$

Table B-3 shows the design checks for the columns using the values from table 1-2 plus the dead loads. The $\phi$ factors listed when the design strength is calculated are included in the table. The $M_u/M_y+P_u/P_y$ check is tabulated to show the yielding moment strength and axial load interaction capacity. The interaction diagram gives a value greater than 1.0 for both columns because the design approach considered column yield moments not accounting for the presence of axial force. The $M_u/\phi M_n+P_u/\phi P_n$ ratios are all smaller than 1.0, which means the sections are found adequate to resist the force applied.

Table B-3 Force checking for the columns for the single inclined BRB case

| My | Mu | Pu | Vu | ΦMn | ΦPn |
|---|---|---|---|---|---|
| 126891 | 126891 | -3331 | 2024 | 187800 | -12840 |
| 126891 | 126891 | 437 | 2128 | 187800 | 9918 |

| ΦVn | Mu/My+Pu/ΦPn | Mu/ΦMn+Pu/ΦPn | Vu/ΦVn |
|---|---|---|---|
| 2974.5 | 1.26 | 0.94 | 0.68 |
| 2974.5 | 1.04 | 0.72 | 0.72 |

## Design of structural fuse for BRBs in inverted-V case

The configuration of the bridge bent with BRBs in inverted-V in the transverse direction is shown in figure B-7. The distance between the columns, the numbers of the BRBs, the columns size can be subjected to adjustment.

The length of the BRB is $L_{cb} = \sqrt{\left(\frac{L_c}{2}\right)^2 + h^2} = 267.202$ in

The inclination angle of the BRB with the horizontal axis is $\theta_c = \operatorname{atan}\left(\frac{2 \cdot h}{L_c}\right) = 1.067$

$\cos(\theta_c) = 0.483 \qquad \sin(\theta_c) = 0.876$

The length yielding ratio fo the BRB is obtained by setting the strain limit, to be attained, when the expected spectrum displacement Δy is reached.The corresponding displacement of the BRB is $\Delta_y \cos\theta$. Noting that 1.5% strain limit is assumed to be conservative here, and larger strain limit can be used. A small strain limit can also be used, however, this would result in a longer yielding core and thus a larger brace section and yielding force to achieve the same target brace stiffness.

$$c_{cb} = \frac{\Delta_y}{0.015 \cdot L_{cb}} \cdot \cos(\theta_c) = 0.085$$

The corresponding displacement of the CFT column when the BRBs yield is

$$\Delta_{fc} = \frac{f_{ybrb} \cdot c_{cb} \cdot L_{cb}}{E_s \cdot \cos(\theta_c)} = 0.069 \quad \text{in}$$

The area of the BRB required to attain the stiffness calculated above is

$$A_{cb} = \Delta_{fc} \cdot \frac{\frac{K_{fuse}}{2}}{f_{ybrb} \cdot \cos(\theta_c)} = 17.178 \quad \text{in}^2$$

The yielding force of the BRB brace is

$$f_{ybrb} \cdot A_{cb} = 721.46 \quad \text{kips}$$

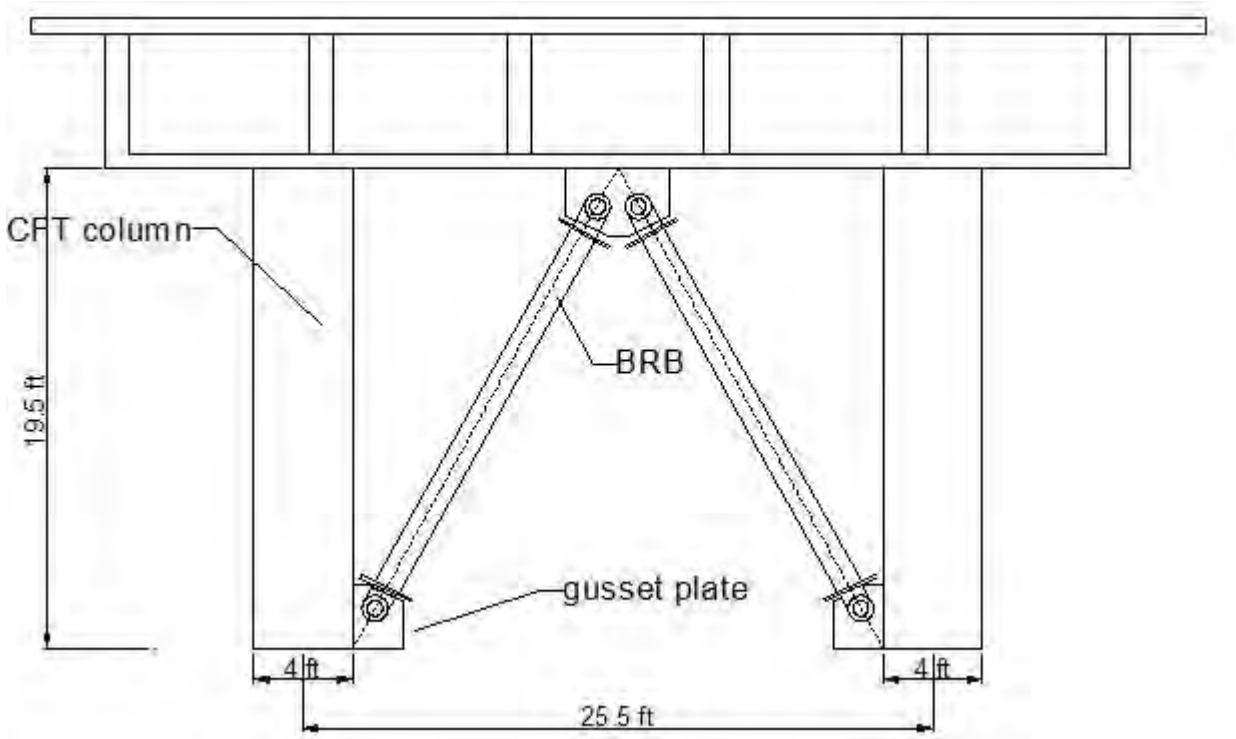


Figure B-7 The elevation of the bridge bent in the transverse direction with chevron BRBs

After the BRB yields, it will enter into the strain hardening stage. The axial force in the BRB will increase, and the strain hardening factors used before for the single inclined BRB case is used to calculate the largest forces that the BRBs can develop under compression or tension forces.

The largest force that can be developed in the BRB subjected to compressive force is

$\omega\beta \cdot f_{ybrb} \cdot A_{cb} = 1.082 \times 10^3$ kips

The largest force that can be developed in the BRB subjected to tensile force is

$\omega \cdot f_{ybrb} \cdot A_{cb} = 973.97$ kips

The lateral shear resistance provided by the compressive BRBs in inverted-V is

$V_{cbc} = \omega\beta \cdot f_{ybrb} \cdot \cos(\theta_c) \cdot A_{cb} = 522.46$ kips

The lateral shear resistance provided by the tensile BRBs in inverted-V is

$V_{cbt} = \omega \cdot f_{ybrb} \cdot \cos(\theta_c) \cdot A_{cb} = 470.214$ kips

The maximum axial force added to the CFT columns by the BRB in compression is

$P_{cbc} = \omega\beta \cdot f_{ybrb} \cdot A_{cb} \cdot \sin(\theta_c) = 947.718$ kips

The maximum axial force added to the CFT columns by the BRB in tension is

$P_{cbt} = \omega \cdot f_{ybrb} \cdot A_{cb} \cdot \sin(\theta_c) = 852.946$ kips

Under the lateral load, the vertical reactions as shown in figure 1-10 in the columns are

$F_{cc} = F_{re} + P_{cbt} = 1.837 \times 10^3$ kips

$F_{ct} = F_{re} + P_{cbc} = 1.931 \times 10^3$ kips

The force demands in the columns for two cases are tabulated in table B-4. The governing design forces are shown in the box. The difference is caused by the eccentricity between the point when the brace and the column workline meet around the foundatio, similar to what is shown in figure B-6a and B-6b.

Table B-4 shows the design force for the column with and without eccentricity considered.

| case | column | M(kips*in) | P(kips) | V(kips) |
|---|---|---|---|---|
| w/o eccentricity | left | 126891 | 983 | 1084 |
| | right | 126891 | -983 | 1084 |
| w eccentricity | left | 126891 | 1837 | 1554 |
| | right | 126891 | -1931 | 1606 |

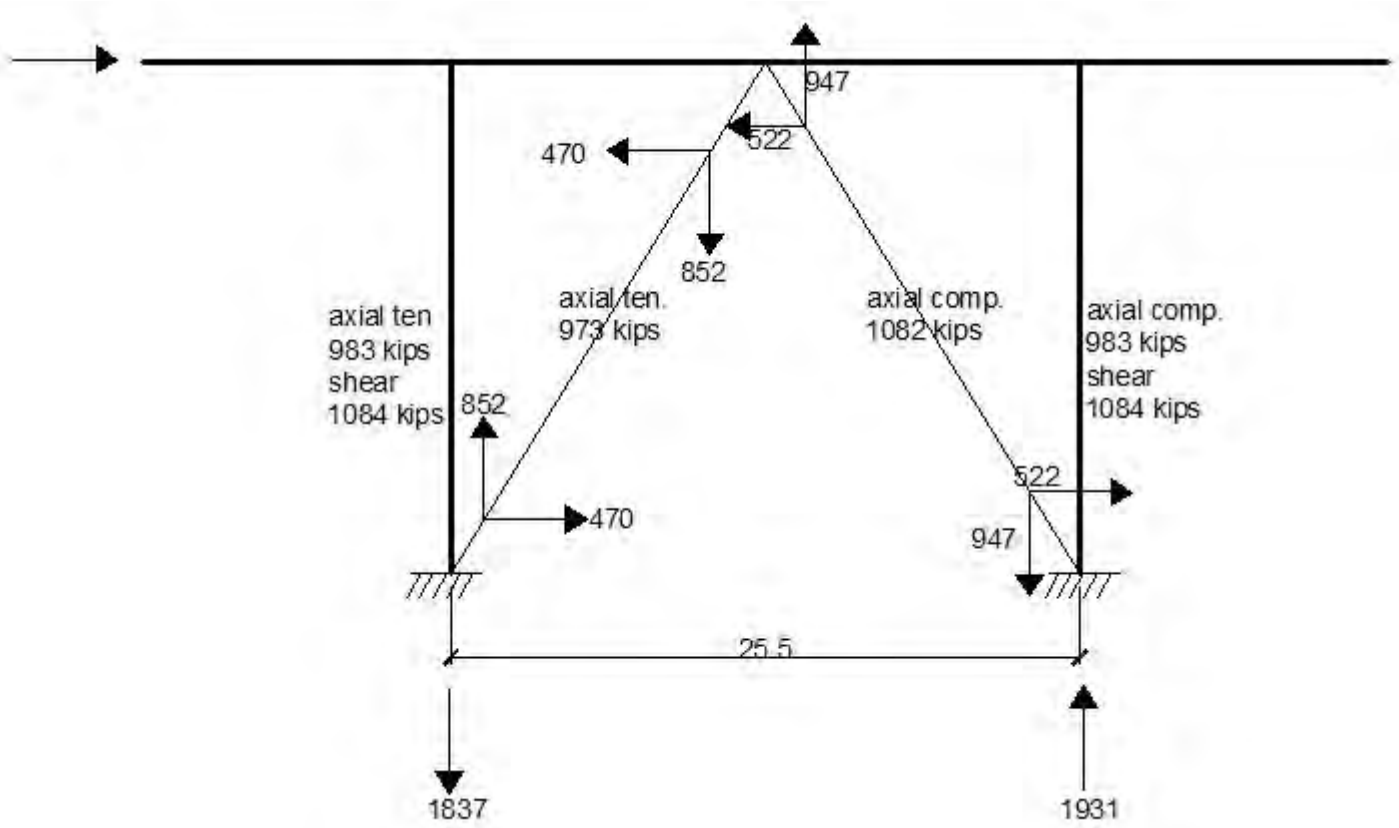


Figure B-8 Reactions at the base and forces in the bridge member for the BRBs in inverted-V case

The design checks for the columns in the chevron BRB case is shown in table B-5 plus the dead load effect. The columns are found adequate to resist the force applied.

Table B-5 Force checking for the columns in the chevron BRB case

| My | Mu | Pu | Vu | ΦMn | ΦPn |
|---|---|---|---|---|---|
| 126891 | 126891 | 343 | 1554 | 187800 | 9918 |
| 126891 | 126891 | -3425 | 1606 | 187800 | -12840 |

| ΦVn | Mu/My+Pu/ΦPn | Mu/ΦMn+Pu/ΦPn | Vu/ΦVn |
|---|---|---|---|
| 2974.5 | 1.03 | 0.71 | 0.52 |
| 2974.5 | 1.27 | 0.94 | 0.54 |

# B.2 Box pier bent with BRBs

This design example illustrates how BRBs are designed as structural fuses to limit damage to the bridge bent. The design procedure for box pier (eight CFT columns) with BRBs inserted between the columns, is shown below.

## CFT column properties

Start with a trial circular CFT column with the following properties

| | | |
|---|---|---|
| The height of the bent column | $h = 234$ | in |
| The diameter of the CFT column | $D = 32$ | in |
| The thickness of the steel tube | $t = 0.75$ | in |
| The inside diameter of the concrete infill | $D_c = D - 2 \cdot t = 30.5$ | in |
| The area of the steel tube | $A_s = \pi \cdot \frac{\left(D^2 - D_c^2\right)}{4} = 73.631$ | $in^2$ |
| The area of the concrete infill | $A_c = \frac{\pi \cdot D_c^2}{4} = 730.617$ | $in^2$ |
| The area of the reinforcement in the infill concrete | $A_{sr} = 0$ | $in^2$ |
| The moment of inertia of the steel tube | $I_s = \pi \cdot \frac{\left(D^4 - D_c^4\right)}{64} = 8.993 \times 10^3$ | $in^4$ |
| The moment of inertia of the concrete infill | $I_c = \pi \cdot \frac{D^4}{64} = 5.147 \times 10^4$ | $in^4$ |
| The moment of inertia of the reinforcement in the concrete | $I_{sr} = 0$ | $in^4$ |
| The strength of the steel shell using A572 alloy steel plate Gr60 | $F_y = 60$ | ksi |
| | $F_u = 75$ | ksi |
| The strength of the infill concrete | $f_c = 4$ | ksi |
| The elastic modulus of concrete | $E_c = \frac{57000}{1000} \cdot \sqrt{f_c \cdot 1000} = 3.605 \times 10^3$ | ksi |

The elastic modulus of steel $E_s = 29000$ ksi

EI of the CFT column $EI = E_s \cdot I_s + E_c \cdot I_c = 4.464 \times 10^8$ $in^4$

## Strength calculation

### Axial Compressive and tensile strength

Per AISC 2010, the design compressive strength of the CFT section is calculated below using the LRFD approach. Additional information about why AISC equations instead of the AASHTO Bridge Design Specifications can be found in appendix A.

The stability limit using Width-to-thickness ratio is first checked according to table I1.1 A & B

$\frac{D}{t} = 42.667$ smaller than $\lambda p_1 = 0.15 \cdot \frac{E_s}{F_y} = 72.5$ for compression

$\lambda p_2 = 0.09 \cdot \frac{E_s}{F_y} = 43.5$ for flexure

The composite section is categorized as a compact section both under axial force and moment

To calculate the compressive strength, section I2.b is used per AISC2010

For circular section $C_2 = 0.95$

For compact section $P_p = F_y \cdot A_s + C_2 \cdot f_c \cdot \left( A_c + A_{sr} \cdot \frac{E_s}{E_c} \right) = 7.194 \times 10^3$ kips

$P_{n0} = P_p$

To get the effective stiffness of the CFT section, the coefficient C3 is calculated

$C_3 = 0.6 + 2 \cdot \left( \frac{A_s}{A_c + A_s} \right) = 0.783$ smaller than 0.9, ok

The effective stiffness of the CFT section

$EI_{eff} = E_s \cdot I_s + 0.5 \cdot E_s \cdot I_{sr} + C_3 \cdot E_c \cdot I_c = 4.061 \times 10^8$ $in^4$

Check global buckling of the CFT column under axial compression load

The CFT column is fixed at both ends $K_c = 0.5$

The elastic critical buckling load is determined by using equatioin I2-5 (AISC,2010) with the unsupported lateral length of h/2

$$P_e = \pi^2 \cdot \frac{EI_{eff}}{\left(K_c \cdot \frac{h}{2}\right)^2} = 1.171 \times 10^6 \qquad \text{kips}$$

$$n_1 = \frac{P_{n0}}{P_e} = 6.142 \times 10^{-3} \qquad \text{smaller than 2.25, OK}$$

The axial compression strength of the CFT column is calculated according to equation I2-2 (AISC,2010)

$$P_n = P_{n0} \cdot 0.658^{n_1} = 7.176 \times 10^3 \qquad \text{kips} \qquad \phi_c = 0.75$$

The axial tension strength of the CFT column is determined based on I2-8

$$T_n = F_y \cdot A_s = 4.418 \times 10^3 \qquad \text{kips} \qquad \phi_t = 0.9$$

The strength reduction factor for design is listed on the right side, and not included into the strength calculations at this stage.

Per AISC 2010, shear strength for filled composite members can be determined using the available shear strength of the steel alone. The nominal shear strength for round HSS per AISC 2010 Chapter G, is calculated using the equations listed below. The limit states of shear yielding and buckling is considered. The same equation is provided in the AASHTO Bridge Design Specifications (2010) section 6.12.1.2.3c

The critical shear stress is calculated to be the smaller of

$$F_{cr1} = 1.60 \cdot \frac{E_s}{\sqrt{\frac{h}{D}} \cdot \left(\frac{D}{t}\right)^{\frac{5}{4}}} = 157.353$$

$$F_{cr2} = 0.78 \cdot \frac{E_s}{\left(\frac{D}{t}\right)^{\frac{3}{2}}} = 81.163$$

$$F_{cr3} = 0.6 \cdot F_y = 36$$

therefore, $F_{cr} = F_{cr3}$

The shear strength of the CFT section: $V_n = F_{cr} \cdot \frac{A_s}{2} = 1.325 \times 10^3$ kips

$$\phi_v = 0.9$$

## Flexural strength calculation

Two approaches are identified as appropriate to calculate the flexural strength in AISC (2010), namely, (1) the plastic stress distribution, (2) the strain compatibility method. Per AASHTO Guide Specifications for LRFD Seismic Bridge Design (2009) section 7.6 , the design flexural strength of the composite section is calculated below using a method similiar to the plastic distribution method.

β is the central angle formed between the neutral axis chord line and the center point of the steel shell found by the following recursive equation (unit: rad)

$$\beta = 2.404 \quad \frac{A_s \cdot F_y + 0.2 \cdot D^2 \cdot f_c \cdot \left[ \sin\left(\frac{\beta}{2}\right) - \left(\sin\left(\frac{\beta}{2}\right)\right)^2 \cdot \tan\left(\frac{\beta}{4}\right) \right]}{0.125 \cdot D^2 f_c + D \cdot t \cdot F_y} = \beta \qquad (7.6.2-8)$$

The following are parameters shown in figure B-1 for calculating the flexural strength of the CFT section

$$b_c = D \cdot \sin\left(\frac{\beta}{2}\right) = 29.848 \qquad (7.6.2-7)$$

$$a = \frac{b_c \cdot \tan\left(\frac{\beta}{4}\right)}{2} = 10.232 \qquad (7.6.2-6)$$

$$e_1 = b_c \cdot \left(\frac{1}{2 \cdot \pi - \beta} + \frac{1}{\beta}\right) = 20.111 \qquad (7.6.2-4)$$

$$e_2 = b_c \cdot \left[\frac{1}{2 \cdot \pi - \beta} + \frac{{b_c}^2}{1.5 \cdot \beta \cdot D^2 - 6 \cdot b_c \cdot (0.5 \cdot D - a)}\right] = 17.693 \qquad (7.6.2-5)$$

$$C_{r1} = F_y \cdot \beta \cdot D \cdot \frac{t}{2} = 1.731 \times 10^3 \qquad (7.6.2-2)$$

$$C_{r2} = f_c \cdot \left[\beta \cdot \frac{D^2}{8} - \frac{b_c \cdot \left(\frac{D}{2} - a\right)}{2}\right] = 886.524 \qquad (7.6.2-3)$$

$$\phi_f = 1.0$$

Therefore the plastic strength of the CFT section is

$$M_n = \phi_f \cdot \left(C_{r1} \cdot e_1 + C_{r2} \cdot e_2\right) = 5.049 \times 10^4 \quad \text{kips} \cdot \text{in}$$

## Flexural strength, yielding displacement, and stiffness

The yielding flexural strength is obtained when the extreme point in the steel shell reaches the yielding strain of 0.002. Hand calculation is not performed here; instead this value is obtained from SAP2000 Section Designer.

The yielding flexural strength of the section is $M_y = 34199$ kips·in

The yielding curvature of the CFT column $\phi_y = 0.00011515$ $in^{-1}$

The yielding displacement of the CFT column $\Delta_y = 2 \cdot \phi_y \cdot \frac{\left(\frac{h}{2}\right)^2}{3} = 1.051$ in

The effective stiffness of the CFT column $K_{col} = \frac{2 \cdot M_y}{h \cdot \Delta_y} = 278.153$ $\frac{kip}{in}$

The gross stiffness of the CFT column based on the gross section properties $K_{gross} = 12 \cdot \frac{EI}{h^3} = 418.044$ $\frac{kip}{in}$

The ratio of the effective stiffness over the gross stiffness is $\frac{K_{col}}{K_{gross}} = 0.665$

# Fuse stiffness calculation

There are eight CFT columns in the bridge bent, so the total stiffness of the bridge bent is

$K_{bent} = 8 \cdot K_{col} = 2.225 \times 10^3$ $\frac{kip}{in}$

Assuming the period of the bridge bent in the transverse direction is in the range of the design spectrum plateau, which is the largest value of the spectrum

$S_a = 2\ g$

The relationship between the expected displacement of the bridge δe , the acceleration Sa, and the period T is

$$\delta_e = S_a \cdot T^2 \cdot \frac{g}{4 \cdot \pi^2}$$

The period of the bridge bent combined with the fuse can be calculated, assuming the expected displacement of the bridge bent to be the yielding displacement of the CFT columns $\Delta_y$.

$$T_s = \sqrt{\Delta_y \cdot 4 \cdot \frac{\pi^2}{S_a \cdot 386}} = 0.232 \quad s$$

The weight of the superstructure (includes all the dead loads calculated in chaper 3)

$$W_{super} = 4692 \quad kips$$

The total stiffness of the bridge required to make the period of the bridge to be Ts is

$$K_t = \frac{W_{super} \cdot 4 \cdot \pi^2}{386 \cdot T_s^2} = 8.93 \times 10^3 \quad \frac{kip}{in}$$

The required stiffness of the fuse is obtained by substracting the stiffness of the bent columns

$$K_{fuse} = K_t - K_{bent} = 6.705 \times 10^3 \quad \frac{kip}{in}$$

The ratio of the stiffness of the fuse over the bent is

$$\frac{K_{fuse}}{K_{bent}} = 3.013$$

The following demonstrates the necessity of adding fuses to prevent column yielding

The period of the bridge for the bare bent alone is $T=2\pi \sqrt{\frac{m_{super}}{K_{bent}}}$

$$T_b = 2 \cdot \pi \cdot \sqrt{\frac{W_{super}}{386 \cdot K_{bent}}} = 0.464 \quad s$$

From the acceleration spectrum in figure 1-2, the spectrum acceleration

$$S_b = 1.35 \quad g$$

The corresponding expected spectrum displacement is

$$\delta_t = S_b \cdot T_b^2 \cdot \frac{386}{4 \cdot \pi^2} = 2.847 \quad in$$

which is much larger than the expected displacement $\Delta y$

$$\frac{\delta_t}{\Delta_y} = 2.709$$

This shows that the added structural fuse is effective to prevent the yielding of the bent columns.

## Design of BRBs

### Transverse direction

The configuration of one of the bridge bent with inserted BRBs between the columns is shown in figure B-9. There are two bent with the same layout in parallel to each other. Note that, the distance between the columns, the numbers of the BRBs, the columns size will vary from bridge to bridge.

The material used for BRB is A500Gr.B steel with yielding strength requirement of 42 ksi $f_{ybrb} = 42$ ksi

The clear distance between the CFT columns is 6 ft in this case. There are four BRBs between the adjacent columns. The overhang of the bridge box girder is 3 ft.

$L_c = 6 \cdot 12 = 72$ in

The length of the BRB is $L_{brb} = \sqrt{L_c^2 + \left(\frac{h}{4}\right)^2} = 92.77$ in

The inclination angle of the BRB with the horizontal axis is $\theta = \operatorname{atan}\left(\frac{\frac{h}{4}}{L_c}\right) = 0.682$

$\cos(\theta) = 0.776 \quad \sin(\theta) = 0.631$

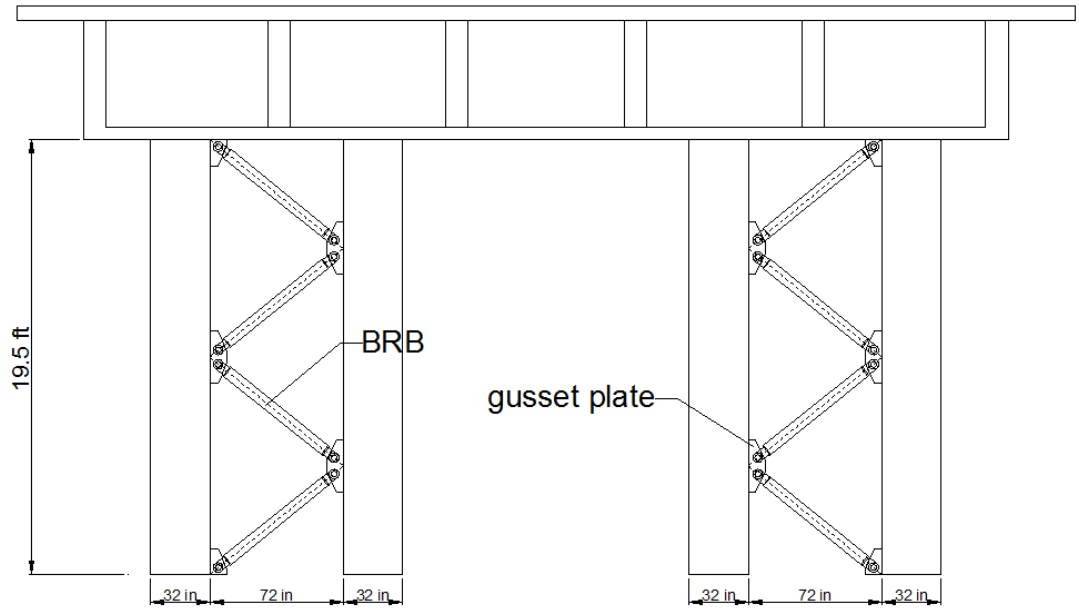


Figure B-9 The elevation view of the bridge bent in the transverse direction with inserted BRBs

A typical BRB consists of a yielding streel core encased to restrain buckling, non-yielding and buckling-restrained transition segments, and non-yielding and unrestrained end zones. When the BRB yields, yielding is limited to the buckling restrained yielding segment. The length of this yielding core is $c_{brb} * L_{brb}$, where $c_{brb}$ is the yielding length ratio, which needs to be calculated.

The yielding length ratio of the BRB is obtained here by having the BRB strain limit to be attained, when the expected spectrum displacement at the top of the bent reach Δy. The corresponding displacement of the BRB is $\Delta_y\cos\theta/4$. Noting that 1.5% strain limit is assumed to be conservative here, and larger strain limit can be used. A small strain limit can also be used, however, this would result in a longer yielding core and thus a larger brace section and yielding force to achieve the same target brace stiffness.

$$c_{brb} = \frac{\frac{\Delta_y}{4}}{0.015 \cdot L_{brb}} \cdot \cos(\theta) = 0.147$$

The corresponding displacement of the CFT column when the BRB yields is

$$\Delta_{fuse} = \frac{4 \cdot f_{ybrb} \cdot c_{brb} \cdot L_{brb}}{E_s \cdot \cos(\theta)} = 0.101 \quad \text{in}$$

The area of the BRB required to obtain the stiffness calculated above is

$$A_{brb} = \Delta_{fuse} \cdot \frac{K_{fuse}}{4 \cdot \left(4 \cdot f_{ybrb} \cdot \sin(\theta) \cdot \frac{L_c}{h}\right)} = 5.217 \quad \text{in}^2$$

The yielding force in the BRB is

$$f_{ybrb} \cdot A_{brb} = 219.126 \quad \text{kips}$$

After the BRB yields, it will enter into the strain hardening stage. The axial force in the BRB will increase,and the strain hardening factors below are used to calculate the largest forces the BRB can develop under compression or tension forces. To note, strain hardening factors will vary with BRB size and suppliers.

$$\omega\beta = 1.5 \quad \omega = 1.35$$

The largest force that can be developed in the BRB subjected to compressive force is

$$\omega\beta \cdot f_{ybrb} \cdot A_{brb} = 328.688 \quad \text{kips}$$

The largest force that can be developed in the BRB subjected to tensile force is

$$\omega \cdot f_{ybrb} \cdot A_{brb} = 295.819 \quad \text{kips}$$

The overall largest lateral load resistance provided by four BRBs between the adjacent

$$V_{bc} = (2 \cdot \omega + 2\omega\beta) \cdot f_{ybrb} \cdot \sin(\theta) \cdot A_{brb} \cdot \frac{L_c}{h} = 242.345 \quad \text{kips}$$

The overall largest axial force added to the CFT columns by four BRBs between the

$$P_{bc} = (2 \cdot \omega + 2\omega\beta) \cdot f_{ybrb} \cdot \sin(\theta) \cdot A_{brb} = 787.62 \quad \text{kips}$$

To note, the axial forces from the BRBs are added to the columns at different points.

## Longitudinal direction

To be consistent with the transverse direction, the distance between the adjacent columns in the longitudinal direction would still be 6 ft. There are four parallel longitudinal bent as shown in figure B-10.

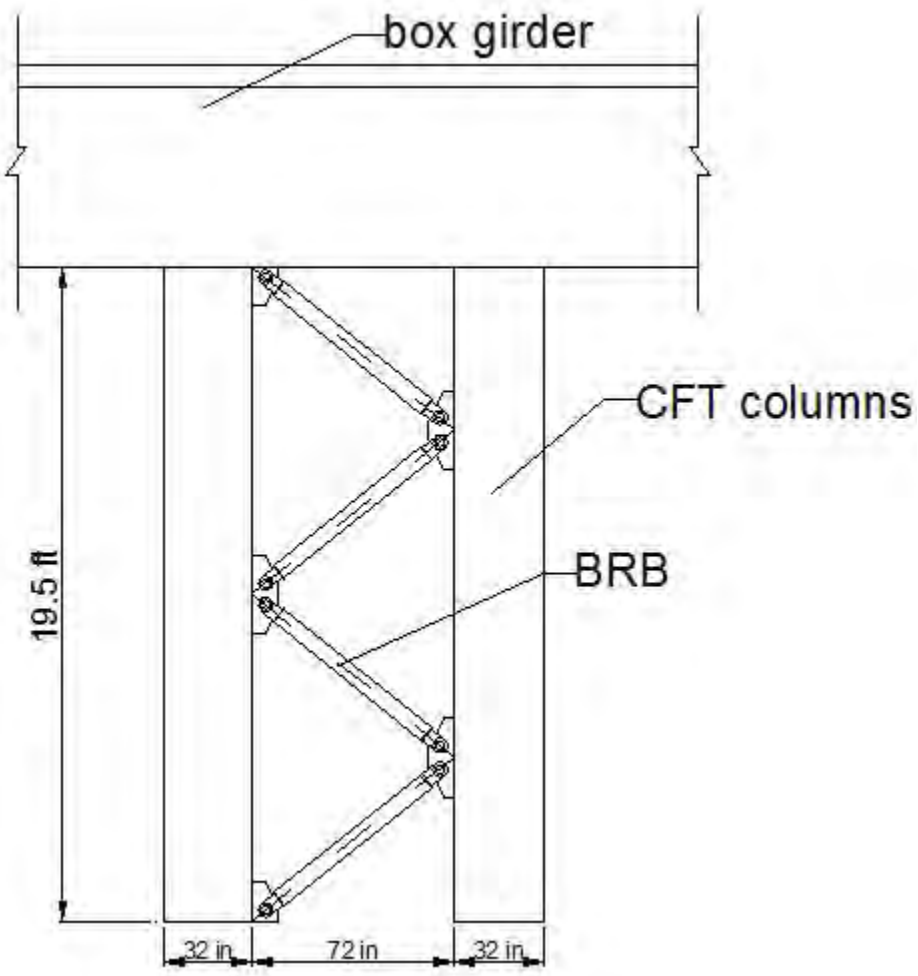


Figure B-10 The elevation view of the bridge bent in the longitudinal direction with inserted BRBs

Since the bridge is designed to have the same increase of the stiffness in both directions, the period and target displacement in each direction would be the same. The columns will reach the target displacement, a.k.a, the yielding displacement $\Delta_y$. The layout of the BRBs between the columns is the same as the ones between the adjacent columns in the transverse direction. Therefore, the design of the BRBs does not change. The BRBs will still have the assumed strain hardening limit of 1.5% when the bridge reached the yielding displacement in the longitudinal direction.

The axial-flexure interaction, and shear capacity check of the columns under the bi-directional earthquake load effect will be checked using the analysis results in chapter 3.

# Appendix C Section designer analysis in SAP2000 and comparison with code design values

Some properties of the CFT column used in analyses are obtained using SAP2000's Section Designer (which provides cross-section properties and moment-curvature relationship, using a fiber analysis). The outside diameter of the section is 48". The thickness of the steel shell is 1.25". A grid of 20 by 20 fibers is used for calculating the capacity of the section and plastic hinge analysis.

Table C-1 compares the axial strength of the section per AISC (2010) in Chapter 3, AASHTO (2010) in Appendix B, and the value obtained from section designer. The tabulated values are those calculated without reduction factors, $\phi$. The value for the axial strength from section designer is obtained for bi-linear material properties, considers no strain hardening. The bi-linear stress-strain curve for A572 Gr 60 steel is shown in Figure C-1. The yielding strength is 60 ksi, reached at the strain of 0.002069. The ultimate strain is set to be 0.17, the same as the unmodified A572 Gr60 steel based on the material properties provided by the ASTM A572 for high-strength low-alloy Columbium-Vanadium structural steel.

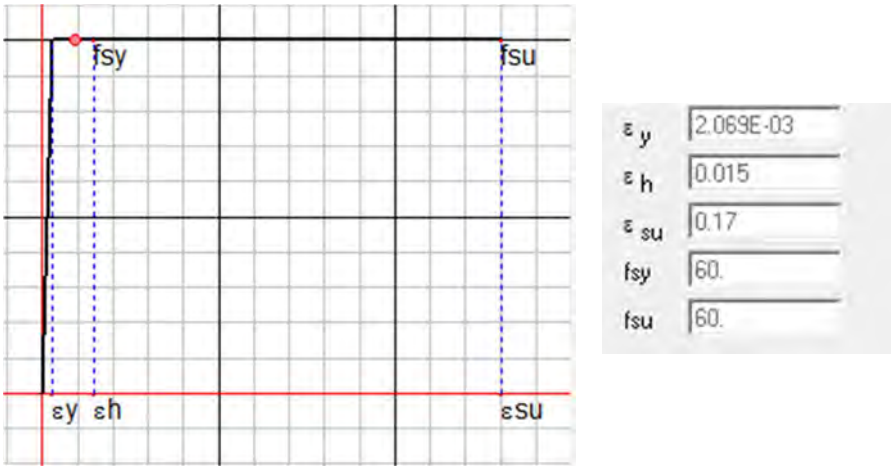


Figure C-1 The bilinear model of the steel stress-strain curve

The concrete tensile strength is not considered in the concrete material properties. Confined concrete model is used here. The compressive strength of the concrete is 4 ksi, which is reached at the strain of 0.002219. Then the compressive strength drops to 2 ksi at the largest strain of 0.02.

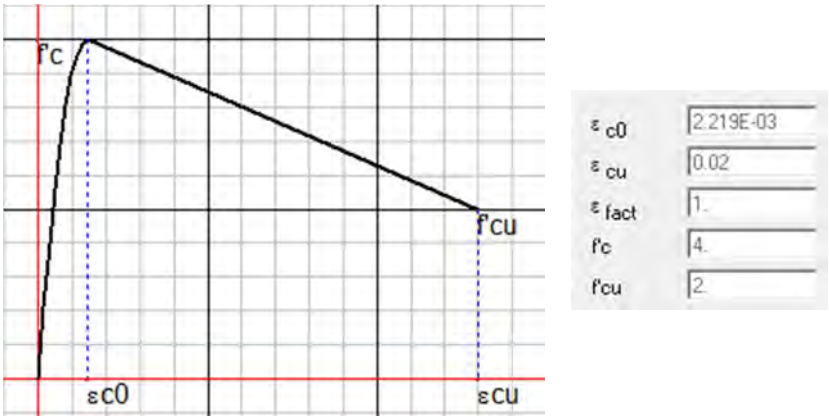


Figure C-2 The confined concrete material stress-strain curve

Table C-1 shows the axial strength under compressive and tensile forces calculated based on the equations from AISC (2010) and AASHTO Bridge Design Specifications (2010). The tensile strength of the section is the same for the two equations from the design codes as $f_y A_s$.

Note that the reduction factor for the concrete compressive strength per AISC (2010) and AASHTO (2010) is 0.95 and 0.85, respectively. Therefore, the compressive strength design value from AISC (2010) is close to the value obtained from Section Designer value calculated without the reduction factor, while the compressive strength design value from AASHTO (2010) is closer to the one with reduction factor.

Table C-1 Comparison of axial strengths obtained from AISC 2010 and from SAP2000 section designer

| | Tension | Compression | Difference with Section Designer having 0.85 concrete reduction factors |
|---|---|---|---|
| AISC (2010) (kips) | 11020 | -17120 | 4.16% |
| AASHTO (2010) (kips) | 11020 | -16470 | 0.20% |
| Section Designer ($f_yA_s$+ $f_cA_c$) for comp. strength (kips) | | -17332 | |
| Section Designer ($f_yA_s$+0.85 $f_cA_c$) for comp. strength (kips) | | -16437 | |

The value from section designer with the reduction factor is the one retained for the axial strength when performing capacity check. The AASHTO equations to calculate axial strength are identical to those in an older edition of the AISC Specifications; the new AISC equations are assumed to reflect the latest knowledge on this topic and are used here.

A moment curvature curve from Section Designer is calculated using elasto-plastic material models, with steel yielding at $F_y$=60 ksi and concrete strength of $f'_c$=4 ksi. The curve is shown in Figure C-3. The plastic flexural strength is 184 036 kip-in, when the assumed ultimate strain of the concrete of 0.02 is reached. The moment curvature curve drops due to degradation of concrete strength per Figure C-2. For

comparison, if the concrete was modeled to have no strength degradation, the plastic flexural strength reached would have been 185710 kip-in.

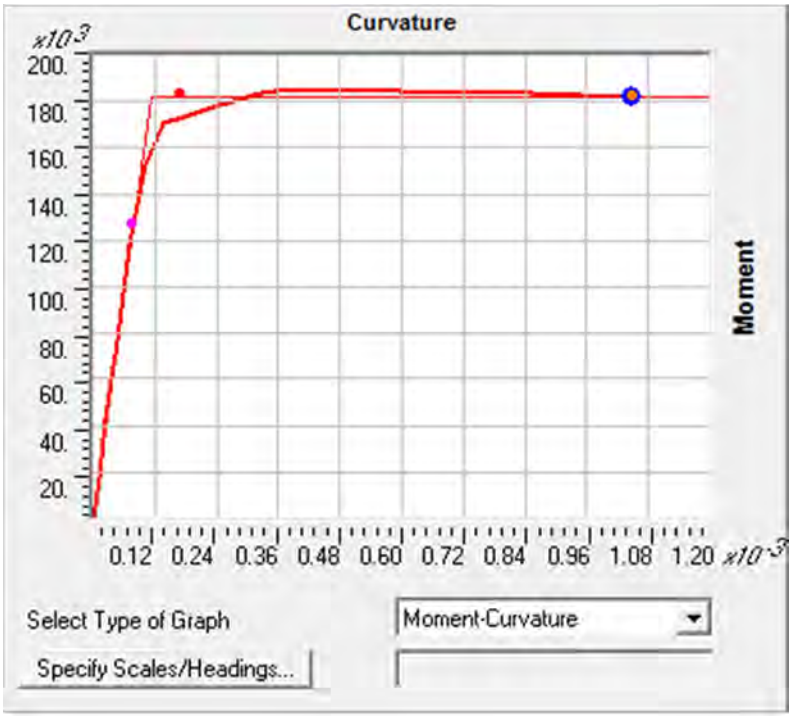


Figure C-3 Moment-curvature curve of the fiber model analysis w/o strain hardening

For design purposes, it is desirable to simplify the actual moment curvature considering strain hardening effects into an equivalent elastic perfectly plastic curve. In particular, the Caltrans seismic design criteria (2010) specifies that such an idealized bi-linear model can be used to estimate the plastic moment capacity of a member's cross section. For that purpose, the SAP2000 Section Designer includes an option to calculate the flexural strength of the section using what it defines as the "Caltrans idealized model." It first defines the elastic portion of the idealized curve by a straight line passing through the point when first yielding of the steel shell occurs. The value of the plastic moment is then obtained by balancing the areas between the actual and the idealized moment-curvature curve beyond the first yielding of the steel shell. Following this procedure, the resulting Caltrans idealized flexural strength in Figure C-3 is 183 328 kip-in.

The design flexural strength of the CFT section per AASHTO is 187800 kip-in

(Appendix B). The difference of 2.4% compared with the Caltrans idealized design value is negligible. The yielding of the CFT section in section designer is set to be at the first yielding of the extreme steel fiber. The corresponding yielding moment is 126891 kip-in, which is the value used in chapter 1 for the structural fuse design.

An alternative way to use Section Designer is to consider material properties having strain hardening. The stress-strain curve of the steel and concrete material is shown in Figure C-3. The yielding strength of the steel is 60 ksi, which is reached at the strain of 0.002069. The steel enters the strain hardening stage at the strain of 0.015. The ultimate tensile strength of the steel material is 75 ksi, which is reached at the strain of 0.11. The ultimate rupture strain of the steel would be 0.17.

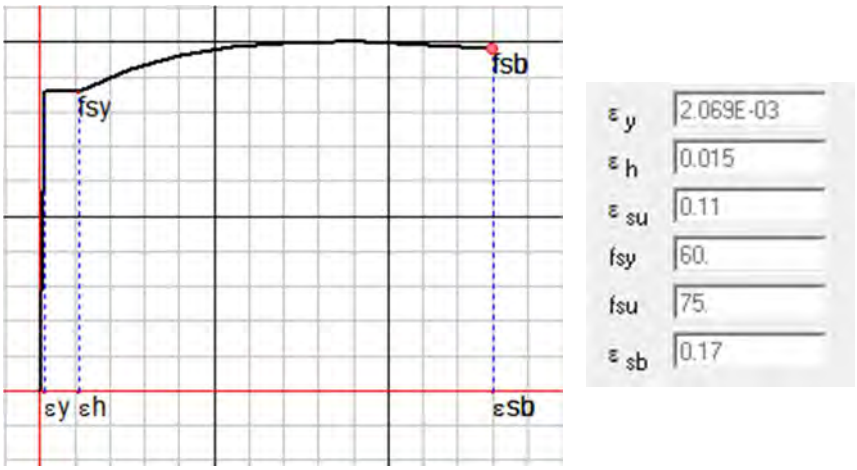


Figure C-4 Steel stress-strain curve considering the strain hardening

The resulting moment curvature curve is obtained as in Figure C-5. The plastic flexural strength is 194147 kip-in, shown as the blue point in Figure C-5 and obtained when the assumed ultimate strain of the concrete of 0.02 is reached. The corresponding Caltrans idealized flexural strength (i.e., calculated per the procedure described above) is 185621 kip-in. Interestingly, this is within 1.17% of the AASHTO value calculated in Appendix B.

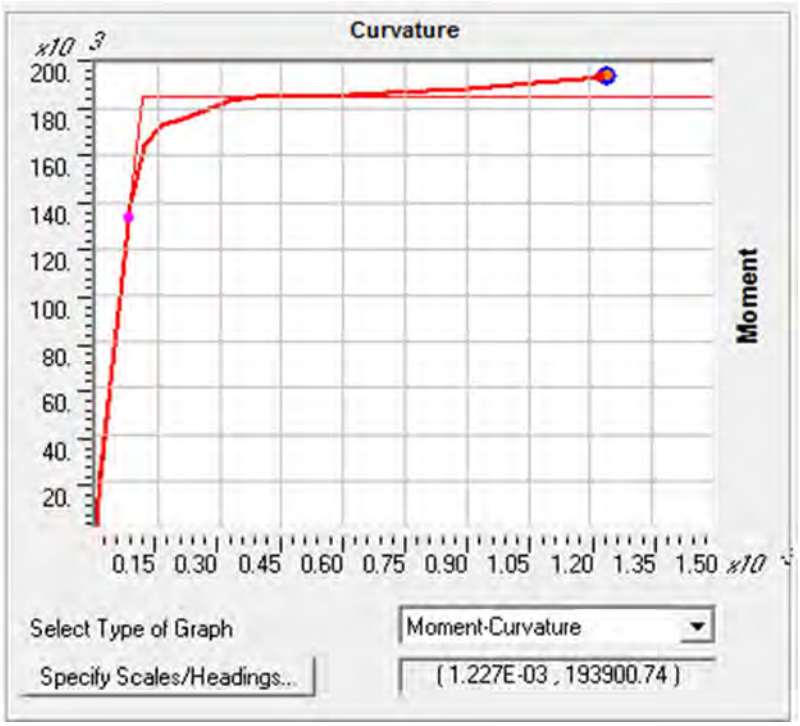


Figure C-5 Moment-curvature curve of the CFT column

Note that the design checks performed by hand calculations use the values from AISC (2010) for axial strength and shear strength and AASHTO for flexural strength. However, when analyses are performed with SAP2000 to check the resulting design, the forces obtained from SAP2000 are compared to the strength values obtained from SAP2000 Section Designer. The flexural strength use the Caltrans idealized flexural strength of 185621 kip-in. The compression strength is -16437 kips, using the value having the concrete reduction factor of 0.85. The tension strength is 11020 kips, the same as the values from the design codes.

# Appendix D Anchor rod design calculation sheet

This design example illustrates two example design of the BRBs using anchor rods to conect to the foundation or cap beam. The first one for two column bent with the inverted-V BRBs are designed to be connected (1) at the bottom only to the foundation for the tensile BRB; (2) at the top to the cap beam for both BRBs. The second one for box pier with BRBs are designed to be connected (1) at the bottom only to the foundation for the tensile BRB; (2) at the top to the cap beam for both BRBs.

## D.1 Two column bent with Chevron BRBs

### (1) Tensile BRB with footing

The force demand is

$V_t := 470.43$ kips $N_t := 853.44$ kips

Use the anchor rod Grade 55

Minimum tensile strength $F_u := 58$ ksi

Minimum yielding strength $F_y := 36$ ksi

16 anchor rods are used for this design $n := 16$

The diameter of the anchor rod is $d := 2$ in

The area of the anchor rod is $A_d := \pi \cdot \frac{d^2}{4} = 3.142$ $in^2$

The bearing area of the anchor rod from table is $A_{brg} := 5.35$ $in^2$

The concrete strength is $f_c := 5$ ksi

### ACI 318-08 Appendix D

The steel anchor strength under tension force is $N_s := 0.75 \cdot F_u \cdot A_d = 136.659$ kips

The steel anchor strength under tension force is $V_s := 0.65 \cdot F_u \cdot A_d = 118.438$ kips

The concrete pullout strength of a single anchor rod in tension calculated is according to section D5.3 in ACI318-08

$N_p = \phi_1 \cdot \psi_1 \cdot A_{brg} \cdot 8 \cdot f_c$

where : the concrete cracking parameter $\psi_1 := 1$

the resistance reduction factor $\phi_1 := 0.75$

$N_p := \phi_1 \cdot \psi_1 \cdot A_{brg} \cdot f_c \cdot 8 = 160.5$ kips

Table D-1 Anchor rod dimensions and areas (Hogan and Thomas, 1994)

| Rod Diameter, in. | Rod Area, $A_n$, in² | Bearing Area, in² |
|---|---|---|
| ⅝ | 0.307 | 0.689 |
| ¾ | 0.442 | 0.906 |
| ⅞ | 0.601 | 1.22 |
| 1 | 0.785 | 1.50 |
| 1⅛ | 0.994 | 1.81 |
| 1¼ | 1.23 | 2.24 |
| 1½ | 1.77 | 3.13 |
| 1¾ | 2.41 | 4.17 |
| 2 | 3.14 | 5.35 |
| 2¼ | 3.98 | 6.69 |
| 2½ | 4.91 | 8.17 |
| 2¾ | 5.94 | 9.80 |
| 3 | 7.07 | 11.4 |
| 3¼ | 8.30 | 13.3 |
| 3½ | 9.62 | 15.3 |
| 3¾ | 11.0 | 17.5 |
| 4 | 12.6 | 19.9 |

The concrete breakout strength of a single anchor rod in tension calculated is according section D5.2 in ACI318-08

$$N_b = \phi_2 \cdot \left[ 16 \cdot \sqrt{f_c \cdot 1000} \cdot \frac{\left(h_{ef}\right)^{\frac{5}{3}}}{1000} \right]$$

where : the resistance reduction factor $\phi_2 := 0.7$

The embedment length of the anchor rod is $h_{ef} := 30$ in

$$N_b := \phi_2 \cdot 16 \cdot \sqrt{f_c \cdot 1000} \cdot \frac{\left(h_{ef}\right)^{\frac{5}{3}}}{1000} = 229.389 \quad \text{kips}$$

The group effect of the anchor rods is considered in the following equation for the concrete breakout strength:

The design horizontal center-to-center distance of the anchor rod in the x-axis direction is

$$h_{dis} := 40 \quad in$$

The design horizontal center-to-center distance of the anchor rod in the y-axis direction is

$$v_{dis} := 40 \quad in$$

The layout of the anchor rods group is shown in figure 5-21a, 5-21b.

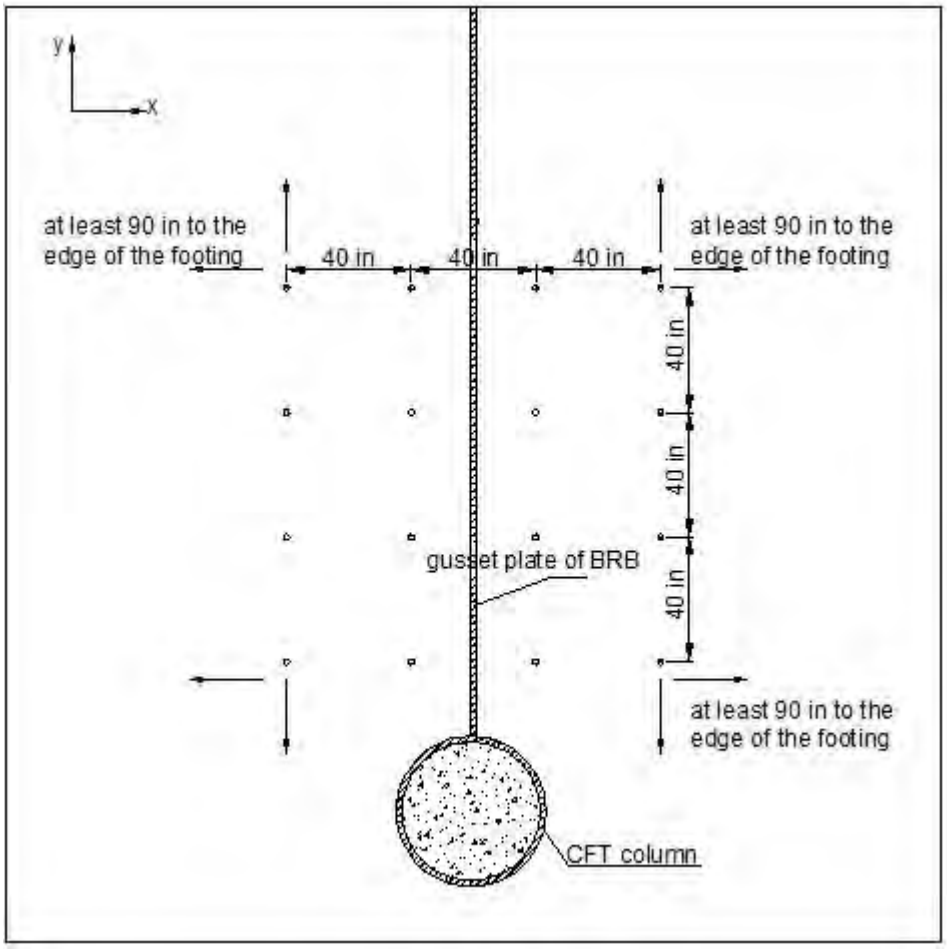


Figure 5-21a The layout of the anchor rods from top view

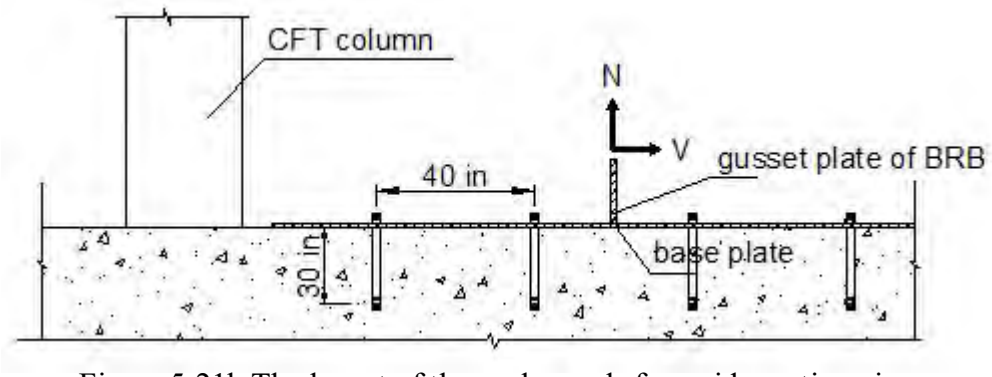


Figure 5-21b The layout of the anchor rods from side section view

The projected concrete failure area of the anchor rods group is

$$A_n := \left(3 \cdot h_{ef} + 3 \cdot h_{dis}\right) \cdot \left(3 \cdot h_{ef} + 3v_{dis}\right) = 4.41 \times 10^4 \quad in^2$$

The projected concrete failure area of a single anchor with an edge distance equal to or greater than $1.5h_{ef}$ is

$$A_{no} := 9 \cdot h_{ef}^{\,2} = 8.1 \times 10^3 \quad in^2$$

The reduced tensile resistance of the anchor rods group is

$$N_{bg} := N_b \cdot \frac{A_n}{A_{no}} = 1.249 \times 10^3 \quad kips$$

Smaller than $n \cdot N_b = 3.67 \times 10^3$ kips

$n \cdot N_s = 2.187 \times 10^3$ kips

$n \cdot N_p = 2.568 \times 10^3$ kips

The concrete prying out strength of anchor rods group in shear is calculated according to section D6.3 in ACI318-08

$$Vp = k_{cp} \cdot N_{bg}$$

where : the factor for $h_{ef}$ larger than 2.5" $k_{cp} := 2.0$

$$V_{pg} := k_{cp} \cdot N_{bg} = 2.498 \times 10^3 \quad kips$$

The concrete breakout strength of a single anchor rod in shear is calculated according to section D6.2 in ACI318-08

$$Vb = \phi_3 \cdot 10.4 \cdot \sqrt{d} \cdot \sqrt{f_c \cdot 1000} \cdot \frac{c_1^{1.5}}{1000}$$

where : the resistance reduction factor $\phi_3 := 0.7$

The side distance of the anchor rod to an edge $c_1 := 90$ in

$$V_b := \phi_3 \cdot 10.4 \cdot \sqrt{d} \cdot \sqrt{f_c \cdot 1000} \cdot \frac{c_1^{1.5}}{1000} = 621.577 \quad \text{kips}$$

The projected concrete failure area of the anchor rods group is

$$A_v := \left(3 \cdot c_1 + 3h_{dis}\right) \cdot h_{ef} = 1.17 \times 10^4 \quad \text{in}^2$$

The projected concrete failure area of a single anchor in a deep member with a distance from edges equal or greater than 1.5 $h_{ef}$ in the direction perpendicular to the shear surface

$$A_{vo} := 3 \cdot c_1 \cdot h_{ef} = 8.1 \times 10^3 \quad \text{in}^2$$

The reduced shear strength of the anchor rods group is

$$V_{bg} := V_b \cdot \frac{A_v}{A_{vo}} = 897.834 \quad \text{kips}$$

Smaller than

$$n \cdot V_b = 9.945 \times 10^3 \quad \text{kips}$$

$$V_{pg} = 2.498 \times 10^3 \quad \text{kips}$$

For the anchor rod group, the interaction of the shear and tension force interaction is checked using the following equation.

$$\left(\frac{V_t}{V_{bg}}\right)^{\frac{5}{3}} + \left(\frac{N_t}{N_{bg}}\right)^{\frac{5}{3}} = 0.871$$

smaller than 1.0, therefore the anchor rod group design is sufficient to resist the forces.

## AISC (2010)

AISC (2010) provided the following equation for the shear and tension stress check in a single anchor rod. The available tensile strength of a single anchor rod subjected to combined tension and shear forces shall be determined according to the limit state of tension and shear rupture as follows:

$$R_n = \phi_4 \cdot F_{nt} \cdot A_d$$

where: nominal tensile stress modified to include the effects of shear stress.

$$F_{nt1} = 1.3 \cdot F_{nt} - \frac{F_{nt} \cdot f_s}{0.75 \cdot F_{nv}}$$

the resistance reduction factor is. $\phi_4 := 0.75$

The nominal tensile stress in the anchor rod $F_{nt} := 0.75 \cdot F_u = 43.5$ ksi

The nominal shear stress in the anchor rod $F_{nv} := 0.4 \cdot F_u = 23.2$ ksi

The shear stress in the anchor rod is $f_s := \frac{V_t}{n \cdot A_d} = 9.359$ ksi

The total tension force can be taken by the anchor rod group would be

$$F_{nt1} := 1.3 \cdot F_{nt} - F_{nt} \cdot \frac{f_s}{0.75 \cdot F_{nv}} = 33.153 \quad \text{ksi}$$

$$F_t := n F_{nt1} \cdot A_d \cdot \phi_4 = 1.25 \times 10^3 \quad \text{kips}$$

The tension force demand is $N_t = 853.44$ kips

The anchor rod group is sufficient to resist the forces per AISC(2010).

## (2) Two BRBs top connection with cap beam

The force demand is

$V_t := 992$ kips

Use the anchor rod Grade 55

| | | |
|---|---|---|
| Minimum tensile strength | $F_u := 58$ | ksi |
| Minimum yielding strength | $F_y := 36$ | ksi |
| 16 anchor rods are used for this design | $n := 16$ | |
| The diameter of the anchor rod is | $d := 2$ | in |
| The area of the anchor rod is | $A_d := \pi \cdot \frac{d^2}{4} = 3.142$ | $in^2$ |
| The bearing area of the anchor rod from table B-1 is | $A_{brg} := 5.35$ | $in^2$ |
| The concrete strength is | $f_c := 5$ | ksi |

## ACI 318-08 Appendix D

The steel anchor rod strength under tension force $V_s := 0.65 \cdot F_u \cdot A_d = 118.438$ kips

The concrete breakout strength of a single anchor rod in tension is calculated according section D5.2 in ACI318-08

$$N_b = \phi_2 \cdot \left[ 16 \cdot \sqrt{f_c \cdot 1000} \cdot \frac{\left(h_{ef}\right)^{\frac{5}{3}}}{1000} \right]$$

where : the resistance reduction factor $\phi_2 := 0.7$

The embedment length of the anchor rod is $h_{ef} := 30$ in

$$N_b := \phi_2 \cdot 16 \cdot \sqrt{f_c \cdot 1000} \cdot \frac{\left(h_{ef}\right)^{\frac{5}{3}}}{1000} = 229.389 \text{ kips}$$

The group effect of the anchor rod group is considered in the following equation for the concrete breakout strength:

The design horizontal center-to-center distance of the anchor rod in the x-axis direction is

$$h_{dis} := 40 \quad in$$

The design horizontal center-to-center distance of the anchor rod in the y-axis direction is

$$v_{dis} := 40 \quad in$$

The layout of the anchor rod group is shown in figure 5-21a, 5-21b.

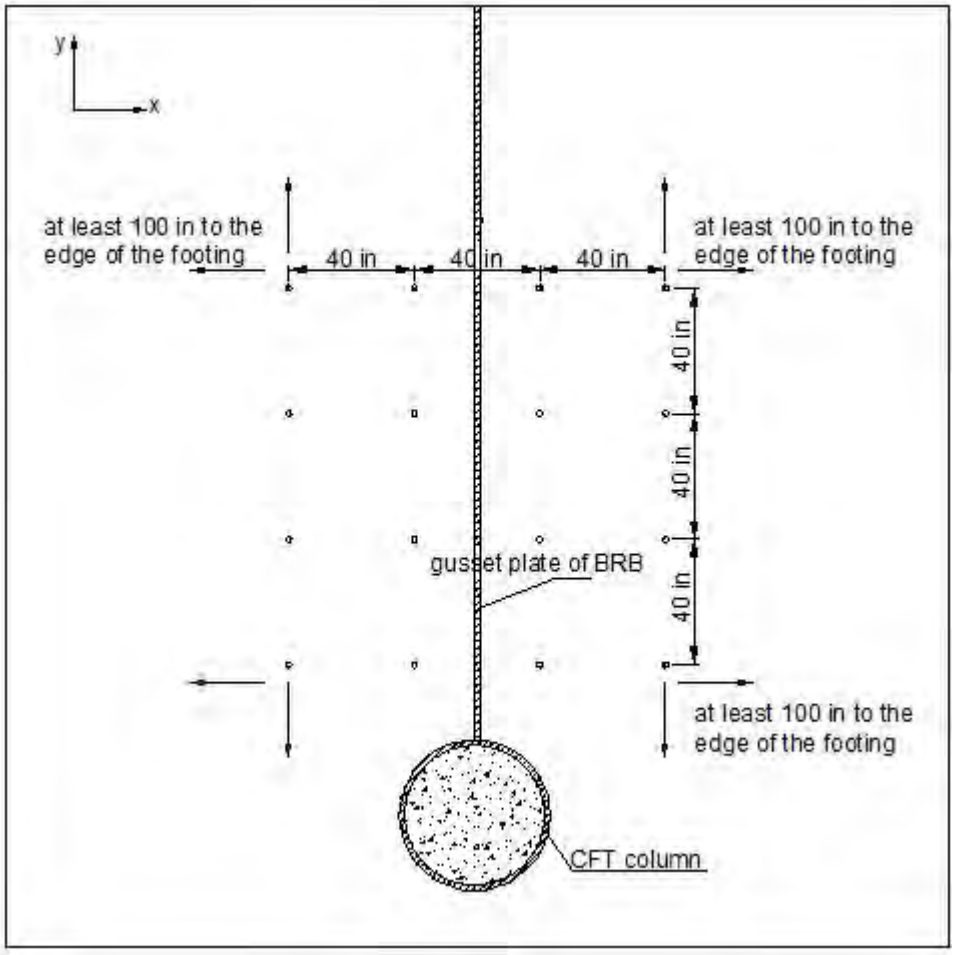


Figure 5-21a The layout of the anchor rod from top view(with center-to-center distance change from 90 in to 100 in)

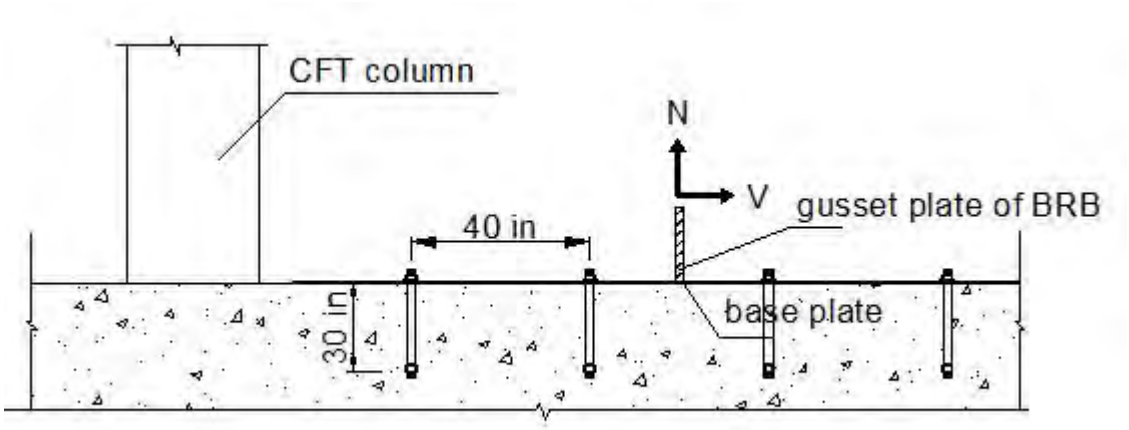


Figure 5-21b The layout of the anchor rod from side section view

The projected concrete failure area of the anchor group is

$$A_n := \left(3 \cdot h_{ef} + 3 \cdot h_{dis}\right) \cdot \left(3 \cdot h_{ef} + 3 v_{dis}\right) = 4.41 \times 10^4 \quad in^2$$

The projected concrete failure area of a single anchor with an edge distance equal to or greater than $1.5h_{ef}$ is

$$A_{no} := 9 \cdot h_{ef}^{\,2} = 8.1 \times 10^3 \quad in^2$$

The reduced tensile resistance of the anchor rod group is

$$N_{bg} := N_b \cdot \frac{A_n}{A_{no}} = 1.249 \times 10^3 \quad kips$$

The concrete prying out strength of anchor rod group in shear is calculated according to section D6.3 in ACI318-08

$$Vp = k_{cp} \cdot N_{bg}$$

where : the factor for $h_{ef}$ larger than 2.5" $\quad k_{cp} := 2.0$

$$V_{pg} := k_{cp} \cdot N_{bg} = 2.498 \times 10^3 \quad kips$$

The concrete breakout strength of a single anchor rod in shear is calculated according to section D6.2 in ACI318-08

$$Vb = \phi_3 \cdot 10.4 \cdot \sqrt{d} \cdot \sqrt{f_c \cdot 1000} \cdot \frac{c_1^{\,1.5}}{1000}$$

where : the resistance reduction factor $\phi_3 := 0.7$

The side distance of the anchor rod to an edge $c_1 := 100$ in

$$V_b := \phi_3 \cdot 10.4 \cdot \sqrt{d} \cdot \sqrt{f_c \cdot 1000} \cdot \frac{c_1^{1.5}}{1000} = 728 \quad \text{kips}$$

The projected concrete failure area of the anchor rod group is

$$A_v := \left(3 \cdot c_1 + 3h_{dis}\right) \cdot h_{ef} = 1.26 \times 10^4 \quad \text{in}^2$$

The projected concrete failure area of a single anchor in a deep member with a distance from edges equal or greater than 1.5 $h_{ef}$ in the direction perpendicular to the shear surface

$$A_{vo} := 3 \cdot c_1 \cdot h_{ef} = 9 \times 10^3 \quad \text{in}^2$$

The reduced shear strength of the anchor rod group is

$$V_{bg} := V_b \cdot \frac{A_v}{A_{vo}} = 1.019 \times 10^3 \quad \text{kips}$$

Smaller than $n \cdot V_b = 1.165 \times 10^4$ kips

$V_{pg} = 2.498 \times 10^3$ kips

$n \cdot V_s = 1.895 \times 10^3$ kips

$$\frac{V_{bg}}{V_t} = 1.027 \quad \text{OK}$$

## AISC (2010)

The nominal shear stress in the anchor rod $F_{nv} := 0.4 \cdot F_u = 23.2$ ksi

The shear stress in the anchor rod is $f_s := \frac{V_t}{n \cdot A_d} = 19.735$ ksi

$$\frac{F_{nv}}{f_s} = 1.176 \quad \text{OK}$$

## D.2 Box pier with BRBs

The force demand is

$V_t := 186.65$ kips $N_t := 229.54$ kips

Use the anchor rod Grade 55

| | | |
|---|---|---|
| Minimum tensile strength | $F_u := 58$ | ksi |
| Minimum yielding strength | $F_y := 36$ | ksi |
| 6 anchor rods are used for this design | $n := 6$ | |
| The diameter of the anchor rod is | $d := 2$ | in |
| The area of the anchor rod is | $A_d := \pi \cdot \frac{d^2}{4} = 3.142$ | $in^2$ |
| The bearing area of the anchor rod from table B-1 is | $A_{brg} := 5.35$ | $in^2$ |
| The concrete strength is | $f_c := 5$ | ksi |

## ACI 318-08 Appendix D

The steel anchor rod strength under tension force i $N_s := 0.75 \cdot F_u \cdot A_d = 136.659$ kips

The steel anchor rod strength under tension force i $V_s := 0.65 \cdot F_u \cdot A_d = 118.438$ kips

The concrete pullout strength of a single anchor rod in tension is calculated according to section D5.3 in ACI318-08

$= \phi_1 \cdot \psi_1 \cdot A_{brg} \cdot 8 \cdot f_c$

where : the concrete cracking parameter $\psi_1 := 1$

the resistance reduction factor $\phi_1 := 0.75$

$N_p := \phi_1 \cdot \psi_1 \cdot A_{brg} \cdot f_c \cdot 8 = 160.5$ kips

The concrete breakout strength of a single anchor rod in tension is calculated according section D5.2 in ACI318-08

$$N_b = \phi_2 \cdot \left[ 16 \cdot \sqrt{f_c \cdot 1000} \cdot \frac{\left(h_{ef}\right)^{\frac{5}{3}}}{1000} \right]$$

where : the resistance reduction factor $\phi_2 := 0.7$

The embedment length of the anchor rod is $h_{ef} := 20$ in

$$N_b := \phi_2 \cdot 16 \cdot \sqrt{f_c \cdot 1000} \cdot \frac{\left(h_{ef}\right)^{\frac{5}{3}}}{1000} = 116.704 \quad \text{kips}$$

The group effect of the anchor rod group is considered in the following equation for the concrete breakout strength:

The design horizontal center-to-center distance of the anchor rod in the x-axis direction is $h_{dis} := 20$ in

The design horizontal center-to-center distance of the anchor rod in the y-axis direction is $v_{dis} := 20$ in

The layout of the anchor rod group is shown in figure 5-22a, 5-22b.

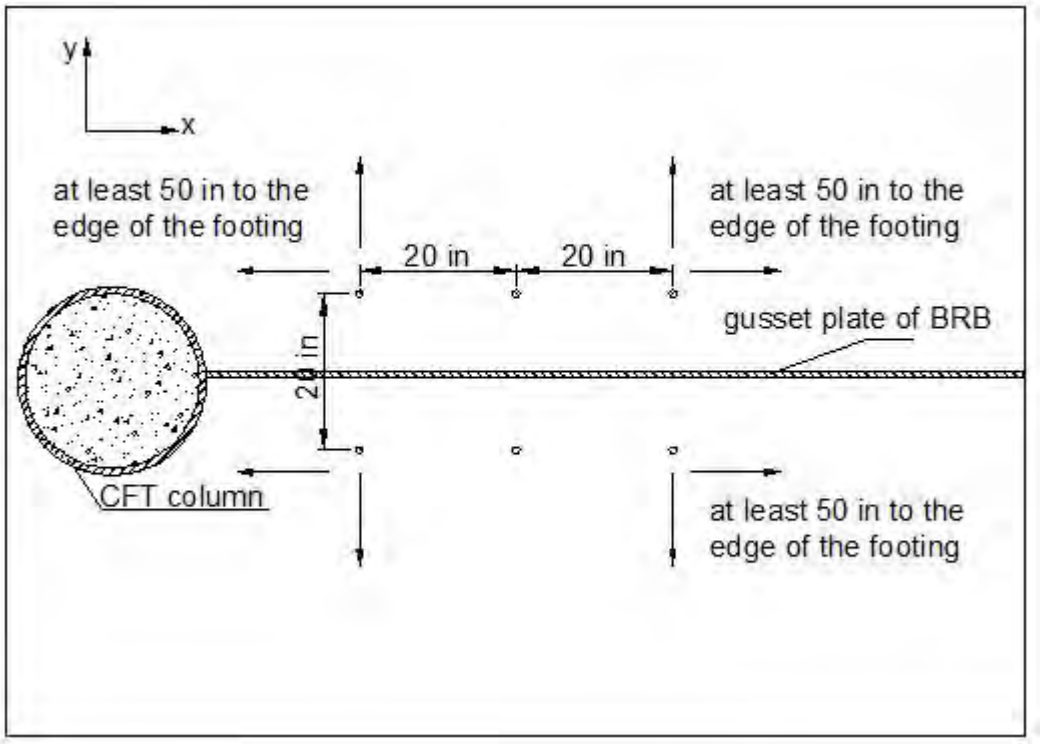


Figure 5-22a The layout of the anchor rod from top view

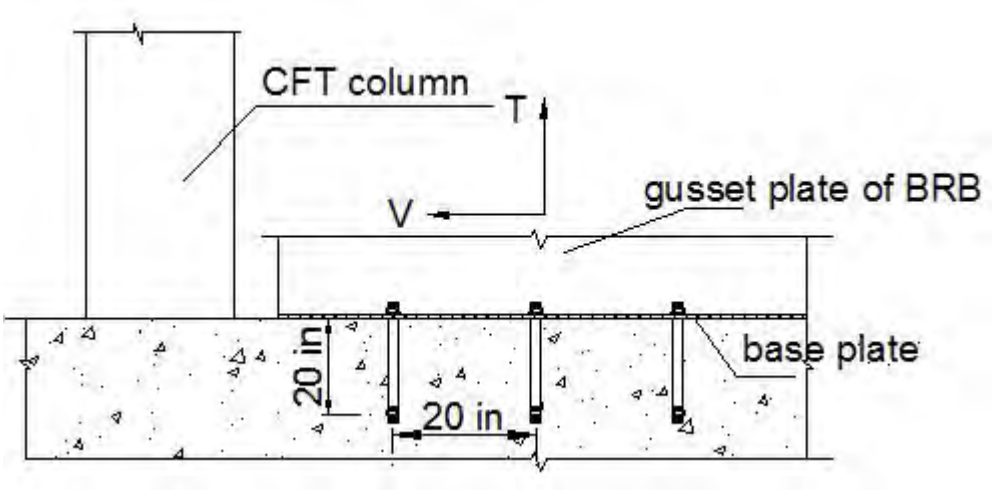


Figure 5-22b The layout of the anchor rod from side section view

The projected concrete failure area of the anchor rod group is

$$A_n := \left(3 \cdot h_{ef} + 2h_{dis}\right) \cdot \left(3 \cdot h_{ef} + 2v_{dis}\right) = 1 \times 10^4 \quad in^2$$

The projected concrete failure area of a single anchor rod with an edge distance equal to or greater than $1.5h_{ef}$ is

$$A_{no} := 9 \cdot h_{ef}^{\,2} = 3.6 \times 10^3 \quad in^2$$

The reduced tensile resistance of the anchor rod group is

$$N_{bg} := N_b \cdot \frac{A_n}{A_{no}} = 324.178 \quad kips$$

Smaller than $n \cdot N_b = 700.225$ kips

$n \cdot N_s = 819.956$ kips

$n \cdot N_p = 963$ kips

The concrete prying out strength of the anchor rod group in shear is calculated according to section D6.3 in ACI318-08

$$Vp = k_{cp} \cdot N_{bg}$$

where : the factor for $h_{ef}$ larger than 2.5" $k_{cp} := 2.0$

$$V_{pg} := k_{cp} \cdot N_{bg} = 648.356 \quad kips$$

The concrete breakout strength of a single anchor rod in shear calculated is according to section D6.2 in ACI318-08

$$Vb = \phi_3 \cdot 10.4 \cdot \sqrt{d} \cdot \sqrt{f_c \cdot 1000} \cdot \frac{c_1^{1.5}}{1000}$$

where : the resistance reduction factor $\phi_3 := 0.7$

The side distance of the anchor rod to an edge in the direction of the applied shear force $c_1 := 50$ in

$$V_b := \phi_3 \cdot 10.4 \cdot \sqrt{d} \cdot \sqrt{f_c \cdot 1000} \cdot \frac{c_1^{1.5}}{1000} = 257.387 \quad \text{kips}$$

The projected concrete failure area of the anchor rod group is

$$A_v := \left(3 \cdot c_1 + 2h_{dis}\right) \cdot h_{ef} = 3.8 \times 10^3 \quad \text{in}^2$$

The projected concrete failure area of a single anchor rod in a deep member with a distance from edges equal or greater than 1.5 $h_{ef}$ in the direction perpendicular to the shear surface

$$A_{vo} := 3 \cdot c_1 \cdot h_{ef} = 3 \times 10^3 \quad \text{in}^2$$

The reduced shear strength of the anchor rod group is

$$V_{bg} := V_b \cdot \frac{A_v}{A_{vo}} = 326.023 \quad \text{kips}$$

Smaller than $n \cdot V_b = 1.544 \times 10^3$ kips

$V_{pg} = 648.356$ kips

For the anchor rod group, the interaction of the shear and tension force interaction is checked using the following equation.

$$\left(\frac{V_t}{V_{bg}}\right)^{\frac{5}{3}} + \left(\frac{N_t}{N_{bg}}\right)^{\frac{5}{3}} = 0.957$$

smaller than 1.0, therefore the anchor rod group design is sufficient to resist the forces.

## AISC (2010)

AISC (2010) provided the following equation for the shear and tension stress checks in the a single anchor rod. The available tensile strength of a anchor rod subjected to combined tension and shear forces shall be determined according to the limit state of tension and shear rupture as follows:

$$R_n = \phi_4 \cdot F_{nt} \cdot A_d$$

where: nominal tensile stress modified to include the effects of shear stress.

$$F_{nt1} = 1.3 \cdot F_{nt} - \frac{F_{nt} \cdot f_s}{0.75 \cdot F_{nv}}$$

the resistance reduction factor is. $\phi_4 := 0.75$

The nominal tensile stress in the anchor rod $F_{nt} := 0.75 \cdot F_u = 43.5$ ksi

The nominal shear stress in the anchor rod $F_{nv} := 0.4 \cdot F_u = 23.2$ ksi

The shear stress in the anchor rod is $f_s := \frac{V_t}{n \cdot A_d} = 9.902$ ksi

The total tension force can be taken by the anchor rod group would be

$$F_{nt1} := 1.3 \cdot F_{nt} - F_{nt} \cdot \frac{f_s}{0.75 \cdot F_{nv}} = 31.795 \quad \text{ksi}$$

$$F_t := n F_{nt1} \cdot A_d \cdot \phi_4 = 449.488 \quad \text{kips}$$

The tension force demand is $N_t = 229.54$ kips

The anchor rod group is sufficient to resist the forces per AISC(2010).